METABOLIC, HEMODYNAMIC AND ELECTROPHYSIOLOGICAL EFFECTS OF TRANSCRANIAL PHOTOBIOMODULATION (tPBM) ON THE HUMAN BRAIN

by

XINLONG WANG

Presented to the Faculty of the Graduate School of

The University of Texas at Arlington in Partial Fulfillment

of the Requirements

for the Degree of

DOCTOR OF PHILOSOPHY

THE UNIVERSITY OF TEXAS AT ARLINGTON

JULY 2017

Acknowledgements

First and foremost I want to thank my advisor Prof. Hanli Liu. I would like to thank her for her patience in training me as a researcher. She taught me to think independently and solve problems innovatively. Also, I appreciate all her spiritual and financial support in my Ph.D. experience. Her professional guidance and powerful encouragement made my dissertation possible.

Furthermore, I appreciate Prof. Francisco Gonzalez-Lima for leading me into the field of Photobiomodulation. His professional knowledge and experience guided me to find the optimized path to reach the goal in research. Also, I would like to thank the rest of my committee members. I appreciate Prof. George Alexandrakis for all of the valuable suggestions in theoretical derivation and experimental design of my research. I am thankful to Prof. Mustafa Husain for his interest in my work and his willingness to be my committee member in a short notice.

On top of that, I should also express my appreciation to my colleagues. Dr. Fenghua Tian provided me a lot of useful suggestions in experimental design and manuscript writing. Mr. Sahil Nalawade and Ms. Divya Reddy helped me with in vivo human photobiomodulation experiments, which significantly increased the speed and efficiency of my research. My senior students Dr. Zijing Lin, Dr. Lin Li and Dr. Venkaiah Kavuri shared their experience with me without any reservation.

Last but not the least, I would like to thank my family: I thank my parents, Mr. Anping Wang and Ms. Na Yu, for giving birth to me at the first place and supporting me financially and mentally throughout my life. I appreciate my wife, Ms. Yujie Hu, and my new born daughter, Olivia Wang, for their emotional support that has kept me going to solve challenging problems during every day and night!

June 13, 2017.

Abstract

METABOLIC, HEMODYNAMIC, AND ELECTROPHYSIOLOGICAL EFFECTS OF TRANSCRANIAL PHOTOBIOMODULATION (tPBM) ON THE HUMAN BRAIN

Xinlong Wang, PhD

The University of Texas at Arlington, 2017

Supervising Professor: Hanli Liu

Photobiomodulation (PBM) refers to the use of red-to-near-infrared light to stimulate cellular functions for physiological or clinical benefits. Transcranial photobiomodulation (tPBM) is a noninvasive form of cerebral photobiomodulation that has been observed with various improvements in human cognitive functions. The mechanism of tPBM is assumed to rely on photon absorption by cytochrome c oxidase (CCO), the terminal enzyme in the mitochondrial respiratory chain that catalyzes the reduction of oxygen for energy metabolism. However, few studies have objectively investigated hemodynamic, metabolic and electrophysiological response of the human brain to tPBM. To address this gap, my dissertation research has focused on objective measures of metabolic, hemodynamic, and electrophysiological effects of tPBM on the human brain, for the first time, by implementing broadband near infrared spectroscopy (bb-NIRS) hardware, designing novel methodology and experiments, developing new data analysis algorithms, and validating the overall development with computer simulations.

Specifically, my dissertation in Chap. 2 validated the bb-NIRS methodology and demonstrated the interplay between increases in [CCO] and hemoglobin concentrations for the first time during PBM, indicating that a hemodynamic response of oxygen supply and blood volume closely coupled to the up-regulation of CCO induced by PBM. In Chap. 3, my research work further confirmed that tPBM can (1) significantly increase cerebral concentrations of oxidized CCO (Δ[CCO]; >0.08 μM; p<0.01), oxygenated hemoglobin (Δ[HbO]; >0.8 μM; p<0.01),

and total hemoglobin (Δ[HbT]; >0.5 μM; p<0.01) during and after the laser stimulation, and (2) also introduce a linear interplay between Δ[CCO] versus Δ[HbO] and between Δ[CCO] versus Δ[HbT]. This study provided the first demonstration that tPBM causes up-regulation of oxidized CCO in the human brain, and contributes important insight into the physiological mechanisms. To discriminate thermal confounding effects of tPBM on the above results, I with my research colleagues conducted human thermal experiments and confirmed, as reported in Chap. 4, that heat-based stimulation would give rise to Δ[CCO] and Δ[HbO] changes opposite to those by tPBM. Furthermore, in Chap 5 I reported a novel algorithm/methodology to quantify absolute concentrations of cytochrome c oxidase (CCO) and other tissue components including oxygenated hemoglobin (HbO), deoxygenated hemoglobin (HHb), water fraction (water%), fat fraction (fat%) and reduced light scattering coefficient by utilizing an Ant colony optimization model. The algorithm utilized characteristic spectral features of the 1st and 2nd derivatives of wavelength-dependent extinction coefficients based on Diffusion Approximation. Computational simulation was performed to verify proper estimation accuracy. Finally, in Chap. 6, I explored the electrophysiological effect of tPBM by collecting 64-channel electroencephalogram (EEG) from each human subject' head during and after tPBM in a placebo-controlled experiment. Dose-dependent increases of EEG power were observed during and after tPBM at five frequency bands. An EEG source-reconstruction algorithm and the Phase Transfer Entropy (PTE) analysis were used to analyze tPBM-induced changes in neural electrophysiology. The results demonstrated strong enhancement of cerebral information flow from selected regions and potential benefit of tPBM to human global cerebral activation and cognitive functions.

Table of Contents

Acknowledgements iii

Abstract iv

List of Illustrations xii

List of Tables xviii

Chapter 1 Introduction 1

1.1 History of PBM 1

1.2 Rationale of This Thesis 1

1.3 Organization of This Thesis 2

Chapter 2 Interplay between up-regulation of cytochrome c oxidase and hemoglobin oxygenation induced by Photobiomodulation 5

2.1 Introduction 5

2.2 Material and Methods 7

2.2.1 Participants 7

2.2.2 Instruments 8

2.2.3 Experiments 11

2.2.4 Theoretical Foundation for Data Processing and Error Analysis 12

2.2.5 Multiple Linear Regression Analysis 15

2.2.6Statistical Analysis 17

2.3 Results 17

2.4 Discussion 19

2.4.1 Interplay between up-regulation of CCO and hemoglobin oxygenation induced by PBM 20

2.4.2 Rationale of using 1064-nm laser for photobiomodulation 22

2.4.3 Measurement accuracy of bb-NIRS on CCO quantification 23

2.4.4 Possible thermal effects of PBM on CCO quantifications 23

2.5 Conclusion 25

Chapter 3 Up-regulation of cerebral cytochrome-c-oxidase and hemodynamics by transcranial photobiomodulation: a broadband near-infrared spectroscopy study 26
3.1 Introduction 26
3.1.1 Transcranial Photobiomodulation 26
3.1.2 Near infrared spectroscopy 27
3.1.3 Novel approaches and findings of this study 28
3.2 Methods 29
3.2.1 Participants 29
3.2.2 Instruments 29
3.2.3 Experiments 31
3.2.4 Data Processing and Statistical Analysis 33
3.3 Results 34
3.3.1 Time courses oftPBM-inducedΔ[CCO], Δ[HbO], Δ[HHb],Δ[HbT], and Δ[HbD] 34
3.3.2 Dependence of cerebral hemodynamic parameters on tPBM-induced cerebral Δ[CCO] 36
3.3.3 tPBM-induced ratios of cerebral Δ[CCO] to increased cerebral hemodynamic parameters 38
3.4 Discussion 40
3.4.1 New findings of this study 40
3.4.2 Comparison of the results between this study and previous ones 41
3.4.3Interpretation of tPBM mechanism 42
3.4.4 tPBM-induced metabolic-hemodynamic coupling 45
3.4.5 Limitations of this study and future work 48
3.5 Conclusion 50
Chapter 4 Impact of heat on hemodynamic and metabolic changes in transcranial photobiomodulation measured by broadband near-infrared spectroscopy 51
4.1 Introduction 51
4.2 Methods 52

4.2.1 Brief review of previous TILS setup and measurements 52
4.2.2 Human subjects participated in TILS and thermal experiments 54
4.2.3 Experimental setup and instruments for thermal stimulation measurements 55
4.2.3 Experimental protocols 59
4.2.3.1Forehead skin-temperature recording in response to tPBM 59
4.2.3.2 Cerebral metabolic and hemodynamic responses to thermal effects/stimulation 60
4.2.4 Data Processing and Statistical analysis 62
4.3 Results 63
4.3.1tPBM-induced time-dependent changes in concentrations of CCO, HbO, HHb, HbTand HbD 63
4.3.2 Dependence of cerebral hemodynamic parameters based on thermal-induced metabolic changes 66
4.4 Discussion 68
4.4.1 Hemodynamic and metabolic responses of forehead tissue to thermal stimulation 68
4.4.2 Possible explanation of heat-induced changes in hemodynamic signals of forehead tissue 69
4.4.3 Limitation of the study and future work 70
4.5 Conclusion 71
Chapter 5 A novel absolute value quantification algorithm for hemoglobin and CCO 72
5.1 Introduction 72
5.2 Methods 74
5.2.1 Algorithm 74
5.2.2 Simulation 76
5.2.2.1 Initial settings 76
5.2.2.2 Ant-colony optimization 77
5.2.2.3 Fitting protocols 78
5.2.3 In vivo experiments 78

5.2.3.1 Participants 78
5.2.3.2 Data acquisition 80
5.3 Results 83
5.4 Discussion 90
5.5 Conclusion 95
Chapter 6 Imaging of human electrophysiological response to tPBM in vivo measured by electroencephalography 96
6.1 Introduction 96
6.1.1 Background 96
6.1.2 Mechanism of Photon-Tissue interaction 96
6.1.3 Electroencephalography 97
6.2 Experimental Methods 98
6.2.1 Participants 98
6.2.2 Experimental setup 99
6.2.3 Experiments 100
6.2.4 Data analysis 101
6.2.4.1 eLORETA 101
6.2.4.2 Phase Transfer Entropy analysis 102
6.2.4.3 Data processing steps 104
6.3 Results 109
6.3.1 Placebo-controlled, time-frequency maps at selected electrodes 109
6.3.2 Improvement of cortical EEG power 111
6.3.3 Enhancement of cerebral information flow during and after tPBM 116
6.4 Discussion 118
6.4.1 Physiological explanation of photon-neuron interaction 119
6.4.2 tPBM holds the potential of photobiomodulating human DMN 121
6.4.3 Possible thermal effects 121
6.4.4 Comparison of mechanism between tPBM versus tDCS and TMS 122

6.4.5 Verification of identical baseline between tPBM and placebo 123
6.4.6 Possible improvement with a larger sample size 123
6.5 Conclusion 124
Chapter 7 Conclusion and future scope 125
7.1 Conclusion 125
7.2 Future scope 125
7.2.1 Depth dependency of tissue response to tPBM 125
7.2.2 Determination of the optimized tPBM wavelength and dosage 126
7.2.3 Estimation on lasting effects of post-tPBM 127
7.2.4 Direct measurement of neuronal activation by tPBM on animals 127
7.2.5 Investigation of the tPBM-induced heat effect on EEG 128
Appendix 129
A. Understanding the bases of Diffuse Correlation Spectroscopy (DCS): the initial contribution to a laboratory customized DCS system. 129
A.1 Diffuse correlation spectroscopy (DCS) study of blood flow changes during low level laser therapy (LLLT) – A preliminary report 129
B. Application of broadband spectroscopy in prostate cancer detection 129
B.1 Light Reflectance Spectroscopy to Detect Positive Surgical Margins on Prostate Cancer Specimens 129
B.2 Detecting Positive Surgical Margins: Utilization of Light Reflectance Spectroscopy on ex vivo Prostate Specimens 129
C. Frequency resolved measurement in prostate cancer detection 129
C.1Measurement of optical properties of ex vivo prostate tissues and design of trans-rectal ultrasound coupled optical probe 129
C.1.1 Introduction 146
C.1.2 Materials and Methods 149
C.1.2.1 Instruments 149
C.1.2.2 Experiments 151

C.1.2.3 Modeling 154
C.1.2.4 Statistical analysis 155
C.1.3 Results 156
C.1.4 Discussion 159
C.1.5 Conclusion 164
Reference 166
Biographical Information 186

List of Illustrations

Figure 1-1 Flowchart of the dissertation organization 3

Figure 2-1Schematic diagram of the experimental setup, including the broadband NIRS system. This bb-NIRS consisted of a tungsten halogen lamp as light source and a miniature back-thinned CCD spectrometer as detector. A laptop computer was used to acquire, display and save the data from the spectrometer. The shutter controlled the on and off of the white light from the tungsten halogen lamp. 9

Figure 2-2 Experimental setup: (a) photograph of the laser aperture for PBM/placebo treatment and bb-NIRS fiber holder on a participant's forearm. (b) Configuration of the I-shaped bb-NIRS probe holder (dark gray). The bundle holder held two optical fiber bundles with a separation of 1.5 cm. One bundle (in red) was connected to the tungsten halogen lamp and the other (in blue color) to the spectrometer. The PBM/placebo treatments were administered on two sides of the middle section alternatively (pink circles). 10

Figure 2-3 Paradigm of the PBM/placebo treatment and interleaved bb-NIRS data acquisition. Each treatment session consisted of eight one-minute treatment cycles, 55-s laser on and 5-s laser off per cycle. The bb-NIRS data acquisition was initiated two minutes before the first treatment session and ceased five minutes after the treatment session. 12

Figure 2-4 A flow chart describing detailed procedures of my multiple linear regression analysis to optimally determine PBM-induced concentration changes in three chromophores. 15

Figure 2-5 PBM/placebo-induced concentration changes of (a) [HbO], (b) [HHb], and (c) [CCO] in human forearms in vivo (mean ± SE, n=11). In each subplot, the pink-shaded region indicates the period of PBM/placebo treatment; * indicates significant differences in respective concentrations between PBM and placebo treatment ($0.01 < p < 0.05$, paired t-test). ** indicates significant differences in respective concentrations between PBM and placebo treatment ($p < 0.01$, paired t-test). 18

Figure 2-6 The relationship of concentration changes between CCO vs. HbO or HHb during PBM and placebo experiment (mean ± SE, N = 11). The horizontal error bars represent variability of CCO and the vertical error bars represent variability of HbO or HHb. The correlation coefficient of the fitted line is $r=0.92$ with a p value of 0.001. 19

Figure 2-7Concentration changes of (1) HbO, (2) HHb and (3) CCO during LLLT (red; n=11), placebo (blue; n=11) and thermal (green; n=4) stimulation. The "*" represents significant difference between LLLT vs thermal effect (p-value <0.05). 24
Figure 3-1Schematic diagram of the experimental setup, including a bb-NIRS spectroscopic system. This bb-NIRS unit consisted of a tungsten halogen lamp as the light source and a miniature high-sensitivity CCD spectrometer as the detector for this study. tPBM was administered underneath the "I" shaped probe holder. The narrow, middle section of the holder was ~8 mm in width. A laptop computer was used to acquire, display and save the data from the spectrometer. The shutter controlled the on and off function for the tungsten-halogen lamp to subject's forehead. A pair of protection goggles was worn during the whole experimental procedure. 30
Figure 3-2 Paradigm of the tPBM/placebo treatment and interleaved bb-NIRS data acquisition. Each treatment session consisted of eight one-minute treatment cycles: 55-s laser on and 5-s laser off per cycle. During the 5-s laser-off periods, the bb-NIRS system (both the light source and detector) was switched on for bb-NIRS data acquisition. The same data acquisition format was followed for baseline and recovery sessions. 32
Figure 3-3Subject-averaged time courses of tPBM/placebo-induced cerebral changes of (a) [HbO], (b) [HHb], (c) [HbT], (d) [HbD], and (e) [CCO] (all in μM) recorded from human foreheads in vivo (mean ± SE, n=11). Time zero (t=0) is the onset of tPBM. In each subplot, the shaded region indicates the period of tPBM/placebo treatment. "*" indicates significant differences (0.01 <p<0.05, two sample t-test) in respective concentrations between tPBM and placebo treatment. "**" indicates significant differences (p<0.01, two sample t-test) in respective concentrations between tPBM and placebo treatment. 35
Figure 3-4 (a) Relationships between subject-averaged Δ[CCO] vs. Δ[HbO] and Δ[CCO] vs. Δ[HHb] that resulted from tPBM and placebo treatment (mean ± SE, N = 11). Solid red diamonds display the relationship of Δ[CCO] vs Δ[HbO]; solid blue dots display the relationship of Δ[CCO] vs Δ[HHb]. Both red open diamonds and blue open squares represent placebo-treated Δ[CCO] vs.Δ[HbO] and Δ[CCO] vs.Δ[HHb], respectively. (b) Relationships between subject-averaged Δ[CCO] vs. Δ[HbT] and Δ[CCO] vs. Δ[HbD] caused by tPBM and placebo treatment. Solid purple circles display the relationship of Δ[CCO] vs Δ[HbT]; solid black triangles display the relationship of Δ[CCO] vs Δ[HbD]. Both red open circles and open

triangles represent placebo-treated Δ[CCO] vs.Δ[HbO] and Δ[CCO] vs.Δ[HHb], respectively. All error bars represent standard errors of means from respective chromophore concentrations. 36
Figure 3-5Ratios of (a) Δ[CCO]/Δ[HbO], (c) Δ[CCO]/Δ[HbT], and (e) Δ[CCO]/Δ[HbD] during and after infrared laser stimulation on the right forehead of 11 human subjects (red symbols) and on the right forearm of another group of 11 human subjects (blue symbols). Time-averaged ratios of (b)Δ[CCO]/Δ[HbO], (d) Δ[CCO]/Δ[HbT], and (f) Δ[CCO]/Δ[HbD] with corresponding standard deviations in both forearm and forehead stimulation cases. "**" marks significant difference ($p<0.01$, two sample t-test) of Δ[CCO]/Δ[HbO] or Δ[CCO]/Δ[HbT] between the stimulated cases."*" marks significant difference ($p<0.05$, two sample t-test) of Δ[CCO]/Δ[HbD] between the stimulated cases. 38
Figure 3-6(a) Model of the photobiochemical mechanism of action of infrared light on the measured cytochrome c oxidase oxidation (CCO oxidized) and hemoglobin oxygenation (HbO2). See text for detailed explanation. (b) The right most panel shows a pyramidal neuron of the cerebral cortex, which is modified from a figure in ref. [68]. The middle dashed rectangle is a zoomed section of apical dendrite, containing an abundant amount of mitochondria, with which CCO can be photo-stimulated and oxidized by tPBM. This photobiomodulation consequently drives increases of HbO, HbT, and HbD. (c) A flow chart to show the conventional neuro-vascular coupling by the black-colored notations and my newly-defined tPBM-induced metabolic-hemodynamic coupling by the red-colored notations. The blue-colored notations represent common endpoints of both mechanisms on the cerebral circulation. The dashed lines represent exclusion from the metabolic-hemodynamic coupling. 45
Figure 4-1 Schematic diagram of the experimental setup for TILS, including a bb-NIRS spectroscopic system. This bb-NIRS unit consisted of a tungsten halogen lamp as the light source and a miniature CCD spectrometer as the detector. TILS was administered underneath the "I" shaped probe holder. The narrow, middle section of the holder was ~8 mm in width. A laptop computer was used to acquire, display and save the data from the spectrometer. A shutter controlled the on and off function for the white light from the tungsten-halogen lamp to the subject's forehead. A pair of protection goggles was worn during the whole experimental procedure. [14] 53
Figure 4-2 Schematic diagram of the experimental setup for the skin-temperature-recording experiment that included a temperature measurement system (TempTraq™,Blue Spark Technologies, Inc. Westlake,

Ohio). The TempTraq unit/patch includes a small thermal sensor (5x5 mm^2), as shown in the figure, and a temperature circuit to determine the temperature value induced by tPBM on the forehead skin surface. The tPBM was delivered on the right side of the TempTraq patch, which was connected via Bluetooth to a mobile device. Protection goggles were worn by the participants during the entire experimental procedure. 56

Figure 4-3 Schematic diagram of the experimental setup for the 2nd phase of experiment using a bb-NIRS monitoring system. The spectroscopic system consisted of a tungsten-halogen lamp as the light source and a high-sensitive CCD spectrometer as the detector. Thermal stimulation was administered above the I-shaped probe holder, which held two optodes with 3 cm apart. A shutter was used for switching the light delivery on and off from the lamp to the participant's forehead. The data from the spectrometer was collected, saved and displayed using a laptop computer. 58

Figure 4-4 Forehead skin-temperature increases during and post tPBM. It displays local skin temperatures of the forehead near the tPBM site. The red curve displays measured temperatures of the skin near the laser (CG -5000) delivery site from the first phase measurement. Each red point displays a single value which was averaged over 1 minute of the thermal data (mean over n=11). The blue curve shows the thermal setting values on the thermal stimulator (Medoc Pathway) used in the second phase of the experiment. Time zero marks the starting time of tPBM delivery. 60

Figure 4-5 Paradigm of the bb-NIRS white light source interleaved with thermal stimulation and bb-NIRS data acquisition. Each experiment consists of 2-min baseline, 8 min of thermal stimulation and 5-min of recovery. The light source is switched on for 5-s for NIRS data acquisition and switched off for the rest of the time in each minute. During the thermal stimulation, there is a gradual increase from the baseline and after 3-min the desired temperature is reached and the temperature was kept constant until the stimulation period ends. 62

Figure 4-6 Participant–averaged time courses of TILS (laser) and heat (thermal) effects on changes in (a) [HbO], (b) [HHb], (c) [HbT], (d) [HbD], and (e) [CCO], measured in vivo from each participant's forehead (mean ± SE, n=11). The initial time at t=0 marks the onset of the TILS/thermal stimulation. The shaded region in each panel displays the stimulation period. The unit for all concentration changes is in μM. In each panel, "*" symbols mark statistical significance with $p<0.05$ (Bonferroni corrected) between TILS-

induced and heat-induced chromophore concentration changes, based on a repeated-measure ANOVA followed by one way ANOVAs. 65
Figure 4-7 (a) Relationships of Dependence between Δ[CCO] vs. Δ[HbO] and Δ[CCO] vs. Δ[HHb] across all subjects (n=11) under the effect of thermal stimulation and tPBM. The solid black diamonds and solid tan squares show the relationship of Δ[CCO] vs. Δ[HbO] and Δ[CCO] vs. Δ[HHb] respectively. Both the open diamonds and squares symbolize tPBM-treated Δ[CCO] vs. Δ[HbO] and Δ[CCO] vs. Δ[HHb], respectively.(b) Relationships of Dependence between Δ[CCO] vs. Δ[HbT] and Δ[CCO] vs. Δ[HbD] across all subjects (n=11) under the effect of thermal stimulation and tPBM. The solid black circles and solid gray triangles illustrate the relationship of Δ[CCO] vs. Δ[HbT] and Δ[CCO] vs. Δ[HbD] respectively. Both the open circles and triangles denote the tPBM-treated relationships. The standard errors of means are also plotted from their respective concentrations of the chromophore.. 67
Figure 5-1. The first derivative–spectral expression of the original photon–diffusion–approximation equation (black circles) and the simplified version (red line). 76
Figure 5-2. The experimental setup for frequency-resolved and CW measurements. The frequency-resolved system consists of two probes and four wavelengths. Each probe detects scattering and absorption properties at two wavelengths. The two probes share the same source-detector geometry. For CW measurement, the yellow box represents the white light source and the blue box represents the spectrometer. The source-detector separation is 3 cm on human foreheads and 1.5 cm on human forearms. 80
Figure 5-3The measured locations by bb-NIRS on human forearms and foreheads. 82
Figure 5-4. A comparison among scattering power measured from human participants versus the literature values—0.9 for human forearms and 1.2 for human heads, respectively. The light gray bar represents scattering power on human forearms (N = 20), and the dark gray bar represents scattering power on human foreheads (N = 18). One sample t-test was performed between the measured data versus literature values, no significant difference was observed in both cases. 83
Figure 5-5. The estimation errors of each parameter under different noise levels with initial settings of (a) combination 1 in Table 5-1; (b) combination 2 in Table 5-1; (c) combination 3 in Table 5-1; and (d) combination 4 in Table 5-1. The blue curves denote the fitting with the first derivative only, the green

curve denotes the fitting with the second derivative only, and the red curve denotes the fitting using both the first and second derivatives. 88
Figure 5-6. The estimation of HbO, HHb, CCO, and the scattering coefficient at 750 nm on 20 human forearms and 18 human foreheads. The error bar denotes the standard deviation of mean. 89
Figure 5-7. The estimation of water%, fat%, and oxygen saturation on 20 human forearms and 18 human foreheads. The error bar denotes the standard deviation of mean. 89
Figure 5-8. The χ2 of fitting with noise levels of (I) 2%; (II) 10%; and (III) 18%. In each figure, (a), (b), (c), and (d) show different views of the scattering factor's related χ2 map. m denotes the scattering size, which ranges from 0–30. n denotes the scattering power, which ranges from 0–3. The color bar denotes the scale of χ2. 92
Figure 6-1The EEG experimental set up of tPBM on human foreheads. 99
Figure 6-2The diagram of stimulation and EEG recording period 101
Figure 6-3 Diagram of Phase Transfer Entropy algorithm 102
Figure 6-4 Data processing steps for time-frequency analysis 106
Figure 6-5 The data processing steps for the 3D cortical reconstruction modals 107
Figure 6-6 Time-frequency maps at 6 selected electrodes 109
Figure 6-7 3D reconstructed cortical activation tomographic images at (a) Alpha, (b) Beta, and (c) Gamma frequency. Yellow color marks the regions with significant improvement of EEG spectral power by tPBM compared with the placebo condition. "T" denotes the tPBM sections and the "R" represents the recovery periods. The threshold of $|T| \geq 2.5$ was set to filter out less significant regions and highlighted the cortical regions with significant improvement (p-value < 0.01). Significant increment is represented by yellow color. Significant deactivation is represented by blue color. The number of subjects was 20 for both tPBM and placebo experiments. 114
Figure 6-8 The enhancement of information flow during and after tPBM (a) from Fp2, (b) from AFz. Red lines mean significant enhancement of ex-flux of information from the ROI, and blue lines mean significant enhancement of information influx to the ROI. T-value was set as $|T| > 1.7$ (p-value<0.05). .. 118
Figure 6-9The flow chart of physiological explanation of photon-neuron interaction. 119

List of Tables

Table 3-1 Comparison of laser-induced metabolic-hemodynamic coupling strength 47

Table 5-1 Initial settings of different parameters in simulation. 76

Table 5-2 Subject information and scattering properties measured by frequency-resolved system on human forearms 79

Table 5-3Subject information and scattering properties measured by frequency-resolved system on human foreheads. 79

Table C-1 Table showing number of measurements made per tissue type 156

Table C-2 Comparison of optical properties of prostate and various wavelengths in literature 163

Chapter 1

Introduction

1.1 History of PBM

Photobiomodulation (PBM) uses red to infrared light to stimulate human tissue functions. The initiation of this technique originated back in year 1967, when Endre Mester in Semmelweis University, Budapest, Hungary was planning to use a 694nm laser to induce cancer on mice[1]. He divided the mice into control and treatment groups respectively. Mice hair in both groups were shaved. Then he started to conduct the 694nm laser on the shaved area of mice tissue with an expectation of generating cancer. However, eventually instead of getting cancer, the mice in the treatment group were observed with faster hair regeneration speed than the control group. This accidental finding marked the first definition of "Photobiomodulation" and the initiation of its revolutionary development in biomedical stimulation. Nowadays, PBM has been used to improve wound healing [2, 3], reduce pain [4, 5], and many other human applications. The light can be supplied by lasers or light-emitting diodes (LEDs). In recent years, transcranial PBM has gained increased recognition for its therapeutic use in various neurological and psychological conditions, including ischemic stroke [6, 7], chronic traumatic brain injuries [8, 9], and depression [10, 11].

1.2 Rationale of This Thesis

The behavioral effects of tPBM were observed in many research and clinical studies. The mechanism of photobiomodulation on cognitive function was proposed to rest on high photon absorption by cytochrome c oxidase (CCO)[12, 13], the terminal enzyme in the mitochondrial respiratory chain that catalyzes 90% of oxygen and energy metabolism[14]. Increases in CCO activity results in greater oxygen consumption and metabolic energy production via mitochondrial oxidative phosphorylation[15]. The dendrite of a neuron contains a

large number of mitochondria, which makes it more sensitive to tPBM[14]. As a result of optical absorption, the photobiomodulation of CCO in neuron cells results in a vast production of ATP[16]. Thus, neuronal activity is then activated in cerebral neuron network, which is proposed as the essential mechanism of human cognitive function improvement. However, there is lack of objective physiology evidences to support the theory. Overall, this dissertation focuses on (1) the establishment of a broadband near-infrared spectroscopy system for detecting the change of chromophore concentrations. (2) Designing and developing of a feasible placebo controlled experimental protocol to perform PBM on human tissue (forearms and foreheads). (3) Measuring and understanding the hemodynamic and metabolic response of tPBM on human forearms and foreheads. (4) Measuring and separating the physiological effect of heat from tPBM. (5) Developing and validating a novel absolute value quantification algorithm for human hemoglobin and cytochrome c oxidase detection. (6) Measuring and understanding the electrophysiological response of human brain to tPBM by EEG.

1.3 Organization of This Thesis

As it is shown in Figure 1-1, this dissertation has 7 chapters, which consist of two peer reviewed publications (Chapter 2 and Chapter 3), one submitted manuscripts (Chapter 4) and two manuscripts that are ready to submit (Chapter 5 and 6). Chapter 1 is a brief introduction of the history of tPBM and the current problems in verifying its physiological mechanism. In Chapter 2, a broadband near-infrared spectroscopy system was established for measuring concentration change of hemoglobin and cytochrome c oxidase. In the meantime, the initial observation of PBM effect on human forearms were reported. In Chapter 3, the physiological effect of tPBM on human brain was explored, the oxygen utilization rate were compared between human arm and brain. In Chapter 4, potential thermal effects were investigated and excluded to purify the tPBM function. To further develop the algorithm in concentration estimation, a novel absolute value calculation algorithm was established and validated by

computational simulation and in vivo human measurements in Chapter 5.In Chapter6, electrophysiological response including cortical power and information flow during and after tPBM were measured and imaged. Finally, Chapter 7 concludes the dissertation and provides directions for future work.

The appendix contains the NIRS and broadband spectroscopy related research topics that I was involved in the first 1.5 years of my research at UT Arlington. It can be divided into three sections. The first section (i.e. Section A) demonstrates the establishment of a laboratory customized diffuse correlation spectroscopy (DCS) system with its preliminary application for monitoring PBM effect on human arms. The second section (i.e. Section B) is about the applications of broadband spectroscopy in prostate cancer identification, which consist two peer reviewed publications. The third section (i.e. Section C) reports the frequency resolved measurements for prostate cancer detection and imaging, which includes one manuscript that is ready for submission.

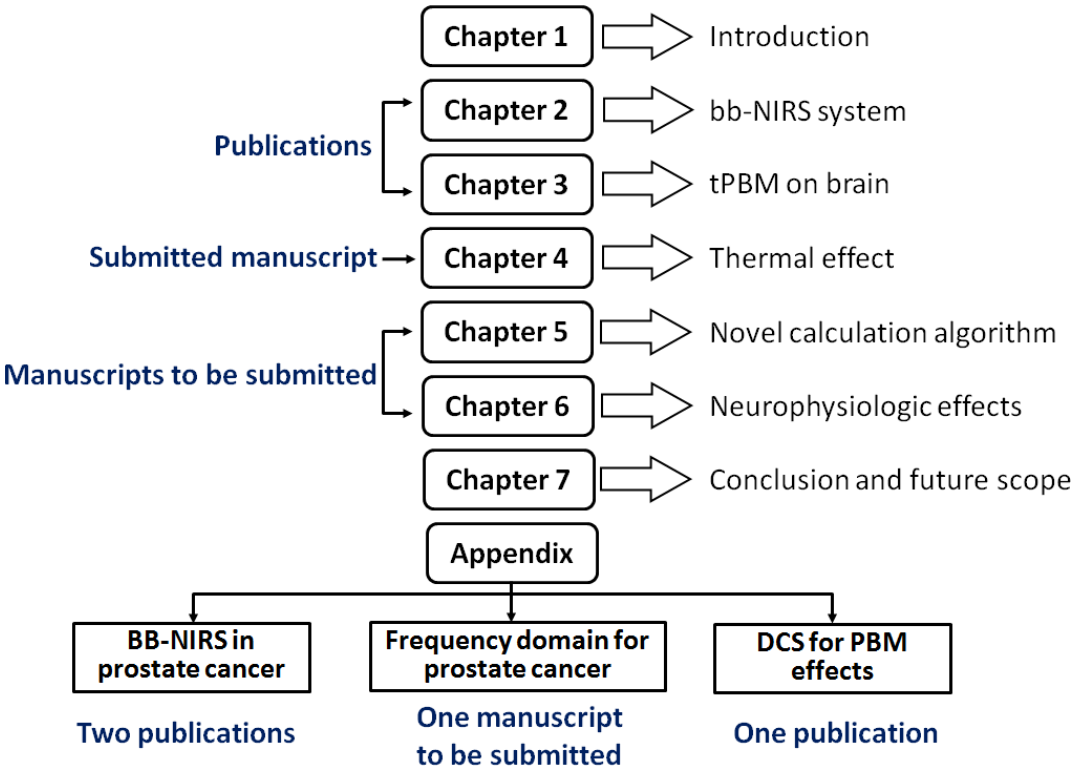

Figure 1-1 Flowchart of the dissertation organization

All in all, Chapter 2 to Chapter 7 demonstrate my major PhD research work from June 2015 to July 2017. And the appendix illustrates the research work from Jan 2013 to May 2015 prior to my conversion to PhD track.

Chapter 2

Interplay between up-regulation of cytochrome c oxidase and hemoglobin oxygenation induced by Photobiomodulation

This chapter is a publication at the journal of Scientific Report on 03 August 2016.(Scientific Reports, vol. 6, p. 30540, 2016.)

***Authorship**: Xinlong Wang*, Fenghua Tian*, Sagar S. Soni, F. Gonzalez-Lima & Hanli Liu*

2.1 Introduction

Low-level laser/light therapy (PBM), also known as photobiomodulation (PBM), refers to the use of low-level light in the red-to-near-infrared range (620–1100 nm) to stimulate cellular functions for physiological or clinical benefits. Photobiomodulation has been used to improve wound healing [2, 3], reduce pain [4, 5], and many other human applications. The light can be supplied by lasers or light-emitting diodes (LEDs). In recent years, PBM has gained increased recognition for its therapeutic use in various neurological and psychological conditions, including ischemic stroke [6, 7], chronic traumatic brain injuries [8, 9], and depression [10, 11]. Furthermore, using a 1064-nm laser, Barrett and Gonzalez-Lima conducted the first placebo-controlled studies demonstrating that PBM to the forehead benefits cognition in healthy humans, including enhanced attention, working memory, and executive functions [17-19].

The mechanism of photobiomodulation is proposed to rest on photon absorption by cytochrome c oxidase (CCO) [12], the terminal enzyme in the mitochondrial respiratory chain that catalyzes the reduction of oxygen for energy metabolism [2, 3, 20, 21]. The more the activity of CCO increases, the more oxygen consumption and metabolic energy is produced via mitochondrial oxidative phosphorylation [15]. Since CCO is an inducible enzyme, a longer-lasting metabolic effect is achieved by PBM's up-regulating CCO concentration, which in turn enhances the capacity for cellular oxygen metabolism [13]. Because neurons are cells highly

dependent on oxygen metabolism, this photonics-bioenergetics mechanism results in metabolic and hemodynamic alterations that facilitate neuronal functioning [20, 22]. To date, most research into effects of PBM on mitochondrial enzymes has been conducted in cultured neurons [2, 3] and animal brains [23] with invasive means. There is lack of experimental or direct observation on how PBM modulates CCO levels and how the up-regulated enzyme affects or interplays with hemodynamic oxygenation in human tissues in vivo. The primary goal of this study was to utilize an experimental optical imaging approach to observe PBM-induced up-regulation of CCO and its relationship with hemoglobin oxygenation in human forearms for better understanding and validation of photobiomodulation in vivo effects.

Near-infrared spectroscopy (NIRS) [24] is a non-invasive and portable technology that can be used to probe biological and physiological states of living tissues based on the level of absorption and scattering of near-infrared light. In the past two decades, NIRS has been broadly investigated for quantification of oxygenated and deoxygenated hemoglobin concentrations (i.e., [HbO] and [HHb], respectively) in a variety of tissues[25], such as the human breast [26-28], the human prostate [29, 30], and the human brain [28, 31], in order to diagnose cancers or to map/image functional brain activities in vivo. In conventional NIRS, two or three wavelengths are adequately employed for characterizing cerebral or tissue HbO and HHb concentrations under different stimulations or psychological conditions. Based on the same working principle, I have recently utilized dual-wavelength NIRS to assess the hemodynamic effects of transcranial PBM (tPBM) in the human brain in vivo. I found that transcranial 1064-nm laser improved cerebral oxygenation, indicated by an increase of [HbO] and a decrease of [HHb] in a dose-dependent manner [32]. However, because of the limited number of measuring wavelengths in dual-wavelength NIRS, I was not able to reliably quantify any change or elevation of CCO. As the mechanistic action of PBM relies on direct photo-activation of CCO, it is crucial to quantify the PBM-induced CCO changes as well. Thus, further improvement in my methodology was sought in order to address this critical need.

Since the initial development of NIRS technology, a significant amount of research effort has been persistently made to utilize broadband NIRS (bb-NIRS) for calculating the redox state of CCO based on its absorption band at 820-840 nm [33]. While the actual implementation of this approach started more than 20 years ago [34, 35], it had uncertainty on the accuracy of the methodology [33, 36, 37]. It is only in recent years when bb-NIRS has been reported by numerous publications to be a reliable means for computing both cerebral hemoglobin and CCO concentration changes during brain activations [38-40] and/or brain injury [41, 42]. Therefore, bb-NIRS has become a unique and valid tool to facilitate my measurement of PBM-induced up-regulation of CCO and its relationship to the alteration of hemoglobin oxygenation in treated tissues. I investigated human forearms as a model to reduce tissue heterogeneity during photobiomodulation and to avoid the complication of extra-cerebral layers (i.e., the human scalp and skull). The current study applied PBM on human forearms using a 1064-nm laser and interleaved the bb-NIRS data acquisition in vivo for simultaneous assessment of interplay between photoactivation/up-regulation of CCO and alteration of hemoglobin oxygenation of the treated tissue.

2.2 Material and Methods

2.2.1 Participants

Eleven healthy human participants were recruited from the local community of The University of Texas at Arlington. Interested individuals were screened by one of the investigators to determine whether they were eligible for the study. The inclusion criteria included: either sex, any ethnic background, and in an age range of 18–40 years old. The exclusion criteria included: (1) diagnosed with a psychiatric disorder, (2) history of a neurological condition, or severe brain injury, or violent behavior,(3) have ever been imprisoned, (4) current intake of any medicine or drug, or (5) currently pregnant. In addition, none of the participants

were smokers or had diabetes. Eligible participants underwent two separate experiments in sequence: in the first experiment, placebo treatment was administered on their right forearms. In the second experiment, PBM was administered on the same location as in the placebo treatment, 5 min after the first experiment. The study protocol was approved by the institutional review board (IRB) at The University of Texas at Arlington and complied with all applicable federal and NIH guidelines. Informed consent was obtained from each participant prior to the experiments.

2.2.2 Instruments

Both placebo and laser treatments were administered with a continuous-wave, 1064-nm laser provided by Cell Gen Therapeutics LLC, Dallas, TX (Model CG-5000). This laser is an FDA-cleared device for various uses on humans, such as relief of muscle and joint pain. It had a hand-held aperture with a button on the handle to open and shut the laser beam. The area of laser beam from the aperture was 13.6 cm^2. Contact delivery is relevant when laser beams are divergent and not well collimated. But in my case, the laser was well collimated, so the laser beam size did not change significantly between the laser aperture and the stimulation spot on the subject's forearm. The non-contact delivery distance was about 2 cm with possible variation of a few millimeters because of the handheld setting. However, such a distance variation did not result in dose fluctuation in laser radiation due to excellent laser collimation. For the laser treatment, the device was operated at a constant power of 3.4 W. The irradiance (or power density) in the beam area was 0.25 W/cm^2, the same as that used in my previous studies [17, 18, 32]. For the placebo treatment, the same device was operated at a minimal power of 0.1 W and the aperture was further covered up by black tapes so that no light came out from the covering tapes. Thus the actual laser power of placebo was zero.

While I used a FDA-cleared Class 4 infrared laser (International standard IEC 60825-1), this laser was used at a lower power density corresponding to that of a Class 3b laser to avoid

potential skin damage. The power density used was 0.25 W/cm^2 (whereas over 0.5 W/cm^2 is used for Class 4 classification). Following previously successful studies with full IRB approvals, my safe laser stimulation parameters were calculated as follows:

Total laser power = 3.4 W;

Area of laser beam radiation = 13.6 cm^2;

Power density = 3.4 W/13.6 cm^2 = 0.25 W/cm^2;

Time radiated per cycle = 55 s;

Total laser energy dose per cycle = 3.4 W $\times$ 55 s = 187 J/cycle.

If another laser with a smaller beam size is used, the total laser power should be adjusted in order to maintain the same safe low power density of 0.25 W/cm^2 and thus avoid potential skin damage.

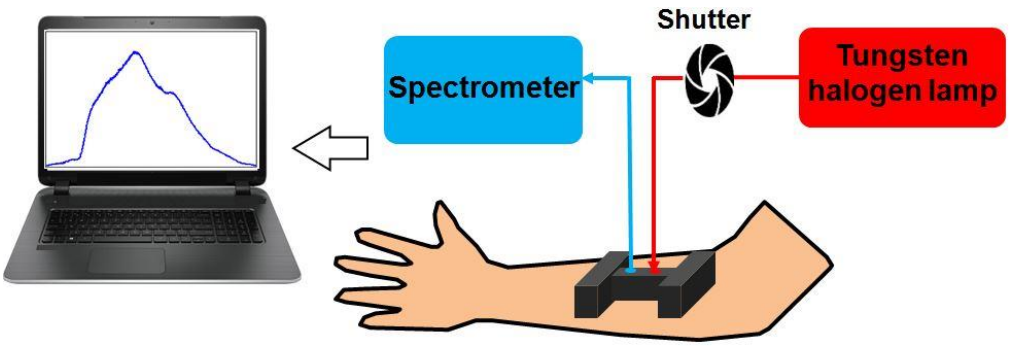

Figure 2-1Schematic diagram of the experimental setup, including the broadband NIRS system. This bb-NIRS consisted of a tungsten halogen lamp as light source and a miniature back-thinned CCD spectrometer as detector. A laptop computer was used to acquire, display and save the data from the spectrometer. The shutter controlled the on and off of the white light from the tungsten halogen lamp.

A single-channel, bb-NIRS system was constructed to measure changes of hemoglobin and CCO concentrations in vivo in PBM and placebo experiments. As shown in Fig. 2-1, this system consisted of a tungsten halogen lamp (Model 3900, Illumination Technologies Inc., East Syracuse, NY) as light source and a miniature back-thinned CCD spectrometer (i-trometer, B&W Tek Inc., Newark, DE) as light detector, in the spectral range of 450-1100 nm. Broadband

white light from the lamp was relayed by an optical fiber bundle of 3.5-mm in diameter to a shutter and then to an I-shaped optical probe holder that was placed on each subject's right forearm. The diffuse light through the arm tissue was collected by another fiber bundle held by the same probe holder and then relayed to the spectrometer. The distance between the source and detector fiber bundles was 1.5 cm. A laptop computer was used to acquire, display and save the data from the spectrometer. The shutter controlled the on and off of the white light delivered to the tissues.

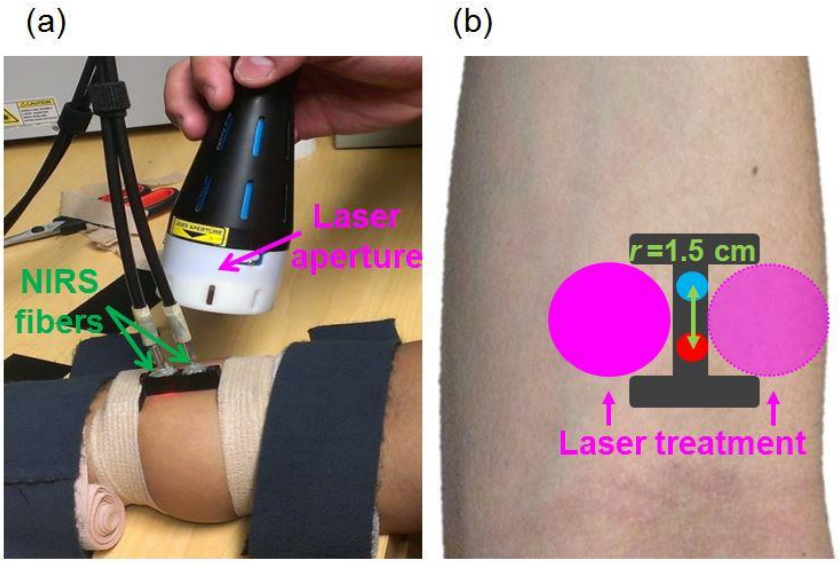

Figure 2-2 Experimental setup: (a) photograph of the laser aperture for PBM/placebo treatment and bb-NIRS fiber holder on a participant's forearm. (b) Configuration of the I-shaped bb-NIRS probe holder (dark gray). The bundle holder held two optical fiber bundles with a separation of 1.5 cm. One bundle (in red) was connected to the tungsten halogen lamp and the other (in blue color) to the spectrometer. The PBM/placebo treatments were administered on two sides of the middle section alternatively (pink circles).

In particular, the I-shaped fiber bundle holder was designed using SolidWorks (SolidWorks Corp., USA) and 3D printed with solid, black material. The two wider ends of the holder were firmly fastened on each participant's right forearm with elastic bandages (see Fig. 2-2a). As each participant might have slight body movements during the corresponding experiment, this experimental setup minimized potential motion artifacts during data acquisition.

The narrow, middle section of the holder is ~8 mm in width. In both experiments, the laser beam from CG-5000 was administered on both sides of this section alternatively (see Fig. 2-2b).

2.2.3 Experiments

The experiments were conducted in a locked room without any reflective surface. The background light from outside of the room was minimized by covering the windows and door slits with black curtains. Furthermore, when the laser was in use, a warning sign of “Laser on” was shown on the outer door. Protective goggles (900−1000 nm: 5+, 1000−2400 nm: 7+; 2900−10600 nm: 7+) were worn by all individuals present in the room. The participants were further instructed to close eyes during the treatments. After each participant was comfortably seated, an experimenter first measured the absorption coefficient (μ_a) and reduced scattering coefficient (μ_s') at 750 nm and 830 nm from the participant’s right forearm using a frequency-domain NIRS tissue oximeter (OxiplexTS, ISS Inc., Champaign, IL). Then the I-shaped optical probe holder was placed on the same location. A trained experimenter held the aperture of CG-5000 laser closely to the participant’s right forearm to administer the placebo or PBM treatment on two sides of the holder alternatively. As illustrated in Fig. 2-3, each treatment session consisted of eight one-minute cycles, 55-s laser on and 5-s laser off per cycle. The participant was given a 2-minute break between the two experiments.

The participants received no information about the treatment type (placebo or PBM) in each experiment. Instead, they were instructed that they would receive the same laser treatment at a power of 3.4 W in both experiments. Furthermore, the laser at a power of 3.4 W generated negligible heat on the participants’ skin. Thus, the two experiments were designed to cause approximately the same sensations and expectations in the participants.

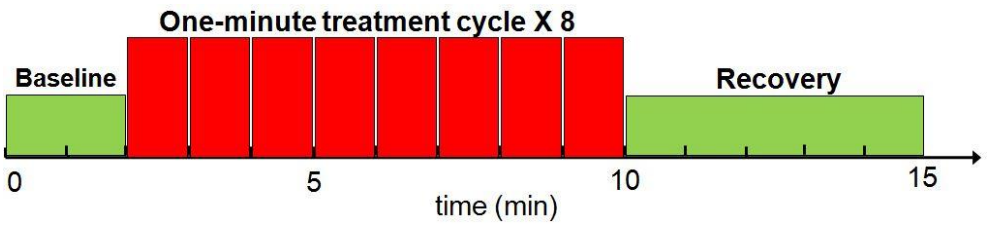

Figure 2-3 Paradigm of the PBM/placebo treatment and interleaved bb-NIRS data acquisition. Each treatment session consisted of eight one-minute treatment cycles, 55-s laser on and 5-s laser off per cycle. The bb-NIRS data acquisition was initiated two minutes before the first treatment session and ceased five minutes after the treatment session.

The data acquisition of bb-NIRS was initiated two minutes before each treatment session and ceased five minutes after the treatment session. Because the power of treatment laser from CG-5000 was high enough to contaminate the bb-NIRS readings, data acquisition interleaved with the treatment cycles during the 5-s laser-off periods. Following the similar format/fashion, the data during pre-treatment baseline and post-treatment recovery were also acquired at 55-second interval. In this way, a total of 15 data points (see Fig. 2-3) were obtained throughout each experiment. The shutter was switched on only for 5 seconds during each data acquisition period and then off in the rest of the time.

2.2.4 Theoretical Foundation for Data Processing and Error Analysis

Raw data from the broadband spectrometer was processed using MATLAB to calculate relative changes in [HbO], [HHb] and [CCO] from the initial baseline. First, the relative optical density, ΔOD, was calculated at each wavelength, λ:

$$\Delta OD(\lambda) = \log_{10}[\frac{I_0(\lambda)}{I(\lambda)}] \quad , \qquad 2\text{-}1$$

where $I_0(\lambda)$ is the spectral data acquired at the initial baseline (i.e., the first spectrum collected in each experiment), and $I(\lambda)$ is the data acquired at each time point thereafter.

According to the Modified Beer-Lambert Law [25, 43], ΔOD at each λ could be expressed as a sum of optical absorbance contributed by HbO, HHb and CCO components:

$$\Delta OD(\lambda) = \{\Delta[HbO] * \varepsilon_{HbO}(\lambda) + \Delta[Hb] * \varepsilon_{Hb}(\lambda) + \Delta[CCO] * \varepsilon_{CCO}(\lambda)\} * L(\lambda), \quad 2\text{-}2$$

where Δ[HbO] is the relative change in HbO concentration, Δ[HHb] is the relative change in HHb concentration, Δ[CCO] is the relative change in CCO concentration, $\varepsilon_{HbO}(\lambda)$, $\varepsilon_{Hb}(\lambda)$ and $\varepsilon_{CCO}(\lambda)$ are the extinction coefficients of HbO, HHb and CCO, which can be found in ref. [39], and L(λ) denotes the effective pathlength of the detected photons through the tissues. According to the Modified Beer-Lambert Law [25, 43], L(λ) can be estimated as:

$$L(\lambda) = r * DPF(\lambda), \quad 2\text{-}3$$

where 'r' is the source-detector distance, and DPF(λ) is the wavelength-dependent differential pathlength factor. Note that in this study, I did not assume that DPF was a wavelength-independent constant across the wavelength range. By substituting Eq. (2-3) into Eq. (2-2) for multiple wavelengths, I can express Δ[HbO], Δ[HHb] and Δ[CCO] in a matrix format in association with broadband ΔOD(λ) over DPF(λ) ,as follows:

$$\begin{bmatrix} \Delta[HbO] \\ \Delta[Hb] \\ \Delta[CCO] \end{bmatrix} = \frac{1}{r} * \begin{bmatrix} \varepsilon_{HbO}(\lambda_1) & \varepsilon_{Hb}(\lambda_1) & \varepsilon_{CCO}(\lambda_1) \\ \varepsilon_{HbO}(\lambda_2) & \varepsilon_{Hb}(\lambda_2) & \varepsilon_{CCO}(\lambda_2) \\ \ldots & & \\ \varepsilon_{HbO}(\lambda_n) & \varepsilon_{Hb}(\lambda_n) & \varepsilon_{CCO}(\lambda_n) \end{bmatrix}^{-1} \begin{bmatrix} \frac{\Delta OD(\lambda_1)}{DPF(\lambda_1)} \\ \frac{\Delta OD(\lambda_2)}{DPF(\lambda_2)} \\ \ldots \\ \frac{\Delta OD(\lambda_n)}{DPF(\lambda_n)} \end{bmatrix}. \quad 2\text{-}4$$

In this study, the DPF(λ) values were estimated based on the μ_a and μ_s' values measured with a frequency-domain OxiplexTS tissue oximeter in the beginning of the experiments. In principle, an OxiplexTS tissue oximeter provides measurement readings of μ_a and μ_s' values at 750 nm and 830 nm as well as absolute concentrations of [HbO] and [HHb]. To achieve μ_a and μ_s' values across the entire wavelength range of 740–900 nm, I interpolated and extrapolated the two measured μ_s' values at 750 nm and 830 nm by following Mie theory, which

is usually expressed by $k\lambda^{-b}$, where k and b were obtained by fitting this equation to both μ_s'(750 nm) and μ_s'(830 nm). In the meantime, the absorption coefficients in the same wavelength range (740–900 nm) were estimated based on the HbO and HHb concentrations measured by the same tissue oximeter. Then, the wavelength-dependent DPF values were calculated using the diffusion theory with the semi-infinite boundary geometry [44]:

$$DPF(\lambda) = \frac{\sqrt{3\mu_s'(\lambda)}}{2\sqrt{\mu_a(\lambda)}} * \frac{r\sqrt{3\mu_a(\lambda)\mu_s'(\lambda)}}{r\sqrt{3\mu_a(\lambda)\mu_s'(\lambda)}+1} \quad \text{2-5}$$

Where $\mu_a(\lambda)$ and $\mu_s'(\lambda)$ are the estimated absorption and reduced scattering coefficients across the wavelength range of interest.

Next, the final and key step was to quantify or determine three chromophore concentrations based on Eq. (2-4). To do so, multiple linear regression analysis was implemented in the wavelength range of 740–900 nm (with a total of 161 wavelengths) using a MATLAB-based function. This regression algorithm afforded the best fit of the chromophore-specific concentrations to the measured $\Delta OD(\lambda)$ spectrum by minimizing the squared residual or the objective function. The detailed fitting procedures are given next.

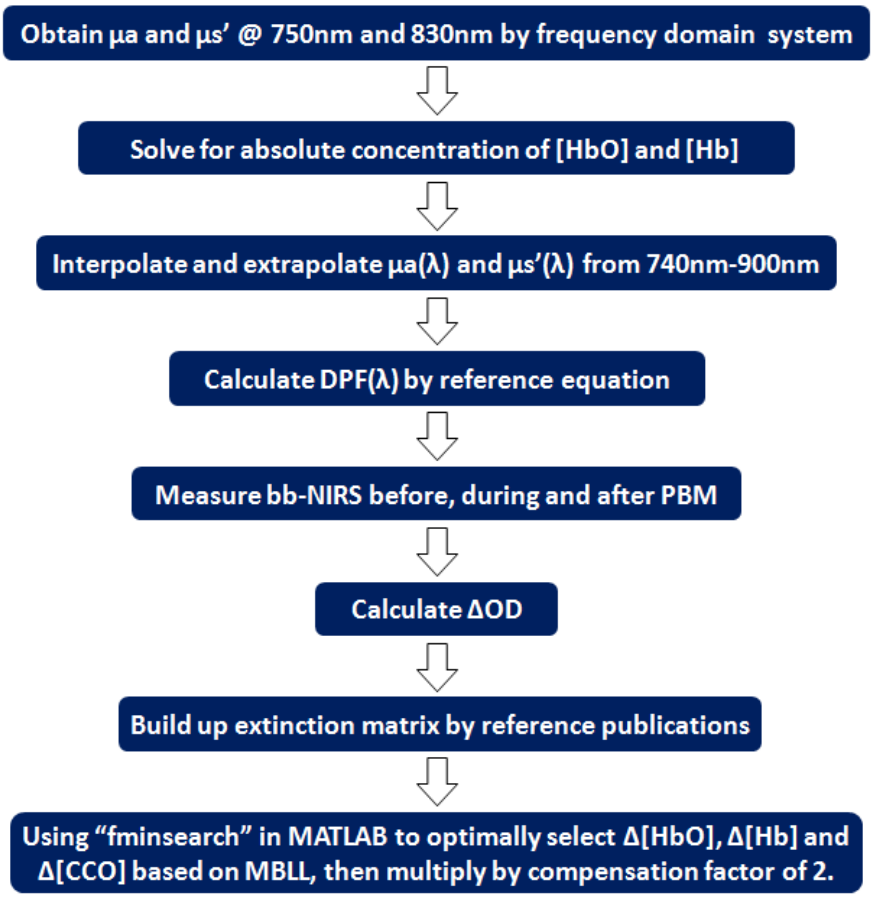

Figure 2-4 A flow chart describing detailed procedures of my multiple linear regression analysis to optimally determine PBM-induced concentration changes in three chromophores.

2.2.5 Multiple Linear Regression Analysis

The procedure for multiple linear regression analysis is outlined with a flow chart in Fig. 2-4.

(1) Start data collection and quantification of μ_a and μ_s' values at 750nm and 830nm of the subject's right forearm by the OxiplexTS tissue oximeter.

(2) Obtain output readings from the oximeter for absolute concentrations of [HbO] and [HHb].

(3) Interpolate and extrapolate $\mu_a(\lambda)$ and $\mu_s'(\lambda)$ values across 740nm to 900nm, based on μ_a and μs' values at 750 nm and 830 nm, by fitting Mie theory ($k\lambda^{-b}$) and calculating [HbO] and [HHb] with their corresponding extinction coefficients given in ref.[39].

(4) Calculate DPF(λ) values across 740nm to 900nm for each wavelength with Eq. (2-5);

(5) Perform bb-NIRS experiments to acquire optical spectra (with 161 wavelengths from 740-900 nm) from the subject's arm before, during and after PBM (or placebo);

(6) Quantifying ΔOD(λ)at different time points, using Eq. (2-1), to form a time series for each wavelength.

(7) Build up or form the 161×3 extinction coefficient matrix, based on ref. [39]; this matrix would list extinction coefficients at 161 wavelengths (740-900nm) for 3 chromophores.

(8) Solve accurately Δ[HbO], Δ[HHb] and Δ[CCO] based on Eq. (2-4). For the last step, specifically, I applied the MATLAB function of "fminsearch" to find/fit for the optimal combination of Δ[HbO], Δ[HHb] and Δ[CCO] as the final output parameters. In theory,"fminsearch" function finds the minimum of a scalar function (often called the objective function) of several variables, starting at an initial estimate (http://www.mathworks.com/help/optim/ug/fminsearch.html). This is generally referred to as unconstrained nonlinear optimization. In my study, for example, "fminsearch" attempted to model the relationship between three explanatory variables (e.g., Δ[HbO], Δ[HHb] and Δ[CCO]) and a set of response variables (e.g., ∆OD at multi-wavelengths) by fitting a linear equation to observed data, as expressed in Eq. (2-4). This function tries different combination of Δ[HbO], Δ[HHb] and Δ[CCO] starting from the "initial guess" to match with the measured set of ∆OD(λ)across the spectra until a minimized value of the objective equation is achieved. Then, this set of values (Δ[HbO], Δ[HHb] and Δ[CCO]) are considered as the "best fit" and to be used as the final results.

2.2.6Statistical Analysis

To determine whether the PBM induced significant changes in hemoglobin and CCO concentrations with respect to the placebo treatment, paired t-test between these two treatment types was conducted for each chromophore (HbO, HHb and CCO) at each time point. A two-tailed level of $0.01 < p < 0.05$ and $p < 0.01$ was chosen to be statistically significant in these tests.

2.3 Results

A total of 11 normal subjects (seven males and four females, mean ± SD age = 26.1 ± 5.0 years) participated in the experiments. Figure 2-5 shows dose-dependent (energy density dose = exposure time $\times$ laser power density) concentration changes in [HbO], [HHb], and [CCO] induced by the PBM and placebo treatments at the group level (mean ± SE, n=11). Overall, PBM significantly increased the HbO and CCO concentrations as compared with placebo ($0.01 < p < 0.05$ and $p < 0.01$), while the HHb concentration was nearly unaltered by either placebo or laser treatment. However, the initial laser effect on CCO seemed to precede in time the effect on HbO; i.e., for [HbO] the laser-induced effect was significantly greater than placebo after two minutes of laser treatment [Fig. 2-5(a)), whereas for [CCO] the significant effect started after one minute [Fig. 2-5(c)]. Also note that the increased CCO concentration showed a slightly faster recovery trend towards the baseline than HbO after PBM.

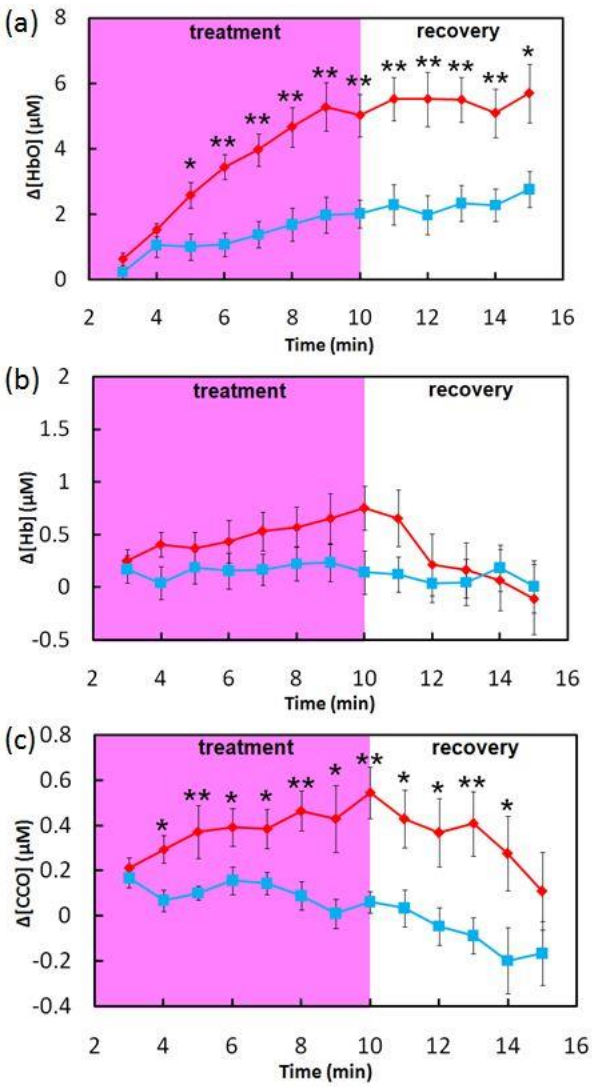

Figure 2-5 PBM/placebo-induced concentration changes of (a) [HbO], (b) [HHb], and (c) [CCO] in human forearms in vivo (mean ± SE, n=11). In each subplot, the pink-shaded region indicates the period of PBM/placebo treatment; * indicates significant differences in respective concentrations between PBM and placebo treatment ($0.01 < p < 0.05$, paired t-test). ** indicates significant differences in respective concentrations between PBM and placebo treatment ($p < 0.01$, paired t-test).

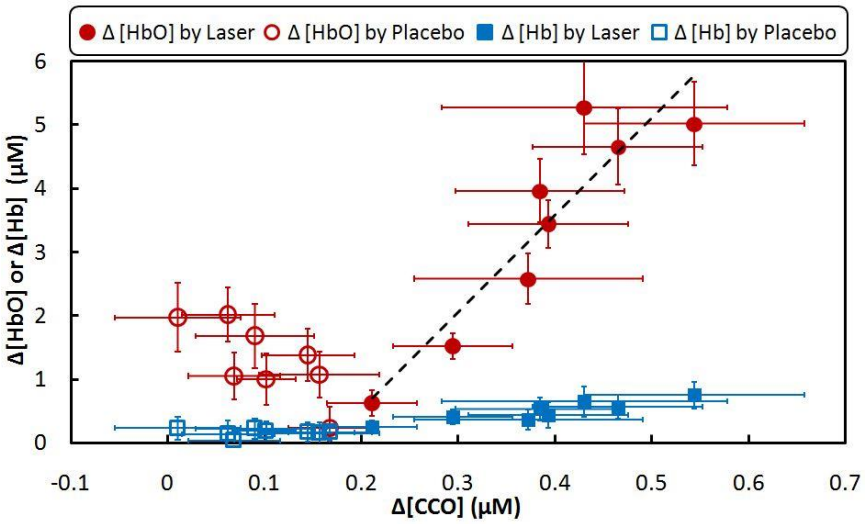

Figure 2-6 The relationship of concentration changes between CCO vs. HbO or HHb during PBM and placebo experiment (mean ± SE, N = 11). The horizontal error bars represent variability of CCO and the vertical error bars represent variability of HbO or HHb. The correlation coefficient of the fitted line is r=0.92 with a p value of 0.001.

After close inspection of the data in Fig. 2-5, I reorganized the respective concentrations and replotted them to show the relationship between concentration increases of CCO vs. HbO or HHb, induced by either PBM or placebo treatment. As shown in Fig. 2-6, the solid red dots display the relationship of Δ[CCO] vs Δ[HbO] during PBM, with a linear fit by the dashed line (with a correlation coefficient of r=0.92 and a p value of 0.001), confirming an excellent linear relationship between them. On the other hand, the open red circles, obtained under the placebo treatment, were gathered within a lower Δ[CCO] range with no relationship between Δ[CCO] and Δ[HbO]. The concentration change of HHb also showed no response to the change of CCO, as plotted by the blue squares in Fig 2-6.

2.4 Discussion

In this placebo-controlled study, I used broadband NIRS to measure the PBM-induced changes or increases in oxygenated hemoglobin and CCO concentrations in human forearms in

vivo. For the first time, I demonstrated that 1064 nm laser can induce significant increases of CCO and HbO concentrations in a dose-dependent manner over time, as compared with placebo treatment. In addition, Δ[CCO] and Δ[HbO] displayed a clear linear relationship as the dose of PBM increased. Especially, I carefully measured and quantified the wavelength-dependent DPF factor, DPF(λ) as given by Eq. (2-5), to minimize crosstalk artifacts [39, 40]. To the best of my knowledge, this is the first study to assess the CCO enzyme up-regulation effects of photobiomodulation in human tissues in vivo. These results demonstrate the great potential of bb-NIRS as a non-invasive technology for mechanistic studies and treatment evaluations of PBM.

2.4.1 Interplay between up-regulation of CCO and hemoglobin oxygenation induced by PBM

The observed linearity between Δ[CCO] and Δ[HbO] induced by PBM is of great significance, showing a close interplay between the up-regulation of CCO and corresponding hemodynamic oxygenation in the treated tissue. As compared to placebo, the infrared laser treatment induced a significant increase in [CCO] that preceded the increase in [HbO]. Together these data suggest that laser-induced CCO up-regulation leads to a linear increase in HbO. This may indicate that a hemodynamic oxygenation response occurs in vivo as a result of up-regulation of CCO induced by the infrared laser treatment. The mechanism of the observed effects can be explained based on what is known about the role of CCO on photobiomodulation[3, 45] and the three main steps in cell respiration: glycolysis, Krebs cycle and the electron transport chain. During the first two steps, comparatively little amount of ATP is synthesized. High energy electrons are stored in NADH/FADH; CO_2 and water are produced as waste products. In the electron transport chain, where the most amount of energy is produced, CCO (as the terminal enzyme) transfers electrons to enable an oxygen molecule to combine with protons and form a water molecule. At the same time, this process accompanies ATP

synthesis (oxidative phosphorylation). Since CCO is the main photo-acceptor within the effective optical window of PBM, up-regulation of CCO will boost the electron transport, up-regulate the enzymatic activity, and result in a significant increase in oxygen consumption rate within tissue mitochondria. Consequently, an increase in hemodynamic oxygen supply and total blood volume will occur around the PBM area due to the need for more oxygen and electrons. Therefore, during PBM, the more the redox state of CCO is activated, the more the oxygenated hemoglobin concentration, HbO, increases proportionally.

In a previous study on the hemodynamic effects of transcranial PBM on the human brain using dual-wavelength NIRS [32], I have reported that transcranial 1064 nm laser improved cerebral oxygenation as indicated by an increase of [HbO] and a decrease of [HHb]. In the current study, I have consistently observed PBM-induced increases of [HbO] in the human forearms, but [HHb] remained nearly unchanged. A couple of factors may be attributed to this discrepancy in the alteration of [HHb] between the two studies. The first factor can result from the large difference in anatomy and physiology between the human forearm and the brain. The brain is much more vascularized than the forearm and it has a much greater rate of tissue oxygenation. This may lead to a greater differential hemoglobin concentration in the PBM-stimulated brain region, with a relative [HbO] increase and [HHb] decrease [24]. The second factor may stem from differences in experimental setups and quantification algorithms that were used to measure and quantify changes in [HbO] and [HHb]. In my previous study, a dual-wavelength NIRS system was used. In consequence, changes in [HbO] and [HHb] were determined using the dual-wavelength-based, modified Beer-Lambert law with a fixed pathlength factor (i.e., DPF is independent of wavelength) [32]. While the use of a constant DPF is a common practice in the NIRS field, the derived quantifications of Δ[HbO] and Δ[HHb] are more likely subject to cross-talk errors due to the inaccurate assumption of constant pathlength[36, 37], particularly when changes of [CCO] are involved. In the current study, on the other hand, I employed a bb-NIRS system, carefully determined wavelength-dependent DPF

values, and fitted the measured optical density spectra with a more rigorous expression of Eq. (2-4) using linear regression analysis. All of these procedures, in principle, should minimize cross-talk errors and lead to improved accuracy of ∆[HbO] and ∆[HHb] determination [39, 41]. A limitation of this study for transcranial PBM applications is that the PBM-induced linear interplay between ∆[CCO] and ∆[HbO] was demonstrated on the human forearm, but not on the brain. My future work plans to follow similar PBM experimental protocols and perform bb-NIRS measurements on the human forehead in order to confirm in the brain the findings reported in this paper.

2.4.2 Rationale of using 1064-nm laser for photobiomodulation

It is noteworthy that the CCO enzyme effects of PBM are dependent on the wavelength of the stimulation laser (light). A previous study on cultured neurons [3] has shown that the most effective wavelengths paralleled the near-infrared absorption peaks of CCO. The current study used a 1064-nm laser that was also employed in my previous studies [17, 18, 32]. This wavelength may not be optimal for photon absorption by CCO because its known peaks of light absorption are at lower wavelengths [45]. However, none of the previous absorption studies have measured photon absorption by CCO at 1064 nm, and the present study demonstrated a clear effect of this wavelength on CCO up-regulation. The primary reason for selecting this wavelength is its ability to better penetrate the human scalp and skull in transcranial applications. In biological tissues, light scattering is the dominant light-tissue interaction and its influence is two orders of magnitude greater than that of light absorption. According to Mie theory, the light scattering in biological tissues decreases with longer wavelengths[46]. The 1064-nm wavelength used in my studies is approximately the longest one in the near-infrared optical window where water absorption remains low [46]. Therefore, 1064 nm is expected to

have better penetration depth and stimulation efficiency in the human brain than shorter wavelengths in transcranial laser treatments.

2.4.3 Measurement accuracy of bb-NIRS on CCO quantification

Quantification of the redox state of cytochrome oxidase in living tissue has been a scientific topic and continuously studied over the last 20+ years[34, 35, 37, 39, 41, 42, 47]. In particular, continuous development on measurement techniques and improved algorithms have been done by the research group from the University College London, which has continuously made significant efforts to validate and improve the sensitivity, specificity, and accuracy of quantified CCO sensed in living tissues. The listed references of [37, 39, 41, 42, 47] demonstrate and support the scientific basis and rigor for CCO quantification by bb-NIRS that I utilized in this manuscript.

A possible question is whether, besides CCO, there is any other target or biomarker at the cellular level that contributes to photobiomodulation by absorbing 1064 nm laser. With the current scientific knowledge available, my answer is “No”, which is based on many scientific observations reported in the last 20 or more years. A recent review paper summarized that the major biological tissues that absorb light in 700-1200 nm are blood, water, melanin, adipose tissue/fat, and yellow pigments[46]. On the other hand, I have not found much reporting in the literature that other PBM biomarkers at the cellular level (besides CCO) absorb light at 1064 nm in vivo. Future scientific discovery may alter my current view, but the conclusion given in this paper holds its scientific foundation and rigor.

2.4.4 Possible thermal effects of PBM on CCO quantifications

It is reasonable to expect that infrared light at 1064 nm with a power of 3.4 W would generate some thermal effect that may lead to an increase in skin blood flow (SBF). Such an increase of SBF may give rise to an increase of hemoglobin concentration in the adjacent area

surrounding or near the PBM stimulation spot. To address this concern, I conducted a pilot study, including 4 out of the 11 subjects who participated in the PBM/Placebo study. The clear observation in Figure 2-7 was that thermally induced Δ[HbO] followed a similar trend to that of the placebo trace, while the PBM-induced Δ[HbO] remained significantly higher during and after the 8 continuous laser treatments. On the other hand, in the case of Δ[CCO], the thermal effect was non-significant on changes in CCO, while significant increases of CCO were clearly observed due to PBM stimulations.

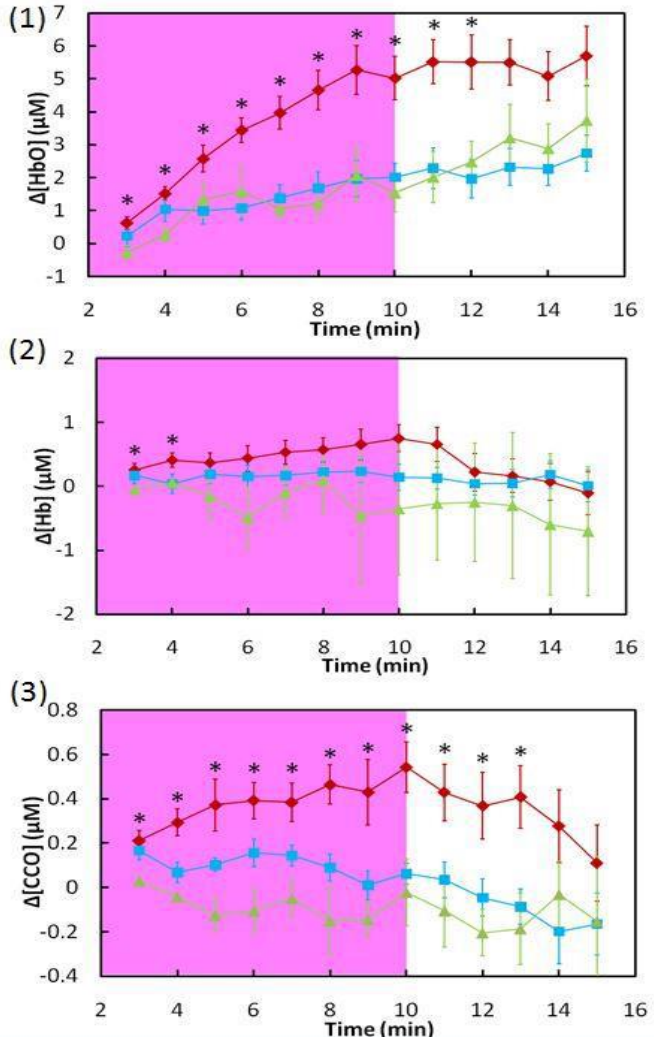

Figure 2-7Concentration changes of (1) HbO, (2) HHb and (3) CCO during LLLT (red; n=11), placebo (blue; n=11) and thermal (green; n=4) stimulation. The "*" represents significant difference between LLLT vs thermal effect (p-value <0.05).

The overall conclusion from the pilot thermal test was that thermal effects on skin surface may be non-significant to cause changes in tissue redox CCO concentrations that are measured by bb-NIRS with a separation larger than 1.5 cm. However, my sample size for the pilot study was only 4, so this conclusion was not statistically solid, and further studies with more participants are highly desirable to confirm this finding.

2.5 Conclusion

In final conclusion, this study has clearly demonstrated that PBM can induce significant increases of [CCO] and [HbO] on the human forearm as the laser energy dose is accumulated over time, as compared with the placebo treatments. A strong linear interplay between Δ[CCO] and Δ[HbO] was observed for the first time during the laser treatment, indicating a hemodynamic response of oxygen supply coupled to the increase of cellular metabolic rate induced by photobiomodulation. These results demonstrate the tremendous potential of bb-NIRS as a non-invasive optical means to study in vivo mechanisms and perform treatment evaluations of PBM.

Chapter 3

Up-regulation of cerebral cytochrome-c-oxidase and hemodynamics by transcranial photobiomodulation: a broadband near-infrared spectroscopy study

This chapter is a publication at the Journal of Cerebral Blood Flow & Metabolism on 09 Feb 2017.(J Cereb Blood Flow Metab, p. 271678X17691783, Jan 01 2017.)

***Authorship**: Xinlong Wang, Fenghua Tian, Divya D. Reddy, Sahil S. Nalawade, Douglas W. Barrett ,Francisco Gonzalez-Lima & Hanli Liu*

3.1 Introduction

3.1.1 Transcranial Photobiomodulation

Photobiomodulation is a non-invasive intervention shown to regulate cellular functions in cell cultures, animal models, and clinical conditions[2, 3, 6, 7, 17]. To avoid any confusion between the method I use for spectroscopy and the method I use for laser stimulation, let me clarify the terminology between them: Infrared light is in the wavelength range from 700 nm to 1 mm, a branch of which is 760-1440 nm and is often called near infrared light (NIR) [48]. Since I use “NIR” to express NIR spectroscopy (NIRS) utilized in my spectroscopy measurements, I name my laser stimulation at 1064 nm as “infrared” laser stimulation. Within the wavelength spectrum of approximately 620−1100 nm, the light absorption by tissue chromophores is weak [49]. The primary mechanism of photobiomodulation rests on photon absorption by cytochrome c oxidase (CCO)[12], which is the terminal enzyme in the mitochondrial respiratory chain that plays a key role in neuronal oxygen utilization for energy metabolism[50]. The greater the oxidized CCO increases, the greater oxygen consumption and metabolic energy is produced via mitochondrial oxidative phosphorylation[15]. This photonics-bioenergetics mechanism results in unique metabolic effects on the brain, with benefits for cognitive enhancement and neuroprotection [20, 22]. In recent years, brain photobiomodulation has gained attention for its

therapeutic potential in many neurological and psychological conditions[15, 51]. It is reported being safe for treating ischemic stroke [6, 7] and chronic traumatic brain injury [52]. Schiffer et al. [10] also found that a single session of PBM at 810 nm to the forehead could have psychological benefits in patients with major depression and anxiety. Stimulating with the same light irradiance as Schiffer et al. [10]but at 1064 nm, Barrett and Gonzalez-Lima conducted the first controlled study in healthy humans that demonstrated Transcranial Photobiomodulation (tPBM) improves frontal-cortex-based cognitive and emotional functions[17]. Subsequent controlled studies by the same group showed that tPBM improves executive functions[18] and reduces depression symptoms[53]. tPBM is also as effective as vigorous aerobic exercise to improve cognition[54].

Despite the numerous preclinical studies and promising outcomes from a few clinical trials, however, brain photobiomodulation has not been widely adopted by mainstream medicine. One reason is that uncertainty still remains about the mechanism of action of photobiomodulation in the human brain in vivo. In order for tPBM to be adopted as an objective scientifically-based brain intervention, it is essential to quantitatively assess and better understand the cerebral metabolic and hemodynamic effects of tPBM.

3.1.2 Near infrared spectroscopy

As it was shown in Chapter 2, NIRS can monitor the redox state of mitochondrial CCO with suitable algorithms and broadband components[39, 40]. In particular, I recently reported that broadband NIRS (bb-NIRS) can be used successfully to quantify the photobiomodulation effects of 1064-nm laser on the human forearm in vivo[13].Both CCO and HbO up-regulation were primary metabolic and hemodynamic effects of photobiomodulation, which served as direct and quantitative measures of cellular oxygen metabolism. Because bb-NIRS shares similar pathways of light through the biologic and/or cerebral tissues with tPBM, a combination

of these two techniques may provide an ideal imaging tool for in vivo mechanistic study and treatment evaluation of tPBM.

The present study integrated bb-NIRS and tPBM to quantitatively assess the cerebral metabolic (CCO) and hemodynamic (HbO, HHb) effects of a single photobiomodulation session, as well as to assess their relationships. I tested two hypotheses: (1) single-session tPBM induces reliable and measurable CCO changes in the human brain in vivo, and (2) these CCO changes result in and correlate with the subjects' hemodynamic alterations.

3.1.3 Novel approaches and findings of this study

In the current study, I utilized a bb-NIRS system along with a tPBM unit at 1064 nm; I interleaved tPBM intervention and the bb-NIRS data acquisition on the right forehead of 11 human controls in vivo throughout the pre-, during, and post-tPBM and placebo intervention. I was able to simultaneously assess/quantify concentration changes in CCO, HbO, and HHb(i.e., Δ[CCO], Δ[HbO], and Δ[HHb], respectively), which also allowed me to readily quantify total and differential hemoglobin concentrations (i.e., Δ[HbT] and Δ[HbD], respectively).Consequently, I was able to investigate relationships among up-regulation of oxidized[CCO] versus corresponding alterations of cerebral blood flow, cerebral blood volume, and cerebral hemodynamic oxygenation. Overall, the results of this study provided the first demonstration that photobiomodulation up-regulates oxidized CCO concentrations in the human brain in vivo. They also confirmed the feasibility of a non-invasive, cost-effective cerebral stimulation-with-imaging approach that integrates two transcranial optical technologies. This novel approach provided insight into the underlying mechanism of tPBM-induced effects on brain and behavior [15].

3.2 Methods

3.2.1 Participants

Eleven healthy human participants with a mean (±standard deviation) of 31(±13.7) years of age were recruited from the local community of The University of Texas at Arlington (UTA). Interested individuals were screened based on the same inclusion criteria as those in ref. [13].Eligible participants underwent two separate experiments in sequence: the placebo treatment was administered on their right forehead, followed by tPBM administered on the same location, 5 min after the first experiment. The exclusion and inclusion criteria were the same as those in ref. [13]. The study protocol was approved by the institutional review board (IRB) of UTA. Informed consent was obtained from each participant prior to the experiments.

3.2.2 Instruments

It is noted that the laser stimulation and the spectroscopic measurement were two different optical methods that used two different light sources with non-overlapping wavelengths. The laser stimulation used monochromatic infrared at 1064 nm, whereas the spectroscopic measurement used a broadband light source starting at 400 nm and filtered to 1000 nm.

An FDA-cleared 1064-nm continuous wave laser device (HD Laser Model CG-5000, Cell Gen Therapeutics LLC, Dallas, TX)was used for both placebo and laser treatments. It has been approved by the FDA for various uses in humans [4, 5]. The laser was emitted from a handpiece, and the measured laser beam had an area of 13.6 cm^2. There was a button to turn on/off the laser beam on the hand piece. To avoid any undesirable artifacts in the experiment, a 2-cm distance between laser aperture and stimulation site was kept during the stimulation process. Because of collimation, the laser beam’s size was kept approximately the same from the laser aperture to the stimulation spot on the participant's forehead.

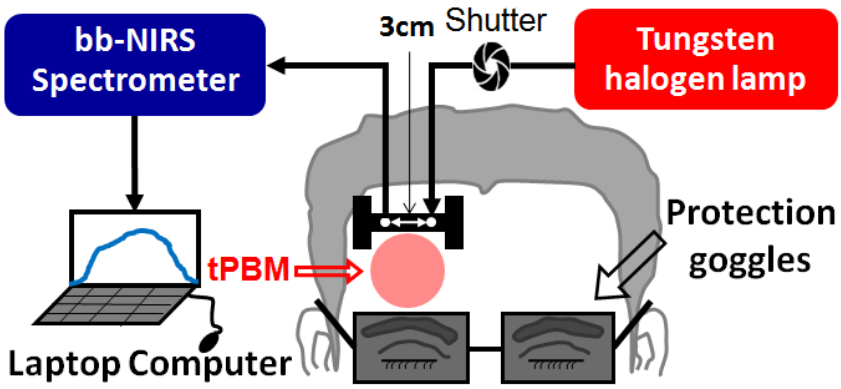

Figure 3-1Schematic diagram of the experimental setup, including a bb-NIRS spectroscopic system. This bb-NIRS unit consisted of a tungsten halogen lamp as the light source and a miniature high-sensitivity CCD spectrometer as the detector for this study. tPBM was administered underneath the "I" shaped probe holder. The narrow, middle section of the holder was ~8 mm in width. A laptop computer was used to acquire, display and save the data from the spectrometer. The shutter controlled the on and off function for the tungsten-halogen lamp to subject's forehead. A pair of protection goggles was worn during the whole experimental procedure.

The laser power during the stimulation treatment was controlled at 3.4 W. The power density in the beam area was 0.25 W/cm^2, the same as that used in my previous studies[13, 17, 18, 55]. For the placebo treatment, the same device was applied to the subject's forehead while the laser power was tuned down to 0.1 W. The laser aperture was further covered by a black cap so that no laser was delivered to the subject. In this way, the sham appeared similar to the actual laser stimulation but without any light released.

To avoid any potential skin damage, the power density of the FDA-cleared Class 4 laser (International standard IEC 60825-1)was kept low corresponding to that of a Class 3b laser. Specifically, irradiance was kept at 0.25 W/cm^2. Following previously successful studies [13, 17, 18, 55], my safe laser stimulation parameters were as follows:

Total laser power = 3.4 W;

Area of laser beam radiation = 13.6 cm^2;

Power density = 3.4 W/13.6 cm^2 = 0.25 W/cm^2;

Time radiated per cycle = 55 s;

Total laser energy per cycle = 3.4 W $\times$ 55 s = 187 J/cycle.

Total laser energy density per cycle = 0.25 $W/cm^2 \times$ 55 s = 13.75 J/cm^2/cycle.

The experimental setup was also similar to Chapter 2. Briefly, a single-channel, bb-NIRS system was built to measure Δ[HbO], Δ[HHb] and Δ[CCO] in vivo during tPBM and placebo experiments. Figure 3-1 shows(1) a tungsten-halogen lamp with a spectral range of 400-1500nm(Model 3900, Illumination Technologies Inc., East Syracuse, NY), (2) a miniature high-sensitivity CCD bb-fNIRS spectrometer with a spectral range of 735-1100 nm (QE-Pro, Ocean Optics Inc.), (3) a self-designed, "I"- shaped probe holder to hold a 3.5-mm optical fiber bundle relayed to the white light, and (4) an optical shutter to switch on and off the white light. A low-pass filter with a cut-off frequency of 1000 nm was attached at the bundle tip within the holder to reduce the tissue heating effect from the broadband light of the tungsten halogen lamp (400-1500 nm) used as a light source for the spectroscopic measurement when the 1064 nm laser is turned off. The diffuse light was collected by another fiber bundle and relayed to the bb-NIRS spectrometer. The distance between two optodes in the holder was 3 cm (see Fig. 3-1). A laptop computer was used to acquire, display and save the experimental data. Clinical non-residual hypoallergenic double-sided tape (Noraxon USA Inc.) was used to minimize motion artifacts between the holder and forehead. In both experiments, the laser beam from CG-5000 was administered at the lower site of the holder, but above the eye brow. (see Fig. 3-1).

3.2.3 Experiments

The experiments were conducted in a similar environment as that reported in Chapter 2 and refs. [13, 55]. Briefly: While investigators and participants wore protective goggles, the participants were instructed to close their eyes during the experiments. After each participant

was comfortably seated, a quick measurement of absorption coefficient (μa) and reduced scattering coefficient (μ_s') at 750 nm, 785nm, 811nm and 830 nm from the participant's right forehead was acquired using a frequency-domain NIRS tissue oximeter (OxiplexTS, ISS Inc., Champaign, IL). Then the I-shaped optical probe holder was firmly placed at the same location (see Fig. 3-1). During both placebo and tPBM experiments, a well-trained graduate researcher held the aperture of CG-5000 laser closely to the participant's right forehead to deliver stimulations.

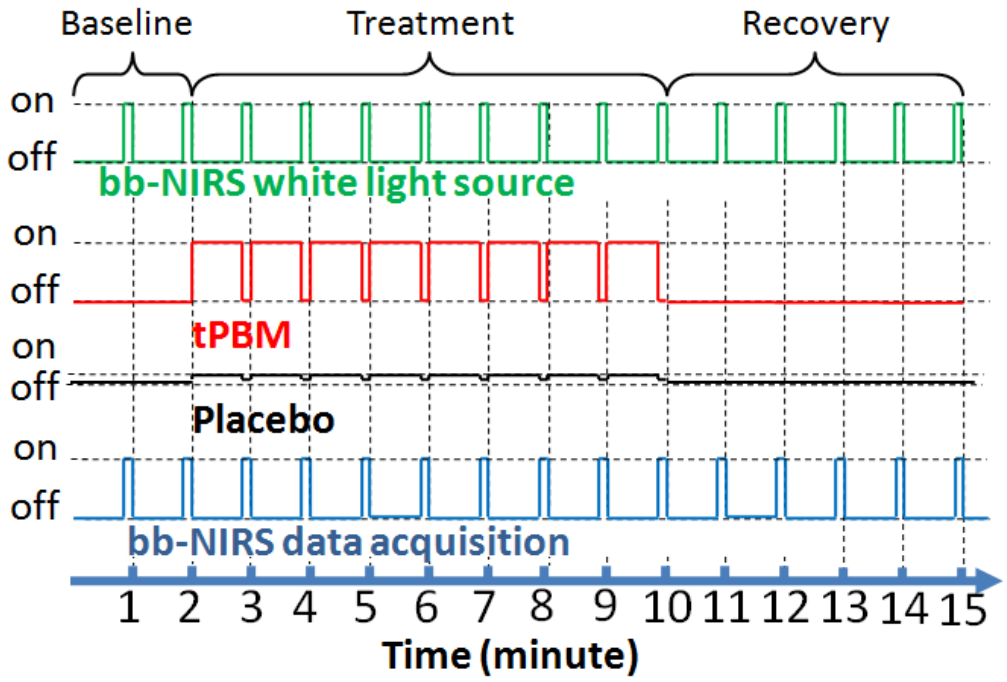

Figure 3-2 Paradigm of the tPBM/placebo treatment and interleaved bb-NIRS data acquisition. Each treatment session consisted of eight one-minute treatment cycles: 55-s laser on and 5-s laser off per cycle. During the 5-s laser-off periods, the bb-NIRS system (both the light source and detector) was switched on for bb-NIRS data acquisition. The same data acquisition format was followed for baseline and recovery sessions.

Each treatment session consisted of eight one-minute cycles, 55-s laser on and 5-s laser off per cycle (see the 2nd row from top in Fig. 3-2). In each treatment session, a 2-minute baseline was acquired by bb-NIRS. To avoid potential contamination between the laser from

CG-5000 and white light for bb-NIRS readings, data acquisition and laser stimulation were interleaved: During the 5-s laser-off periods, the shutter for white light was on and bb-NIRS data were collected (see the top and bottom rows of Fig. 3-2). Keeping the same acquisition format, data during pre-treatment baseline and post-treatment recovery were also acquired at 55-second intervals. A total of 15 data points (see Fig. 3-2) were obtained throughout each experiment under placebo and tPBM conditions. To minimize possible stimulation effect from the white light, the optical shutter was open only during the 5-s data acquisition per 60-s cycle.

Similar to Chapter 2, the participants were blinded for the placebo and tPBM treatments. I verified that negligible heat was generated by tPBM at the stimulation power of 3.4 W, on the participants' skin[13]. During the placebo experiment, the laser device was also turned on, so the participant could hear the same operation sound from the laser unit as that heard during actual tPBM. Thus, the two experiments were designed to cause approximately the same sensations and expectations in the participants. The participant was given a 5-minute break between the two experiments.

3.2.4 Data Processing and Statistical Analysis

The estimations of Δ[HbO], Δ[HHb] and Δ[CCO] from raw spectral data taken by the bb-NIRS were performed, following the same steps given in ref. [13], which is also given in the Supplementary Material of this paper. After completing the regression algorithm, I was able to obtain the best fit of the chromophore-specific concentrations to the measured spectrum. Then temporal values of Δ[HbO], Δ[HHb] and Δ[CCO] at 13 time points were evaluated for each human participant under either placebo or tPBM conditions. Furthermore, since total and differential concentrations of hemoglobin are defined as Δ[HbT]= Δ[HbO]+Δ[HHb] and Δ[HbD]=Δ[HbO]-Δ[HHb], respectively, time courses of Δ[HbT] and Δ[HbD] at 13 points were readily obtained and averaged across all the subjects under either treatment condition. Further

statistical analysis was followed to determine respective significant difference of Δ[HbO], Δ[HHb], Δ[HbT], Δ[HbD], and Δ[CCO] between the placebo versus tPBM experiment across 11 human subjects.

To evaluate the tPBM treatment effect with respect to the placebo treatment, the sample average and sample standard deviation of the 11 human participants in both treatments were calculated. A two sample t-test between these two treatment types was conducted for each chromophore (ΔHbO, ΔHHb, ΔHbT, ΔHbD, and ΔCCO) at each time point. A two-tailed level of $0.01 < p < 0.05$ and $p < 0.01$ was chosen to be statistically significant in these tests.

3.3 Results

3.3.1 Time courses oftPBM-inducedΔ[CCO], Δ[HbO], Δ[HHb],Δ[HbT], and Δ[HbD]

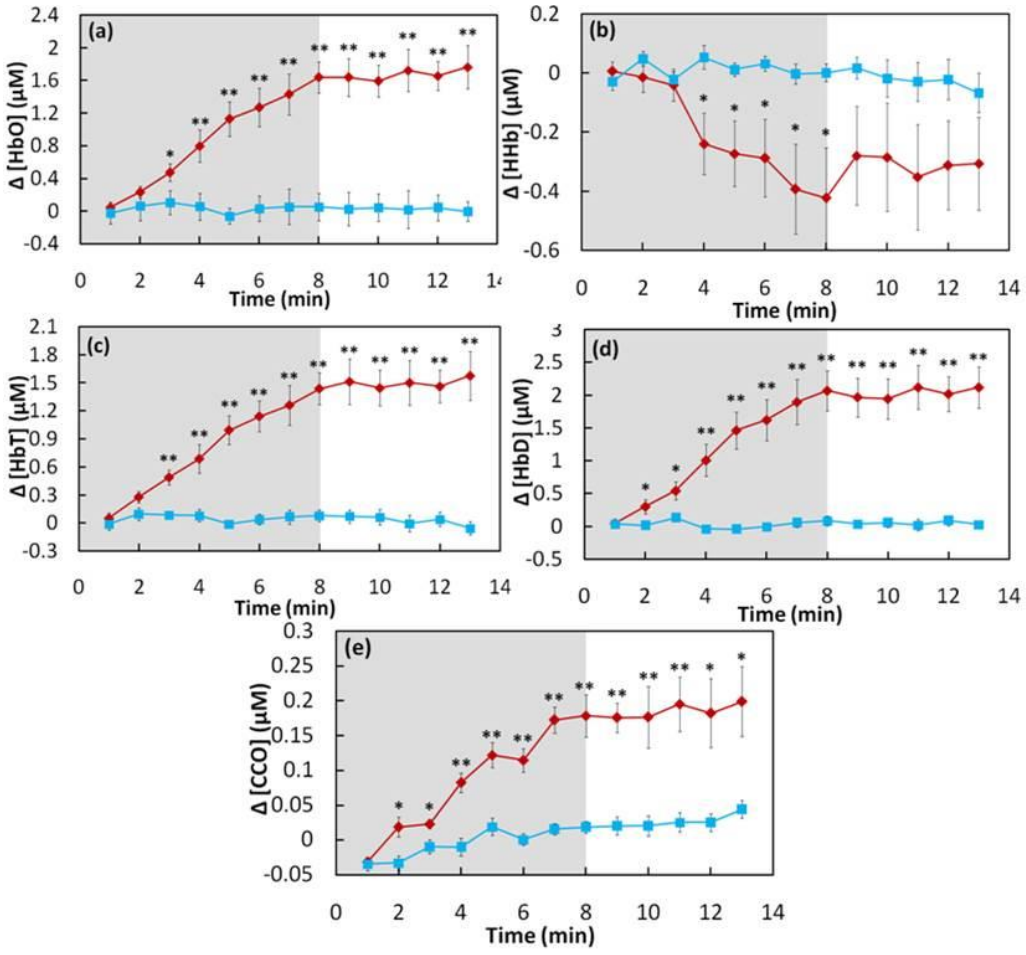

Figure 3-3Subject-averaged time courses of tPBM/placebo-induced cerebral changes of (a) [HbO], (b) [HHb], (c) [HbT], (d) [HbD], and (e) [CCO] (all in μM) recorded from human foreheads in vivo (mean ± SE, n=11). Time zero (t=0) is the onset of tPBM. In each subplot, the shaded region indicates the period of tPBM/placebo treatment. "*" indicates significant differences ($0.01 < p < 0.05$, two sample t-test) in respective concentrations between tPBM and placebo treatment. "**" indicates significant differences ($p < 0.01$, two sample t-test) in respective concentrations between tPBM and placebo treatment.

Figure 3-3(a) shows two time courses of Δ[HbO] at pre-, during, and post-tPBM (red symbols) or placebo (blue symbols)treatments for over 15 min (i.e., 2-min baseline, 8-min tPBM/placebo, and 5-min recovery), with each data point being averaged across all the subjects (n=11).Since laser energy density dose is often defined as exposure time×laser power density, Fig. 3-3(a) illustrates the time-dependent dose-response relationship between tPBM/placebo-induced transcranial Δ[HbO] and laser energy dosage at the group level. In a similar format to Fig. 3-3(a), Figs. 3-3(b) to 3-3(e) present the group-averaged time courses of Δ[HHb], Δ[HbT], Δ[HbD], and Δ[CCO], respectively, under either tPBM or placebo conditions.

Focusing on the data shown in Figs. 3-3(a), 3-3(b), and 3-3(e), it was clear that tPBM significantly increased Δ[HbO] and Δ[CCO] and decreased Δ[HHb] as compared to the placebo treatment. Inspection on these three figures also revealed time-dependent tPBM effects, as follows: (1) a significant tPBM-induced increase in Δ[CCO]appeared to occur fastest in time, 2 minutes right after tPBM started [Fig. 3-3(e)]; (2) the increase in Δ[HbO] became significant 3 minutes after the laser onset [Fig. 3-3 (a)], followed by (3) a steep significant decrease in Δ[HHb] 4 minutes after the initiation of tPBM [Fig. 3-3 (b)].

Next, considering Figs. 3-3(c) and 3-3(d), it is important to recall literature [56-59]indicating that cerebral Δ[HbT] is proportional to a change in cerebral blood volume (ΔCBV) while Δ[HbD] is closely correlated with changes in cerebral blood flow (ΔCBF). Thus, Figs. 3-3(c) and 3-3(d) reflect significant increases of ΔCBV and ΔCBF induced by tPBM. These two

figures also revealed that tPBM-induced Δ[HbD] (or ΔCBF) increased significantly as fast as Δ[CCO] while the corresponding Δ[HbT] (or ΔCBV) delayed a little with respect to Δ[CCO], but about the same increasing rate as Δ[HbO] (3 min after tPBM onset).

3.3.2 Dependence of cerebral hemodynamic parameters on tPBM-induced cerebral Δ[CCO]

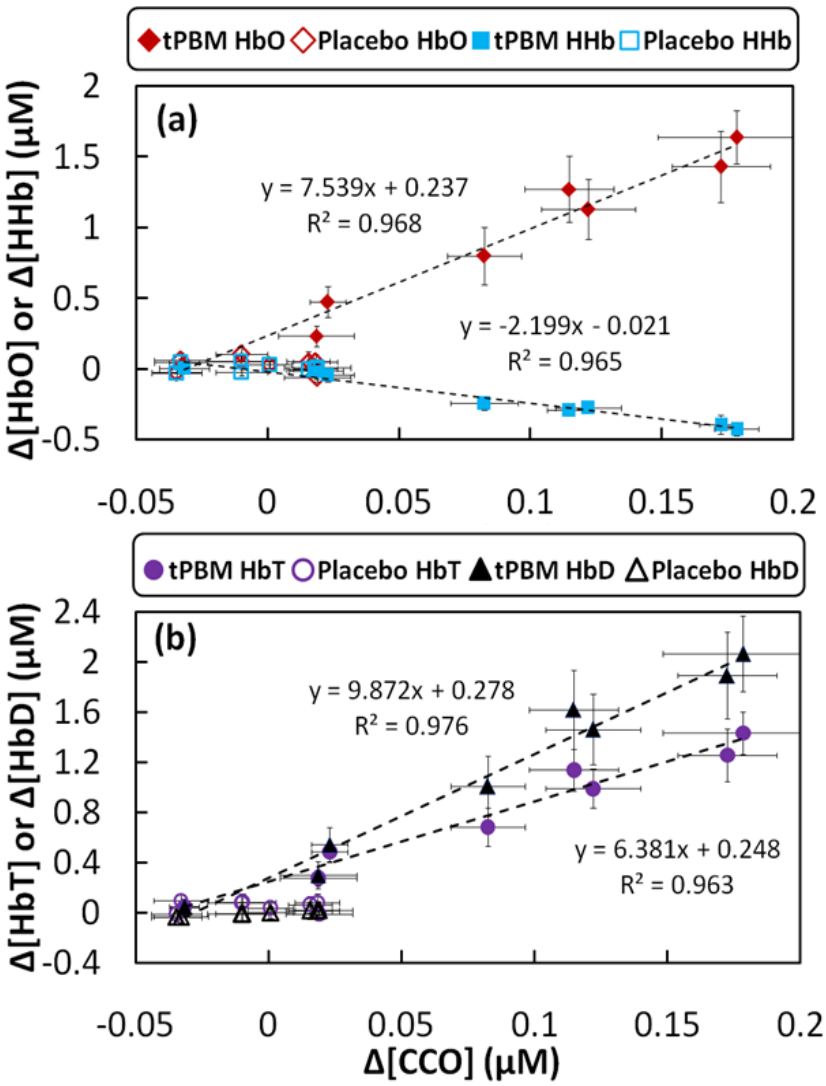

Figure 3-4 (a) Relationships between subject-averaged Δ[CCO] vs. Δ[HbO] and Δ[CCO] vs. Δ[HHb] that resulted from tPBM and placebo treatment (mean ± SE, N = 11). Solid red diamonds display the relationship of Δ[CCO] vs Δ[HbO]; solid blue dots display the relationship of Δ[CCO] vs Δ[HHb]. Both red open diamonds and blue open squares represent placebo-treated Δ[CCO] vs.Δ[HbO] and Δ[CCO]

vs.Δ[HHb], respectively. (b) Relationships between subject-averaged Δ[CCO] vs. Δ[HbT] and Δ[CCO] vs. Δ[HbD] caused by tPBM and placebo treatment. Solid purple circles display the relationship of Δ[CCO] vs Δ[HbT]; solid black triangles display the relationship of Δ[CCO] vs Δ[HbD]. Both red open circles and open triangles represent placebo-treated Δ[CCO] vs.Δ[HbO] and Δ[CCO] vs.Δ[HHb], respectively. All error bars represent standard errors of means from respective chromophore concentrations.

By extracting chromophore concentrations differences in response to tPBM and placebo, I reorganized and replotted the data to display the close dependence of each cerebral hemodynamic parameter on tPBM-induced cerebral Δ[CCO], as shown in Fig. 3-4. Figure 3-4(a) clearly exhibited a strong, positive linear relationship between Δ[CCO] vs Δ[HbO] (with a correlation coefficient of R^2=0.968 and a p value of p<0.001),and a strong, negative linear relationship between Δ[CCO] vs Δ[HHb] (with a correlation coefficient of R^2=0.965 and a p value of p<0.001). On the other hand, both open diamonds and open squares represent placebo-induced Δ[HbO] and Δ[HHb] values, which were all within a lower Δ[CCO] range without any obvious linear relationship shown in the figure. In addition, similar to Δ[HbO], Fig. 3-4(b) also demonstrated strong, positive linear dependences of Δ[HbD] and Δ[HbT] on tPBM-generated Δ[CCO] with R^2>0.96.

3.3.3 tPBM-induced ratios of cerebral ∆[CCO] to increased cerebral hemodynamic parameters

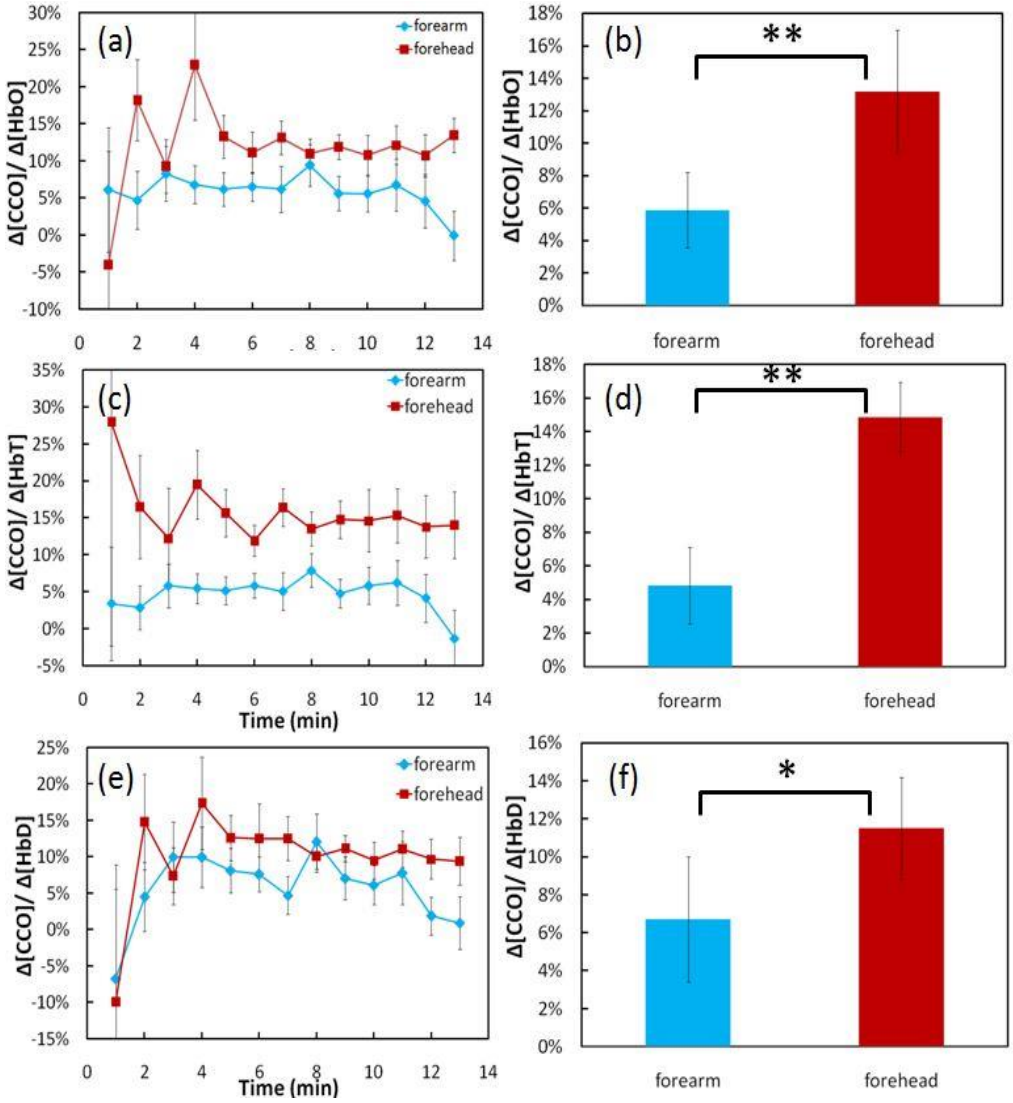

Figure 3-5Ratios of (a) ∆[CCO]/∆[HbO], (c) ∆[CCO]/∆[HbT], and (e) ∆[CCO]/∆[HbD] during and after infrared laser stimulation on the right forehead of 11 human subjects (red symbols) and on the right forearm of another group of 11 human subjects (blue symbols). Time-averaged ratios of (b)∆[CCO]/∆[HbO], (d) ∆[CCO]/∆[HbT], and (f) ∆[CCO]/∆[HbD] with corresponding standard deviations in both forearm and forehead stimulation cases. "**" marks significant difference ($p<0.01$, two sample t-test) of ∆[CCO]/∆[HbO] or ∆[CCO]/∆[HbT] between the stimulated cases."*" marks significant difference ($p<0.05$, two sample t-test) of ∆[CCO]/∆[HbD] between the stimulated cases.

Furthermore, I examined ratios of tPBM-induced cerebralΔ[CCO] to three of the increased cerebral hemodynamic parameters, i.e., Δ[HbO], Δ[HbT], and Δ[HbD], since these three parameters reflect increased cerebral oxygenation, CBV, and CBF initiated by tPBM, respectively. These ratios revealed quantitative physiological associations between the cerebral metabolic up-regulation of [CCO]and corresponding hemodynamic oxygen supply. In Fig. 3-5(a), red symbols and lines plot the ratios of Δ[CCO]/Δ[HbO] at each time point during and post-tPBM periods. It was clear that 2 minutes after tPBM started, this ratio remained above or around 12.5-13%,withan initial but non-significant variability across the 11 subjects. Following the same format, I also plotted the subject-averaged ratio of Δ[CCO]/Δ[HbT] during and post-tPBM periods, in Fig. 3-5(c), by the red symbols and lines. Similar to Fig. 3-5(a), I found that 2 minutes after tPBM started, this ratio from the forehead recording reached above 15% and remained relatively constant across the entire 12 minutes (7 min during tPBM and 5 min post-tPBM).

For a better comparison, I also quantified the ratios of the same parameters from identically laser-stimulated human forearms (n=11) based on the data reported in my previous study [13]. The blue symbols and lines in Fig. 3-5(a) represent the ratios of Δ[CCO]/Δ[HbO] obtained from the laser-stimulated human forearms, with an average of ~6% across all the subjects. The group-averaged ratio of Δ[CCO]/Δ[HbT] from the stimulated forearms were also small (~5%), as illustrated in Fig. 3-5(c).Similar trends also existed for Δ[CCO]/Δ[HbD] for both the laser-treated foreheads and forearms across most of time points, as illustrated in Fig. 3-5(e).

In order to test for statistically significant group differences in these ratios between laser-treated foreheads and forearms, I further time-averaged the mean ratios of Δ[CCO]/Δ[HbO] Δ[CCO]/Δ[HbT], and Δ[CCO]/Δ[HbD] across the time during and post-tPBM periods (excluding the 1st time point at t = 1 min) from 2-13 min for all three cases. Figures 3-5(b), 3-5(d), and 3-5(f) show bar plots (mean ± SD, N = 11) and clearly demonstrated that these ratios of laser-

induced Δ[CCO] to corresponding hemodynamic increases in the human forehead are significantly larger than those in the human forearms.

3.4 Discussion

3.4.1 New findings of this study

Following the first demonstration of increased oxidized CCO and hemoglobin concentrations in response to laser photobiomodulation on the human forearm in my previous study[13], I utilized a similar experimental design and protocol and applied the same laser stimulation transcranially on the right forehead of 11 human subjects in this study. For the first time, bb-NIRS was used to quantify tPBM-induced cerebral Δ[CCO] and four hemodynamic parameters, namely, Δ[HbO], Δ[HHb], Δ[HbT], and Δ[HbD] (Fig. 3-3). With this novel approach and careful data acquisition and analysis, I demonstrated that 1064-nm laser could induce significant increases of cerebral Δ[CCO] and corresponding Δ[HbO], Δ[HbT], as well as Δ[HbD] in a dose-dependent manner over time, as compared with those under the placebo treatment (Fig. 3-3). In addition, clear positive linear relationships between Δ[CCO] versus Δ[HbO], Δ[HbT], and Δ[HbD](Fig. 3-4) suggested that tPBM resulted in not only rapid up-regulation of [CCO] but also subsequent increases of cerebral blood flow (in proportion to Δ[HbD]), blood volume (in proportion to Δ[HbT]), and blood oxygenation (in proportion to Δ[HbO]).

Furthermore, I carefully reviewed, derived, and quantified the wavelength-dependent DPF factor, DPF(λ),which played a critical role for this study to minimize crosstalk artifacts[39, 40] and improve the accuracy of [CCO] quantification. This study demonstrates the great utility of bb-NIRS as a non-invasive technology for mechanistic investigations and treatment evaluations of tPBM that has great potential to become an intervention tool for improving cognitive and emotional functions in subjects with and/or without neurological disorders[17, 51].

3.4.2 Comparison of the results between this study and previous ones

I published two papers: refs. [13] and [55]. In ref. [13], I reported that laser-stimulated∆[CCO]on the human forearm was strongly and linearly correlated with ∆[HbO], which is consistent with this study when the same laser and stimulation paradigm were performed on the human forehead. These consistent findings demonstrated a significant effect of photobiomodulation on human tissue CCO and a close interplay between metabolic CCO and hemodynamic oxygenation, which remains even after ending the laser treatment (i.e., in the recovery phase). Furthermore, Fig. 3-3 clearly showed that a significant tPBM-induced increase of Δ[CCO] started first, and was then followed in time by significant changes in Δ[HbO] and Δ[HHb]. This implies that the metabolic up-regulation of [CCO] occurred prior to any hemoglobin responses, and that Δ[HbO] increased a little faster than Δ[HHb].This "Δ[CCO]-lead-Δ[HbO]" observation was also confirmed in ref. [13].

One difference between this paper and ref. [13]is noted below: Laser-induced Δ[HHb] on the human forearm showed a gradual, non-significant increase while tPBM-induced Δ[HHb] on the human forehead exhibited a significant decrease. One important observation of the current study is that tPBM-induced Δ[HbT] and Δ[HbD] correlated highly and linearly with Δ[CCO] on the human forehead [Fig. 3-4(b)], implying tPBM-driven increases in CBV and CBF at the treated site. For quantitative comparison, I went back to the human forearm data and calculated the relationships between laser-induced Δ[HbT] vs. Δ[CCO] and Δ[HbD] vs. and Δ[CCO]. This additional calculation confirms that the laser-treated arms also exhibited increases in Δ[HbT] and Δ[HbD] and thus in total blood volume and blood flow, consistent with the observation seen in the treated human forehead, as reported in this paper.

In ref. [55], with use of a dual-wavelength NIRS system, I reported significant increases in ∆[HbO], ∆[HbD], and ∆[HbT] as well as a decrease in ∆[HHb] in response to tPBM given on the human forehead. All the trends in changes of chromophore concentrations were very

consistent with the results shown in this current paper. Note that the sites to deliver tPBM and to acquire NIRS data were about at the same location on each subject's right forehead in both studies, supporting good reproducibility and reliability for my findings. However, the magnitude of decreased ∆[HHb] in the current study is much smaller than that in ref. [55]. This quantitative difference in ∆[HHb] could be attributed to the exclusion of ∆[CCO]. In principle, dual-wavelength measurements permit determinations of concentration changes in only two chromophores (i.e., ∆[HbO] and ∆[HHb]) without consideration of ∆[CCO]. In contrast, this current study carefully analyzed wavelength dependence of DPF(λ) by applying a frequency domain OxiplexTS tissue oximeter to accurately determine absorption and reduced scattering coefficients on the human forehead. Instead of employing two wavelengths, I applied a total of 161 wavelengths to perform a broadband linear regression. All of these procedures should minimize calculation errors and lead to improved accuracy of ∆[HbO], ∆[HHb] and ∆[CCO] determination[39, 41], and thus more accurate ∆[HbT] and ∆[HbD] as well. Furthermore, with the bb-NIRS approach in this study, I observed larger increases in blood volume, which is consistent with a previous report that laser stimulation could lead to an increase of blood flow [60].

3.4.3Interpretation of tPBM mechanism

Based on the results observed in this study and the existing literature, I can better interpret and understand the mechanism of tPBM, which can be explained schematically using Fig. 3-6(a).Specifically, infrared light initiates a series of reactions linked to energy production inside mitochondria, which may be summarized into six biochemical processes: CCO photon absorption, CCO oxidation, proton pumping and nitric oxide (NO) release, CCO-catalyzed oxygen reduction to water, ATP synthesis by oxidative phosphorylation, and coupled hemoglobin oxygen transport. Each of these processes may be briefly explained as follows: (1)

CCO photon absorption: infrared light photons are absorbed by copper ions inside CCO, the primary molecular photoacceptor at this wavelength. The extensive spectroscopic evidence from in vitro studies of how CCO absorbs infrared photons has been reviewed by Karu[61]. In neurons in particular, Wong-Riley et al [3] have demonstrated that CCO mediates the biochemical effects of photobiomodulation on cultured neuronal cells. (2) CCO oxidation: four electrons are removed from the heme aa3 group inside CCO, increasing the concentration of oxidized CCO. This biochemical process of CCO oxidation has been determined by numerous in vitro studies, as reviewed by Wikstrom et al[62]. Cerebral concentration of oxidized CCO has been measured in vivo by bb-NIRS during neural activation and/or in neonatal brain injury by Kolyva, Tachtsid is and others [39-41]. (3) CCO proton pumping and NO release: the oxidized CCO pumps four protons ($4H^+$) to the inter-membrane space (space between inner and outer membranes of mitochondria); another four protons ($4H^+$) are added to the matrix (central part of mitochondria). The evidence for this process has been reviewed by Hatefi [63]. When photo-stimulated, CCO also releases NO from the CCO catalytic site[64]. (4)CCO catalyzes oxygen reduction to water: CCO enzyme catalytic activity reduces $2O_2$ to $2H_2O$ using $4H^+$ and $4e^-$.But not all the molecular oxygen is fully reduced to water, resulting in a small fraction of superoxide that forms a cascade of reactive oxygen species[65]. Photobiomodulation stimulates oxygen reduction as well as the formation of reactive oxygen species that activate cellular signaling[2]. When molecular oxygen levels decrease, then CCO catalyzes the synthesis of NO, as determined by Poyton and Ball[66]. (5) ATP synthesis by oxidative phosphorylation: $4H^+$ pumped by CCO oxidation to the inter-membrane space return to the matrix going through ATP synthase powered by the proton electrochemical gradient, resulting in the phosphorylation of ADP into ATP[63]. (6) Hemoglobin oxygen transport: the hemodynamic response of increased HbO_2 is triggered by increased O_2 utilization in the reaction catalyzed by CCO, which consumes most of the O_2 transported by hemoglobin in the cerebral circulation[50]. In addition, the increased CBF caused by photobiomodulation may be facilitated by local vasodilation produced

by the NO synthesis and release from CCO[66]. While there are many other possible effects induced by photobiomodulation[67], I provide here in vivo evidence consistent with the interpretation that tPBM mechanisms involve a primary action on CCO.

Since tPBM delivers light to a stimulated cortical tissue area much larger than a single mitochondrion or larger than a single neuron, a large group of mitochondria receive the laser stimulation, which would lead to significant increases of oxidized CCO concentration and corresponding hemodynamic activities. As a result, significant increases in cerebral HbD, HbT, and HbO would occur in the adjacent region of tPBM, as I have detected by my bb-NIRS. Indeed, the observed increases of these hemodynamic parameters reflect tPBM-triggered increases of regional CBF, CBV, and cerebral hemoglobin oxygenation (i.e., HbO), as schematically shown in Fig. 3-6(b).

3.4.4 tPBM-induced metabolic-hemodynamic coupling

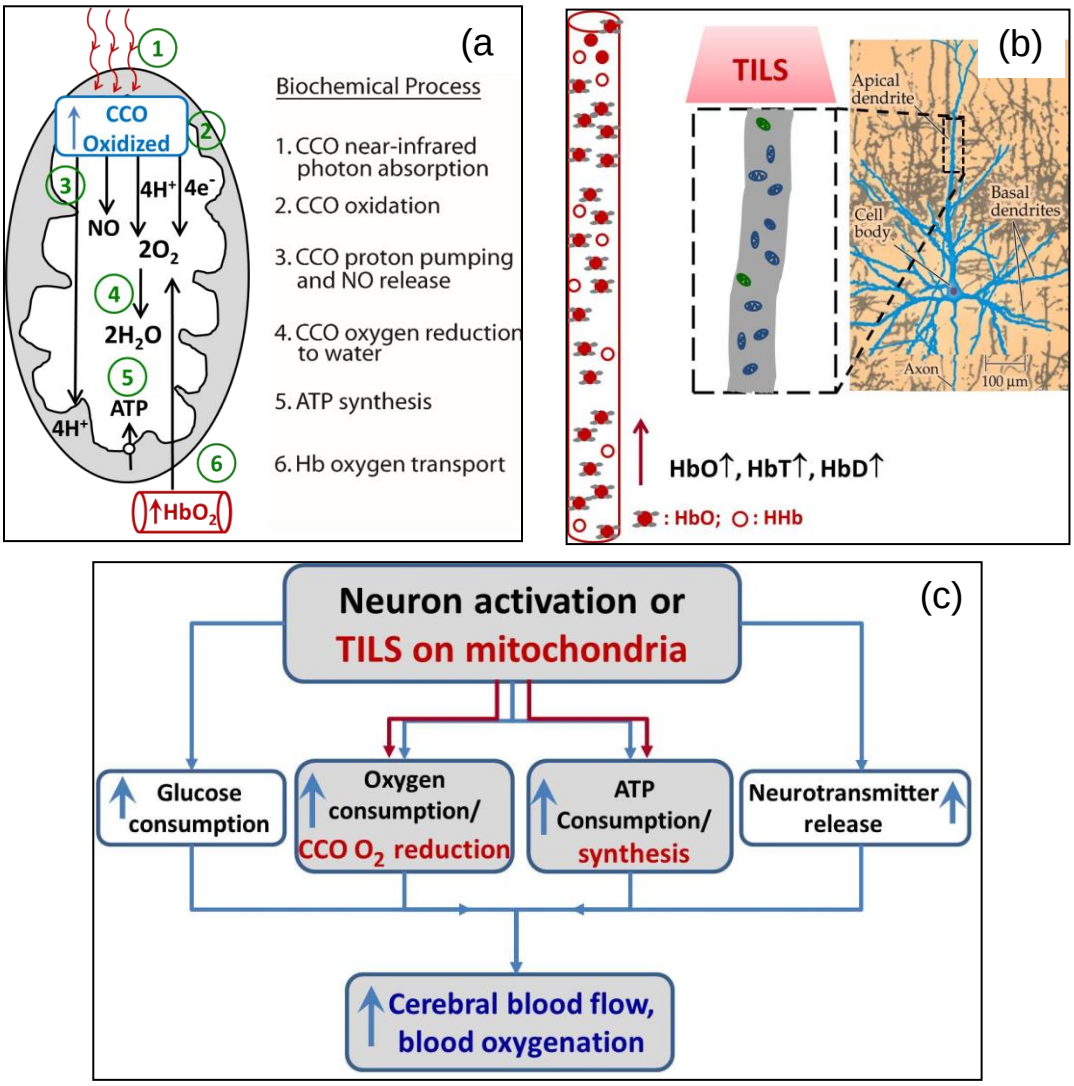

Figure 3-6(a) Model of the photobiochemical mechanism of action of infrared light on the measured cytochrome c oxidase oxidation (CCO oxidized) and hemoglobin oxygenation (HbO2). See text for detailed explanation. (b) The right most panel shows a pyramidal neuron of the cerebral cortex, which is modified from a figure in ref. [68]. The middle dashed rectangle is a zoomed section of apical dendrite, containing an abundant amount of mitochondria, with which CCO can be photo-stimulated and oxidized by tPBM. This photobiomodulation consequently drives increases of HbO, HbT, and HbD. (c) A flow chart to show the conventional neuro-vascular coupling by the black-colored notations and my newly-defined tPBM-induced metabolic-hemodynamic coupling by the red-colored notations. The blue-colored notations

represent common endpoints of both mechanisms on the cerebral circulation. The dashed lines represent exclusion from the metabolic-hemodynamic coupling.

By close inspection on Figs. 3-6(a) and 3-6(b), I realize that the relationships between Δ[CCO] vs. Δ[HbO] and/or Δ[CCO] vs. Δ[HbT] (and Δ[CCO] vs. Δ[HbD] as well) reflect or infer a neuro-vascular coupling relationship, except that tPBM deals with a large anatomical/physiological scale since tPBM excites a large group of neurons in a relatively large cortical tissue area. To differentiate forehead (transcranial) and forearm (peripheral) laser-triggered coupling between CCO and hemodynamic parameters, I computed CCO/HHb ratios as indices of metabolic-hemodynamic coupling. Specifically, based on my data shown in Figs. 3-5(b) and 3-5(d), I introduced three metabolic-hemodynamic coupling indices, C_M-HbO, C_M-HbT, and C_M-HbD, which are defined as the ratios of Δ[CCO]/Δ[HbO], Δ[CCO]/Δ[HbT], and Δ[CCO]/Δ[HbD], respectively. With these newly defined indices, I can compare the metabolic-hemodynamic coupling strength quantitatively between the laser-treated human forehead and forearm. Table 3-1 below lists the metabolic-hemodynamic coupling indices of C_M-HbO, C_M-HbT, and C_M-HbD for both the laser-treated human forehead and human forearm cases. This table clearly demonstrates that the metabolic-hemodynamic coupling in the brain is much stronger than that in the human forearm. To quantitatively measure/mark how strong this coupling is in the brain, I took the ratio of each index (i.e., C_M-HbO, C_M-HbT, and C_M-HbD) between the brain and forearm cases and listed it in the 2nd right-most column of Table 3-1. It indicates that the laser-induced metabolic-hemodynamic coupling strength between CCO and total blood volume/oxygenation in the brain was ~200-300% more efficient or stronger than that in the forearm, while the coupling strength between CCO and blood flow in the brain is about 160% stronger than that in the forearm. The 1st right-most column lists p-values for statistical significance of each metabolic-hemodynamic coupling index between the laser-treated human

forehead and human forearm cases across all the subjects. It clearly shows much significant differences between the two cases for each of the coupling indices.

Table 3-1 Comparison of laser-induced metabolic-hemodynamic coupling strength Determined in the human forehead and forearm

Metabolic-hemodynamic coupling index	forehead (mean±s.d.%)	forearm (mean±s.d.%)	forehead/forearm (%)	P-value
$C_{M\text{-}HbO}$=([CCO]/[HbO])	12.6 ± 3.5	5.9 ± 2.3	214%	< 0.01
$C_{M\text{-}HbT}$=([CCO]/[HbT])	15.3 ± 7.5	4.8 ± 2.2	318%	< 0.01
$C_{M\text{-}HbD}$=([CCO]/[HbD])	12.2 ± 4.7	7.6 ± 3.4	161%	<0.015

The large difference in metabolic-hemodynamic coupling strength could be expected because neurons do not store energy and need fast/efficient conversion to extract oxygen from the blood supply. Using the principle of conventional neuro-vascular coupling as an example for comparison, the flow chart written in black in Fig. 3-6(c) demonstrates how neural activation drives consumption increases of glucose, oxygen, and ATP, as well as neurotransmitter release. All of these increased consumptions then lead to increases of cerebral blood flow and blood oxygenation[68]. The metabolic-hemodynamic coupling that I introduced above for explaining the mechanism of tPBM can be thought and explained by analogy to neuro-vascular coupling, following the flow chart with red-colored notation in Fig. 3-6(c). Namely, tPBM provides CCO photobiomodulation on a large group of mitochondria from the laser-stimulated human forehead. This laser intervention drives CCO-catalyzed oxygen reduction to water and NO release coupled with ATP synthesis, as explained/illustrated in detail by Fig. 3-6(a). Subsequently, cerebral CBF, CBV, and hemoglobin oxygenation are promptly elevated in order to meet the oxygen demand caused by tPBM.

Earlier in Section 3.1, I described my observation of "Δ[CCO]-lead-Δ[HbO]", which can be explained well by my metabolic-hemodynamic coupling concept, as shown by Fig. 3-6(c). Furthermore, I also observed from Fig. 3-3 that the significant decrease in Δ[HHb] occurred last compared to Δ[CCO] and all other hemodynamic parameters. This observation matches well the results reported in ref.[68, 69]about the interaction between neural electrical activity and the microcirculation, and thus can be explained as follows: In the initial phase of tPBM, Δ[HHb] would increase due to the higher consumption and demand of O_2 caused by [CCO] up-regulation/oxidation (this is similar to the "initial dip" phase). Since this process should occur fast right after tPBM onset, my bb-NIRS system would not be able to catch or record it due to the limited time resolution. Then, under low local O_2 conditions, CCO-catalyzed NO release[66] would induce vasodilation and significant increases in both CBF and CBV. This occurred quickly following the onset of tPBM and over-supplied the oxygenated blood, leading to a large increase of Δ[HbO] but a delayed decrease of Δ[HHb], which was recorded by my bb-NIRS.

3.4.5 Limitations of this study and future work

There are still a few limitations in this study. First, due to the single channel bb-NIRS system, the readings were taken with a single source-detector (S-D) separation of 3cm. This large S-D separation enabled a deep photon penetration depth to reach cerebral tissue underneath the skin and skull[31, 70]. However, in the meantime, the measured optical signal shad to go through multiple layers of the subject's head. In other words, the quantified values of Δ[HbO], Δ[HHb] and Δ[CCO] in my experiments might be contaminated by those from the skin and skull. In future studies, therefore, a two/multiple channel bb-NIRS system with a short S-D separation of 1cm needs to be implemented; the corresponding 1-cm readings can be used to regress the scalp/skull effect from the cerebral metabolic and hemodynamic response from the 3-cm channel. Second, the temporal resolution of the combined tPBM/bb-NIRS protocol is

limited to 1 min because of the interleaved design between the laser stimulation and bb-NIRS data acquisition. I am not able to observe any fast response of cerebral tissue to tPBM. A possible solution may be to apply a low pass filter at the laser aperture so as to filter out the affecting optical signal within the bb-NIRS wavelength range.

A recent study reported that photobiomodulation by 810-nm and 980-nm lasers operated via different mechanisms of action in the same tissue cultures of adipose cells [71]. It is likely that my 1064-nm laser acting transcranially on brain cells operated via a different mechanism of action. Since many different factors and conditions existed between ref. [71] and my study, such as: in vitro vs. in vivo measures, adipose cells vs. brain cells, 810 nm and 980 nm vs. 1064 nm lasers, it is difficult to obtain a fair comparison. Further studies are needed by using 810-nm laser/LEDs to repeat my in vivo experiments and examine if similar changes in ΔHbO, ΔHHb, and ΔCCO will occur.

It is known that the NIR absorption peak of CCO is around 800-850 nm, but within this spectral region light scattering is also rather strong. The latter aspect will prevent the NIR light from traveling deep into the brain tissue. At 1064 nm, on the other hand, while light absorption of CCO is reduced compared to that at 810 nm, the light scattering effect is significantly reduced too. It implies that the 1064-nm laser may be able to travel deeper into the cortex through the scalp and skull and provide photobiomodulation[13]. No other in vivo human studies in the literature demonstrated yet that other lower wavelengths, such as 810 nm, have the same effects on CCO. The answer to whether 1064-nm laser is the optimal wavelength for neuromodulation is out of the scope of this paper. Future computer simulations and laboratory experiments are good approaches to provide solid and quantitative answers.

3.5 Conclusion

In conclusion, the findings suggest the hypothesis that 1064-nm laser stimulation causes CCO oxidation, and oxidized CCO is the conformation of the enzyme that has the highest activity. I reported for the first time that tPBM can induce significant increases of [CCO] on the human forehead in vivo. Particularly, the treatment effect on [CCO] and [HbO] can last for at least 5 more minutes after tPBM stops. Strong linear interplay between Δ[CCO] versus Δ[HbO] and Δ[CCO] versus CBF(in proportion to Δ[HbD]) as well as Δ[CCO] versus CBV (in proportion to Δ[HbT]) were observed for the first time on human forehead during tPBM, indicating a hemodynamic response of oxygen supply coupled to the increase of cellular oxygen metabolism induced by transcranial photobiomodulation. This gives a potential biochemical and physiological explanation of the beneficial effects of tPBM to a variety of clinical and psychological conditions[6, 7, 10, 15, 18, 20, 22, 51-54]. Furthermore, I introduced tPBM-induced metabolic-hemodynamic coupling indices, which allowed me to better understand the interaction between neural electrical activity and the microcirculation or between the tPBM-enhanced cerebral metabolism and corresponding blood oxygen supply. Overall, this study provides the first demonstration that tPBM causes up-regulation of CCO in the human brain, and contributes important insight into the cerebral physiological mechanisms. The results also reveal a tremendous potential for bb-NIRS as a non-invasive optical means to study in vivo mechanisms of cerebral blood flow and metabolism and perform treatment evaluations of tPBM.

Chapter 4

Impact of heat on hemodynamic and metabolic changes in transcranial photobiomodulation measured by broadband near-infrared spectroscopy

This chapter is accepted for publication at the Journal of Neurophotonics in September 2017.

***Authorship**: Xinlong Wang, Divya D. Reddy, Sahil S. Nalawade, Suvra Pal, F. Gonzalez-Lima, and Hanli Liu**

4.1 Introduction

The concept of using near-infrared or infrared light to modulate biological functions, also known as photobiomodulation (PBM), has recently gained rising attention since it may serve as an effective, non-invasive, interventional tool for multiple neural applications [6, 10, 15, 17]. For example, transcranial infrared laser stimulation (TILS) with 1064-nm laser applied to the forehead has served as a particular approach of brain PBM for improving human neurocognitive functions, such as attention, memory and executive functions [17, 18, 53, 54, 72]. A couple of mechanistic studies on TILS were recently reported by Wang et.al [13, 14], supporting the hypothesis that photons at 1064 nm oxidize cytochrome c oxidase (CCO), the terminal enzyme in the mitochondrial respiratory chain. Light absorption of CCO [12] effectively contributes to oxygen and energy metabolism in neurons [3]. TILS leads to up-regulation of cerebral CCO and hemodynamics as well as increases in cerebral oxygen consumption [13, 14, 55]. The mechanism of TILS supported/discussed in refs. [13, 14] helps me understand the relationship between metabolic and hemodynamic changes [20], and provides a mechanistic explanation for beneficial neural effects of PBM and/or TILS in a number of medical conditions [10-13].

However, besides metabolic and hemodynamic effects on cerebral tissues, TILS may generate non-negligible thermal effects that may confound the results of previous studies [13, 14] due to laser heating on the tissue. Up to now, while several beneficial effects of PBM have

been reported for its therapeutic use [51, 73], the contribution of heat generated from near-infrared or infrared light towards any of the studied positive effects has never been tested. In principle, continuous irradiance with laser or light-emitting diodes (LED) over a period of time at a particular region of interest would result in an accumulated thermal effect and thus lead to an increase of skin or local temperature at the stimulated region. Such a thermal effect could lead to local increases of blood flow and tissue oxygenation, which could confound the association or interplay between metabolic and hemodynamic effects induced by TILS [5, 6]. Specifically, it was unclear whether my measured changes of oxy-hemoglobin, deoxy-hemoglobin, and total-hemoglobin concentration (i.e., Δ[HbO], Δ[HHb], and Δ[HbT]) under TILS were induced by the enhanced metabolism (i.e., increased oxidized CCO concentration, Δ[CCO]) or by the TILS-produced thermal effect. The objective of this study was to quantitatively assess TILS-induced thermal effects on metabolic and hemodynamic changes of forehead tissue measured by broadband near infrared spectroscopy (bb-NIRS), as well as to confirm/demonstrate the potential role of such thermal effects on hemodynamic changes of forehead tissue determined by bb-NIRS.

4.2 Methods

4.2.1 Brief review of previous TILS setup and measurements

I recently reported that TILS could result in up-regulation of cerebral CCO and hemodynamics as well as increases in cerebral oxygen consumption [13, 14, 55]. While details on TILS setup and experimental protocols were given in Refs. [13, 14, 55], I briefly review related information on the TILS experimental setup and protocols here for the reader's convenience.

The laser used in my previous TILS studies was a 1064-nm continuous wave laser device (HD Laser Model CG-5000, Cell Gen Therapeutics LLC, Dallas, TX), which has been Food and Drug Administration (FDA) cleared for various uses in humans [4, 5]. The laser light was delivered from a handpiece with a beam area of 13.6 cm^2. Since the laser was collimated, the

laser beam's size was kept approximately the same from the laser aperture to the stimulation spot on the participant's forehead. The laser power during TILS was kept ~ 3.4 W with a power density in the beam area of 0.25 W/cm^2, the same as that reported in previous studies [13, 14, 17, 18, 55]. For the sham experiment, the laser power was reduced close to zero (i.e., 0.1 W) with a black cap covering the laser aperture. In this way, the sham stimulation seemed similar to the actual TILS but without any light delivered to the subject's forehead.

Specifically, following previously successful studies [13, 17, 18, 55], my safe laser stimulation parameters were as follows: Total laser power = 3.4 W; area of laser beam radiation = 13.6 cm^2; power density = 3.4 W/13.6 cm^2 = 0.25 W/cm^2; time radiated per cycle = 55 s; total laser energy per cycle = 3.4 W $\times$ 55 s = 187 J/cycle; total laser energy density per cycle = 0.25 W/cm^2 $\times$ 55 s = 13.75 J/cm^2/cycle. The TILS stimulation and measurement consisted of a two-minute baseline period, an eight-minute laser stimulation period, followed by a five-minute recovery period. The stimulation site was on the right frontal forehead above the eye brow (see Fig. 4-1). Within each minute, the stimulation was on for 55 seconds and off for 5 seconds, when the bb-NIRS data acquisition was performed.

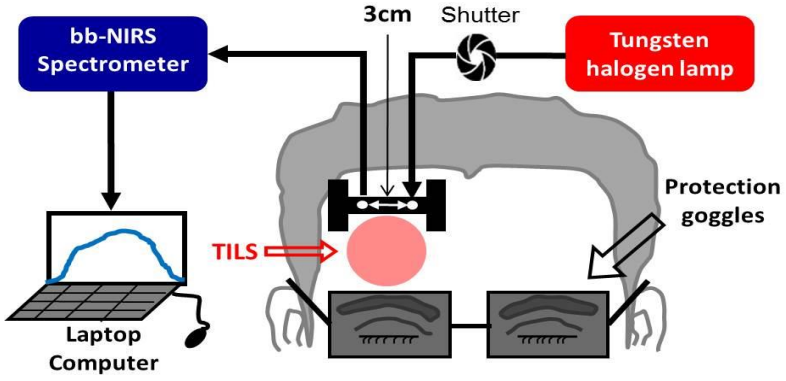

Figure 4-1 Schematic diagram of the experimental setup for TILS, including a bb-NIRS spectroscopic system. This bb-NIRS unit consisted of a tungsten halogen lamp as the light source and a miniature CCD spectrometer as the detector. TILS was administered underneath the "I" shaped probe holder. The narrow, middle section of the holder was ~8 mm in width. A laptop computer was used to acquire, display and save the data from the spectrometer. A shutter controlled the on and off function for the white light

from the tungsten-halogen lamp to the subject's forehead. A pair of protection goggles was worn during the whole experimental procedure. [14]

The experimental setup of a bb-NIRS system used for the previous TILS study is shown in Fig. 4-1; it was also utilized in the current heat-effect study. Section 4.2.3 below will provide detailed information on the bb-NIRS setup and related parameters chosen for bb-NIRS measurements.

4.2.2 Human subjects participated in TILS and thermal experiments

Eleven healthy human subjects were recruited from the local community of The University of Texas at Arlington (UTA) with 31±13.7 years of age (i.e. average ± standard deviation) in TILS and thermal experiments. The two sets of experiments were carried out by two independent experimental designs with three visits (one visit for the TILS-induced effect and two visits for the heat-induced effects) of the same human participants. Pre-study screening was taken for each human participant during each visit prior to the stimulation/data acquisition. The inclusion criteria included: either sex, any ethnic background, and in an age range of 18–50 years old. The exclusion criteria included: (1) Diagnosed with a psychiatric disorder; (2) had history of a neurological condition, or any brain injury, or violent behavior; (3) had ever been institutionalized/imprisoned; (4) took any long-term or short-term medicine; (5) was currently pregnant; (6) was a smoker or had diabetes.

TILS-induced metabolic and hemodynamic responses were measured and reported earlier [14]. The current study focused on heat-induced changes of metabolic and hemodynamic signals on the forehead to determine whether thermal effects of TILS would potentially confound photobiomodulation effects that I observed previously [14]. Specifically for the current thermal-effect study, the chosen individuals were assigned to participate in two separate experiments done on the forehead: (1) skin-temperature recording under TILS and (2) thermal stimulation

done at the same forehead location as that of TILS, together with bb-NIRS measures as in my previous studies [5, 6]. These two experiments were performed during two separate visits. Specifically, skin-temperature-recording experiments were performed for all participants within one week. After the subject-averaged time-dependent temperature curve was acquired, all subjects underwent thermal stimulation experiments on their foreheads in the following week.

The experimental protocols adhered to National Institutes of Health (NIH) guidelines, and were approved by the institutional review board (IRB) at UTA for ethical guidelines which govern human experiments. Each participant received explanations of the instruments and procedures of the experiment. A written consent was taken from participants before the start of every experiment.

4.2.3 Experimental setup and instruments for thermal stimulation measurements

The entire experiment was divided into two different phases. The first phase was to measure the skin temperature increase by the laser that was used in studies by Wang et. al [13, 14]. As illustrated in Fig. 4-2, the laser used for the set-up was a FDA-cleared 1064-nm laser device (Model CG-5000, HD Laser, Cell Gen Therapeutics LLC, Dallas, Texas, USA) also used before [13, 14] for laser stimulation. The uniform laser beam with an area of 13.6 cm^2 was emitted from a safe distance of 2 cm from the handpiece during the experiment. Collimation of the laser facilitated the size of the laser beam at the stimulation area to be maintained as that emitted from the laser aperture. The laser power was maintained at a constant value of 3.4 W and laser power density in the laser beam was 0.25 W/cm^2. The values of laser power and power density were chosen to replicate the experimental procedure conducted in previous studies [13, 14] so as to acquire the same TILS-induced temperature changes as before.

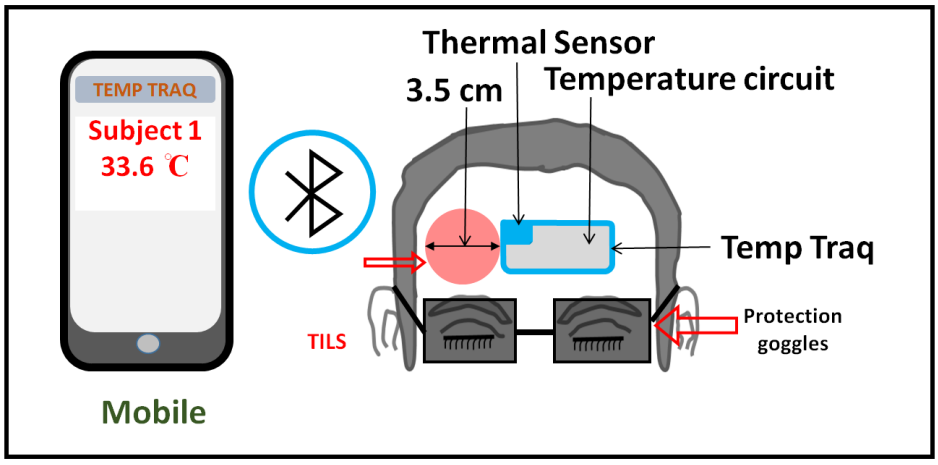

Figure 4-2 Schematic diagram of the experimental setup for the skin-temperature-recording experiment that included a temperature measurement system (TempTraq™,Blue Spark Technologies, Inc. Westlake, Ohio). The TempTraq unit/patch includes a small thermal sensor (5x5 mm^2), as shown in the figure, and a temperature circuit to determine the temperature value induced by tPBM on the forehead skin surface. The tPBM was delivered on the right side of the TempTraq patch, which was connected via Bluetooth to a mobile device. Protection goggles were worn by the participants during the entire experimental procedure.

A thermal patch, TempTraq (hands-free temperature monitoring system) was used for measuring thermal readings near the tPBM delivery site (right forehead) continuously during the entire experiment. This patch was made with safe, soft, flexible, durable, water resistant and non-latex materials (TempTraq™, Blue Spark Technologies, Inc. Westlake, Ohio, USA). In general, TempTraq uses Bluetooth 4.0 to pair and connects to any iOS or Android device for continuous monitoring of body temperature. It is self-powered for 24 hours. Any mobile device connected with TempTraq could record remotely temperature data from the TempTraq patch within a range of 40 feet. For my experiment, the distance between the mobile device and the TempTraq patch was maintained within 5 feet. The accuracy of the device was approved by the American Society for Testing and Materials (ASTM); it has been tested and verified to ASTM Standard E1112-00 as required for all digital thermometers[74]. The patch was placed on the

clean and dry skin surface and ensured that no hair was trapped beneath the patch. The thermally sensitive area (5x5 mm^2 –Confirmed) on the patch was located near the tPBM location (marked by blue-shaded area in Fig. 4-2); the rest of the patch included the embedded thermal detection circuit and the Bluetooth device (marked by gray-shaded area in Fig. 4-2).

The second phase of experiments was the thermal-stimulation measurements using a thermal stimulator (Pathway model ATS, Pain and Sensory Evaluation system, Medoc advanced medical systems, Israel), which was employed to simulate tPBM-induced thermal effects at the same location of tPBM. Temperature output of the stimulator was set according to the forehead skin-temperature experiment in response to tPBM. The Medoc Pathway was a temperature management system using liquid coolant. The coolant was a combination of 70% water and 30% ethanol. The system also contained a cooling unit and a transformer that helped in maintaining the desired temperature. The equipment was mounted on a cart, whose dimension was 103x52x62 cm^3. The stimulation area of the ATS Thermode (probe) that came in contact with the skin surface was 16x16 mm. The temperature range that could be achieved was from 0˚C to 55˚C with an accuracy of 0.1˚C. The rate of increase or decrease of the temperature could be programmed up to 8˚C / sec. As it is shown in Fig. 4-3, the ATS Thermode of the Medoc Pathway was placed on a clean surface of the right frontal forehead for delivering thermal stimulation. The stimulator was placed in close proximity of the 3D-printed, I-shaped, probe older, which held the source and detector fibers to measure the cerebral metabolic and hemodynamic responses to thermal heating equivalent to that induced by tPBM.

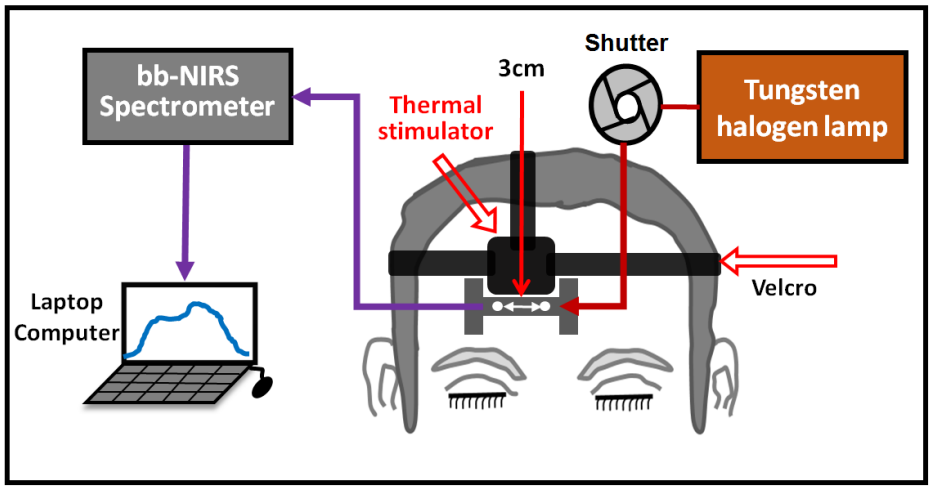

Figure 4-3 Schematic diagram of the experimental setup for the 2nd phase of experiment using a bb-NIRS monitoring system. The spectroscopic system consisted of a tungsten-halogen lamp as the light source and a high-sensitive CCD spectrometer as the detector. Thermal stimulation was administered above the I-shaped probe holder, which held two optodes with 3 cm apart. A shutter was used for switching the light delivery on and off from the lamp to the participant's forehead. The data from the spectrometer was collected, saved and displayed using a laptop computer.

The bb-NIRS system consisted of a broadband light source (i.e., a tungsten-halogen lamp) having a spectral range of 400–1500 nm (Model 3900, Illumination Technologies Inc., East Syracuse, New York, USA), a high-sensitivity CCD spectrometer with a spectral range of 735–1100nm (QE-Pro, Ocean Optics Inc., Dunedin, Florida, USA), and a laptop computer for data acquisition. Specifically, the light emitted from the light source was directed through a multimode fiber optode (diameter = 3mm) to the subject's forehead. The average optical power at the optode tip was ~20-40 mW. The diffused light from the forehead was collected by another fiber optode with the same size to the bb-NIRS spectrometer. The two fiber bundles were held by a 3D-printed I-shaped holder very closed to the stimulation site (see Fig. 4-3). Each acquired optical signal was sent to the QE-Pro spectrometer and then converted to a spectrum of 735–1100 nm for further spectroscopic analysis. The laptop computer would display and store the

results for off-line analysis and interpretation. Details of the bb-NIRS system can also be found in refs. [13, 14].

4.2.3 Experimental protocols

4.2.3.1Forehead skin-temperature recording in response to tPBM

During each experiment in both measurement phases, the subjects were comfortably seated, and procedures of the experiments were well explained. They were also asked to wear protective glasses for safety purpose and were instructed to close their eyes during the entire experimental procedure. The 1064-nm laser (CG - 5000) was used to stimulate the right forehead of each subject, and the laser hand piece was held by a well-trained research assistant to deliver TILS. A temperature sensor patch, TempTraq (a wireless wearable thermometer), was placed on the right forehead, close to the TILS site (see Fig. 4-2 for details). The protocol and timeline used for TILS remained the same as those given in refs. [13, 14]. In order to achieve accurate TILS-induced, skin-temperature readings, the thermal recording was on continuously during the entire TILS experiment. Then, time-dependent (averaged over 1 min) temperatures across the pre-, during, and post-stimulation period were calculated and are plotted in Fig. 4-4, outlining estimated skin temperatures near the light delivery site during and after TILS. This time-dependent, thermal profile then was used to set the temperature setting on the thermal stimulator (Medoc Pathway) to simulate TILS-induced thermal effects. The blue lines in Fig. 4-4 mark the thermal temperature setting that was used to create thermal stimulations in the second phase of the experiments, namely to measure metabolic and hemodynamic responses to thermal effects.

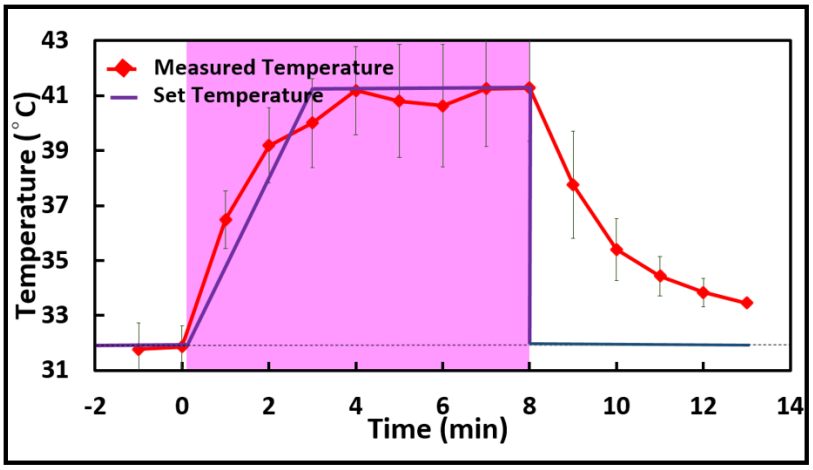

Figure 4-4 Forehead skin-temperature increases during and post tPBM. It displays local skin temperatures of the forehead near the tPBM site. The red curve displays measured temperatures of the skin near the laser (CG -5000) delivery site from the first phase measurement. Each red point displays a single value which was averaged over 1 minute of the thermal data (mean over n=11). The blue curve shows the thermal setting values on the thermal stimulator (Medoc Pathway) used in the second phase of the experiment. Time zero marks the starting time of tPBM delivery.

4.2.3.2 Cerebral metabolic and hemodynamic responses to thermal effects/stimulation

For the second phase of the experiments, each participant was asked to relax without moving the head while readings of reduced light scattering coefficient (μ_s') and absorption coefficient (μ_a) of the forehead were taken using a tissue oximeter (OxiplexTS, ISS Inc., Champaign, IL), as described Refs. [13, 14]. After this set of optical property measurements, a 3D-printed, I-shaped, optical probe holder was fixed on the right forehead near the location of used in the first phase study (see Figs. 4-1 and 4-2). the distance between the source and detector probes in the holder remained 3cm, same as in my earlier study. As it is shown in Fig. 4-2 and Fig. 4-3, the thermal stimulation was provided by the Medoc Pathway system. The thermal probe used for stimulation has surface area of 256 mm^2 and the probe was used in contact with the skin to stimulate the thermal effect to the right side of the forehead. The thermal probe was also fixed in close proximity with “I”-shaped probe and was fixed on the upper side of

the “I”-shaped probe. A special bandage, hospital graded double sided tape and Velcro was also used to affix the thermal probe and also the “I”-Shaped probe, to make a good contact with the skin and to eliminate any possible motion artifacts. The experimental protocol is as illustrated in Fig. 4-5. The thermal stimulation was divided into three different parts, baseline (pre-stimulation) for 2 mins, thermal stimulation for 8 mins and recovery (post-stimulation) for 5 mins. The bb-NIRS white light source was switched "on" during the entire experiment while the shutter was kept on only during the five-second acquisition and off for the rest of the experiment to avoid stimulation effect from the light source as explained in Fig. 4-5. The data was acquired in the same format during the baseline (pre-stimulation) for 2 mins, thermal stimulation for 8 mins and recovery (post-stimulation) for 5 mins. The tissue heating that could have been caused by the white light was reduced by using an optical filter of wavelength of 1000 nm and the optical shutter was switched on only during the 5-sec period per 60-second cycle. The temperature used for thermal stimulation was initiated at 32˚Celsius and it was increased steadily for 180 seconds to reach 41˚Celsius and was maintained the same for the rest of the 300 seconds of thermal stimulation, using the Thermode placed on the right side of the forehead. After 8 mins of thermal stimulation, the temperature reading was brought abruptly to 32˚Celsius, which was my baseline temperature.

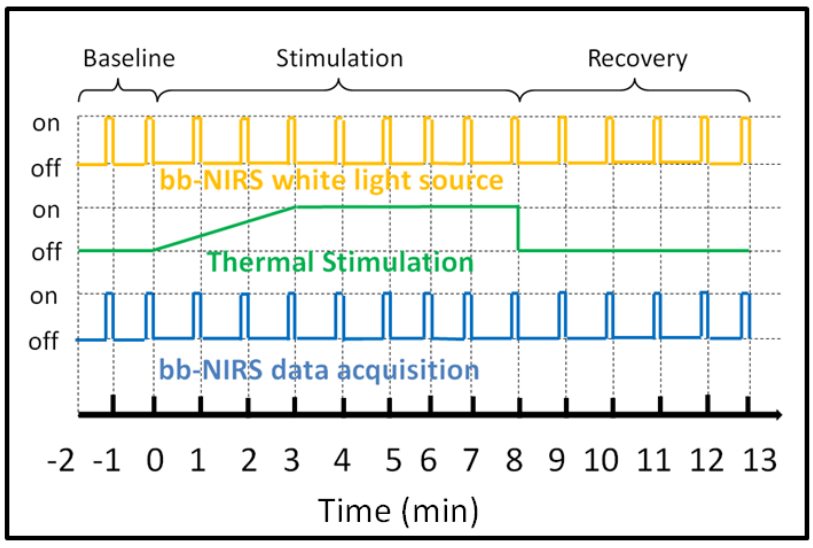

Figure 4-5 Paradigm of the bb-NIRS white light source interleaved with thermal stimulation and bb-NIRS data acquisition. Each experiment consists of 2-min baseline, 8 min of thermal stimulation and 5-min of recovery. The light source is switched on for 5-s for NIRS data acquisition and switched off for the rest of the time in each minute. During the thermal stimulation, there is a gradual increase from the baseline and after 3-min the desired temperature is reached and the temperature was kept constant until the stimulation period ends.

4.2.4 Data Processing and Statistical analysis

Based on the modified Beer-Lambert law, a multi-linear regression model was applied to the acquired spectral data for estimations of Δ[HbO], Δ[HHb], and Δ[CCO] in response to thermal effects. Mathematical details on both the modified Beer-Lambert law and multi-linear regression model can be found in Refs. [13, 14]. Additionally, concentration changes of total hemoglobin (Δ[HbT]) and differential hemoglobin(Δ[HbD])were estimated by Δ[HbT]=Δ[HbO]+Δ[HHb] and Δ[HbD]= Δ[HbO]-Δ[HHb], respectively, for all the 13 time points. The data for each time point across all eleven subjects were averaged. Also, the standard deviation and standard error of mean were computed. Statistical analysis was then carried out to determine statistically significant differences between the thermally-induced and TILS-induced effects on Δ[HbO], Δ[HHb], Δ[HbT], Δ[HbD] and Δ[CCO] using a repeated-measure ANOVA, followed by one way ANOVAs with the level of Bonferroni corrected significance of $p<0.05$ (to account for multiple-time measurements) in order to identify significant differences at individual time points, for each of the five chromophore concentrations.

4.3 Results

4.3.1tPBM-induced time-dependent changes in concentrations of CCO, HbO, HHb, HbTand HbD

Figure 4-6 illustrates changes in concentrations of HbO, HHb, HbT, HbD and CCO over the entire experiment of 15 min, including 2-min baseline, 8-min TILS/thermal stimulation and 5-min recovery. Figure 4-6(a) displays two time-dependent curves of ∆[HbO] in response to TILS and thermal (heat) stimulation. Note that the TILS-induced ∆[HbO] values were reported previously in Ref. [14], but they are reused and replotted in this Section for easy comparison. For each respective case, each data point was averaged over all the subjects; the shaded region indicates the time period under either TILS or thermal stimulation. The initial time at t=0 marked the onset of the TILS/thermal stimulation. Since the laser energy density (*E*) delivered to the forehead can be defined as a product of the exposure time ($t_{exposure}$) and the laser power density (*P*), namely, $E = t_{exposure}xP$, the delivered stimulation dose is in proportion to the exposure time, as marked in Fig. 4-6. All five panels in Fig. 4-6 indeed present dose-response curves, showing the dependence of metabolic/hemodynamic response parameters (i.e., ∆[CCO], ∆[HbO], ∆[HHb], ∆[HbT], and ∆[HbD]) on the TILS or heat stimulation dose over the entire experiment time course.

The repeated-measure ANOVA showed that either time or stimulation (i.e. thermal and laser) could create overall statistical significance for each of four chromophore concentration changes, namely, ∆[HbO], ∆[HbT], ∆[HbD] and ∆[CCO]. Next, one way ANOVAs with Bonferroni correction, performed at each individual time point for each of the chromophore concentrations, presented that significant differences between heat-induced and TILS-induced changes in [HbO], [HbD], [HbT], and [CCO] started to appear 1 min, 2 min, 2 min, and 3 after the stimulation, respectively, as marked in each panel of Fig. 4-6. However, the repeated-measure ANOVA given on the time-dependent changes in [CCO] values showed that there was no significant difference in [CCO] changes with respect to that at 1 min after the heat stimulation.

Based on the published work by Tsuji et al. [56, 57], Soul et al. [58], and Hupert et al. [59], changes in [HbT] are directly linked to changes in tissue blood volume (ΔTBV), while changes in [HbD] are associated to changes in tissue blood flow (ΔTBF). Hence, Figs. 4-6(c) and 4-6(d) imply that the heat-based thermal stimulation on the human forehead resulted in significant changes in ΔTBV and ΔTBF during the thermal stimulation period.

Two other findings are worthwhile to point out: (1) All of the heat-induced hemodynamic decreases in ∆[HbO], ∆[HbD] and ∆[HbT] returned toward baseline within 2-3 min as soon as the termination of thermal heating, while the TILS-induced increases in both hemodynamic and metabolic (i.e., ∆[CCO]) measures stayed constant, without any clear trend to quickly go back to baseline during the 5-min post stimulation period. (2) Fig. 4-6(b) illustrates that heat-induced ∆[HHb] were not showing significant difference between those caused by TILS.

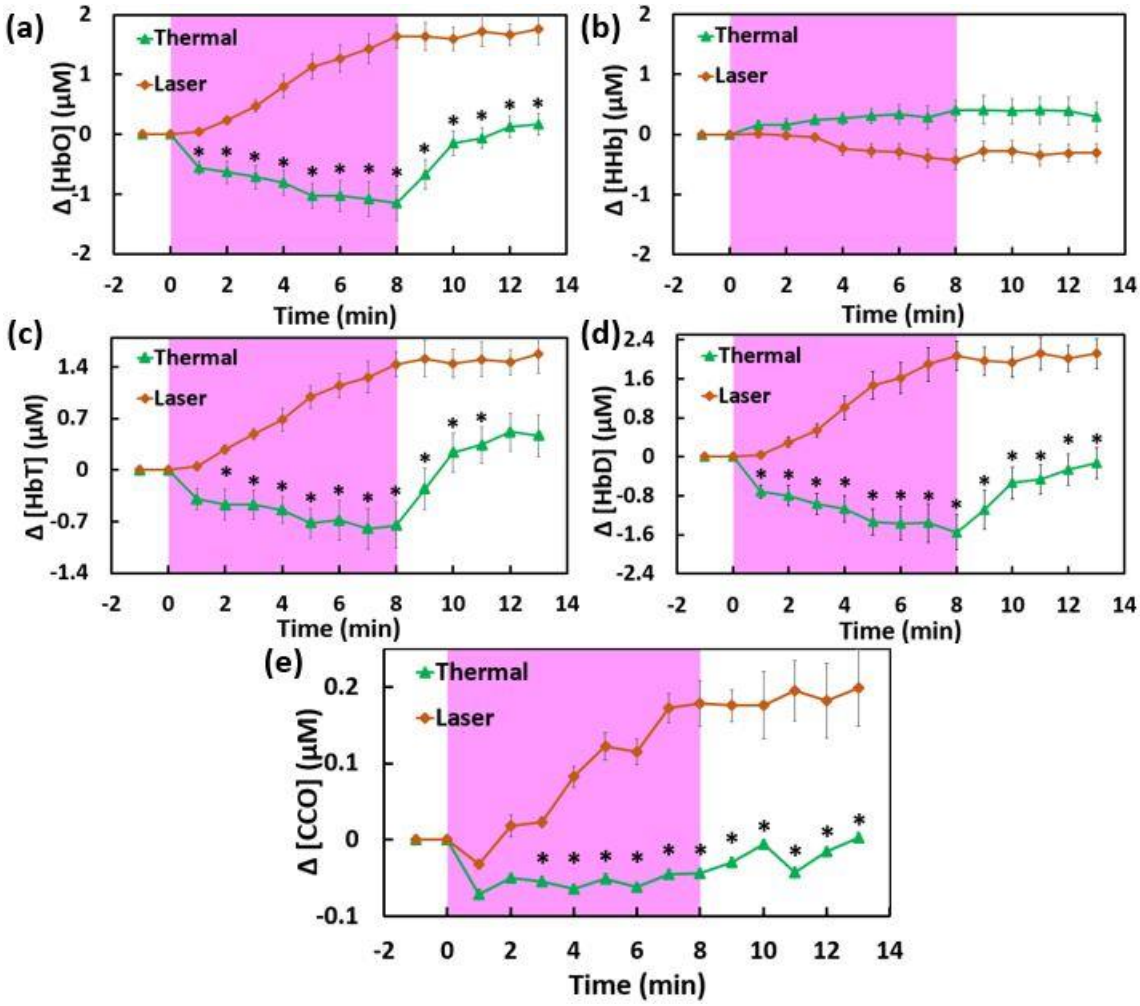

Figure 4-6 Participant–averaged time courses of TILS (laser) and heat (thermal) effects on changes in (a) [HbO], (b) [HHb], (c) [HbT], (d) [HbD], and (e) [CCO], measured in vivo from each participant's forehead (mean ± SE, n=11). The initial time at t=0 marks the onset of the TILS/thermal stimulation. The shaded region in each panel displays the stimulation period. The unit for all concentration changes is in μM. In each panel, "*" symbols mark statistical significance with $p<0.05$ (Bonferroni corrected) between TILS-induced and heat-induced chromophore concentration changes, based on a repeated-measure ANOVA followed by one way ANOVAs.

4.3.2 Dependence of cerebral hemodynamic parameters based on thermal-induced metabolic changes

∆[HbO], ∆[HHb], ∆[HbT] and ∆[HbD]under tPBM and thermal stimulation respectively were extracted, regrouped and re-plotted as shown in Figure 4-7 to demonstrate the dependence of each cerebral hemodynamic parameter (namely ∆[HbO], ∆[HHb], ∆[HbT] and ∆[HbD]) on the cerebral metabolic indicator, (Δ[CCO]) under the influence of both thermal stimulation and tPBM. The key observation is that distinct with tPBM, there exists no significant linear relationship between Δ[CCO] versus Δ[HbO] and Δ[CCO] versus Δ[HHb] under thermal stimulation. And all the Δ[HbO] and Δ[HHb] values lie within a lower range of Δ[CCO] that is symbolized by the solid diamonds and solid squares respectively in Figure 4-7 (a) as compared to the significant linear relationship displayed under laser stimulation denoted by the open diamonds and squares. Figure 4-7 (b) also exhibits the similar results of the nonlinear relationship between Δ[CCO] versus Δ[HbT] and Δ[HbD] denoted by solid rounds and solid triangles respectively clustering within specified lower range of Δ[CCO].

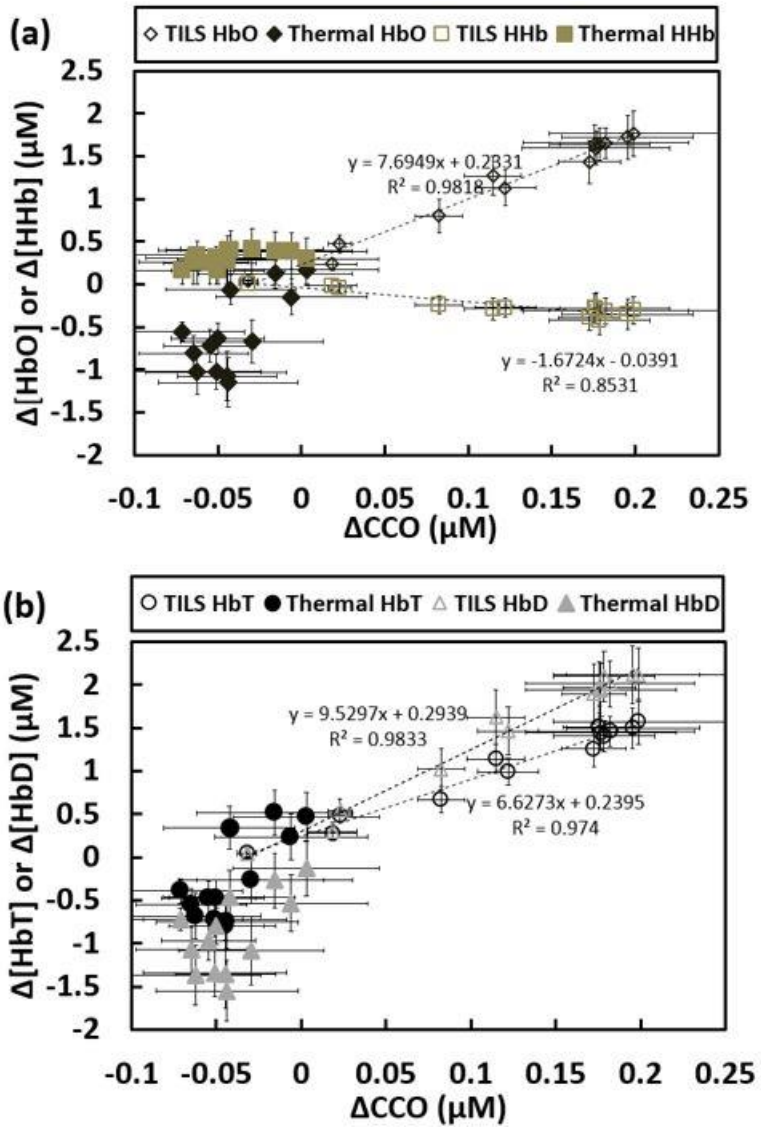

Figure 4-7 (a) Relationships of Dependence between Δ[CCO] vs. Δ[HbO] and Δ[CCO] vs. Δ[HHb] across all subjects (n=11) under the effect of thermal stimulation and tPBM. The solid black diamonds and solid tan squares show the relationship of Δ[CCO] vs. Δ[HbO] and Δ[CCO] vs. Δ[HHb] respectively. Both the open diamonds and squares symbolize tPBM-treated Δ[CCO] vs. Δ[HbO] and Δ[CCO] vs. Δ[HHb], respectively.(b) Relationships of Dependence between Δ[CCO] vs. Δ[HbT] and Δ[CCO] vs. Δ[HbD] across all subjects (n=11) under the effect of thermal stimulation and tPBM. The solid black circles and solid gray triangles illustrate the relationship of Δ[CCO] vs. Δ[HbT] and Δ[CCO] vs. Δ[HbD] respectively. Both the open circles and triangles denote the tPBM-treated relationships. The standard errors of means are also plotted from their respective concentrations of the chromophore..

4.4 Discussion

4.4.1 Hemodynamic and metabolic responses of forehead tissue to thermal stimulation

In one of my recent studies, I clearly demonstrated that transcranial photobiomodulation by the 1064-nm laser gave rise to up-regulation of oxidized CCO concentrations and hemoglobin oxygenation in vivo assessed/quantified by non-invasive bb-NIRS [14]. However, it was not clear whether the measured signals were contaminated by potential thermal effects that could result from possible TILS-related laser heating on the human forehead. To address this concern, I designed a novel protocol that utilized the same bb-NIRS to quantify thermal effects caused by the laser heating. In this way, I were able to assess heat-generated metabolic and hemodynamic parameters in vivo for the first time. To simulate the same thermal effects created by the 1064-nm laser, a thermal sensor was calibrated and used to facilitate time-dependent, skin-temperature recording near the TILS delivery site (Fig. 4-2). Then, a computer-controlled thermal stimulator was set carefully to deliver the same thermal variation pattern as that during TILS (Fig. 4-3). By comparing the chromophore concentration changes caused by both TILS (as reported in ref. [14]) and heat stimulation, I successfully demonstrated the distinction between the hemodynamic and metabolic responses to heat and TILS, which enabled me to exclude the potential confounding effect due to laser heating to the subject's forehead.

Specifically, the experimental results shown in Figs. 6 and 7 clearly illustrated that transcranial Δ[HbO], Δ[HbT] and Δ[HbD] during the 8-min heat stimulation decreased significantly, implying reduced blood oxygenation, blood flow, and blood volume at the measured site. All three of the altered hemodynamic parameters returned promptly to baseline after the heat stimulation was removed. The statistical analysis, based on a repeated measure ANOVA followed by one-way ANOVAs, on the chromophore concentration alterations between the two stimulation methods revealed statistically significant distinctions between the sample means at most of time points during and after heat/TILS stimulation periods. Namely, TILS resulted in strong hemodynamic oxygenation and metabolism, whereas heat applied to the

forehead, on the other hand, generated cerebral hemodynamic effects distinct from those of TILS. Moreover, as seen in Fig. 4-7, no obvious linear interplay between hemodynamic and metabolic effects was observed during and after pure thermal stimulation.

While TILS-induced and thermally-induced Δ[CCO] changes showed significant differences, the statistical analysis revealed that heat stimulation could not make Δ[CCO] significantly deviate from its initial onset value (i.e., 1 min after the heat stimulation) [Fig. 4-6(e)]. This observation implies that forehead thermal stimulation over 8 minutes up to 41 oC does not significantly alter oxygen metabolism of forehead tissue, and thus would not significantly affect/confound my previous results and conclusions that TILS is able to up-regulate CCO concentrations and hemoglobin oxygenation in vivo in human subjects [14]. Another significant difference in forehead tissue responses to TILS and thermal stimulation is that both metabolic and hemodynamic changes during post TILS tended to stay for a longer duration of time, while these respective parameters returned quickly back to their baselines as soon as the heat stimulation stopped (Fig. 4-6). This observation supports that TILS is highly desirable for treating certain neurological disorders because of its longer-lasting after-effects compared to thermal stimulation.

The heat intervention was observed to generate hemodynamic and metabolic changes in the distinct direction with respect to TILS. Thus, it is possible that the actual TILS-evoked changes in hemodynamic and metabolic enhancement could be greater than being reported in ref. [14] if appropriate calibrations were taken to compensate for the laser-heating effect.

4.4.2 Possible explanation of heat-induced changes in hemodynamic signals of forehead tissue

In principle, thermal heating on a subject's forehead should result in a temperature rise of forehead tissue, leading to dilation of blood vessels and increase of regional blood flow at the stimulation site. This would also give rise to increases of total hemoglobin concentrations in the local stimulation site. However, the major temperature enhancement should happen only on the

skin surface without affecting cerebral hemodynamics. Thus, any increase of tissue blood flow and blood volume (i.e., ΔTBF and ΔTBV) would occur only at the heating site, driving more blood from nearby superficial layers and resulting in decreases of ΔTBF and ΔTBV of nearby forehead tissue. Close inspection of Fig. 4-3 reveals that my bb-NIRS interrogated a region of forehead tissue very adjacent to the heat-stimulation site. Thus, my observations on heat-induced hemodynamic changes shown in Fig. 4-6 match well the fore-mentioned expectation.

While a 3-cm source-detector separation of bb-NIRS could sense changes of hemodynamic signals in the cerebral regions, it measures all the signals coming from multiple layers, including the scalp, skull, and cerebral regions. It is noted that bb-NIRS detects only changes with respect to a baseline. Thus, contributions from the superficial layers to the measured signals will become dominant if no or little change occurs within the cerebral region. To confirm my speculation or expectation, a 2-channel bb-NIRS system is needed with a short (1 cm) and long (>3 cm) source-detector separation in future studies, as pointed out in the following sub-section.

4.4.3 Limitation of the study and future work

First, this heat-stimulation study did not include a placebo experiment with respect to thermal stimulation, assuming that there were no variations in any of the NIRS parameters over the baseline readings. This assumption may not be accurate since cerebral hemodynamic signals (such as HbO, HHb, and HbT) do fluctuate over time. Moreover, both bb-NIRS and thermal probes placed on the subject's forehead could give rise to time-dependent signal variations. All of these factors could confound the measured signals in the heat-stimulation group. In my future studies, I will conduct placebo controlled experiments in order to understand/reveal more rigorous/accurate thermal effects on hemodynamic and metabolic variations of forehead tissue.

Second, I were limited by the number of spectrometers (or channels) used in this study, so I could not perform a two-channel (for long- and short-separation) broadband NIRS measurements to simultaneously monitor hemodynamic and metabolic changes at different tissue depths on the human forehead. Further upgrade on my instrumentation is needed for more comprehensive experiments to confirm my speculation.

4.5 Conclusion

In conclusion, I measured time-dependent temperature increases on 11 subjects' foreheads using clinical-grade thermometers following the TILS experimental protocol used in my previous study. According to the broadband near infrared spectroscopy readings on the same subjects, significant differences in hemodynamic and metabolic responses (i.e., ΔHbO, ΔHbT, ΔHbD, and ΔCCO) were observed between the heat-induced and laser-induced effects on human foreheads. No obvious linear interplay between hemodynamic and metabolic effects was observed during and after pure thermal stimulation. The observations indicated that the tissue-heat interaction exhibited distinct response patterns from those during the tissue-photon interaction during the laser stimulation. This study overall demonstrated that the observed effects of TILS on cerebral hemodynamics and metabolism are not induced by heating the skin.

Chapter 5

A novel absolute value quantification algorithm for hemoglobin and CCO

This Chapter is a manuscript to be submitted soon.

5.1 Introduction

Near-infrared spectroscopy (NIRS) uses near-infrared light to determine oxygenated hemoglobin (HbO) and deoxygenated hemoglobin (HHb) concentrations based on their wavelength-dependent extinction coefficients and scattering properties [28, 31]. This noninvasive detection method is usually performed to determine the scattering features or hemoglobin oxygenation in human tissue [56, 70, 75]. It has three major detection technique types: time resolved, frequency resolved, and continuous-wave (CW) measurement.

A time-domain system determines tissue absorption and scattering ability based on the histogram of a photon's time-of-flight due to the system's high speed of photon emitters and detectors. Using a time-resolved system, Bruno Montcel et al. calculated cerebral hemodynamics in 2006 [76]. In 2007, Ken M. Brady et al. investigated the cerebrovascular autoregulation for acute brain injury with a time-resolved system [77]. A frequency-domain system applies amplitude sinusoid modulation to its laser sources—usually about 100 MHz. Based on the phase delay and amplitude changes of the diffused light, it is possible to determine the hemodynamic and scattering information in absolute values. For example, Fantini et al. calculated the hemoglobin concentrations and scattering coefficients on the foreheads of young and senior adults [44]. However, although time- and frequency-resolved measurements can accurately determine absorption and scattering coefficients, both techniques are complex and expensive. The third NIRS system category is the CW system, which emits non-modulated light and uses slower detectors such as photodiodes or spectrometers [41, 78]. The CW system calculates chromophore concentrations from attenuated optical density based on the Beer–

Lambert Law. However, it is hard to separate the effect of scattering from absorption due to its non-modulated light and slow emitter and detector [25]. Nevertheless, CW systems are more cost effective than time- and frequency-resolved systems. It can also be built to perform broadband spectroscopic measurement, which can potentially improve the CW system's quantification accuracy [40, 79]. In this study, I applied a CW system to detect the diffused broadband spectrum on human tissue. Scattering power was obtained from the literature and verified with a frequency-resolved system [46, 80]. 1st and 2nd derivatives of the detected spectrum were obtained and fitted with simplified expressions of photon flux, based on Diffusion [81, 82]. I then quantified the absolute values of chromophore concentrations and scattering properties through a multistep ant-colony-optimization curve-fitting algorithm.

The quantification algorithms of most NIRS applications rely on the inaccurate assumption that HbO and HHb (sometimes with water) are the only sources of absorption contribution, which results in undesirable errors [37]. Actual tissue has multiple absorption sources, whose absorption contributions and physiological meanings are non-negligible.

Cytochrome c oxidase (CCO) is the terminal enzyme of the Electron Transportation Chain, which contributes in 95% of oxygen metabolism and adenosine–triphosphate (ATP) synthesis [2, 40, 83]. The concentration alteration of CCO directly relates to cellular oxygenation, energy supplements, and health conditions [3, 84, 85]. This enzyme is crucial for reflecting the tissue-metabolism condition. Further, it has a high absorption ability in the near-infrared (NIR) wavelength range, which makes it detectable by NIRS—and especially by broadband NIRS [39, 79]. Based on the modified Beer–Lambert Law, in 1995, S. J. Matcher et al. applied the multi-wavelength NIRS to quantify the concentration change of CCO [34]. In 2012, Arnab Ghosh et al. developed a hybrid probe to measure the concentration change of CCO after cerebral–functional activation by considering the wavelength dependency of differential pathlength factors for better estimation accuracy [84]. Employing a similar broadband approach, Xinlong Wang et al. investigated the concentration change of CCO during and after

photobiomodulation [13, 14]. However, this study limited the monitoring of chromophore concentration to relative-value quantification, which was susceptible to artificial movement and systematic noise [36]. To execute the absolute-value approach, S. J. Matcher initially proposed utilizing the water-extinction spectral features found after derivation in 1994 [86]. Later, in 2012, Keith St. Lawrence et al. improved the algorithm and applied CW measurements to calculate tissue HbO, HHb, water concentration, and scattering coefficients with the help of their characteristic derivative spectral features [82], however, CCO was not included into consideration, and the fitted values were lack of accuracy support. In this study, for the first time, I applied derivation-based CW optical measurement to determine the absolute concentration values of CCO with other tissue components, including the HbO, HHb, water fraction (water%), fat fraction (fat%), and scattering coefficient factors (m and n). The fitting algorithm was based on photon–diffusion approximation with mathematical derivations and simplifications. I performed simulations to ensure proper estimation accuracy. Further, in vivo measurements were taken on human foreheads and forearms. The results were consistent with concurrent frequency-resolved readings, previous studies, and general physiological facts [40, 46, 80, 87].

5.2 Methods

5.2.1 Algorithm

Photon propagation in a turbid medium can be approximately described as Eq. 5-1, which denotes the photon flux for continuous wave system[81],

$$R(\rho, z_0) = \frac{1}{4\pi}\left[z_0\left(\mu_{eff} + \frac{1}{r_1}\right)\frac{\exp(-\mu_{eff} r_1)}{r_1^2} + (z_0 + 4AD)\times\left(\mu_{eff} + \frac{1}{r_2}\right)\frac{\exp(-\mu_{eff} r_2)}{r_2^2}\right] \quad 5\text{-}1$$

where $\mu_{eff} = \sqrt{\frac{\mu_a}{D}}$, $r_1 = \sqrt{z_0^2 + \rho^2}$, $r_2 = \sqrt{(z_0 + 4AD)^2 + \rho^2}$, A is a constant related to the internal reflection[88]. ρ is the source detector separation. D represents the diffusion coefficient, which can be calculated by absorption coefficient μ_a and scattering coefficient μ_s' as $D = \frac{1}{3(\mu_a + \mu_s')}$. z_0 defines the boundary condition that is defined as z_0=3D. The wavelength dependency of μ_s' was definedin Eq. 5-2based on Mie theory[89, 90].

$$\mu_s'(\lambda) = m * (\frac{\lambda}{750})^{-n} \quad 5\text{-}2$$

where λ denotes the wavelength in nm. Factor "m" and "n" denote the size and power of scatterers in the medium[89-91].

In human in vivo experiments, the source– detector separation were set as 1.5 cm (i.e., on human forearms) or 3 cm (i.e., on human foreheads), and the μa and μs' were 0.1 cm-1 and 10 cm-1, respectively. In this way, (z0)2 is in the scale of 10-2, which is less than 1% of ρ2, whose scale is about 101. Therefore, (z0)2 is negligible in Eq. 5-1 for simplification. Furthermore, due to the diffusion regime, (i.e. $\mu_a << \mu_s'$), diffusion factor D can be simplified as $D = \frac{1}{3\mu_s'}$. Taking logarithm on both sides of Eq. 5-1. The equation can be simplified as,

$$\log(R) = \log(1 + \rho * \sqrt{3 * \mu_a * \mu_s'}) - \rho * \sqrt{3 * \mu_a * \mu_s'} - \log(\mu_s') + C \quad 5\text{-}3$$

Where C is a constant term, which can be eliminated during derivation process. Fig. 5-1 shows the spectral representations of Eq. 5-1 and Eq. 5-3. The black circles denote a signal generated by the photon–diffusion–approximation equation (Eq. 5-1) from Liu et al. [81], with 2% noise and the red curve as the simplified equation (Eq. 5-3). As Fig. 5-1 demonstrates, the algebraic-approximation process successfully simplified the complexity of the mathematical terms in the equation without varying its general scale or spectral features. To further rectify the

feasibility and accuracy of the simplification, during my simulation, I employed an equation (i.e., Eq. 5-1) consistent with previous absolute-value studies to generate a signal, and I used the simplified version (i.e., Eq. 5-3) to perform the fitting.

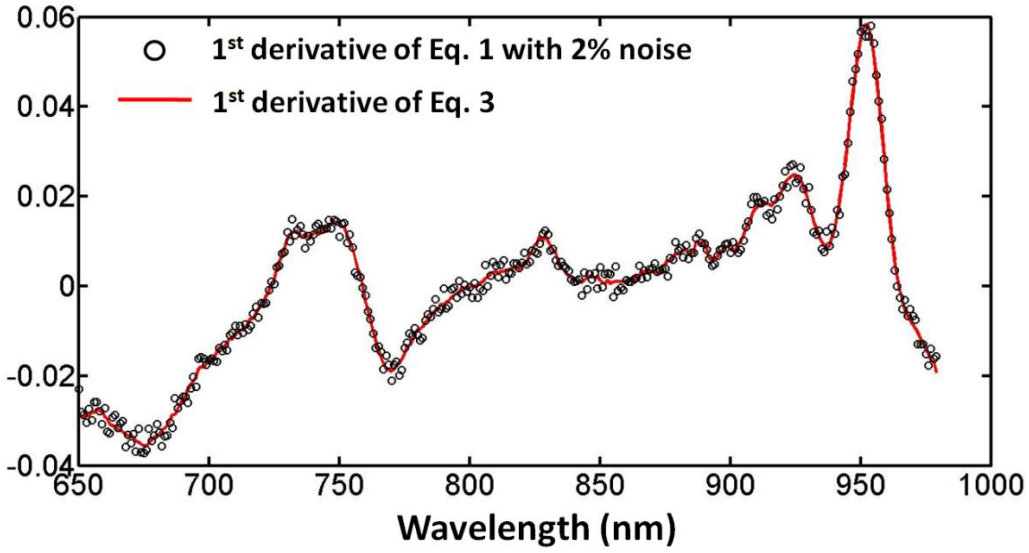

Figure 5-1. The first derivative–spectral expression of the original photon–diffusion–approximation equation (black circles) and the simplified version (red line).

5.2.2 Simulation

5.2.2.1 Initial settings

According to previous literature [46, 80, 82, 87], I initialized four groups of chromophore concentrations and scattering properties to simulate human tissue. Table 5-1 shows the four groups of values.

Table 5-1 Initial settings of different parameters in simulation.

	HbO (μM)	HHb (μM)	CCO (μM)	Water%	Fat%	m (μM)	n (μM)
1	40	20	5	80%	25%	10	1.2
2	30	20	3	80%	25%	10	1.2
3	40	20	8	80%	25%	10	1.2
4	40	20	3	80%	25%	10	1.2

Further, 1%, 2%, 5%, 8%, 10%, 12%, 15%, 18% and 20% of noise were added to the simulated data, respectively. Next, I compared the fitted results of the concentration values

under each noise level were compared with their initial settings to evaluate the percentage of estimation error.

5.2.2.2 Ant-colony optimization

Ant-colony optimization is a computational algorithm used for finding the shortest path toward a target. It was initially proposed and established in 1992 by Marco Dorigo in his PhD thesis. Since then, this algorithm have been widely applied in various of fields[92-94].

Ants travel randomly while searching for food, and once they locate food, they return to their nest, leaving a trail of a specific chemicals called a pheromone. If another randomly wandering ant finds this pheromone trail, it stops traveling randomly and instead follows the trail until it reaches the food (optimization condition). This ant then leaves another layer of pheromone on top of the pheromone trail the first ant left. As more ants follow the trail, pheromones accumulate on this optimized path connecting the food with their nest. Finally, most ants will walk along the optimized path with the highest concentration of pheromones, which usually indicates the optimized solution to a computational problem.

In this study, I simulated a nest of randomly walking “ants” to find the combination of proper concentrations and scattering factors that optimally minimized the difference ($\chi 2$) of Eq. 5-3 with the detected CW spectrum in the first and second derivative domains. To reduce unnecessary complexity, I defined the upper and lower bounds of each fitting parameter under general physiological ranges. For example, in most of the previous NIRS studies on human tissue, the HbO concentration was usually reported as 30–40 μM. Therefore, I set 0 and 80 μM as the lower and upper bounds for HbO, which confined HbO within 0–200% of its reasonable human tissue value. This could significantly reduce the complexity of computational calculation and the estimation time, without artificially interfering with the calculation process. With the same standard, I set the upper and lower bounds of other parameters as follows: HHb between 0–60 μM; CCO between 0–20 μM; water% between 60–95%; fat% between 0–90%; scattering

factor m between 0–30; and, particularly, scattering factor "n" was set as 0.9 to 1.1 on human arms and 1.2 to 1.4 on human brains to reduce cross talk and fitting variability.

5.2.2.3 Fitting protocols

In the simulation, three different $\chi 2$ were calculated and compared with estimation accuracy. $\chi 12$ denotes the minimized difference between the first derivative of Eq. 5-3 versus the first derivative of the CW spectrum. $\chi 22$ denotes the minimized difference between the second derivative of Eq. 5-3 versus the second derivative of the CW spectrum. $\chi 32$ denotes the minimized summation of $\chi 2$ for the simultaneous first and second fitting. I then calculated the estimation error with respect to the initial setting and compared it with the three fitting methods.

5.2.3 In vivo experiments

5.2.3.1 Participants

The human participants were recruited from the local community of The University of Texas at Arlington (UTA). Interested individuals were screened by one of the investigators to determine their eligibility to this study. The inclusion criteria included: (1) either sex, (2) any ethnic background and (3) in an age range of 18–55 years old. The exclusion criteria included (1) a psychiatric-disorder diagnosis, (2) a history of a neurological condition, (3) a history of severe brain injury, (4) a history of violent behavior, (5) institutionalization or imprisonment, (6) current intake of any medicine, (7) a diabetes diagnosis, (8) a history of smoking, (9) excessive alcohol abuse, or (10) current pregnancy. Here, 20 subjects (33.8 ± 8.7) participated in forearm experiments, and 18 subjects (31.5 ± 5.6) participated in forehead experiments. Detail of subjects information are provided in Tables 5-2 and 5-3 for forearm and forehead experiments, respectively. The exclusion and inclusion criteria were the same as those in The study protocol was approved by the institutional review board (IRB) of UTA. Informed consent was obtained from each participant prior to the experiments.

Table 5-2 Subject information and scattering properties measured by frequency-resolved system on human forearms

Subject #	Age	Gender	mus750	mus785	mus811	mus830	b
1	27	M	5.1	5	4.9	4.6	-0.91
2	28	M	5.5	5.3	5.1	5.1	-0.8
3	26	F	4.6	4.4	4.3	4.2	-0.88
4	53	F	4.5	4.3	4.3	4	-0.79
5	55	M	5.3	5.2	5	4.8	-0.95
6	43	M	4.8	4.6	4.4	4.3	-1.1
7	25	F	4.7	4.4	4.3	4.2	-1.14
8	27	M	5.5	5.3	5.2	5	-0.88
9	37	F	5.6	5.5	5.3	5.2	-1.2
10	29	F	5.1	4.9	4.7	4.5	-1.2
11	23	F	5.4	5.1	5	4.9	-0.94
12	25	M	4.6	4.5	4.3	4.2	-0.92
13	35	M	6	5.7	5.6	5.4	-0.98
14	36	F	5.5	5.2	5.1	4.9	-1.08
15	37	M	4.9	4.6	4.6	4.5	-0.78
16	36	F	5.1	5	4.8	4.7	-0.82
17	29	F	5.3	5.1	5	4.8	-0.92
18	36	M	5	4.9	4.6	4.5	-1.09
19	35	M	4.7	4.5	4.4	4.2	-1.04
20	33	M	5.1	5	4.8	4.7	-0.82
Average	33.75	11 Male	5.12	4.93	4.79	4.64	-0.96
Std	8.72	9 Female	0.40	0.40	0.39	0.39	0.14

Table 5-3Subject information and scattering properties measured by frequency-resolved system on human foreheads.

Subject #	Age	Gender	mus750	mus785	mus811	mus830	b
1	27	M	11	10.5	10.1	9.8	-1.13
2	28	M	10.5	10	9.7	9.3	-1.15
3	26	F	10.6	10.2	9.8	9.6	-0.99
4	43	M	9.8	9.5	9.1	8.7	-1.14
5	25	F	10.4	10	9.5	9	-1.39
6	27	M	9.6	9.3	8.8	8.5	-1.21
7	37	F	9.6	9.5	9	8.7	-0.99
8	29	F	10.1	9.9	9.5	9	-1.09
9	23	F	9.4	9.1	8.7	8.5	-1.01
10	25	M	9.6	9.3	9.1	8.7	-0.9
11	35	M	10	9.7	9.2	8.8	-1.25

12	36	F	10.5	10.1	9.7	9.4	-1.08
13	37	M	10.9	10.5	10.1	9.7	-1.12
14	36	F	11.1	10.6	10.2	9.9	-1.12
15	29	F	10.3	9.9	9.5	9.1	-1.19
16	36	M	9.2	8.9	8.7	8	-1.23
17	35	M	9.7	9.3	9	8.6	-1.14
18	33	M	11.2	10.5	10.2	9.8	-1.27
Average	31.50	10 Male	10.20	9.82	9.44	9.06	-1.13
Std	5.60	8 Female	0.62	0.53	0.51	0.55	0.12

5.2.3.2 Data acquisition

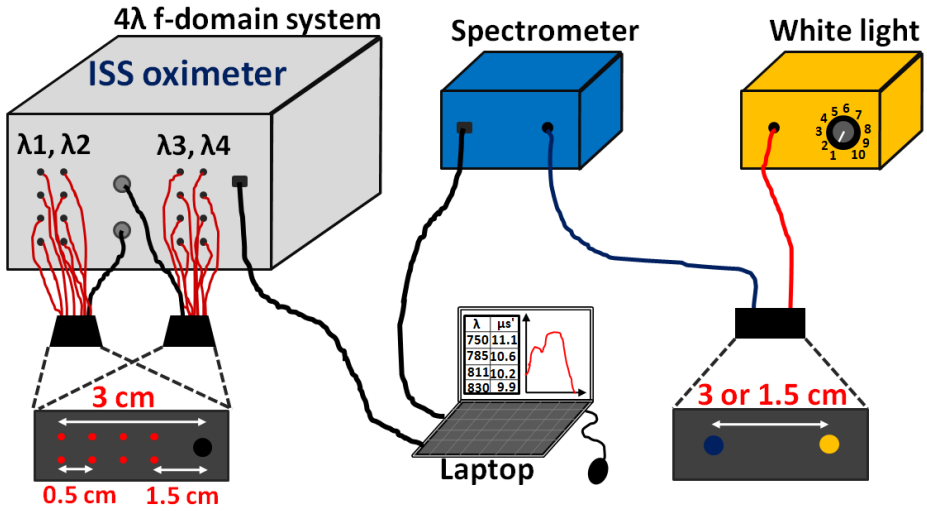

Figure 5-2. The experimental setup for frequency-resolved and CW measurements. The frequency-resolved system consists of two probes and four wavelengths. Each probe detects scattering and absorption properties at two wavelengths. The two probes share the same source-detector geometry. For CW measurement, the yellow box represents the white light source and the blue box represents the spectrometer. The source-detector separation is 3 cm on human foreheads and 1.5 cm on human forearms.

Fig. 5-2 shows the experimental setup this study used. I used a four-wavelength frequency-resolved system (OxiplexTS, ISS Inc., Champaign, IL) to obtain scattering coefficients. The system consists of 16 laser diodes at 750 nm, 785 nm, 811 nm, and 830 nm. They are modulated at 110 MHz. Two probes were used to define source-detector separations to confine the penetration depth of the measurement. Each probe was in charge of

measurement at two wavelengths. The system measured the absolute values of scattering coefficients of human tissue at four wavelengths. Then, based on Mie theory, the four wavelength dependent values are fitted with Eq. 5-2 to obtain scattering size and power.

Next, one sample t-test were performed among the fitted factor n from all the subjects versus the literature values on human foreheads and human forearms [46]. No significant difference was observed between my data versus previous studies. Therefore, in the fitting the upper and lower bounds of factor "n" were defined as [0.9 1.1] on human forearm and [1.2 1.4] on human forehead. Detailed explanation is provided in discussion part.

After the frequency-resolved measurement, a broadband NIRS (bb-NIRS) system was used to obtain a CW spectrum on the human tissue. The bb-NIRS system consists of a broadband white-light source (Model 3900, DC Regulated, Light Feedback Fiber Optic Light Source, Illumination Technologies, Inc. 5 Adler Drive, East Syracuse, NY 13057 USA) and a back-thinned CCD spectrometer (i-trometer, B&W Tek Inc., Newark, DE). An optical fiber bundle guides photons from the light source to human tissue, and the spectrometer can then detect the diffused light in the form of a spectrum. A laptop was used to save both scattering coefficients from the frequency-domain system and the spectrum from the CW system, which were them be used as input in the fitting model to fit for [HbO], [HHb], [CCO], [water%], [fat%], and scattering coefficients from the human tissue. The raw spectrum measured from human tissue was initially subtracted with dark noise and calibrated with a reflectance standard to remove spectral artifacts from the optical components [78, 94, 95]. Eq. 5-4 shows the mathematical expression.

$$R_1(\lambda) = \frac{R_0(\lambda) - dark\,noise}{R_r(\lambda) - dark\,noise} \qquad 5\text{-}4$$

Where R0(λ) denotes the measured raw data of the spectrum from human tissue, Rr(λ) denotes the measured spectrum from the reflectance standard, and R1(λ) denotes the calibrated spectrum used in the parameter fitting.

Fig. 5-3 shows the specific locations where the bb-NIRS system took measurements on human forearms and foreheads. The right side of human foreheads, close to the hair line was measured. This is the same location as in reference [14, 80]. On human forearm, the flexor digitorium muscle was selected as the region of interest[96]. When performing the exam, Human subjects were asked to grip and relax their fists, while investigators located this muscle on the subjects' arms. Then, the selected region on human skin was marked with a square, which has the same length and width with respect to both the CW and frequency-resolved probes. This ensured that both measurements were taken at the same location on each subject.

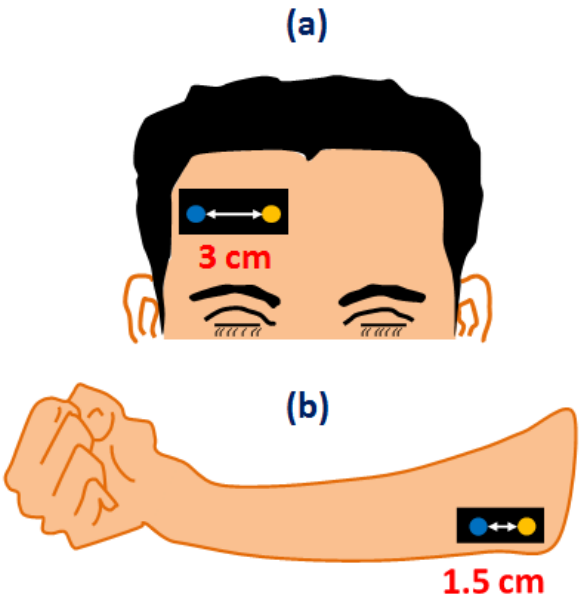

Figure 5-3The measured locations by bb-NIRS on human forearms and foreheads.

Based on the estimation-error comparison from the simulation process, the most accurate HbO can be was achieved from the first derivative fitting. The most accurate HHb, CCO, water%, fat%, m, and n were in the fitting with the simultaneous first and second derivation. Therefore, during the parameter- (chromophore concentrations and scattering factors) estimation process, I initially performed the first derivative to obtain the final HbO concentration. Then, the fitting results of other parameters from the 1st derivative fit were then be regarded as the initial guess of the second fitting. The second fitting was based on the

simultaneous first and second derivation, where the final results for the parameters other than [HbO] were determined.

5.3 Results

Frequency resolved system was initially used to predetermine the scattering properties on human tissue, which were then be used to compare with the literature to rectify a proper range for scattering power (i.e., n in Eq. 5-2). The measurement provides scattering coefficients at 750 nm, 785 nm, 811 nm, and 830 nm on human tissue (both forearms and foreheads). Next, the four values were fitted with Eq. 5-2 to obtain scattering power in Mie Theory. Tables 5-1 and 5-2 show the scattering coefficients and fitted-scattering power factor.

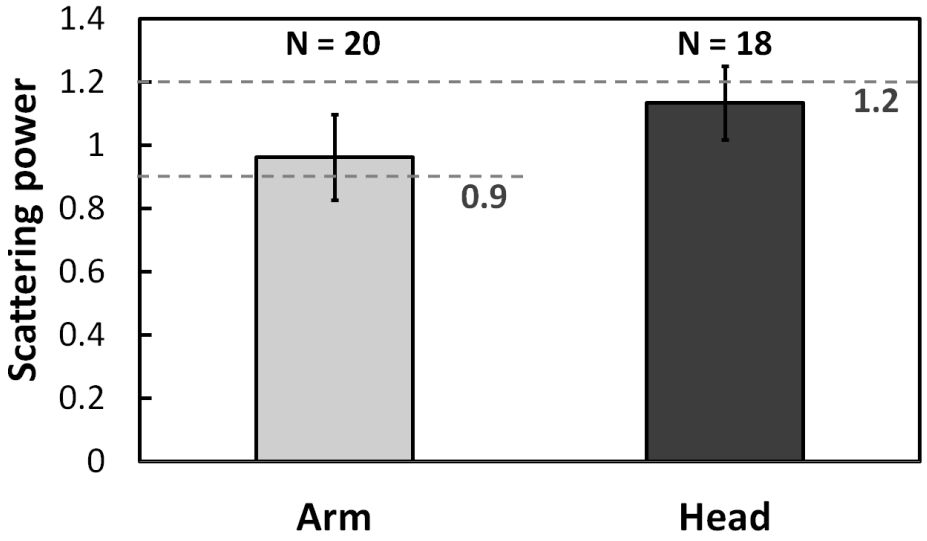

Figure 5-4. A comparison among scattering power measured from human participants versus the literature values—0.9 for human forearms and 1.2 for human heads, respectively. The light gray bar represents scattering power on human forearms (N = 20), and the dark gray bar represents scattering power on human foreheads (N = 18). One sample t-test was performed between the measured data versus literature values, no significant difference was observed in both cases.

According to previous studies, the scattering powers on human forearms and foreheads were 0.9 and 1.2, respectively. Fig. 5-4 shows a comparison of the n factors obtained from the

human participants with the literature values—0.9 for human forearms and 1.2 for human heads. I performed one sample t-test to compute the significant different levels among scattering powers in Table 5-1, 0.9, and Table 5-2, 1.2. As Fig. 5-4 shows, the data from the human participants does not differ from the literature results. Therefore, it was safe to set the initial guess of factor n as the literature values, with a narrow flexible range to confine its vulnerability to noise.

In the simulation, the simulated curve for different combinations of chromophores was generated by Eq. 5-1 with various noise levels added. Specifically, four combinations of chromophores were generated, which is shown in Table. 5-1. The setting of hemoglobin concentrations are based on Fantini et al.. And concentration of CCO was set to be approximately 5-10% of hemoglobin concerntations [40, 87]. Water fraction was set as 80%, and fat fraction was set as 60% to simulate the human brain. The upper and lower bounds were defined as [0, 70] for HbO, [0, 50] for HHb, [0, 20] for CCO, [60%, 95%] for water, [0%, 100%] for fat, [0, 30] for factor m, and [1.2, 1.4] for n (i.e., lower bound, higher bound). I then performed the fitting based on Eq. 5-3. Fig. 5-5 plots the percentage of estimation error with respect to the initial setting.

(a)

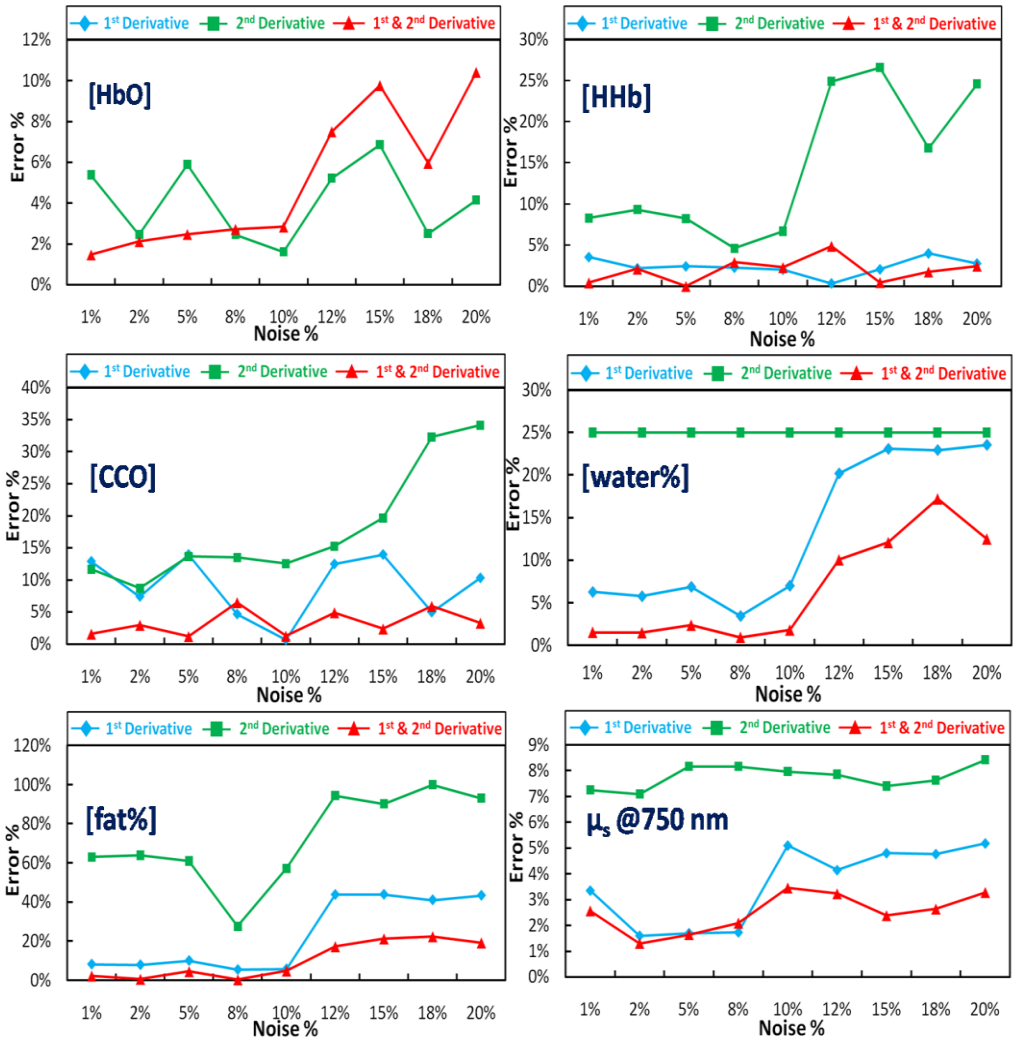
1st Derivative
2nd Derivative
1st & 2nd Derivative
[HbO]
[HHb]
[CCO]
[water%]
[fat%]
μs @750 nm
Error %
Noise %
1% 2% 5% 8% 10% 12% 15% 18% 20%

(b)

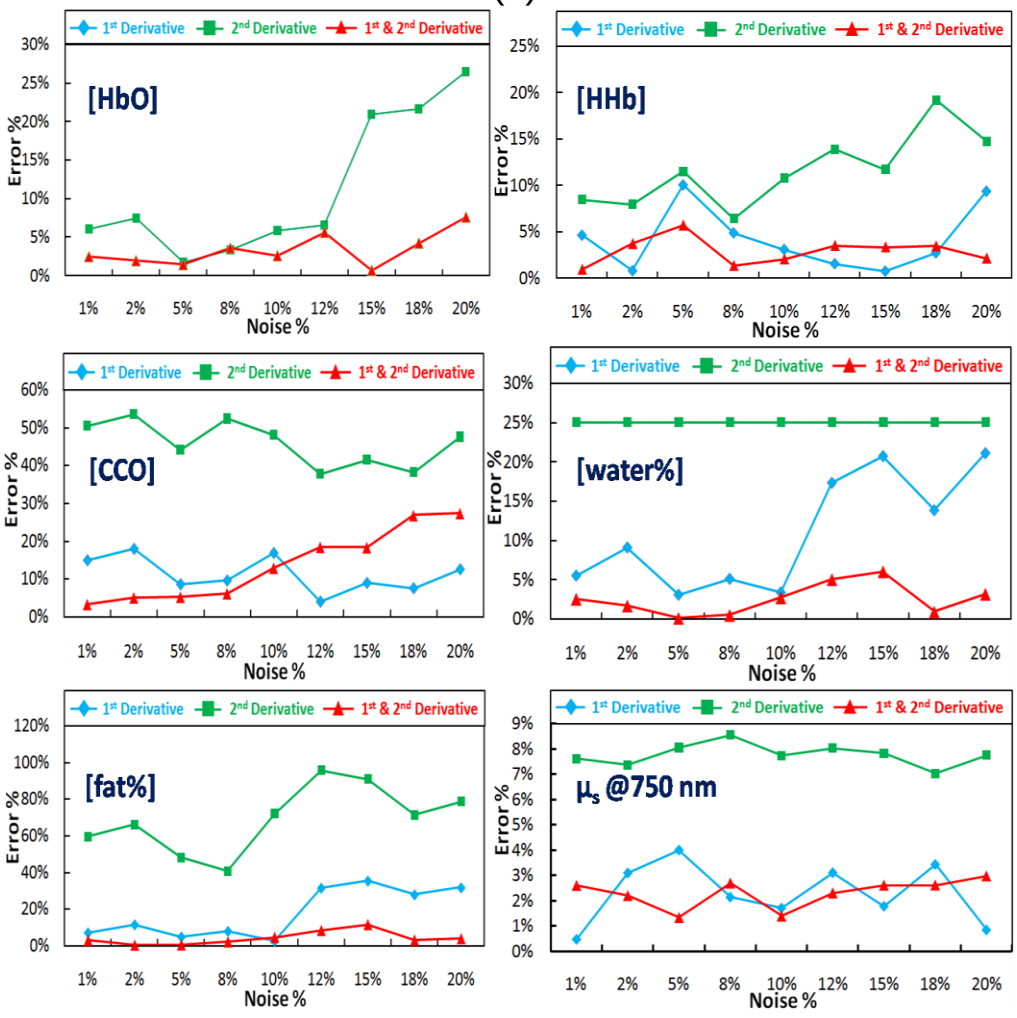
1st Derivative
2nd Derivative
1st & 2nd Derivative
[HbO]
[HHb]
[CCO]
[water%]
[fat%]
μs @750 nm
Error %
Noise %
1% 2% 5% 8% 10% 12% 15% 18% 20%

(c)

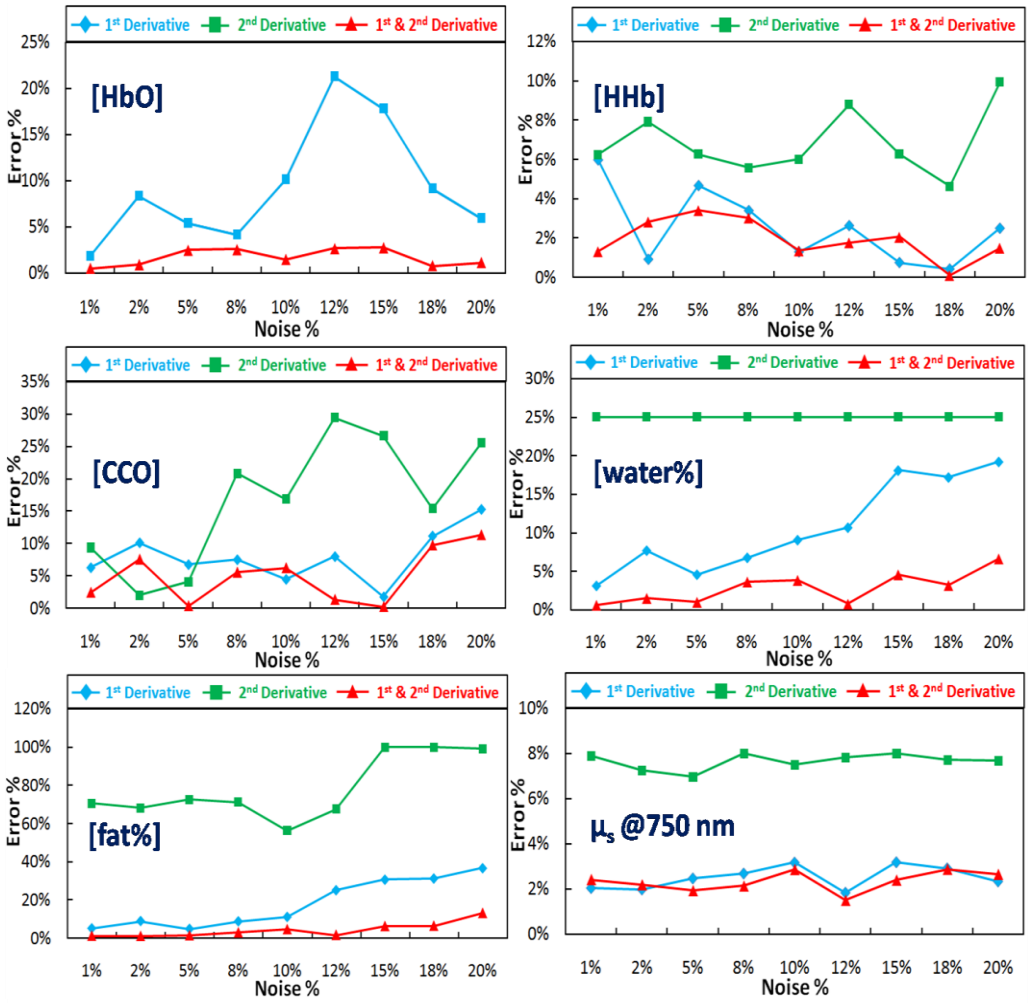
1st Derivative
2nd Derivative
1st & 2nd Derivative
[HbO]
[HHb]
[CCO]
[water%]
[fat%]
μs @750 nm
Error %
Noise %
1% 2% 5% 8% 10% 12% 15% 18% 20%

(d)

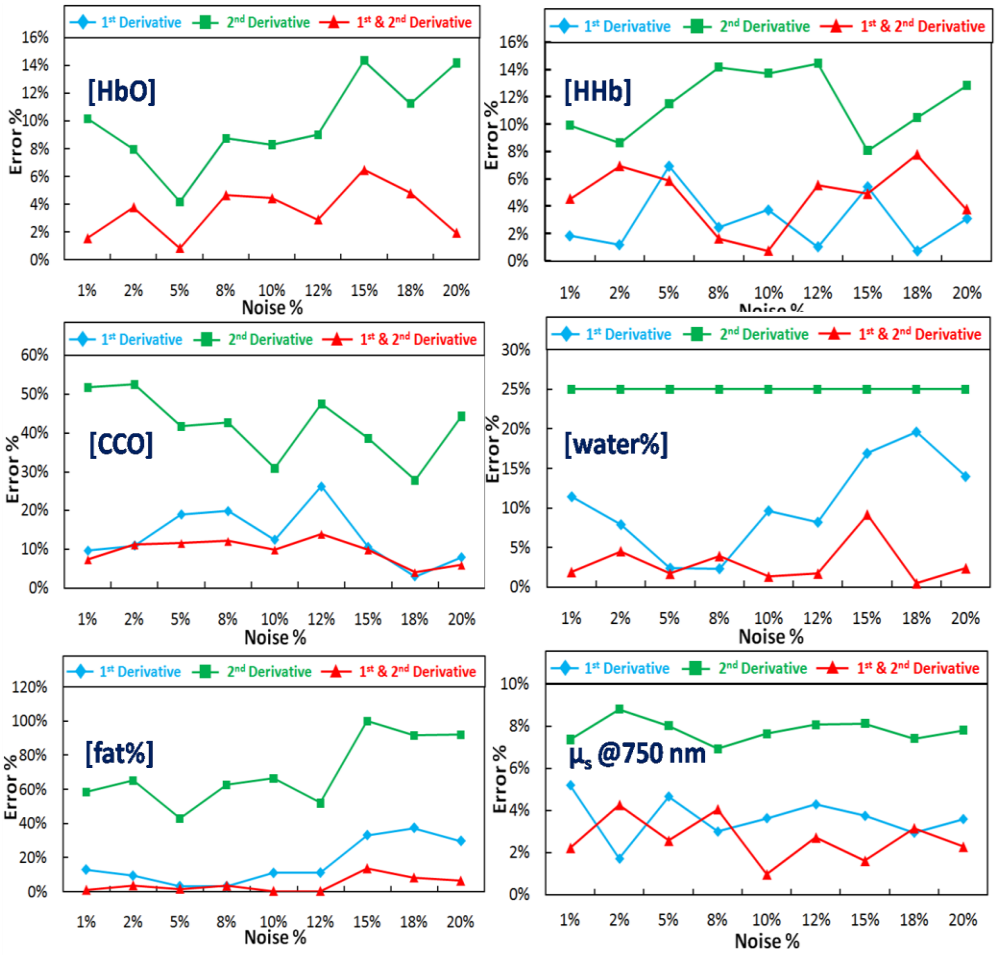

Figure 5-5. The estimation errors of each parameter under different noise levels with initial settings of (a) combination 1 in Table 5-1; (b) combination 2 in Table 5-1; (c) combination 3 in Table 5-1; and (d) combination 4 in Table 5-1. The blue curves denote the fitting with the first derivative only, the green curve denotes the fitting with the second derivative only, and the red curve denotes the fitting using both the first and second derivatives.

In Fig. 5-5, the blue curves denote the fitting with the first derivative only, the green curve denotes the fitting with the second derivative only, and the red curve denotes the fitting using the first and second derivatives simultaneously. It is clear that, for each single curve, the estimation error increases as the noise level increases. Comparing the fitting methods, when the noise level is controlled within 10%, the fitting with the second derivative only shows the largest estimation error, whereas the fitting with the first derivative and both the first and second

derivatives shows estimation errors of less than 5%. As CCO has a small concentration, the estimation error is within 10%, which is comparatively larger than other chromophores.

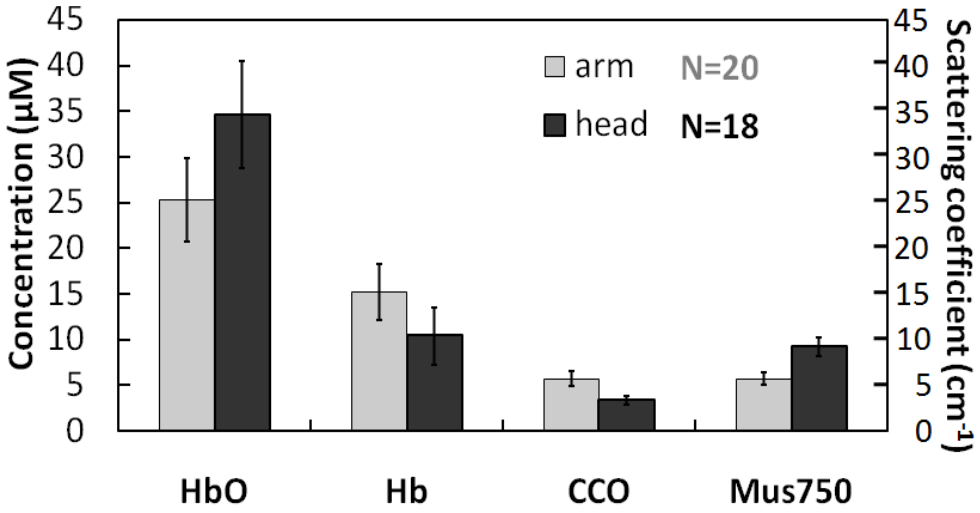

Figure 5-6. The estimation of HbO, HHb, CCO, and the scattering coefficient at 750 nm on 20 human forearms and 18 human foreheads. The error bar denotes the standard deviation of mean.

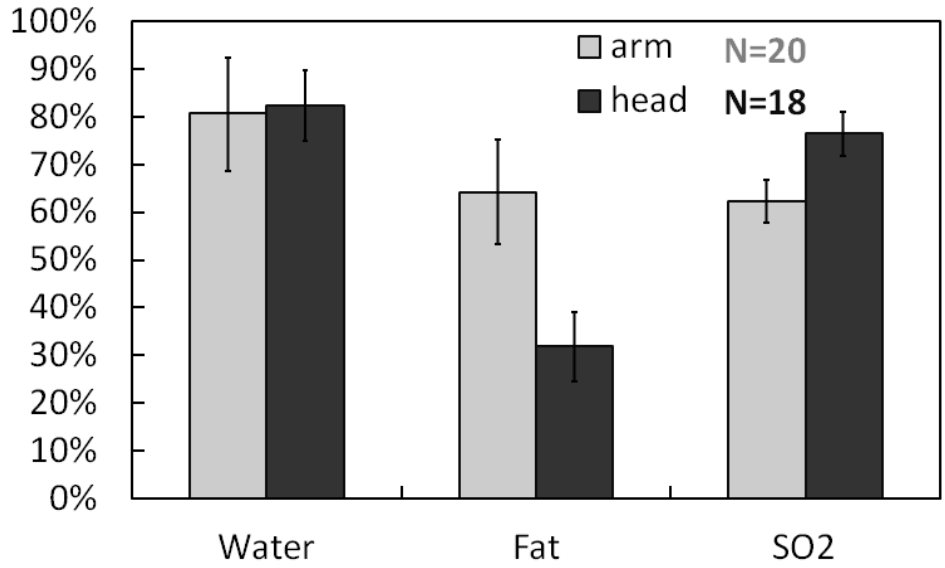

Figure 5-7. The estimation of water%, fat%, and oxygen saturation on 20 human forearms and 18 human foreheads. The error bar denotes the standard deviation of mean.

The fitting of the chromophore concentrations on human tissue kept the same initial guess and upper/lower bounds the simulation had, except it confined factor n as [0.9 1.1] on

human arms and [1.2 1.4] on human foreheads (i.e., lower bound, higher bound). The results on 18 human arms and 20 human heads are shown in Fig. 5-6 and 5-7. Fig. 5-6 depicts the HbO, HHb, CCO, and μs' at 750 nm on 20 human forearms and 18 human foreheads. The HbO concentration was about 34.7 μM on the human foreheads and 25.3 μM on the human forearms. The HHb concentration was about 10.5 μM on the human foreheads and 15.3 μM on the human forearms. The CCO concentration was about 3.4 μM on the human foreheads and 5.7 μM on the human forearms. Furthermore, generally the CCO concentration was 7.5–14% of total hemoglobin concentrations, which is consistent with physiological facts [37, 39, 40, 87]. The scattering coefficient was 9.2 cm-1 on human foreheads and 5.7 cm-1 on human forearms. Fig. 5-7 denotes the percentage of water, fats, and oxygen saturation. Water concentration on human foreheads and arms was 82.3% and 80.6%, respectively. The fat fraction was 64.2% on human arms and 31.8% on human heads. The oxygen saturation was 76.4% on human foreheads and 62.4% on human forearms, which indicates higher oxygenation on human brains than arms.

Furthermore, one statistical t-test compared the fitted scattering coefficient at 750 nm from the human forearms and foreheads with their concurrent frequency-resolved readings in Tables 5-2 and 5-3. No significant difference was observed, which verifies the great accuracy of this Ant Colony Optimization model.

5.4 Discussion

I established a broadband spectroscopy system to measure absolute-value chromophore concentrations and scattering properties by utilizing spectral features of the first and second derivatives of diffused CW spectra from human tissue. Computational simulation was initially used to verify proper estimation accuracy under different noise levels. In vivo measurements were then performed on human forearms and foreheads. Physiologically

reasonable results of HbO, HHb, CCO, water%, fat%, and scattering coefficients indicated the feasibility and potential of further applications in tissue-component quantification and imaging.

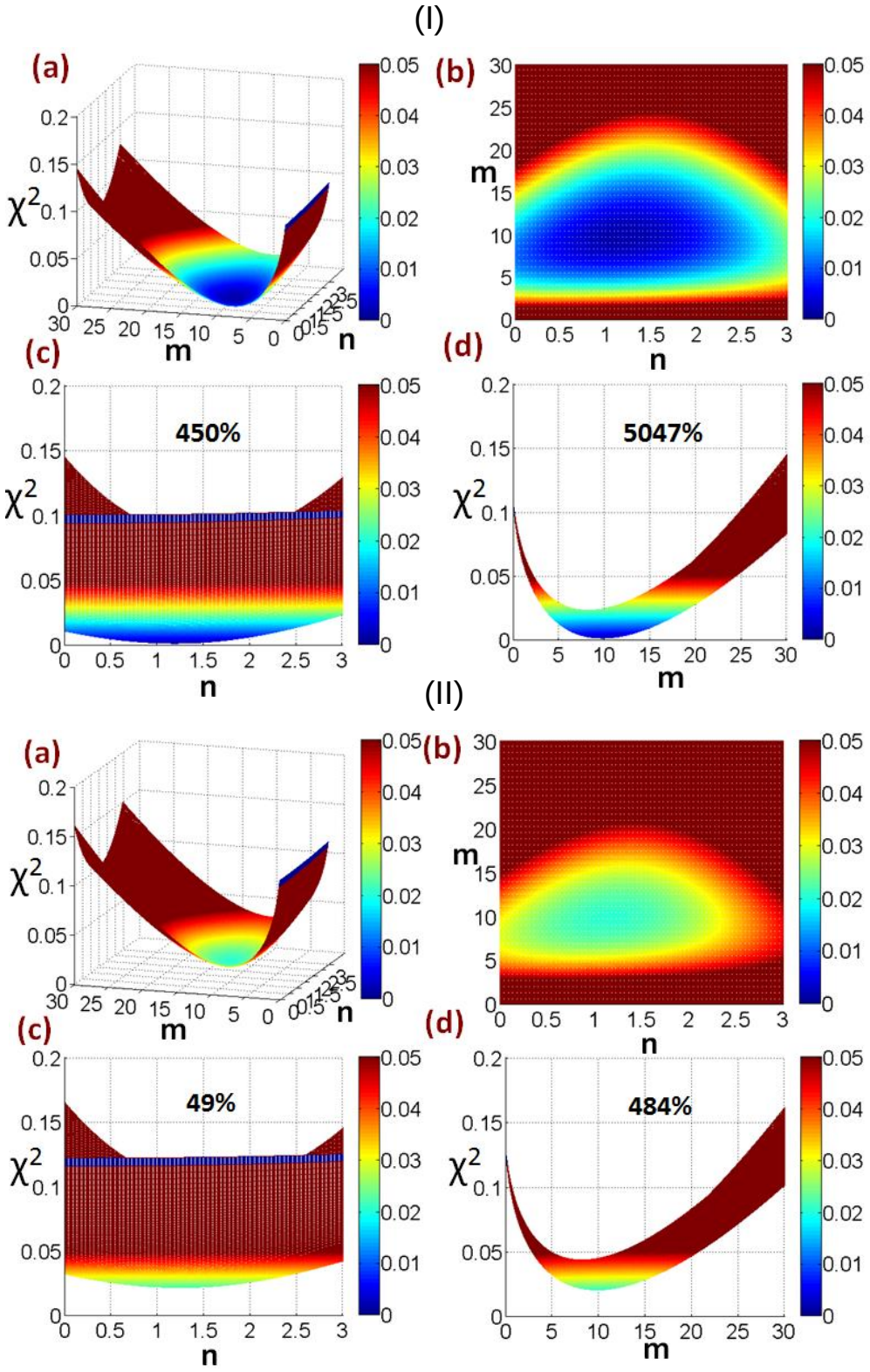

(III)

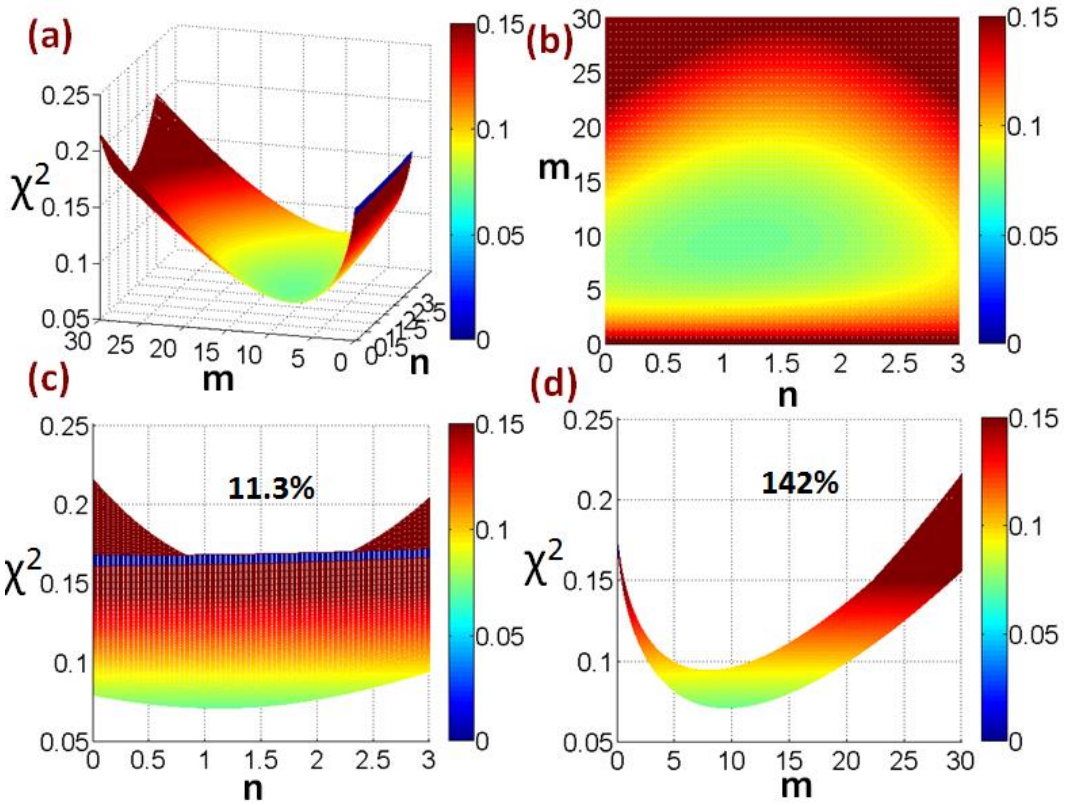

Figure 5-8. The χ2 of fitting with noise levels of (I) 2%; (II) 10%; and (III) 18%. In each figure, (a), (b), (c), and (d) show different views of the scattering factor's related χ2 map. m denotes the scattering size, which ranges from 0–30. n denotes the scattering power, which ranges from 0–3. The color bar denotes the scale of χ2.

To reduce error and inter-parameter cross talk, during the fitting process, factor n was constrained within a narrow range near its common value, which was found from previous studies and rectified in this study with frequency-resolved measurements. Because the simulation found n to be very sensitive to noise, this could significantly affect the fitting accuracy. Fig. 5-8 demonstrates the high influence of noise on scattering power (i.e., factor n in Mie theory) in my fitting algorithm. Fig. 5-8. I, II, and III depict noise levels of 2%, 10%, and 18%, respectively, in a measured spectrum. In a range of 0–30, factor m has a prominent local minimum in the presence of all the noise levels. However, in the range of 0–3, factor n shows a

comparatively weaker distinction for the local minimum. The percentage denotes the distance between the highest χ2 and the lowest. For example, in Fig. 5-8.I.c, the highest χ2 at “m = 0” is 0.011033, and the lowest χ2 at “m = 10” is 0.002; the ratio of distance is (0.011033-0.002007) / 0.002007 ≈ 450%, which indicates a distinct difference of χ2 along the n axis with a noise level of 2%. Thus, it is easy for the fitting to find the prominent local minimum. In contrast, the ratio of distance in Fig. 5-8.III.c is 11.3%, which indicates a blurred local minimum that the noise affected. Thus, errors could occur in factor n when there is a high level of noise. To address this potential error, in the ant-colony-optimization fitting, the initial guess and upper, lower bound of factor n were set according to the literature values [46]. Furthermore, frequency resolved readings were taken on all the human participants to rectify the setting value.

According to the simulation results, I observed a noise level dependent manner for the estimation error in Fig. 5-5. For most chromophores, when noise levels are greater than 10%, the estimation error enhances to a higher level compared with errors for noise levels less than 10%. This implies that the derivative-dependent fitting is sensitive to noise. Due to the mathematical process of derivation, noise is amplified in the 1st derivative stage and will be further amplified with additional second derivative process. In other words, the small, unsmooth effect that noise causes in the normal stage of the spectrum is composed of small line/linear segments with alternating positive and negative slopes, which will be translated into huge spikes fluctuating between positive and negative values with significant variability in the derivative domain. Therefore, the enhanced variation buries the spectral features of chromophores, which affects quantification accuracy. Nevertheless, the spectrometer I employed in the experiments can provide a high signal-to-noise ratio that keeps noise levels below 5%. Thus, according to the simulated data, the fitted results from my spectrometer can be limited within 5–10%.

According to human in vivo experiments on 20 forearms and 18 foreheads, in Fig. 5-6, concentration values of CCO were observed as 7.5-14% of total hemoglobin. This is consistent with physiological facts. Higher CCO concentration on human forearms than on foreheads was

observed. This is also consistent with physiological facts. According to the literature, muscles have the most mitochondria of all human tissues [97-99]. I selected the flexor digitorium muscle as the measurement site on the human forearm because it is a major red muscle used for gripping and lifting, which requires simultaneous and vast energy production (i.e., ATP). Therefore, a higher mitochondria density is located in this region, which results in higher concentrations of ATP producer CCO. Furthermore, according to the simulation, a 1–10% noise level within a 3–8 μM CCO concentration range ensures less than 10% estimation errors. Therefore, I can trust the accuracy of the results.

Another potential estimation error that in vivo human experiments cause is the cross talk from neglected chromophores. Although the major attenuation contributors in the NIRS range for human skin/tissue are hemoglobin, CCO, water, and fat, there are still other contributors such as melanin (on skin) and collagen. To avoid over-fitting by including too many parameters, I assumed that the contributions of these absorbers were negligible. This could result in additional estimation errors caused by the cross talk of unconsidered chromophores on top of my simulation. Nevertheless, the concentration of collagen in human tissue is small, so it will generate limited attenuation. Furthermore, melanin is mostly located on the skin's surface, and my optical probes detected tissue with depths of 0.7–1.0 cm and 1.7–2.0 cm. Thus, the attenuation of melanin can be minimized.

Although I observed physiologically reasonable results on human forearms and foreheads, my algorithm has limitations. First, I lacked the invasive-biochemistry gold-standard measuring method to verify the accuracy of my CCO and hemoglobin concentration findings and confirm the computational simulation. Second, the estimation error was about 10% when the concentration of CCO was less than 3 μM. A further minimized error scale will be necessary to ensure the feasibility of this algorithm in monitoring the alteration of CCO during certain perturbations, such as functional brain stimulation or transcranial laser stimulation [13]. Previous

studies found the change of CCO concentrations during these perturbations to be tiny (i.e., within 0.3–0.7 μM.).

5.5 Conclusion

I developed an ant-colony-optimization regression algorithm to quantify the absolute value of CCO with other tissue components and properties. The fitting depends on the first and second derivatives of the diffused broadband spectrum from human tissue. Simulations with different combinations of absorbing and scattering factors were performed to determine the proper estimation value. Furthermore, in vivo experiments on human forearms and foreheads were performed. And the resulting concentration values are consistent with concurrent frequency-resolved measurements, previous studies, and physiological facts. This is a good start for future quantification of tissue CCO concentrations and other components with portable and cost-effective optical devices.

Chapter 6

Imaging of human electrophysiological response to tPBM in vivo measured by electroencephalography

This Chapter is a manuscript to be submitted soon.

6.1 Introduction

6.1.1 Background

In the year of 2013, Barrett and Gonzalez-Lima performed 1064nm tPBM on 40 human right forehead with a placebo controlled experiment protocol and reported significant improvement of human cognitive function after tPBM[17]. Shortly after this finding, during a following exploratory study, Tian F et al. applied the same tPBM stimulation protocol on human foreheads and observed significant improvement of cerebral blood oxygenation by functional near-infrared spectroscopy (fNIRS)[32]. For better understanding of tPBM mechanism and the cerebral metabolic and hemodynamic interplay induced by this photobiomodulation, in 2016, Wang X et al. established a novel recording system that can measure the concentration change of oxidized cytochrome c oxidase (oxi-CCO), which is the key enzyme that contributes to 90% of human metabolism[13]. With the same stimulation protocol, significant improvements of oxygenated hemoglobin concentration and oxi-CCO during and after laser stimulation were reported on both the human arm and brain. In addition, a higher metabolic-hemodynamic coupling rate on the human brain was reported with respect to the human forearm [13, 14].

6.1.2 Mechanism of Photon-Tissue interaction

A series of previous in vivo hemodynamic and metabolic studies provided me with clear observation and understanding of behavioral and physiological improvement of tPBM[13, 14]. Based on the behavioral, metabolic and hemodynamic results from previous studies, the

mechanism of tPBM for improving human cognitive functions was based on CCO oxidation (oxi-CCO)[13, 14, 17]. Briefly, energetic photons in the red-to-near-infrared range photobiomodulate CCO, the main cellular photoacceptor in mitochondria[86]. Due to the high optical absorption coefficient of CCO to near-infrared/infrared light, this mitochondrial enzyme is oxidized to a stage that is activated in oxygen metabolism. The increment of oxi-CCO concentration then accelerates ATP production by consuming oxygen molecules[51]. As a consequence, the accelerated consumption rate of oxygen molecules triggers the hemodynamic oxygenation from nearby blood vessels. In the meantime, the increased concentration of ATP is then utilized in variety of cellular activities and biochemical reactions. According to the known neurology knowledge, ATP has two major trails in order to regulate the neuronal functions: (1) to work as an energy supplier in different cellular activities[99, 100], and (2) to work as a neurotransmitter and neuromodulator in regulating the opening-closing states of ion channels and prolonging membrane/action potentials[101]. In this study, I will, for the first time, explore the tPBM-induced electrophysiological response by recording and analyzing human electroencephalogram (EEG) in vivo.

6.1.3 Electroencephalography

Electroencephalography (EEG)is a non-invasive brain imaging tool that can detect multi-channel scalp field potentials originated from the cerebral cortex as time dependent data series in real time with a high temporal resolution [104]. Nowadays, integrations of EEG measurements with brain stimulation tools, such as transcranial Direct Current Stimulation (tDCS) and Transcranial Magnetic Stimulation (TMS), are well established and adopted in research and clinical studies[105, 106]. [107].

According to previous studies, a desynchronization of Alpha (8-13 Hz), Beta (13-30 Hz) and Gamma (30-70Hz) frequencies has been reported during enhanced cognitive operations and memory performance[108]. In the meantime, enhanced cognitive operation and memory

performance were also reported to be highly correlated with tPBM [17]. To the best of my knowledge, no study has investigated on the mapping of cerebral EEG signal alteration in response to tPBM. Therefore, the purpose of this study was to compute and map electrophysiological responses of the human cerebral cortex at different frequency bands before, during, and after tPBM. In this study, I utilized a placebo-controlled protocol and recorded 64-channel, EEG time series before, during, and after 11-min tPBM. I segmented the time series of the recorded EEG data into time sections, each of which lasted 30 seconds or one minute. I calculated the 20-subject averaged EEG power spectra during each temporal section, computed time-frequency analysis maps, and demonstrated alteration of EEG power topography during and after tPBM. In addition, based on the actively responded frequency bands observed in the spectral analyses, a 3D EEG source reconstruction algorithm was applied to compute the tPBM-activated cortical regions during and after tPBM. Furthermore, the Phase Transfer Entropy analysis was applied to reveal frequency-dependent enhancement of effective neural connectivity and cerebral information flow among neural networks.

6.2 Experimental Methods

6.2.1 Participants

Twenty healthy human participants (26.7± 8.7 years of age) were recruited from the local community of the University of Texas at Arlington. Certain criteria were followed to further screen the interested individuals. The exclusion criteria included: 1) diagnosed with a psychiatric disorder, 2) history of a neurological condition, 3) history of severe brain injury, 4) history of violent behavior, 5) have ever been institutionalized/imprisoned, 6) current intake of any medicine or drug, 7) diagnosed with diabetes, 8) history of smoke, 9) excessive alcohol abuse or 10) currently pregnant. The study protocol was approved by the institutional review board (IRB) at The University of Texas at Arlington. A consent form was signed by each subject prior to the experiments.

6.2.2 Experimental setup

I employed an FDA-cleared, 1064-nm, continuous-wave laser (Model CG-5000 Laser, Cell Gen Therapeutics LLC, Dallas, TX, USA). This is the same laser used in the previous studies [13, 17, 32]. Briefly, this laser stimulation system has a user friendly handheld handle. Treatment laser comes out from an aperture at one end of the handle. A button at the other end controls the onset and offset of the laser diode. The area of laser beam from the aperture was 13.6 cm^2. And the stimulation duration and the power of laser stimulation can be set on the main control panel of the system. Specifically, in the case of tPBM experiment, my safe laser stimulation parameters were calculated as follows: Total laser power = 2.2 W; area of laser beam radiation = 13.6 cm^2; power density = 2.2 W/13.6 cm^2 = 0.162 W/cm^2; total laser energy dose = 2.2 W × 660 s = 1452 J. On the other hand, during the placebo experiment, the laser power output was set as 0.1 W. On top of that, a cap covered by black tape was implemented in front of the aperture to totally block and absorb the 0.1 W laser during the sham experiment. Thus, the irradiance (or power density) in the 13.6 cm^2 beam area was ~0 W for the sham experiment.

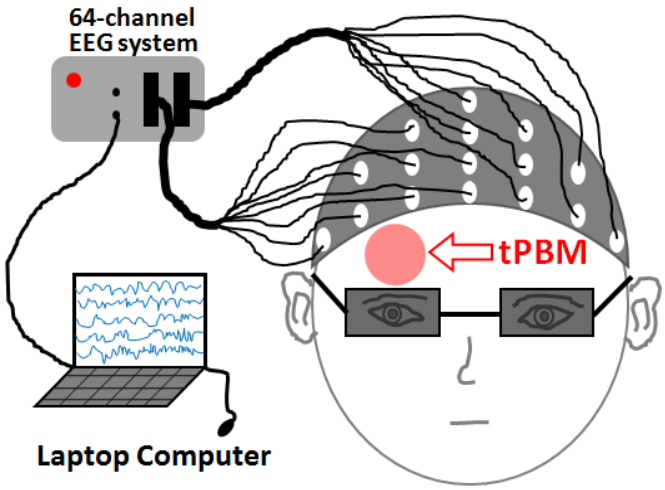

Figure 6-1The EEG experimental set up of tPBM on human foreheads.

Fig.6-1 shows the experimental setup of the combined EEG/tPBM system. tPBM was administered on the right forehead of each subject. A pair of protection goggles was worn by each subject throughout the whole experiment. During the experiments, subjects were required to wear a default 10-10 EEG cap. The cap was manufactured with 64 fixed plastic couplers, which 64 EEG detection electrodes were embedded in. The plastic couplers on the cap were distributed as those in a standard 10-10 EEG system[109]. Furthermore, to increase the signal to noise ratio of the recorded EEG data, electrical conducting gel (MFI medical equipment Inc., CA, USA) was applied at each electrode tip for better EEG data acquisition. The recorded EEG time series were directed to a laptop through electrical cables.

6.2.3 Experiments

Fig.6-2 shows the experimental protocol for both tPBM and placebo experiments. Both experiments lasted for 16 minutes, including a 2-minute baseline period, a 11-minute tPBM/placebo period, and a 3-minute recovery period. EEG data acquisition was kept ongoing throughout the whole experiment. The placebo and tPBM experiments were respectively assigned for the two visits of each human participant. That is, each participant was randomly and blindly assigned with either tPBM or placebo experiment during their first visit. A few days later, in the second trial, the tested subject was then arranged with the tPBM or placebo experiment different from that in his/her first trial. Each subject got no information on the stimulation conditions during each experiment.

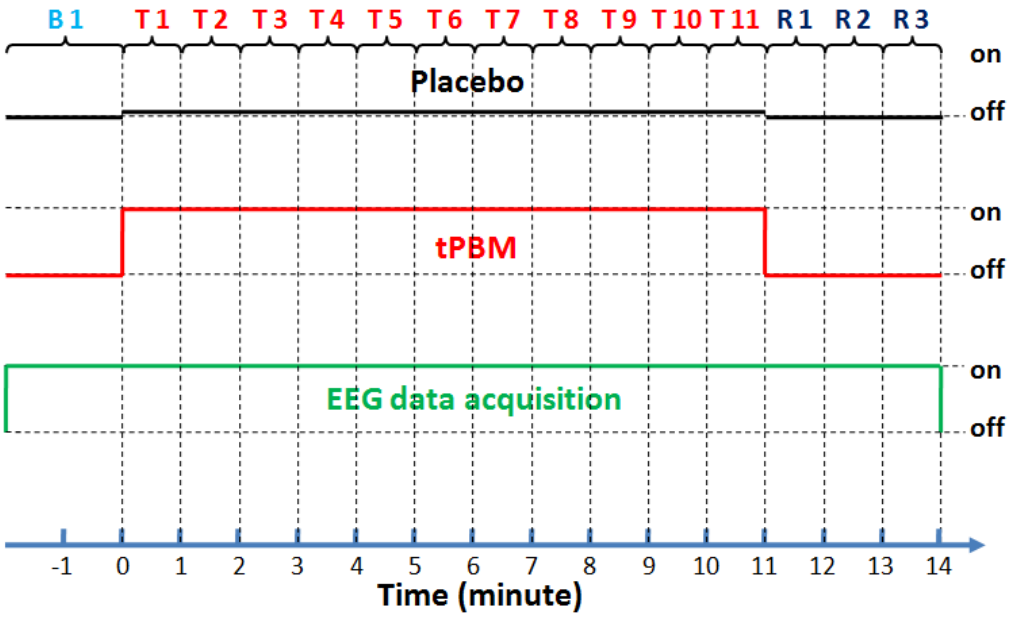

Figure 6-2The diagram of stimulation and EEG recording period

In addition, all the subjects after each experiment (sham and tPBM) were inquired about their sensing of heat from the stimulation. Data was excluded if the subject reported warmness only from the tPBM experiment (i.e., data were retained if subjects reported warmness in the sham experiment only, in both sham and tPBM, or in none of the two experiments.). Furthermore, as drowsiness significantly affected the quality of EEG data, one of the investigators was assigned to observe the vigilance of each subject during the entire experiment.. Therefore, it was confirmed that the EEG data obtained from the 20 subjects were all under a wakeful state.

6.2.4 Data analysis

6.2.4.1 eLORETA

eLORETA refers to "exact Low Resolution Electromagnetic Tomography Analysis". It is a publicly available, academic software package that can be used to compute a 3D cortical source distribution of recorded electric potentials from a human subject's scalp. A zero-localization error weighted minimum inverse solution can be provided by this software under ideal conditions[110]. With a 5-mm spatial resolution, localization of electrical activity on the

cortical gray matter is represented by a total of 6239 voxels. In this study I applied eLORETA to calculate/reconstruct a 3D cortical power distribution at Delta, Theta, Alpha, Beta and Gamma frequency bands so as to analyze EEG signals before, during and after tPBM. The reconstructed brain images produced by eLORETA were based on the standardized Montreal Neurological Institute (MNI) template. The mathematical expression and data processing procedures are clearly illustrated in Figures 6-4 and 6-5.

6.2.4.2 Phase Transfer Entropy analysis

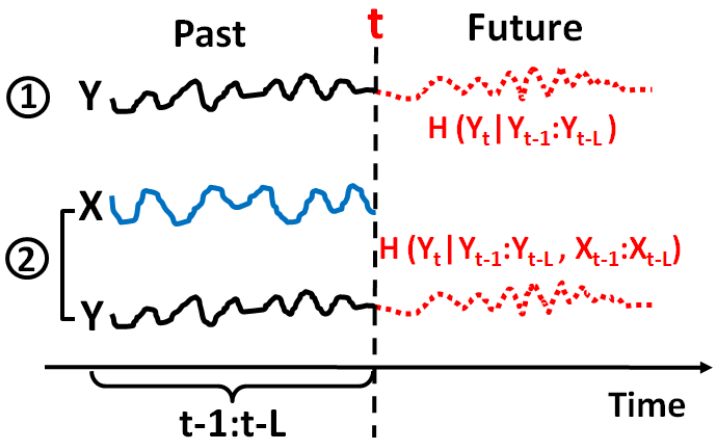

Figure 6-3 Diagram of Phase Transfer Entropy algorithm

The Phase Transfer Entropy (PTE) algorithm measures the information flow between two Regions Of Interest (ROI) using non-parametric statistics [111]. Briefly, if I have two time series, X and Y, PTE determines the causality/information flow between them. It can be estimated/computed by calculating the reduced uncertainty (i.e. entropy, *H*) in predicting future values of time-series, Y, by knowing the past values of time-series, X and Y, with knowing past value of Y only [111, 112]. For example, as shown in Fig. 6-3, if I want to predict a future value of Y_t, in case 1, I know only the past values of $Y_{t-1:t-L}$ (black line) from time "t-1" to "t-L", where L denotes a time span that can be set as a constant in this algorithm. The uncertainty (i.e. entropy, H_y) of future Y_t (red dashed line) can then be represented as:

$$H_y = H(Y_t \mid Y_{t-1:t-L}), \quad 6\text{-}1$$

where H_y denotes the uncertainty of a predicted Y_t with only past values of $Y_{t-1:t-L}$ known. In case 2, past values of $X_{t-1:t-L}$ (blue line) are known on top of past values of $Y_{t-1:t-L}$ (black line); both of them are used to predict future values of $Y_{t-1:t-L}$. The uncertainty (i.e. entropy, H) of the prediction can be calculated as:

$$H_{y,x} = H(Y_t \mid Y_{t-1:t-L}, X_{t-1:t-L}), \quad 6\text{-}2$$

where $H_{y,x}$ denotes the uncertainty of Y_t prediction with past values of $X_{t-1:t-L}$ in addition to past values of $Y_{t-1:t-L}$. The transfer entropy (causality) of X to Y can then be determined by subtracting Eq. 6-2 from Eq.6-1, namely,

$$PTE_{xy} = H(Y_t \mid Y_{t-1:t-L}) - H(Y_t \mid Y_{t-1:t-L}, X_{t-1:t-L}) \quad 6\text{-}3$$

where PTE_{xy} denotes the phase transfer entropy from X to Y. Since PTE_{xy} is lack of a meaningful upper bound, and to reduce biases, a normalization process is needed to normalize PTE into dPTE[111, 113], as follows:

$$dPTE_{xy} = \frac{PTE_{xy}}{PTE_{xy} + PTE_{yx}}, \quad 6\text{-}4$$

where $dPTE_{xy}$ denotes the normalized information flow from X to Y. According to the scale or value of dPTE in Eq. 6-4, direction of the information flow can be determined. If the result in Eq. 6-4 is between 0.5 to1, it means that knowing the past values of X benefits in predicting Y or reducing uncertainty of Y prediction. The net entropy transmission from X to Y is positive, and the information flow is thus from X to Y. On the other hand, if the result in Eq. 6-4 is between 0 to 0.5, the net causality from X to Y is reversed, and the information flow is thus from Y to X.

Specifically, time series acquired from 64 EEG electrodes can be used to quantify regional information flows between selected cortical regions, which also represent effective and/or

directional connectivity between respective cerebral regions [111, 113, 114]. This causality evaluation algorithm has been widely adopted by neurological researchers for mapping neural or brain networks[115]. However, most of the studies have focused on resting state neural networks. In this study, following the same algorithm, I quantified the enhancement of cerebral information flows during and after tPBM at the anterior default mode region and the tPBM stimulation cite.

6.2.4.3 Data processing steps

All data processing procedures were performed by EEGLAB, which is an implemented interface in MATLAB. In the first step, the recorded 64 EEG time series were preprocessed by band-pass filtering between 1-70 Hz, followed by noise removal at 60 Hz and higher frequencies using notch filters within a plug-in function of "CleanLine". Then Independent Component Analysis (ICA) was performed to remove such artifacts as eye blinking, improper electrode contact, and systemic noise caused by breathing and cardiac movement[116]. In the operation of ICA, the extended Infomax ICA with the "Runica" algorithm was applied. Based on the well-developed criteria of pulse artifact determination and correction, independent components contributing to artifacts were rejected under visual identification using the ‘Inverse ICA’ tool [117, 118].

Next, each of the artifact-free EEG time series was segmented into numerous temporal sections (e.g., 30 sec or 60 sec per section for t=0 to 14 min), each of which was used to create its power spectrum by a 1D Fourier Transform function within MATLAB. For each of the 64 EEG time series, all of the temporally segmented power spectra could be concatenated in time and interpolated using MATLAB to generate a time-frequency map. To reveal tPBM-induced characteristic features in frequency, I selected 6 representative electrode sites from frontal, central, and parietal regions, namely, Af7, Af8, C3, C4, P5, and P6.

Specifically, I followed the steps shown in Fig 6-4 to achieve tPBM-induced, placebo-controlled time-frequency maps at the 6 EEG locations. For each subject, each of the 6 preprocessed EEG time series was firstly segmented into 29 temporal sections: one (2-min/section) as baseline, 22 (30-sec/section) during either tPBM or placebo stimulation, and 6 (30-sec/section) during recovery. Next, each of these segmented time series was used to create a respective power spectrum using Fourier Transform under either tPBM or placebo condition and then normalized with respect to their baseline (i.e., dividing each of the power spectra by the power spectrum of the baseline). In this way, a total of 28 normalized power spectra were formed, representing alteration in spectral power during 11 minutes of interventions (either tPBM or placebo stimulations) and 3 minutes of recovery. By concatenation and interpolation of the 28 normalized power spectra, a time-frequency map was generated for each tPBM and placebo case. Next, the aforementioned procedures were repeated for all 20 subjects, and the power spectra at the same time section were averaged over all the subjects for both tPBM and placebo experiment, respectively, to create time-frequency maps for each respective case. Last, an averaged, placebo-controlled (or placebo-subtracted) time-frequency map was obtained by subtracting the time-frequency map under the placebo condition from that under tPBM.

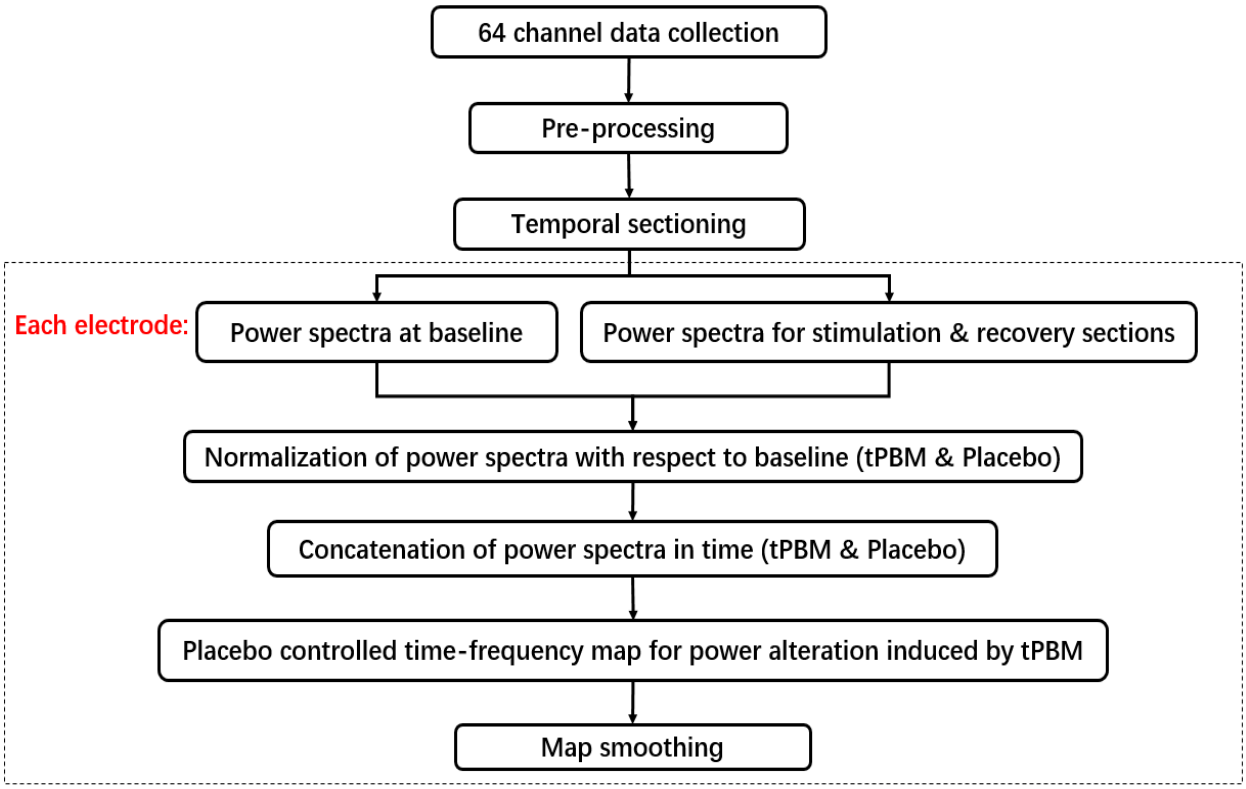

Figure 6-4 Data processing steps for time-frequency analysis

The group-averaged, placebo-controlled time-frequency analysis showed that Alpha, Beta and Gamma frequencies had obvious power increment/enhancement. Therefore, the 3D source reconstruction algorithm was performed at those 3 frequency bands to observe the tPBM-induced, electrophysiological alteration/improvement on the cortical regions. Fig 6-5 is a flow chart showing processing steps of 3D source reconstruction. First, each of the 64-channel, artifact-free, EEG time series was band-pass filtered at five frequency bands: 1-4 Hz for Delta band, 4-7 Hz for Theta band, 8-13 Hz for Alpha band, 13-30 Hz for Beta band, and 30-70 Hz for Gamma band. Each filtered time series was then temporally segmented into 15 time sections: one (2-min) baseline section, 11 (1-min/section) sections during tPBM or placebo, and 3 (1-min/section) sections during recovery. Each set of time series was converted to EEG power and time-averaged over each time section for each frequency band. Then, I created a 64x1 vector to express EEG power distribution (or topographical map) across 64 electrode sites for baseline

(2-min/section), tPBM/placebo intervention (60-sec/section), and recovery (60-sec/section) sections.

Next, eLORETA was employed for each time segment to convert each of the 2D 64-channel power topographies into a 3D, 6239-voxel, electrical source tomography. For spatial normalization, each voxel-wise source power in 3D tomography at 15 temporal points during both intervention (i.e., either tPBM or placebo stimulation) and recovery periods was normalized with respect to its baseline power value (namely, dividing the reconstructed power value at every voxel by its reconstructed baseline value). Now, the normalized values at each voxel represent the percentage of improvement or alteration in cortical activity during tPBM/placebo and recovery periods. For statistical comparison, I performed the two-sample t-test on normalized power values at each voxel between tPBM and placebo experiments and computed T values of 6239 voxels among 20 human subjects. A threshold of $|T| \geq 2.5$ was applied to filter out less significant regions and highlighted cortical regions showing significant improvement by tPBM with a p-value < 0.01.

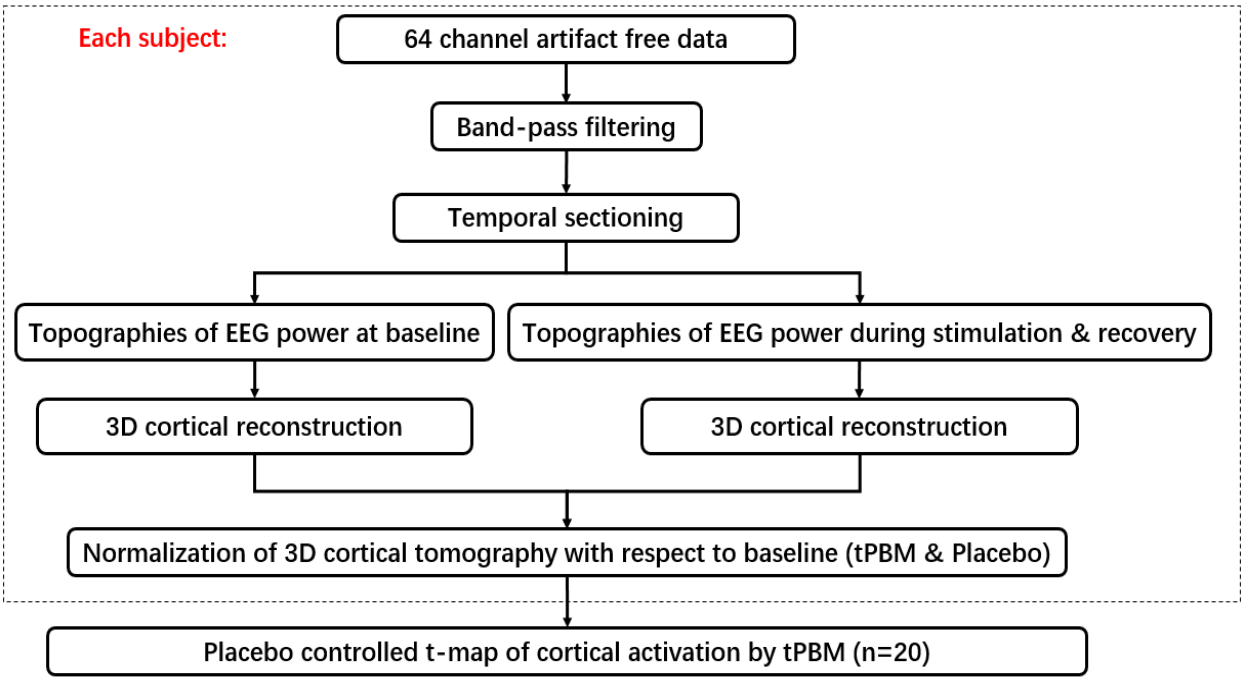

Figure 6-5 The data processing steps for the 3D cortical reconstruction modals

Furthermore, Phase Transfer Entropy (PTE) analysis was applied to calculate human cerebral information flow for all five frequency bands among 20 subjects. For each frequency band, similar to the way aforementioned in the last sub-sections, all 64 sets of EEG time series were segmented into 15 time sections, which were named as Baseline (2-min), Laser 1, Laser 2, Laser 3, Laser 4, Laser 5, Laser 6, Laser 7, Laser 8, Laser 9, Laser 10, Laser 11, Recovery 1, Recovery 2 and Recovery 3, respectively. Except the baseline, each time section lasted 60 seconds. Then, PTE analysis was performed to determine the causality between every two electrodes among all 64 electrodes. The result of PTE values represents the network of cerebral information flow among the 64 regions of interest (ROIs), where the EEG electrodes were located. To reduce biases, PTE values were further normalized into dPTE values [111, 113]. This produced a 64x64 dPTE matrix representing an information flow network between every two electrodes. For example, the value at the 6th row and 7th column of the 64x64 dPTE matrix determines the scale and direction of information flow between electrode 7 to electrode 6. If the dPTE value is within 0.5 to 1, the information flows from electrode 7 to 6. However, if the dPTE value is within 0 to 0.5, the information flows from electrode 6 to 7. Multiple 64x64 (i.e., 64 EEG channels x 64 EEG channels) dPTE matrixes were generated for each subject at each time section. On top of that, the time-sectioned dPTE matrixes from each subject were normalized to the baseline in order to reveal any improvement or alteration of the information flow during and after tPBM. The above procedures were repeated for the placebo experiment. Next, a set of two sample t-tests among 20 human subjects was performed for each time section between the tPBM and placebo experiments. Last, significant enhancements of the information flow from several selected ROIs (i.e., the electrode sites near the stimulation location and the anterior default mode region) were displayed topographically.

6.3 Results

6.3.1 Placebo-controlled, time-frequency maps at selected electrodes

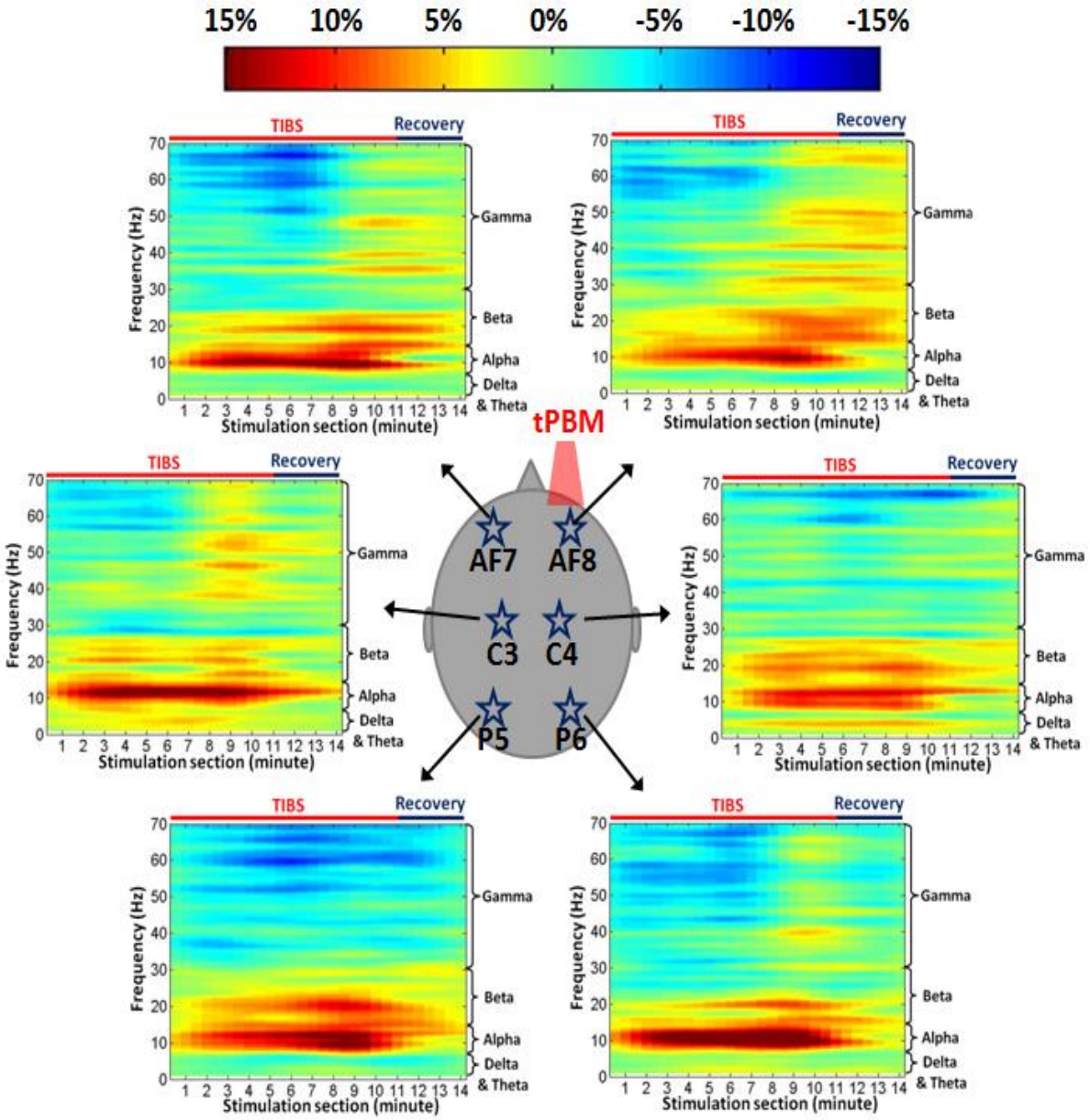

Figure 6-6 Time-frequency maps at 6 selected electrodes.

Based on the procedures listed in Fig. 6-4, time-frequency maps of EEG spectral powers from 6 selected electrodes of Af7, Af8, C3, C4, P5, and P6 were obtained and shown in Fig 6-6, with the tPBM site being on the right forehead. The scalp locations of the 6 electrodes are marked in the center graph. The corresponding time-frequency diagrams are linked by black

arrows to the corresponding electrodes, respectively. tPBM started from t=0 and ended at t=11 min. In all of the 6 time-frequency maps, strong and increased spectral powers in both Alpha band (8-13 Hz) and Beta band (13-30 Hz) were observed. It seems that the tPBM-induced activation started from the second minute after tPBM onset and increased with a dose-dependent manner. After 11 minutes of tPBM, the activated Alpha power decreased and diminished toward the baseline level within the 3-minute recovery period. A minor power improvement in Gamma frequency (30-70Hz) was also observed at Af7, Af8, C3 and P6. Compared to the improvement of spectral power at both Alpha and Beta frequency, the magnitudes of Gamma power increase at those sites were smaller. Additionally, increases of Gamma power started much later than those of Alpha and Beta power.

6.3.2 Improvement of cortical EEG power

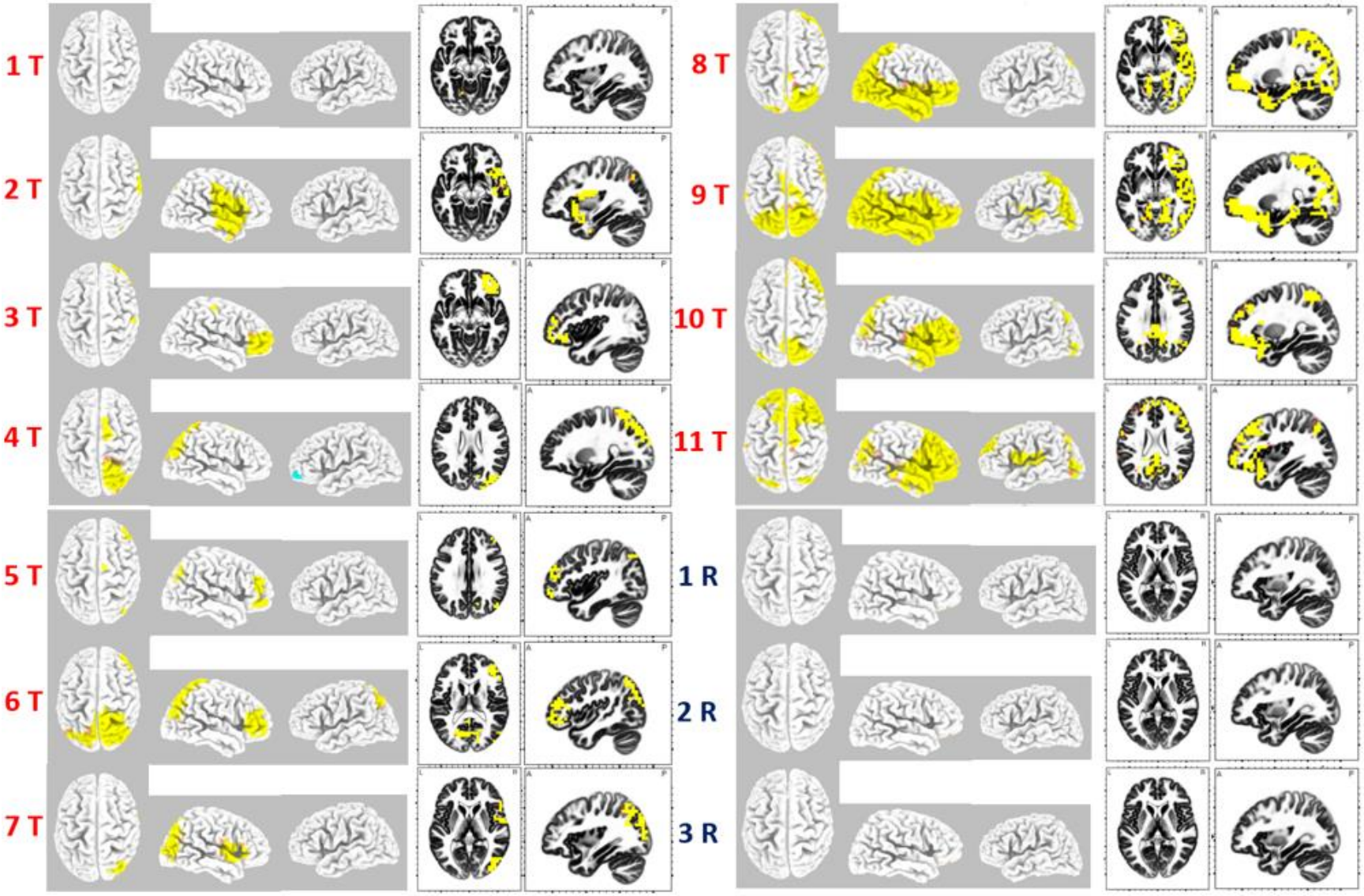

(a)

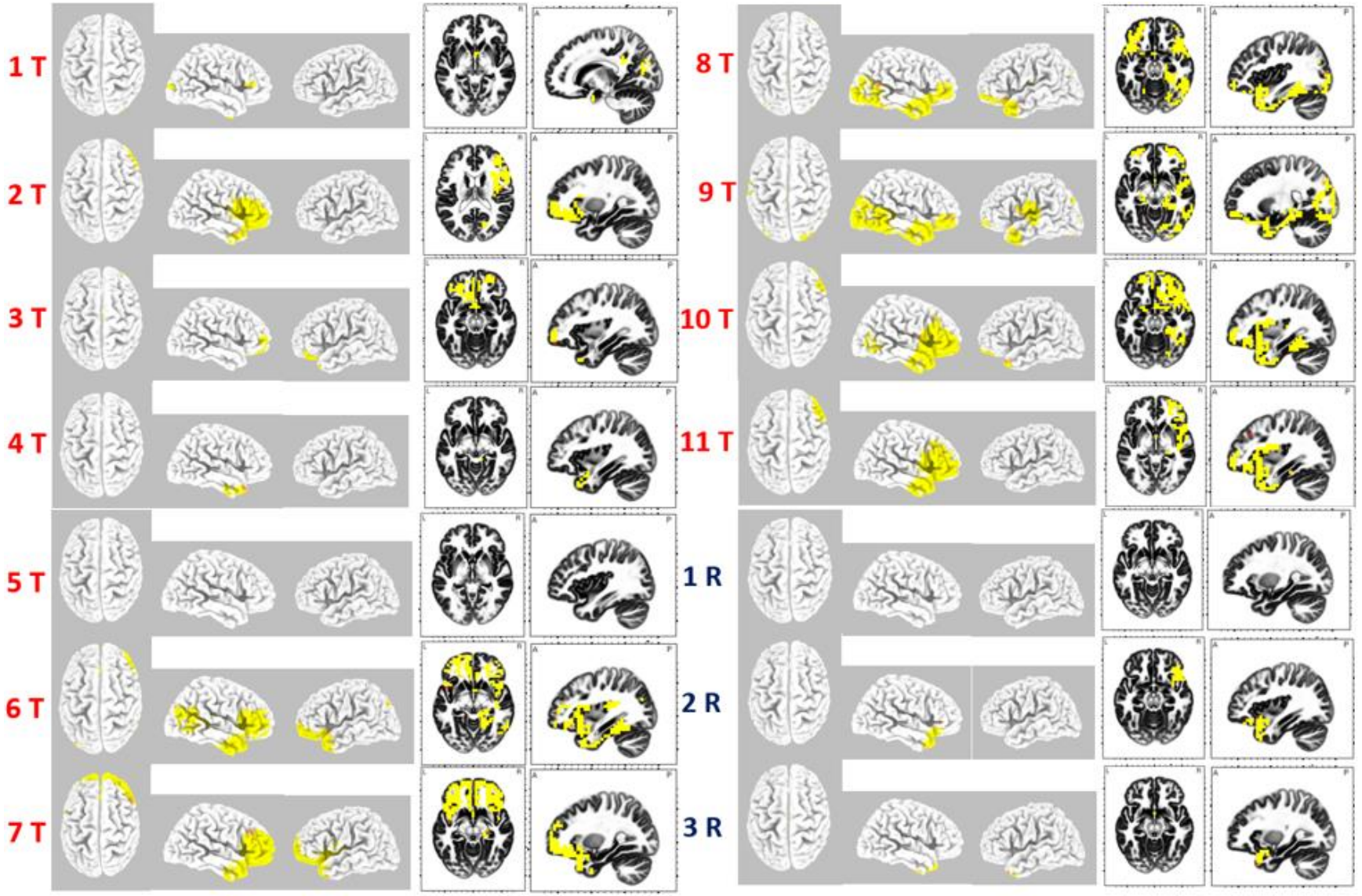

(b)

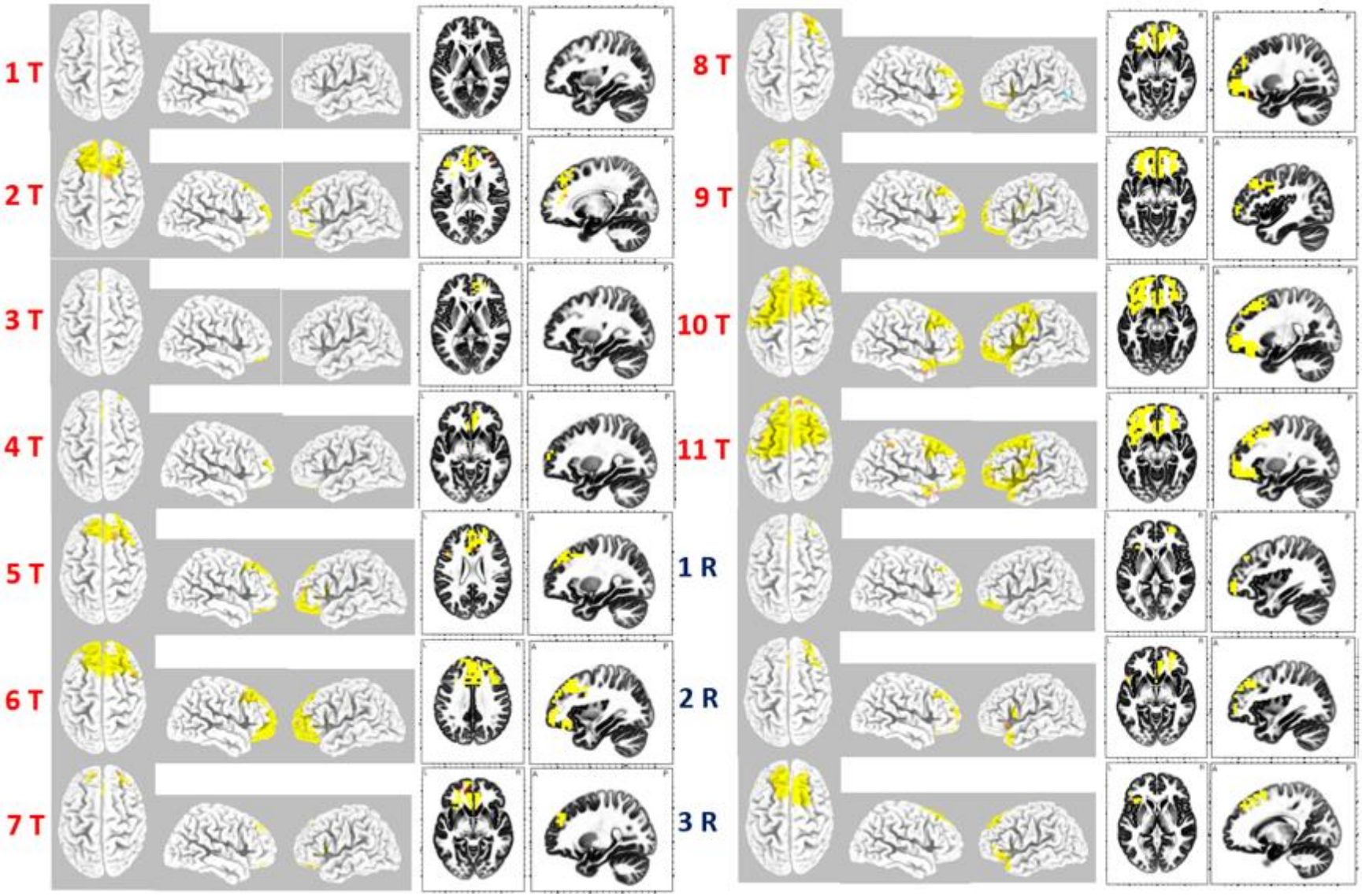

(c)

Figure 6-7 3D reconstructed cortical activation tomographic images at (a) Alpha, (b) Beta, and (c) Gamma frequency. Yellow color marks the regions with significant improvement of EEG spectral power by tPBM compared with the placebo condition. “T” denotes the tPBM sections and the “R” represents the recovery periods. The threshold of $|T| \geq 2.5$ was set to filter out less significant regions and highlighted the cortical regions with significant improvement (p-value < 0.01). Significant increment is represented by yellow color. Significant deactivation is represented by blue color. The number of subjects was 20 for both tPBM and placebo experiments.

Based on the observation given in Section 6.3.1, it was clear that the major improvement of EEG spectral power occurred at Alpha, Beta and Gamma bands. Therefore, I performed 3D EEG source reconstructions using eLORETA at these three frequency bands. The cortical enhancement of EEG power at different frequency bands are shown in Figure 6-7, where “T” denotes the tPBM sections and the “R” represents the recovery periods. The threshold of t-value was set at 2.5 with a p-value < 0.01. The number of subjects was 20 for both tPBM and placebo experiments. In Figure 6-7 (a), the initial response of cortical activation at the Alpha band started from the 2nd minute of tPBM. Ipsilateral power enhancement at frontal lobe was observed before or by the 3rd minute of tPBM. Then, the activation gradually expanded towards ipsilateral parietal and occipital lobes. Finally, from the 8th minute till 11th minute of tPBM, the cortical enhancement of EEG power covered the ipsilateral frontal-tempo-parietal lobes. However, the power enhancement in Alpha frequency recovered to baseline very fast during the recovery period.

Figure 6-7 (b) showed the cortical power enhancement at the beta band. Similar to the activation see at Alpha band, the initial response started from the 2nd minute of tPBM at the frontal lobe and ended up with an expanded activation region covering ipsilateral frontal-tempo-parietal lobes. On top of that, a bilateral frontal power enhancement was observed from the 6th to 10th minute during tPBM, indicating a contralateral propagation/expansion of the cortical activation. During the recovery period, the activation at the beta band recovered fast too.

For the Gamma band, as shown in Fig. 6-7 (c), the initial response was also observed during the 2nd minute of tPBM. Different from those seen at the Alpha and Beta bands, the stimulated region with major power increment at the Gamma band was located mainly on only the frontal lobe. In addition, the activation appeared to be contralateral, covering the anterior Default Mode network area. During the recovery period, there were still some activation remained, indicating a comparatively long-lasting effect of tPBM.

6.3.3 Enhancement of cerebral information flow during and after tPBM

The enhancement of information flow was calculated through Phase Transfer Entropy analysis. As shown in Fig. 6-8, improvements of influx and ex-flux of information toward/from two Regions of Interest (ROIs) [i.e., Fp2 (near the tPBM site) and AFz (near the anterior Default Mode Network)] were displayed topographically at time periods during and after tPBM. The statistical T-values were calculated, thresholded, and imaged to show significant improvements of information flow between the ROIs and other regions of brain. Threshold of $|T| > 1.7$ (p-value<0.05) was applied. Specifically, red lines mean significant improvement of information flow from the ROIs to other electrode sites, whereas blue lines represent significant improvement of information influx toward the ROIs from other electrode sites. Figs 6-8 (a) and (b) demonstrate the changes of information flow from the tPBM stimulation site and the anterior Default Mode point to other electrode sites. Fig 6-8 (a) shows the improvement of information flow at the stimulation site (i.e., electrode Fp2). Enhanced ex-flux of information flow from the tPBM site were observed in the Theta, Alpha and Beta bands. Specifically, in the Theta and Alpha bands, the trails indicating increased information flow (i.e., red lines) were majorly from the anterior frontal lobe (i.e., Fp2) toward the posterior frontal lobe. In the Beta band, on the other hand, the enhanced information flows (i.e., red lines) could majorly reach the parietal and occipital regions/lobes. Furthermore, strong and consistent information influxes towards the tPBM site from many parietal regions contra-laterally were observed in the Gamma band. During the recovery period, the enhanced information flow in all the frequency bands did not return to the baseline.

Fig 6-8 (b) denotes the enhanced information flow at the anterior Default Mode network region. In all the five frequency bands, ex-fluxed trails of information flow (i.e., red lines) were observed throughout the entire tPBM and recovery periods. Especially, many globally enhanced

sets of information flow were observed at the Alpha band. During the recovery period, the enhancement also retained at each frequency band, similar to that seen in Fig. 6-8 (a).

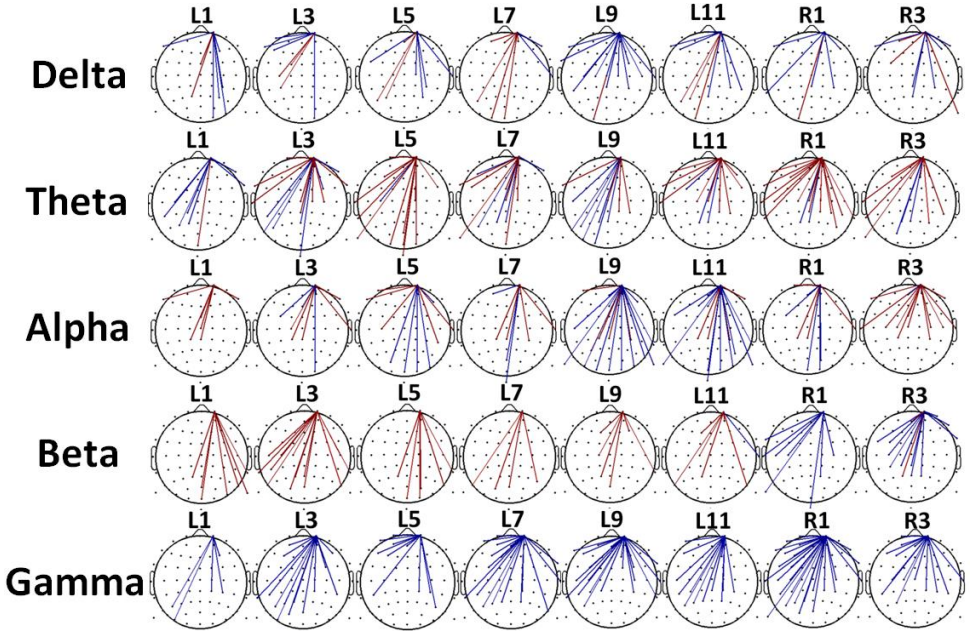

(a)

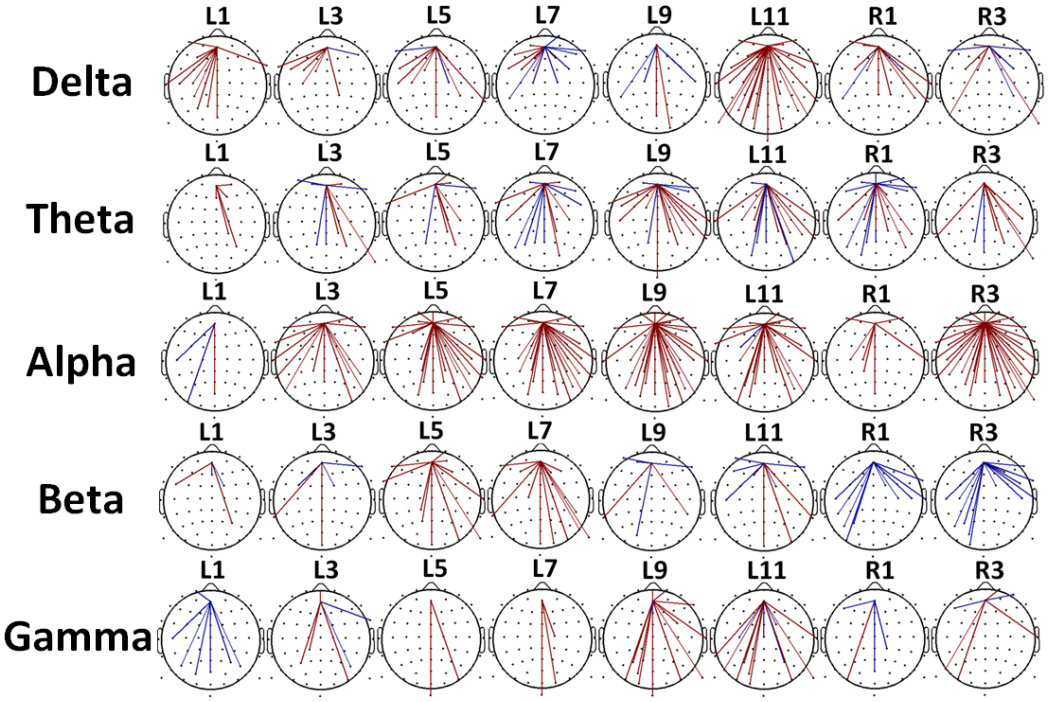

(b)

Figure 6-8 The enhancement of information flow during and after tPBM (a) from Fp2, (b) from AFz. Red lines mean significant enhancement of ex-flux of information from the ROI, and blue lines mean significant enhancement of information influx to the ROI. T-value was set as $|T|>1.7$ (p-value<0.05).

6.4 Discussion

Following a placebo controlled experimental protocol, I applied tPBM and placebo stimulation on the right forehead of 20 human subjects while having EEG to monitor their electrophysiological changes before, during and after the stimulation. As result, I observed strong signal power increments at Alpha, Beta and Gamma bands from 6 selected electrodes at different locations on the scalp during tPBM (Fig. 6-6). Furthermore, by performing a 3D reconstruction algorithm (i.e., eLORETA) on the scalp recorded EEG data, I obtained the following observations:

(1) At the Alpha frequency, Ipsilateral power enhancement at the frontal lobe was observed before or by the 3rd minute of tPBM. The activation gradually expanded towards ipsilateral parietal and occipital lobes. Finally, from the 8th minute till 11th minute of tPBM, the cortical enhancement of EEG power covered the ipsilateral frontal-tempo-parietal lobes.

(2) At the Beta band, the initial response started from the 2nd minute of tPBM at the frontal lobe and then expanded gradually also covering ipsilateral frontal-tempo-parietal lobes. A bilateral frontal power enhancement was also observed from the 6th to 10th minute during tPBM, with contralateral propagation at the frontal region.

(3) At the Gamma band, the initial response was also observed during the 2nd minute of tPBM, but with major power increment located mainly on the frontal lobe contra-laterally, covering the anterior Default Mode network area. In particular, the activated signals remained during recovery, indicating a comparatively long-lasting effect of tPBM with respect to those at Alpha and Beta bands.

(4) Furthermore, Phase Transfer Entropy (PTE) analysis demonstrated the enhancement of information flow from the stimulation cite and anterior Default Mode Network to different cerebral locations where power improvement were observed.

6.4.1 Physiological explanation of photon-neuron interaction

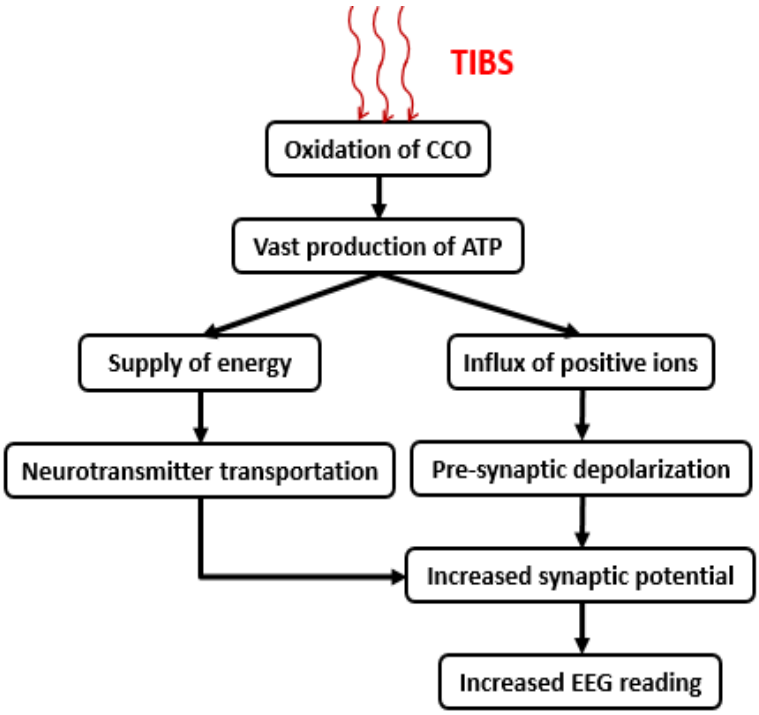

Figure 6-9The flow chart of physiological explanation of photon-neuron interaction.

The frontal-lobe EEG power enhancements are probably induced by the direct stimulation of tPBM. Physiologically, this increase of EEG power by tPBM can be potentially explained by steps shown in Fig. 6-9. Under the continuous stimulation of 1064-nm laser, energetic photons up-regulate CCO in the mitochondria of neurons, which results in the accelerated production of ATP[2]. The increased concentration of ATP nourishes the neuronal metabolism effectively by fueling certain metabotropic ion channels, which results in the influx of intracellular positive ions. Therefore, the presynaptic depolarization induced by positive influx of ions triggers the pre-synaptic action potentials. Then the action potentials conducted through

neuronal networks formed by synaptic connections. In the meantime, it also fuels the neurotransmitter transportation[101], which contributes to the elevation of synaptic potential. The postsynaptic voltage change will then be detected by EEG electrodes.

Furthermore, according to previous studies, the rise in intracellular Ca^{2+} will also contribute to forming posttetanic potentiation (PTP), which is a short duration enhancement of synaptic strength due to neuroplasticity[118]. In other words, during PTP, an increase of effective connectivity (information flow) between neurons was formed. Although the posttetanic potentiation is usually transient and lasts only a few seconds or minutes, it is considered as an induction phase of long term/permanent enhancement of synaptic strength, the long-term potentiation (LTP)[118-120]. LTP provides permanent/long lasting synaptic strength and is widely considered as one of the major cellular mechanisms that underlies learning and memory[120]. This is an optimal goal of my research, namely, to demonstrate that tPBM has the ability of effectively improving and/or enhancing synaptic connectivity and strength that are highly associated with learning and memory. Furthermore, to observe tPBM to be able to modulate or enhance brain effective connectivity, Phase Transfer Entropy analysis was performed. Enhanced directional information flow seen in Fig. 6-8 showed a transformational global increase in effective connectivity of brain networks and activation with a general dose-dependent manner. Therefore, I am confident to expect/speculate that short term exposure of the frontal/pre-frontal cerebral region to tPBM modulates and benefits PTP, which temporally strengthens connections of neural networks due to neuroplasticity. Furthermore, it is reasonable to infer that, by repeated tPBM, one can form LTP and gain cognitive improvement with long-term strengthened synaptic connections. This explains why subjects/patients under repeated interventions of tPBM usually start to show long lasting effects after repeated sessions within a span of weeks or months.

On the other hand, however, excessive intracellular Ca^{2+} could induce excitotoxicity to neurons[121]. Because an influx of Ca^{2+} can activate several enzymes, such as phospho–

lipases, endonucleases and proteases such as calpain[122], a high concentration of these enzymes is detrimental to cell structures, such as components of the cytoskeleton, membrane and DNA[121]. Therefore, in the future, dose-dependent spectra for an optimized stimulation dosage at different wavelengths need to be studied towards different therapeutic goals to avoid overdose of tPBM.

6.4.2 tPBM holds the potential of photobiomodulating human DMN

Default Mode Network (DMN) results from cerebral interaction among different regions of the brain during resting state. DMN will be suppressed once certain tasks are involved[123]. Malfunction and disconnection of DMN were reported to be related to many psychiatric and psychological conditions, such as depression, anxiety and Alzheimer's Disease[123-125]. The abnormal connectivity of DMN in those conditions makes the brain unable to stay in a normal resting state[123]. Enhancement of information flow in DMN during and after tPBM was observed in Fig. 6-8, which indicates that a strengthened neural effective connectivity of DMN is formed during and after tPBM. In addition, an increase of information flow also implies that DMN was stimulated in an active stage. All these alterations/modulation by tPBM to DMN point out that tPBM can improve abnormal connectivity and functions in DMN, showing promising prospective of tPBM to reverse psychiatric and psychological conditions at resting state.

6.4.3 Possible thermal effects

It is possible that tPBM with power density of 0.162 W/cm^2 (2.2 W/13.6 cm^2 = 0.162 W/cm^2) could generate a thermal effect on human forehead, although this power was ~30% reduction compared to my previous studies. On top of that, subjects were asked to report their feelings of heat sensation during both placebo and tPBM experiments. Nevertheless, there could be un-sensible heat generated on the human forehead, which potentially could be a confounding factor of altering cerebral activity measurements[126]. As it is reported by Wang, Y

et al. in 2017[127], water could be a main optical absorber for laser stimulation at 980 nm. Since water has an increased absorption spectrum at 900 nm and longer wavelengths, the findings of tPBM at 980 nm may also suitable for those at 1064 nm, even though the water absorption at 1064 nm is smaller than that at 980 nm[127]. In the future, a heat sensation experiment is needed to exclude thermal contaminations due to laser heating effects and thus to quantify a more accurate electrophysiological response by tPBM.

6.4.4 Comparison of mechanism between tPBM versus tDCS and TMS

There are two major pre-existing neuronal stimulation methods in the field of brain stimulation, transcranial magnetic stimulation (TMS) and transcranial direct current stimulation (tDCS). Both of the techniques are beneficial across a wide spectrum of neurologic and psychiatric diseases[131, 132]. They use magnetic waves and electrical currents to stimulate membrane of neurons in order to rapidly alter the membrane potential and trigger fast action potential as response. By repeatedly sending stimulations to the ROI, neurons in this region are "trained" to be activated together in a sequence of stimulation sessions. As a result, due to neuroplasticity, LTP was formed by high frequency electrical stimulations. Thus, the malfunctioning neurons regain the ability of firing correlated action potentials together with strengthened synaptic connections. Different from TMS and tDCS, tPBM uses energetic photons to modulate neurons. The cellular stimulation target of tPBM is the mitochondria rather than cell membranes [13, 14]. Also, the magnetic and electrical stimulations are comparatively strong and sensible by human subjects, whereas the optical stimulation is much milder that one cannot feel in most of the cases.

The effect of tPBM observed in this study was observed to appear gradually with a delay of 1-2 minutes, where the effects of tDCS and TMS are always rapid and transient [104, 105]. In the case of electrical/magnetic stimulation, the membrane potential is altered rapidly. Due to the drastic change of membrane potential, voltage-gated ion channels depolarize immediately and

trigger action potentials. At the end of the action potential, the membrane potential recovers back to its normal level (i.e. -70 mV), and the neuronal response terminates until a new electrical alteration of the membrane potential comes[133]. The whole process happens usually within mili-seconds. On the other hand, in the case of tPBM, it may take a long period of time (in seconds to minutes) for reduced-state CCO to absorb light and being oxidized, which accelerates the rate of ATP production increasingly [13, 14]. Therefore, the accumulated ATP concentration initiates neuronal response with a few minutes delay after tPBM started.

Furthermore, while tDCS and TMS use high frequency and strong stimulations to build neuronal potentiation by consuming neuronal existing energy, tPBM works in a mild way to gradually build up neuronal potentiation by fueling the neuron with newly generated ATP/energy.

6.4.5 Verification of identical baseline between tPBM and placebo

The comparison of EEG powers between the placebo versus tPBM intervention was based on normalization of the power values with respect to the baseline. Therefore, it is crucial to verify that the electro-potential levels of the baseline at both placebo and tPBM conditions were identical. For this purpose,I performed two-sample t-tests, at all frequency bands, and observed no significant difference of the baseline cerebral electrical potentials between both the placebo and tPBM experiments. This statistical comparison demonstrated/verified that the significant difference in normalized EEG power between tPBM and placebo experiments was derived without any possible baseline bias from two separate experiments.

6.4.6 Possible improvement with a larger sample size

I observed significant difference in electrophysiological responses, including cortical brain networks and effective connectivity (i.e., information flows) at several frequency bands, between placebo versus tPBM. For each analysis, however, my statistical analysis was based

mainly on t-tests, in multiple steps, to identify statistical significances between the two experiments. So, the possibility of having type-I and type-II error adds up during each time/step of a t-test. As a result, the t-values at each voxel or channel needs a correction process in order to minimize a compounded type-I or type-II error [134]. Two common correction methods are Bonferroni correction and False Discovery Rate controlling (FDR-controlling) correction.[134, 135] Both of the correction methods will drastically reduce the scale of t-value at each voxel/channel. Therefore, high uncorrected t-values are required before the correction procedure is taken. Since EEG data have a low signal to noise ratio, a sample/subject size of 20 may not provide a high enough t-value (i.e., a high enough statistical power) to hold the significance of my findings after the correction [136]. Therefore, in order to obtain a more rigorous statistical analysis and conclusion, more human participants are needed in the future.

6.5 Conclusion

In this study, I employed an 64-channel EEG system to monitor electrophysiological responses of the human brain before, during and after tPBM among 20 subjects. I applied time-dependent power spectrum analysis to the time series taken from 6 selected electrode sites at different regions on the scalp. Clear dose-dependent tPBM-induced increases of EEG power in Alpha (8-13 Hz), Beta (13-30Hz) and Gamma (30-70Hz) band were observed. After performing 3D source reconstruction based on 64-channel power densities, I was able to clearly demonstrate, for the first time, that tPBM significantly neuromodulated an ipsilateral frontal network in the beginning and then gradually a frontal-temporal-parietal network at both Alpha and Beta frequency bands. Additionally, it also neuromodulated or enhanced frontal networks bilaterally at the Gamma band. Furthermore, Phase Transfer Entropy analysis showed global increment of information flow from the tPBM site and anterior DMN location to other cerebral locations. These increases of EEG power and information flow revealed potential mechanism of tPBM that links improvement of human cerebral activation and cognitive functions.

Chapter 7 Conclusion and future scope

7.1 Conclusion

In conclusion, the dissertation has accomplished the following points for the research of tPBM: I (1) established a feasible broadband near-infrared spectroscopy system for detecting the change of chromophore concentrations, (2) designed and applied a placebo controlled laser stimulation protocol on human tissue (forearms and foreheads), (3) measured and discussed the hemodynamic and metabolic response of tPBM on human forearms and foreheads, (4) excluded the physiological effect of heat from the result of tPBM, (5) developed and validated a novel absolute value quantification algorithm for human hemoglobin and cytochrome c oxidase detection, and (6) measured and discussed the electrophysiological response of human brain to tPBM by EEG.

7.2 Future scope

7.2.1 Depth dependency of tissue response to tPBM

I performed the first in vivo objective measures and mechanistic study of tPBM in the human brain. Apart from significant and important activations/changes observed in the human brain by comparing with placebo experiments, a number of questions are still unclear. Further investigations are needed in the near future.

For instance, I performed the bb-NIRS measurements with a 3-cm source-detector separation to measure hemoglobin and cytochrome c oxidase improvements by tPBM. However, the single 3-cm separation is deficient to separate the CCO and hemodynamic changes from different depths consisting of the superficial skin, scalp, skull, and cerebral cortex. Because these layers of tissue are related to different tissue/cell types, whose density of mitochondria/ CCO differs drastically.

Similarly, the situation exists in tissue layers of muscles, which has the highest CCO concentration as muscle needs immediate and durable energy. Furthermore, superficial layers of tissue are exposed to the highest dose of tPBM compared to deeper layers. Since they are top layers, more absorption would take place before photons reach deeper tissue cells. Therefore, muscle layer may be the first contributor of oxidized CCO during tPBM. Furthermore, cerebral cortex may also contribute to create oxi-CCO effectively, as dendrites of a neuron also store a considerable amount of mitochondria. Besides the two above tissue components (at two different depths), the cerebrospinal fluid (CSF) also contains limited cell bodies/mitochondria, which is likely to be the least contributor of oxi-CCO.

Thus, different layers of tissue are exposed under different dosages of tPBM, plus they have various densities of mitochondria at respective layers. Therefore, under tPBM, a multi-channel bb-NIRS system with different source-detector separations is needed to cover or interrogate different tissue layers so as to quantify depth-dependent CCO improvement by tPBM.

7.2.2 Determination of the optimized tPBM wavelength and dosage

Although significant stimulation effects were observed in a number of clinical and research studies, there is still no agreement on an optimized tPBM wavelength due to the lack of effect comparison under the same experimental conditions. Therefore, a systematic, normalized, and wavelength-dependent study using the same stimulation conditions on the same human subject groups is needed in order to identify optimal stimulation wavelengths for the adoption of tPBM in mainstream medicine.

Furthermore, to thoroughly evaluate neurophysiological effects of TILS, multiple parameters need to be measured and quantified. Apart from the previous measured hemodynamic and metabolic parameters (i.e., Δ[HbO] and Δ[CCO], ATP concentration is also crucial to directly represent the effects of tPBM as it provides energy to the brain in cognitive

functions. Collaborations with radiologists or physicists with Magnetic Resonance Imaging (MRI) or high-field magnetic resonance spectroscopy (MRS) are necessary. Because MRI is able to provide high spatial resolution images, and MRS can provide information on ATP synthesis in the human brain under tPBM so as to directly quantify the actual effect of tPBM. All in all, with quantified parameters of hemodynamic, metabolic and direct ATP synthesis measured, different tPBM dosage at different wavelength will be compared, and optimized wavelengths and dosages can then be selected.

7.2.3 Estimation on lasting effects of post-tPBM

Furthermore, more investigation is needed on the dose-dependent effect of tPBM on human tissue. In this dissertation, dose-dependent effects were observed in all hemodynamic, metabolic, and electrophysiological signals during tPBM. However, none of the physiological parameters showed to reach their respective saturation within the stimulation duration. In addition, the tPBM-induced effects were observed to be remained during the 3-minute or 5-minute recovery periods, indicating a promising lasting effect of post-tPBM. However, due to a limited duration of the experiments, finite quantification of post-tPBM effects remains unknown, and thus needs to be further investigated.

7.2.4 Direct measurement of neuronal activation by tPBM on animals

Another future work could be related to the direct and indirect measurements of tPBM-induced neurophysiological effects. Up until now, I have indirectly measured and observed tPBM-generated alterations of neural networks through in vivo EEG measurements non-invasively. However, due to the low spatial resolution of EEG, direct neuronal activations by tPBM are not visible and remain unknown. Without knowing actual alterations of ion channels and ion flux, the explanation of tPBM at the neuronal level remains as a speculation.

In future, in vivo invasive animal studies need to be performed. Single ion channels current recording could be performed on two groups of animals, control and tPBM groups, respectively. Current flows through ion channels could be recorded and compared before, during, and after tPBM between the two animal groups. In this way, neuronal perturbations by tPBM at the neuronal level can be verified by direct observation.

7.2.5 Investigation of the tPBM-induced heat effect on EEG

I have studied the neuronal network alteration during and after tPBM by employing EEG measurements. However, although with significant improvements, the results are still lack of calibration for the thermal effect caused by tPBM. It was uncertain whether the global network alterations resulted from the tPBM-generated thermal effect or true PBM. Therefore, a thermal response test is needed to quantify and image potential changes of EEG power and network connectivity induced from a heat source similar to the temperature generated by tPBM. The un-contaminated tPBM effect can be obtained by subtracting the thermal effect from the detected EEG signal during tPBM.

Appendix

A. Understanding the bases of Diffuse Correlation Spectroscopy (DCS): the initial contribution to a laboratory customized DCS system.

A.1 Diffuse correlation spectroscopy (DCS) study of blood flow changes during low level laser therapy (LLLT) – A preliminary report

B. Application of broadband spectroscopy in prostate cancer detection

B.1 Light Reflectance Spectroscopy to Detect Positive Surgical Margins on Prostate Cancer Specimens

B.2 Detecting Positive Surgical Margins: Utilization of Light Reflectance Spectroscopy on ex vivo Prostate Specimens

C. Frequency resolved measurement in prostate cancer detection

C.1Measurement of optical properties of ex vivo prostate tissues and design of trans-rectal ultrasound coupled optical probe

Diffuse correlation spectroscopy (DCS) study of blood flow changes during low level laser therapy (LLLT) – A preliminary report

Sagar Soni, Xinlong Wang, Hanli Liu, Fenghua Tian*
Department of Bioengineering, University of Texas at Arlington, 500 UTA Blvd, Arlington, TX 76010. *Email: fenghua.tian@uta.edu

ABSTRACT

Photobiomodulation with low-power, high-fluence light in the near-infrared range (600-1100nm), also known as low level laser therapy (LLLT), has been used for promoting healing of wounds, reducing pain, and so on. Understanding its physiological effect is essential for treatment optimization and evaluation. In this study, we used diffuse correlation spectroscopy (DCS) to investigate the changes of regional blood flow in skeletal muscle induced by a single session of LLLT. DCS is an emerging optical modality to probe microvascular blood flow in human tissues *in vivo*. We have developed a software-based autocorrelator system with the benefits such as flexibility in raw photon count data processing, portability and low cost. LLLT was administered at the human forearm with a 1064-nm, continuous-wave laser. The emitting power was 3.4 W in an area of 13.6 cm2, corresponding to 0.25W/cm2 irradiance. The emitting duration was 10 minutes. Eight healthy adults of any ethnic background, in an age range of 18-40 years old were included. The results indicate that LLLT causes reliable changes in regional blood flow. However, it remains unclear whether these changes are physiological or attributed to the heating effect of the stimulation laser.

Keywords: Diffuse correlation spectroscopy (DCS), low level laser therapy (LLLT), photobiomodulation, relative blood flow (rBF), blood flow index (BFI).

1. INTRODUCTION

Laser stimulation with near-infrared light (600-1100 nm) is a novel form of non-invasive photobiomodulation or low-level laser therapy (LLLT) which has shown therapeutic potentials. It has been used to promote healing of wound,[1,2] treat stroke,[3,4] enhance cognition,[5,6] and so on. Although LLLT has been practiced for decades, it is still not widely adopted by mainstream medicine. One important reason for this is that the underlying mechanisms of LLLT are not completely understood.[7] It is much needed for more research to reveal its physiological effects at the molecular, cellular and tissue levels.

LLLT uses low-power, high-fluence monochromatic or quasi-monochromatic light from lasers or light emitting diodes (LEDs). The principle behind LLLT is based on the law of conservation of energy. The energy of light photons is converted to metabolic energy with subsequent modulation of the biological functioning of the cells. This indicates that the molecules stimulated enter a temporary excited state which changes its configuration and function and hence it is also called as photobiomodulation. One mechanism of LLLT rests on photon absorption by endogenous chromophores such as cytochrome c oxidase (CCO),[8,9] the terminal enzyme in the mitochondrial respiratory chain that catalyzes the reduction of oxygen for energy metabolism. As the activity of CCO increases, oxygen consumption increases and metabolic energy is produced via mitochondrial oxidative phosphorylation.[10] Because neurons are highly dependent on oxygen metabolism, this photonics-bioenergetics mechanism results in metabolic and hemodynamic alterations that facilitate neuronal functioning.[11,12] The enzyme effects of LLLT has been demonstrated in cultured neurons[9] and animal brains[13] with invasive means. Using noninvasive broadband near-infrared spectroscopy (NIRS), recently we have shown LLLT indeed causes CCO[14] and oxygenation[15] changes in human tissues *in vivo*.

Diffuse correlation spectroscopy (DCS)[16] is an emerging non-invasive technique to probe regional blood flow in human tissues *in vivo*. This technology has been extensively developed, validated and employed in the last decade. Using a hybrid DCS/NIRS system, the metabolic rate of oxygen in human tissues can be further quantified,[17] which would be a useful biomarker in LLLT. In this preliminary report, we used DCS to quantitatively assess the blood flow changes in human skeletal muscle during a single session of LLLT. The confounding effect of heating due to the stimulation laser was also investigated.

Mechanisms of Photobiomodulation Therapy XII, edited by Michael R. Hamblin, James D. Carroll, Praveen Arany, Proc. of SPIE Vol. 10048, 1004806 · © 2017 SPIE · CCC code: 1605-7422/17/$18 · doi: 10.1117/12.2252604

2. MATERIALS AND METHODS

1.1 Participants

Healthy human participants of either sex, any ethnic background and in age range of 23-40 years were recruited from local community of the University of Texas at Arlington. The participants were scheduled for two separate experiments, which would be at least two weeks apart to reduce chance of carryover effects from one experiment to another. On the day of each experiment, the participants were briefed about the experimental procedures. This study was approved by the University of Texas at Arlington Institutional Review Board (IRB). Informed consent was obtained from each participant prior to the experiments.

1.2 Instruments

A continuous-wave, 1064 nm laser (CG-5000, HD Laser Centre, Dallas, TX, USA) was used for LLLT. This laser is FDA-approved and safe for use on humans such as improving blood circulation, temporary pain relief of muscle and joints, muscle spasm. The laser was operated at a constant power of 3.4 Watts. The irradiance in a circle area of $\phi = 4.2$ cm was 0.25W/cm^2, same as that used by Barrett and Gonzalez Lima[5] and Blanco et al.[6]

A portable DCS system (Figure 1), developed and validated in-house, was used to measure the changes in blood flow induced by LLLT and thermal stimulation. The system is designed similar to that of Dong et al.[18] It consists of a long coherence length laser as the light source and an avalanche photo diode (APD) as a photon counting detector. The output of the APD is connected to a computer for processing with a 32-bit, 8-channel data acquisition card (PCI-6602, National Instruments). A multi-mode fiber is connected to the source laser and a single-mode fiber operating in few-mode configuration is connected to the APD detector.

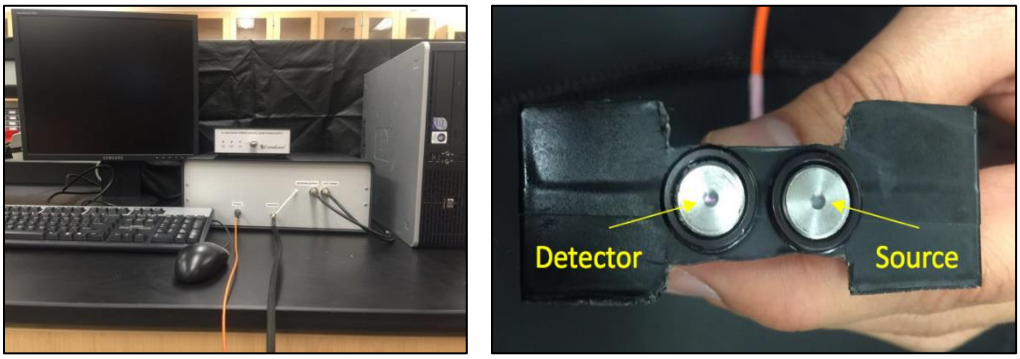

(a) **(b)**

Figure 1. The DCS system (a) and the fiber optic probe (b) used in this study

The administration of LLLT at 3.4 Watts may induce slight heat on the human skin. To explore the potential confounding effect of heating, Medoc's PATHWAY Pain and Sensory Evaluation System was used to generate thermal stimulation on the skin. It has a 16×16 mm thermal probe. The maximum operational temperature range is 0ºC to 55ºC with heating and cooling rate of up to 8ºC/sec.

1.3 Experiments

Two experiments were conducted separately to study the blood flow changes induced due to LLLT and thermal stimulation by using the same stimulation paradigm. Laser stimulation was administered on top of the brachioradialis of the right forearm in the first experiment. In the second experiment, thermal stimulation was applied at the same location as that of LLLT. The DCS probe was secured on the forearm with Velcro in each experiment (Figure 2). The separation between the source fiber and detector fiber was 1.5 cm.

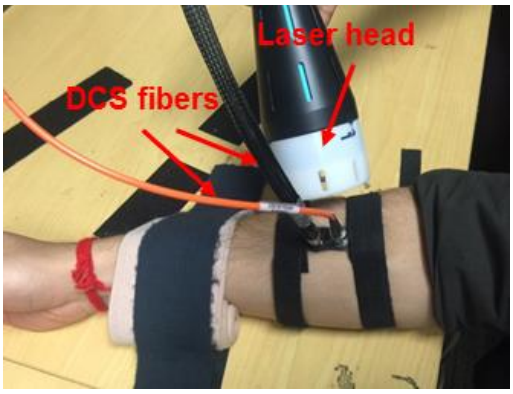

Figure 2. A view of laser stimulation on the forearm

Laser stimulation: After the probe was placed, the participants were instructed to wear an eye-protection goggle and sit stably on the chair during the entire experiment. After 2 minutes of baseline readings were taken, LLLT was administered. The stimulation session was divided into eight cycles, 55 seconds per cycle, with 20 seconds of inter-stimulation gap for DCS data collection (Figure 3). During each cycle an experimenter held the laser aperture closely towards the participant's forearm (Figure 2) and pressed the trigger to shine the laser. The stimulation site on the forearm was alternated for each cycle on both sides of the DCS probe. After the completion of all eight cycles, the participants were asked to sit for another 7 minutes to record the post-stimulation recovery data.

Thermal stimulation: The protocol for thermal stimulation was largely the same as that for laser stimulation, except a thermal probe was placed on one side of the DCS probe. The temperature was 32ºC (skin temperature) during baseline and 38ºC (feeling of warmness) during stimulation, respectively.

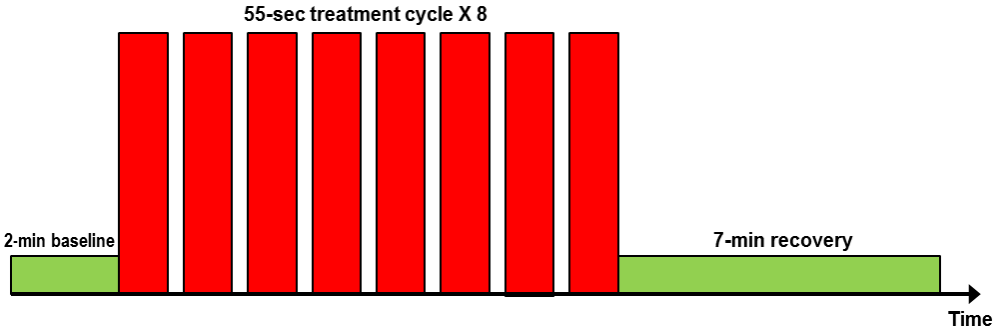

Figure 3. Paradigm for LLLT and thermal stimulations

1.4 Data Processing

The data acquired by DCS system was processed in MATLAB to calculate the relative blood flow (rBF). The analytical solution of the correlation diffusion equation from a point source in a semi-infinite medium is given by

$$G_1(r,\tau) = \frac{vSe^{-K(\tau)r_1}}{4\pi D r_1} - \frac{vSe^{-K(\tau)r_2}}{4\pi D r_2} \quad (1)$$

where, $K^2(\tau) = 3\mu a\, \mu s' + \mu s'^2 k_0^2 \alpha \langle \Delta r^2(\tau) \rangle$, and $\langle \Delta r^2(\tau) \rangle = 6D_b\tau$
To compare the analytical solution with experimental data (G_2) we need to normalize the theoretical data (G_1) to get g_2.

$$g_2(\tau) = 1 + \beta \frac{|G_1(\vec{r},\tau)|}{\langle I(\vec{r},t)\rangle^2} \quad (2)$$

By fitting equation (1) to the measured data of $g_2(\tau)$, we get $\langle \Delta r^2(\tau) \rangle = 6D_b\tau$ and thus D_b which is proportional to the blood flow index (BFI) given by BFI = αD_b.[18]
Data was processed for individual participations and the fitted data was visually inspected to exclude data points with significant discontinuities. An average of 3 data points during 20-second inter-stimulation gap was taken. The first

minute of baseline was rejected to eliminate artifacts. Thus after processing, a total of 16 data points were obtained including baseline, stimulation and recovery.

1.5 Statistical Analysis

To examine the statistical significance of blood flow changes in each experiment, analysis of variance (ANOVA) was performed at a confidence interval of 95%. The null hypothesis stated that there was no significant difference between pre- and post-treatment rBF. The alternative hypothesis states that there was significant difference between rBF during baseline and rBF after treatment.

3. RESULTS

Eight participants (5 males and 3 females, ages 23-40 years) were successfully measured in both experiments.

For both laser and thermal stimulations, there is a clear increase in rBF during the stimulation and recovery periods as compared with the baseline (Figure 4). The ANOVA analysis confirmed the change to be significant with a confidence interval of 95%.

In comparison of two types of stimulations, the changes in rBF have approximately same amplitude during stimulation period. During recovery period, laser stimulation is accompanied with higher rBF changes. There results indicate thermal stimulation can cause a similar change in blood flow to that of LLLT.

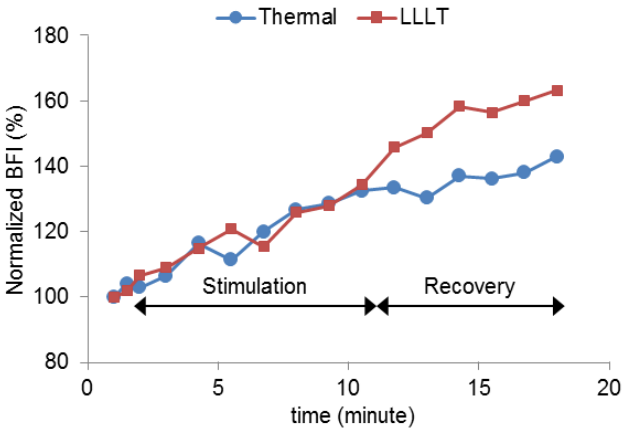

Figure 4. Relative blood flow changes induced by LLLT and thermal stimulations (averaged over eight participants)

4. DISCUSSION AND CONCLUSIONS

We have used DCS to measure *in vivo* changes of blood flow in human tissues during LLLT and thermal stimulation. We observed that LLLT induces significant changes in blood perfusion, which is in line with our previous reports that LLLT induced significant hemodynamic changes in human tissues.[14,15] Our results demonstrate the potential of DCS as a non-invasive technology in mechanistic study of LLLT on humans.

Although it is clear that LLLT induces an increase in blood flow, the exact cause is still unclear as to whether it is due to CCO-related metabolic change or other reasons. We have explored one such possibility here by inducing thermal energy to the target tissue and we observed similar changes in blood flow. It is presumably that such a change during thermal stimulation is mainly contributed by the skin as a process of temperature control in human body. It is evidently clear from this study that although LLLT is referred to as a non-thermal treatment, we should be still cautious on the thermal effects of LLLT as it does induce some thermal energy to the target tissue. Future studies should test this treatment under more controlled conditions (such as temperature). Multi-parametric measurements should also be considered (e.g., measuring blood flow and oxygen metabolic rate together) which will help distinguish the metabolic effects of LLLT from the thermal effects.

REFERENCES

[1] Eells, J. T., Wong-Riley, M. T., VerHoeve, J., Henry, M., Buchman, E. V., Kane, M. P., Gould, L. J., Das, R., Jett, M., Hodgson, B. D., Margolis, D., Whelan, H. T., "Mitochondrial signal transduction in accelerated wound and retinal healing by near-infrared light therapy," Mitochondrion 4(5-6), 559-567 (2004).

[2] Wong-Riley, M. T., Liang, H. L., Eells, J. T., Chance, B., Henry, M. M., Buchmann, E., Kane, M., Whelan, H. T., "Photobiomodulation directly benefits primary neurons functionally inactivated by toxins: Role of cytochrome c oxidase," J. Biol. Chem. 280, 4761-4771 (2005).

[3] Lampl, Y., Zivin, J. A., Fisher, M., Lew, R., Welin, L., Dahlof, B., Borenstein, P., Andersson, B., Perez, J., Caparo, C., Ilic, S., Oron, U., "Infrared laser therapy for ischemic stroke: a new treatment strategy: results of the NeuroThera Effectiveness and Safety Trial-1 (NEST-1)," Stroke 38, 1843-1849 (2007).

[4] Zivin, J. A., Albers, G. W., Bornstein, N., Chippendale, T., Dahlof, B., Devlin, T., Fisher, M., Hacke, W., Holt, W., Ilic, S., Kasner, S., Lew, R., Nash, M., Perez, J., Rymer, M., Schellinger, P., Schneider, D., Schwab, S., Veltkamp, R., Walker, M., Streeter, J., for the NEST-2 Investigators, "Effectiveness and safety of transcranial laser therapy for acute ischemic stroke," Stroke 40, 1359-1364 (2009).

[5] Barrett, D.W. and Gonzalez-Lima, F., "Transcranial infrared laser stimulation produces beneficial cognitive and emotional effects in humans," Neuroscience 230, 13-23 (2013).

[6] Blanco, N. J., Maddox, W. T., Gonzalez-Lima F., "Improving executive function using transcranial infrared laser stimulation," J. Neuropsychol. (2015).

[7] Hamblin, M., "The role of nitric oxide in low level light therapy," Proc. SPIE 6846, 684602 (2008).

[8] Pastore, D., Greco, M., Passarella, S., "Specific helium-neon laser sensitivity of the purified cytochrome c oxidase," Int. J. Radiat. Biol. 76(6), 863-870 (2000).

[9] Karu, T., "Primary and secondary mechanisms of action of visible to near-IR radiation on cells," J. Photochem. Photobiol. B. 49(1), 1-17 (1999).

[10] Rojas, J. and Gonzalez-Lima, F., "Neurological and psychological applications of transcranial lasers and LEDs," Biochem. Pharmacol. 86(4), 447-457 (2013).

[11] Gonzalez-Lima, F. and Barrett, D., "Augmentation of cognitive brain functions with transcranial lasers," Front. Syst. Neurosci. 8, 36 (2014).

[12] Gonzalez-Lima, F. and Auchter, A., "Protection against neurodegeneration with low-dose methylene blue and near-infrared light," Front. Cell Neurosci. 9, 179 (2015).

[13] Rojas, J. C., Bruchey, A. K., Gonzalez-Lima, F., "Low-level light therapy improves cortical metabolic capacity and memory retention," J. Alzheimers Dis. 32: 741-52 (2012).

[14] Wang, X., Tian, F., Soni, S. S., Gonzalez-Lima, F., Liu H., "Interplay between up-regulation of cytochrome-c-oxidase and hemoglobin oxygenation induced by near-infrared laser," Scientific Reports 6, 30540 (2016).

[15] Tian, F., Hase, S. N., Gonzalez-Lima, F., Liu H., "Transcranial laser stimulation improves human cerebral oxygenation," Lasers Surg. Med. 48(4), 343-349 (2016).

[16] Durduran, T. and Yodh, A.G., "Diffuse correlation spectroscopy for non-invasive, micro-vascular cerebral blood flow measurement," NeuroImage 85(1), 51-63 (2014).

[17] Zirak, P., Delgado-Mederos, R., Martí-Fàbregas, J., Durduran, T., "Effects of acetazolamide on the micro- and macro-vascular cerebral hemodynamics: a diffuse optical and transcranial Doppler ultrasound study," Biomed. Opt. Express 1(5), 1443-1459 (2010).

[18] Dong, J., Bi, R., Ho, J. H., Thong, P. S., Soo, K. C., Lee, K., "Diffuse correlation spectroscopy with fast Fourier transform-based software autocorrelator," J. Biomed. Opt. 17, 97004 (2012).

Light Reflectance Spectroscopy to Detect Positive Surgical Margins on Prostate Cancer Specimens

Monica S. C. Morgan,* Aaron H. Lay,* Xinlong Wang, Payal Kapur, Asim Ozayar, Maryam Sayah, Li Zeng, Hanli Liu, Claus G. Roehrborn and Jeffrey A. Cadeddu†

From the Departments of Urology (MSCM, AHL, AO, MS, CGR, JAC) and Pathology (PK), University of Texas Southwestern Medical Center, Dallas and Department of Bioengineering (XW, HL), and Department of Industrial and Manufacturing Systems Engineering (LZ), University of Texas at Arlington, Arlington, Texas

Purpose: Intraoperative frozen section analysis is not routinely performed to determine positive surgical margins at radical prostatectomy due to time requirements and unproven clinical usefulness. Light reflectance spectroscopy, which measures light intensity reflected or backscattered from tissues, can be applied to differentiate malignant from benign tissue. We used a novel light reflectance spectroscopy probe to evaluate positive surgical margins on ex vivo radical prostatectomy specimens and correlate its findings with pathological examination.

Materials and Methods: Patients with intermediate to high risk disease undergoing radical prostatectomy were enrolled. Light reflectance spectroscopy was performed on suspected malignant and benign prostate capsule immediately following organ extraction. Each light reflectance spectroscopy at 530 to 830 nm was analyzed and correlated with pathological results. A regression model and forward sequential selection algorithm were developed for optimal feature selection. Eighty percent of light reflectance spectroscopy data were selected to train a logistic regression model, which was evaluated by the remaining 20% data. This was repeated 5 times to calculate averaged sensitivity, specificity and accuracy.

Results: Light reflectance spectroscopy analysis was performed on 17 ex vivo prostate specimens, on which a total of 11 histologically positive and 22 negative surgical margins were measured. Two select features from 700 to 830 nm were identified as unique to malignant tissue. Cross-validation when performing the predictive model showed that the optical probe predicted positive surgical margins with 85% sensitivity, 86% specificity, 86% accuracy and an AUC of 0.95.

Conclusions: Light reflectance spectroscopy can identify positive surgical margins accurately in fresh ex vivo radical prostatectomy specimens. Further study is required to determine whether such analysis may be used in real time to improve surgical decision making and decrease positive surgical margin rates.

Key Words: prostatic neoplasms, spectrum analysis, prostatectomy, diagnosis, pathology

Abbreviations and Acronyms

IFS = intraoperative frozen section

LRS = light reflectance spectroscopy

PCa = prostate cancer

PSM = positive surgical margin

Accepted for publication May 29, 2015.

No direct or indirect commercial incentive associated with publishing this article.

The corresponding author certifies that, when applicable, a statement(s) has been included in the manuscript documenting institutional review board, ethics committee or ethical review board study approval; principles of Helsinki Declaration were followed in lieu of formal ethics committee approval; institutional animal care and use committee approval; all human subjects provided written informed consent with guarantees of confidentiality; IRB approved protocol number; animal approved project number.

* Equal study contribution.

† Correspondence: Department of Urology, University of Texas Southwestern Medical Center, 5323 Harry Hines Blvd., Dallas, Texas 75390 (telephone: 214-648-2888; e-mail: jeffrey.cadeddu@utsouthwestern.edu).

SURGICAL extirpation is the gold standard treatment for clinically localized prostate cancer and robot-assisted laparoscopic prostatectomy has become the most common technique in North America.[1] The primary goal is

0022-5347/16/1952-0479/0
THE JOURNAL OF UROLOGY®

http://dx.doi.org/10.1016/j.juro.2015.05.115
Vol. 195, 479-484, February 2016
Printed in U.S.A.

to completely excise malignant tissue with negative margins. However, the rate of PSMs on radical prostatectomy specimens can range up to 38%.[2–5] PSMs place patients at higher risk for local and systemic recurrence, thereby increasing the likelihood of adjuvant or salvage radiation and androgen deprivation therapy.[5]

Along with a successful oncologic outcome achieving an optimal result after radical prostatectomy involves the recovery of continence and erectile function. Nerve sparing radical prostatectomy is associated with higher continence and erectile function recovery rates.[6,7] However, the closer dissection plane can be associated with an increased risk of PSMs.[8] Currently to our knowledge no technology exists to allow for rapid detection of PSMs intraoperatively since margin status is determined at pathological analysis after surgery is completed.

LRS measures light intensity reflected or backscattered from tissue within a range of wavelengths. Two major optical parameters that determine the path of light through tissue are light absorption and scattering, of which the latter highly depends on the morphological and cellular properties of the tissue. The spectrum measured by LRS can be used to quantify absorption and scattering and, thus, differentiate tissue types, including malignant from benign tissue, using characteristic signatures in the spectrum.

In recent years LRS has been investigated for medical applications such as localization of specific brain lesions to guide functional neurosurgery,[9] monitoring apoptosis in living cells in real time[10] and rapid diagnosis of different types of cancer in a variety of medical and surgical settings.[11–16] In this study we hypothesized that quantitative measurement of light scattering could identify PSMs of radical prostatectomy specimens using a novel LRS probe.

METHODS

This prospective study was performed in compliance with and was approved by the institutional review board at our institution. Patient inclusion criteria comprised intermediate to high grade (Gleason score 7 or greater) and moderate to high volume prostate cancer (at least 2 contiguous biopsy cores each with 20% or more cancer involvement and/or radiographic T3a disease by endorectal magnetic resonance imaging). All patients underwent robot-assisted laparoscopic prostatectomy between June 2013 and July 2014. Resected prostate specimens were immediately rinsed with saline and submitted for LRS measurements.

The LRS System

The LRS system consists of the HL-2000-HP tungsten-halogen light source and a single channel charge coupled USB device 2000+ array spectrometer (Ocean Optics, Dunedin, Florida), which includes a spectral range of 350 to 1,000 nm, and a laptop computer used to measure the optical spectrum (fig. 1). Data acquisition is controlled by the computer using OOIBase32 software (Ocean Optics). A previously described novel optical probe with a diameter of 1 mm and a detection depth of up to 2 mm[16] was placed on the prostate capsule at select sites.

Immediately after extraction each prostate specimen was evaluated by an experienced genitourinary pathologist. For each prostate 1 area at risk for PSMs and 1 area suspected to be benign based on palpation and biopsy/magnetic resonance imaging were identified. Urethral and bladder neck margins were not included. At each site LRS was performed. Reflectance curves in the wavelength range of 530 to 830 nm were analyzed and later correlated with pathological analysis. Six LRS readings were performed per location and spectral averages were used for analysis.

Pathological Evaluation

After LRS measurement the suspected malignant and benign margin locations were marked with red and yellow ink, respectively. A thin slice of the inked capsule locations 1 to 2 mm deep and with a 3 × 3 mm area were removed. These thin margin slices were embedded ink down and routinely processed. A genitourinary pathologist (PK) evaluated the hematoxylin and eosin stained sections to determine positive (any amount of tumor) or negative margin status.

Feature Selection

LRS features were selected using a forward sequential selection method. Each LRS curve was divided into 7 segments, including segment 1—530 to 540 nm, segment 2—540 to 560 nm, segment 3—560 to 580 nm, segment 4—580 to 595 nm, segment 5—595 to 640 nm, segment 6—640 to 700 nm and segment 7—700 to 830 nm (fig. 2). A polynomial model was then fitted to each segment. Coefficients of the polynomial model were

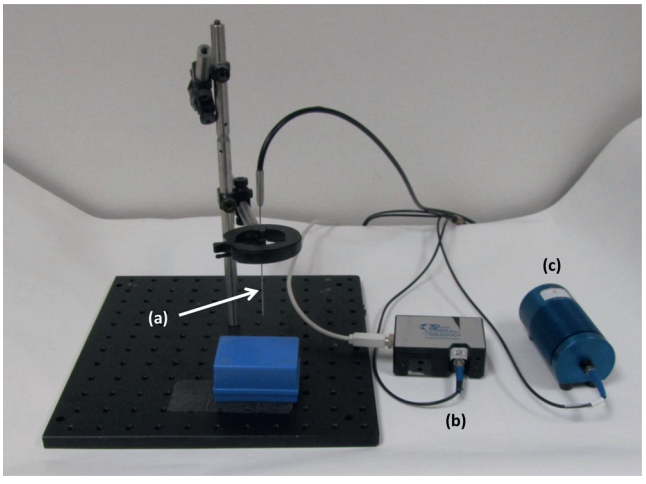

Figure 1. LRS system, including optical probe (*a*), single channel, charge coupled device array spectrometer (*b*) and tungsten-halogen light source (*c*).

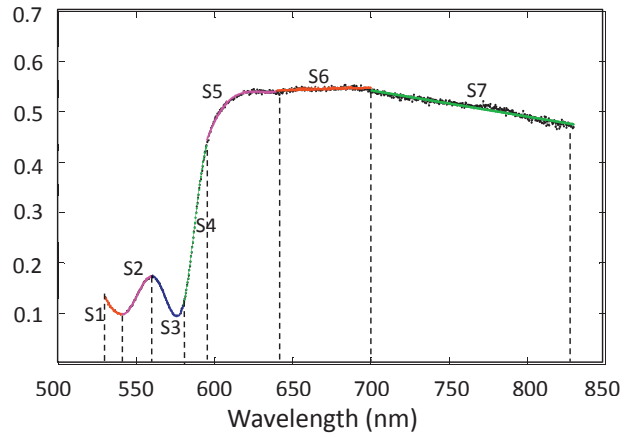

Figure 2. Representative LRS used for feature selection using forward sequential method subdivided by segment (*S*) 1, 2, 3, 4, 5, 6 and 7.

treated as the features of the segment. Through a forward sequential selection algorithm the slope (a′) and the intercept (b′) of a straight line fitted for segment 7 (700 to 830 nm) were determined to be the significant features that differed between malignant and nonmalignant prostate tissues (fig. 3).

Performance Evaluation

Randomized cross-validation was performed to assess how well LRS predicted PSMs of prostate specimens. Of the data 80% were randomly selected to form a training set and the remaining data formed the testing set. A logistic regression model was built using the training set. Predictions were made for the testing set based on this model. This process was repeated 10 times in random fashion to simulate a larger data set and the corresponding sensitivity, specificity, accuracy and ROC AUC were calculated. To test the prediction performance of this cross-validation we further performed 5 runs to achieve averaged values for each evaluation parameter (ie sensitivity, specificity, accuracy and AUC).

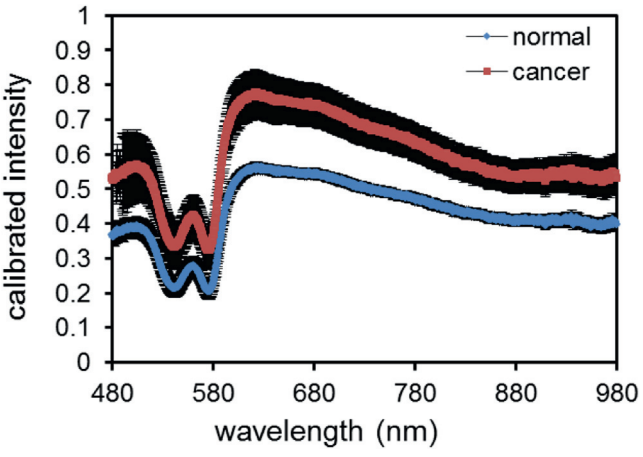

Figure 3. LRS of average malignant (red curve) and benign (blue curve). For cancer tissue mean ± SD a′ = −1.01 ± 0.18 and b′ = 1.37 ± 0.18. For normal tissue mean ± SD a′ = −0.71 ± 0.19 and b′ = 1.02 ± 0.15. Difference in a′ and b′ for normal vs cancer tissues was highly significant (each Student t-test p <0.001).

RESULTS

A total of 17 prostate specimens met inclusion criteria. After pathological analysis there were 22 negative (benign) surgical margin samples and 11 PSM samples. The supplementary table (http://jurology.com/) lists final pathological data. A preliminary evaluation of the LRS study revealed that 1 benign sample was an outlier as the reflectance curve was not measurable. Thus, this sample was removed from further analysis. Figure 3 shows the average LRS taken from true pathological prostate capsule tissue with negative surgical margins and PSMs.

After 5 repeat cross-validation runs LRS predicted prostate specimen PSMs with 86% sensitivity, 85% specificity, 86% accuracy and an AUC of 0.95 (see table).

DISCUSSION

PSMs are generally reported at final pathological analysis such that real-time intraoperative adjustment during radical prostatectomy and excision of additional tissue are not practical. Currently to our knowledge the only alternative is to perform IFSs, which are time intensive and have unproven clinical usefulness. Previous reports demonstrated that IFSs have low sensitivity (40.7% to 70%) but good specificity (95% to 100%).[17–20] Developing new methods or technologies to detect PSMs intraoperatively could significantly impact surgical technique and patient outcomes.

LRS is an emerging technology that captures information from the interaction between light and target tissue. This noninvasive technique can provide information on tissue structure and function by measuring chromophore concentrations such as deoxygenated and oxygenated hemoglobin, and light scattering, which reflect cell size and density.[21] One evident morphological difference between normal and cancerous cells is the increase in nuclear size in the latter. Previous reports demonstrated that changes in nuclear area can be detected by LRS.[22–26] In fact reflectance spectroscopy is a promising technique for diagnosing renal cell carcinoma, Barrett esophagitis, and breast, prostate and skin cancers.[11–16]

In this preliminary study we used LRS to measure and obtain ex vivo light reflectance curves from the capsule of intermediate to high grade PCa

LRS prediction of radical prostatectomy specimen PSMs

Run No.	Sensitivity	Specificity	Accuracy	AUC	Predictive Value	
					Pos	Neg
1	0.883	0.813	0.842	0.957	0.767	0.938
2	0.835	0.847	0.853	0.951	0.768	0.927
3	0.900	0.804	0.858	0.956	0.801	0.971
4	0.908	0.873	0.860	0.944	0.801	0.927
5	0.800	0.904	0.872	0.946	0.782	0.919
Mean ± SD	0.86 ± 0.05	0.85 ± 0.04	0.86 ± 0.01	0.951 ± 0.006	0.78 ± 0.02	0.94 ± 0.02

surgical specimens. We were able to identify features in the 700 to 830 nm wavelength range that distinguished malignant from benign tissue, allowing for the possible detection of PSMs. Although a limited number of sites per prostate was evaluated, the method attained 85% or greater sensitivity and specificity, demonstrating the potential of LRS detection of PSMs and warranting further evaluation. Most promising is that unlike IFS, which logistically and financially must be limited to at most a few samples per specimen, LRS could be used to assess numerous sites across a specimen with no significant additional cost per measurement.

The application of LRS to assess surgical margins in this series builds on our previous study assessing benign and malignant regions in the resected prostate specimen. Sharma et al collected and analyzed LRS and autofluorescence spectra from 37 ex vivo human prostate specimens with high volume, intermediate to high grade PCa (Gleason score 7 or greater).[16] By evaluating benign and malignant regions in the prostate we found that benign prostate tissue has a lower light scattering coefficient (μ_s') than PCa tissue. While Sharma et al used polynomial model fitting to develop a data classification model, the select features in the current study, ie the slope and intercept (a′ and b′, respectively) between 700 and 850 nm, match the characteristic of light scattering of tissue well.[27] The values of a′ and b′ represent the dependence of a decreased light scattering coefficient (μ_s') on wavelength (λ), which served as a biomarker for PCa in the study by Sharma et al. Furthermore, the advantage of selecting the wavelength range of 700 to 850 nm for data analysis in the current series allowed us to eliminate or minimize optical signal contamination from blood since hemoglobin absorption is minimal in this spectral range. Of note autofluorescence spectroscopy was abandoned in the current study since it requires a bulky probe and is more costly and less practical to perform in real time.

In the only other spectroscopy study that we are aware of in which PSMs were assessed on radical prostatectomy specimens Baykara et al investigated elastic light single spectroscopy in the range of 450 to 750 nm wavelengths in 18 ex vivo prostate specimens.[28] They reported 86% specificity and 97% sensitivity to differentiate benign from malignant tissue with a positive predictive value of 0.92, a negative predictive value of 0.94 and an AUC of 0.87. These findings are similar to ours and corroborate the potential of spectroscopy to differentiate malignant from benign prostate tissue.

There are several limitations to our technique that must be addressed before this technique can be translated into clinical intraoperative use. Although the LRS probe is highly sensitive and specific, it is only able to focus on a small area. Current developments are under way to design a larger multifiber probe for clinical use. Data processing during the actual LRS measurement is not automated, which would add to surgical time if clinically implemented in its current form. However, automation and software improvements are feasible such that immediate assessment of the surgical specimen would be possible. The current optical probe has a penetration depth of only 2 mm. Therefore, it is possible that LRS may predict a PSM but a true negative surgical margin would be noted if PCa was less than 2 mm from the capsule. This is a possible explanation for why the sensitivity and specificity measures fall short of 100%. Designing a probe that penetrates only a few cell layers would likely improve LRS performance. All measurements were made ex vivo in a nonperfused organ. Further hardware improvements are needed to perform in vivo measurements. To what degree active perfusion in the prostate and the vicinity of the neurovascular bundle might influence the ability to measure LRS and differentiate malignant from benign tissue remains to be tested if LRS is used as in vivo guidance to find PSMs.

Finally, this study was performed in a small pilot population with intermediate to high grade PCa. Additional experience and validation studies are needed.

CONCLUSIONS

PSMs of fresh ex vivo intermediate to high grade PCa specimens can be identified by LRS. Further

testing and studies of the optimal probe design must be completed to determine whether spectroscopic analysis can be used rapidly in real time during radical prostatectomy to improve surgical decision making and decrease PSM rates.

REFERENCES

1. Stitzenberg KB, Wong YN, Nielsen ME et al: Trends in radical prostatectomy: centralization, robotics, and access to urologic cancer care. Cancer 2012; **118:** 54.
2. Montironi R, Cheng L, Mazzucchelli R et al: Pathological definition and difficulties in assessing positive margins in radical prostatectomy specimens. BJU Int 2009; **103:** 286.
3. Yossepowitch O, Bjartell A, Eastham JA et al: Positive surgical margins in radical prostatectomy: outlining the problem and its long-term consequences. Eur Urol 2009; **55:** 87.
4. Hu JC, Gandaglia G, Karakiewicz PI et al: Comparative effectiveness of robot-assisted versus open radical prostatectomy cancer control. Eur Urol 2014; **66:** 666.
5. Ritch CR, You C, May AT et al: Biochemical recurrence-free survival after robotic-assisted laparoscopic vs open radical prostatectomy for intermediate-and high-risk prostate cancer. Urology 2014; **83:** 1309.
6. Burkhard FC, Kessler TM, Fleischmann A et al: Nerve sparing open radical retropubic prostatectomy—does it have an impact on urinary continence? J Urol 2006; **176:** 189.
7. Kundu SD, Roehl KA, Eggener SE et al: Potency, continence and complications in 3,477 consecutive radical retropubic prostatectomies. J Urol 2004; **172:** 2227.
8. Preston MA, Breau RH, Lantz AG et al: The association between nerve sparing and a positive surgical margin during radical prostatectomy. Urol Oncol 2015; **33:** 18.e.
9. Giller CA, Liu H, German DC et al: A stereotactic near-infrared probe for localization during functional neurosurgical procedures: further experience: Clinical article. J Neurosurg 2009; **110:** 263.
10. Mulvey CS, Bigio IJ, Sherwood CA et al: Wavelength-dependent backscattering measurements for quantitative real-time monitoring of apoptosis in living cells. J Biomed Opt 2009; **14:** 064013.
11. Bensalah K, Tuncel A, Peshwani D et al: Optical reflectance spectroscopy to differentiate renal tumor from normal parenchyma. J Urol 2008; **179:** 2010.
12. Bensalah K, Peswani D, Tuncel A et al: Optical reflectance spectroscopy to differentiate benign from malignant renal tumors at surgery. Urology 2009; **73:** 178.
13. Qiu L, Pleskow DK, Chuttani R et al: Multispectral scanning during endoscopy guides biopsy of dysplasia in Barrett's esophagus. Nat Med 2010; **16:** 603.
14. Sharma V, Shivalingaiah S, Peng Y et al: Autofluorescence lifetime and light reflectance spectroscopy for breast cancer diagnosis: potential tools for intraoperative margin detection. Biomed Opt Express 2012; **3:** 1825.
15. Lue N, Kang JW, Yu CC et al: Portable optical fiber probe-based spectroscopic scanner for rapid cancer diagnosis: a new tool for intraoperative margin assessment. PLoS One 2012; **7:** e30887.
16. Sharma V, Olweny EO, Kapur P et al: Prostate cancer detection using combined autofluorescence and light reflectance spectroscopy: ex vivo study of human prostates. Biomed Opt Express 2014; **5:** 1512.
17. Tsuboi T, Ohori M, Kuroiwa K et al: Is intraoperative frozen section analysis an efficient way to reduce positive surgical margins? Urology 2005; **66:** 1287.
18. Dillenburg W, Poulakis V, Witzsch U et al: Laparoscopic radical prostatectomy: the value of intraoperative frozen sections. Eur Urol 2005; **48:** 614.
19. Goharderakhshan RZ, Sudilovsky D, Carroll LA et al: Utility of intraoperative frozen section analysis of surgical margins in region of neurovascular bundles at radical prostatectomy. Urology 2002; **59:** 709.
20. Lepor H and Kaci L: Role of intraoperative biopsies during radical retropubic prostatectomy. Urology 2004; **63:** 499.
21. Sharma V, He J-W, Narvenkar S et al: Quantification of light reflectance spectroscopy and its application: determination of hemodynamics on the rat spinal cord and brain induced by electrical stimulation. Neuroimage 2011; **56:** 1316.
22. Canpolat M, Gökhan AG, Çiftçioğlu M et al: Differentiation of melanoma from non-cancerous tissue in an animal model using elastic light single-scattering spectroscopy. Technol Cancer Res Treat 2008; **7:** 235.
23. Canpolat M, Akyüz M, Gökhan GA et al. Intraoperative brain tumor detection using elastic light single-scattering spectroscopy: a feasibility study. J Biomed Opt 2009; **14:** 054021.
24. Canpolat M, Akman-Karakaş A, Gökhan-Ocak GA et al: Diagnosis and demarcation of skin malignancy using elastic light single-scattering spectroscopy: a pilot study. Dermatol Surg 2012; **38:** 215.
25. Denkçeken T, Canpolat M, Başsorgun Å et al: Differentiation of cancerous prostate tissue from non-cancerous prostate tissue by using elastic light single-scattering spectroscopy: a feasibility study. World Acad Sci Eng Technol 2011; **59:** 2384.
26. Denkçeken T, Simsek T, Erdogan G et al: Elastic light single-scattering spectroscopy for the detection of cervical precancerous ex vivo. IEEE Trans Biomed Eng 2013; **60:** 123.
27. Jacques SL: Optical properties of biological tissues: a review. Phys Med Biol 2013; **58:** R37.
28. Baykara M, Denkçeken T, Bassorgun I et al: Detecting positive surgical margins using single optical fiber probe during radical prostatectomy: a pilot study. Urology 2014; **83:** 1438.

EDITORIAL COMMENT

PSMs, which are found in up to 38% of patients who undergo radical prostatectomy, are associated with an increased risk of recurrence requiring secondary treatment (reference 3 in article). While the etiology of PSMs is multifactorial, emerging optical imaging technologies hold promise to improve intraoperative tissue interrogation beyond direct visual inspection or standard white light.[1] In this pilot study of 17 radical prostatectomy specimens the authors applied LRS to differentiate

between malignant and benign prostatic tissues with 85% sensitivity and 86% specificity. This promising study adds to similar findings reported recently by Baykara et al (reference 28 in article). As acknowledged by the authors additional hardware and software advances are needed before the technology can be translated to the dynamic setting of the operating room. This report adds to the growing number of technology platforms on the horizon that aim to improve the oncologic and functional outcomes of cancer surgery.

Dimitar V. Zlatev and Joseph C. Liao
Department of Urology
Stanford University School of Medicine
Stanford, California

REFERENCE

1. Hsu M, Gupta M, Su LM et al: Intraoperative optical imaging and tissue interrogation during urologic surgery. Curr Opin Urol 2014; **24:** 66.

BJUI
BJU International

Detecting positive surgical margins: utilisation of light-reflectance spectroscopy on *ex vivo* prostate specimens

Aaron H. Lay*, Xinlong Wang†, Monica S. C. Morgan*, Payal Kapur‡, Hanli Liu†, Claus G. Roehrborn* and Jeffrey A. Cadeddu*

*Department of Urology, University of Texas Southwestern Medical Center, Dallas, TX, †Department of Bioengineering, University of Texas at Arlington, Arlington, TX, and ‡Department of Pathology, University of Texas Southwestern Medical Center, Dallas, TX, USA

Objective

To assess the efficacy of light-reflectance spectroscopy (LRS) to detect positive surgical margins (PSMs) on *ex vivo* radical prostatectomy (RP) specimens.

Materials and Methods

A prospective evaluation of *ex vivo* RP specimens using LRS was performed at a single institution from June 2013 to September 2014. LRS measurements were performed on selected sites on the prostate capsule, marked with ink, and correlated with pathological analysis. Significant features on LRS curves differentiating malignant tissue from benign tissue were determined using a forward sequential selection algorithm. A logistic regression model was built and randomised cross-validation was performed. The sensitivity, specificity, accuracy, negative predictive value (NPV), positive predictive value (PPV), and area under the receiver operating characteristic curve (AUC) for LRS predicting PSM were calculated.

Results

In all, 50 RP specimens were evaluated using LRS. The LRS sensitivity for Gleason score ≥7 PSMs was 91.3%, specificity 92.8%, accuracy 92.5%, PPV 73.2%, NPV 99.4%, and the AUC was 0.960. The LRS sensitivity for Gleason score ≥6 PSMs was 65.5%, specificity 88.1%, accuracy 83.3%, PPV 66.2%, NPV 90.7%, and the AUC was 0.858.

Conclusions

LRS can reliably detect PSMs for Gleason score ≥7 prostate cancer in *ex vivo* RP specimens.

Keywords

spectroscopy, positive surgical margins, prostate cancer, prostatectomy

Introduction

Oncological surgery is extirpative by nature. The primary goal is to perform wide resections to remove all cancerous tissue to provide the patient with the best chance for cure. In radical prostatectomy (RP), this goal is balanced by the interest in preserving quality of life in patients [1,2]. The anatomical nerve-sparing RP was introduced in 1982 and has been shown to have favourable results for erectile function and urinary control recovery after RP [3–5].

At RP, manoeuvres to spare the cavernosal nerves require the surgeon to dissect and develop a surgical plane along the capsule of the prostate to separate the neurovascular bundles from the surgical specimen [6]. This places the patient at risk of having a positive surgical margin (PSM) if the cancer is not organ-confined or if the capsule is violated. Unfortunately, a PSM leads to increased risk of disease recurrence, increased risk of needing adjuvant radiation therapy, and earlier initiation of androgen-deprivation therapy [7,8]. Presently, intraoperative RP surgical margin status can only be assessed with frozen tissue section [9,10]. Systematic neurovascular structure-adjacent frozen-section examination (NeuroSAFE) was evaluated in a large cohort of patients and found a higher rate of nerve sparing with this technique along with fewer PSMs [11]. Other attempts to establish margin status have involved photodynamic diagnosis using fluorescence markers to illuminate cancerous tissue [12].

We have previously published our pilot experience in using light-reflectance spectroscopy (LRS) to detect surgical margins in patients with high-risk prostate cancer after RP [13]. Due to different tissue properties related to nuclear sizes and cell density, we have found that malignant tissues have different light reflective patterns than benign tissue. Our previous

 | doi:10.1111/bju.13503
Published by John Wiley & Sons Ltd. www.bjui.org

study focused on patients with high-risk disease (clinical T3a disease and Gleason score ≥7), and was limited to 17 prostates. In the present study, we expanded the inclusion criteria to all prostate specimens after RP to evaluate the efficacy of LRS in detecting PSMs.

Materials and Methods

A National Institutes of Health (protocol # R01-CA1386620) funded prospective evaluation of *ex vivo* RP specimens using LRS was performed at a single institution from June 2013 to September 2014. The study was conducted in compliance to and approved by the Institutional Review Board. Prostate specimens were procured from patients undergoing robot-assisted laparoscopic RP for biopsy confirmed prostate cancer. LRS measurements were performed immediately after RP specimens were removed.

An optical probe 1 mm in diameter with a detection depth of 2 mm is placed on various points on the capsule of the prostate (Fig. 1). The probe contains two 100-μm fibres, one of which is connected to a tungsten-halogen light source (HL2000HP; Ocean Optics, Inc., Dunedin, FL, USA) and the other connected to a spectrometer (USB 2000+; Ocean Optics, Dunedin, FL USA). Sites on the prostate capsule were selected based on palpation to select suspicious nodular areas and also soft smooth areas for controls. Urethral and bladder neck margins were excluded from analysis, as we wanted to evaluate the technology on a smooth surface. LRS curves from the wavelengths of 530–830 nm were collected and analysed from each selected site on the capsule, which was subsequently marked with ink and sectioned for pathological analysis. Slice of the inked locations (3-mm^2 with a 1–2 mm depth) were histologically processed and analysed by a genitourinary pathologist to determine the existence of a PSM or negative margin.

Our method for analysing LRS curves is described in a previous study [13]. In brief, significant features on the LRS curves differentiating malignant tissue from benign tissue were determined to be the slope (a′) and the intercept (b′) from the wavelength range of 700–830 nm using a forward sequential selection algorithm. Additional features were selected and tested in this study, including the slope between 580 nm and 600 nm (c′), the absolute change in intensity between peak and trough at wavelengths of 530–630 nm (d′), and the intensity at 750 nm (e′) (Fig. 2). Cross-validation was performed by bootstrapping to assess how well LRS predicted PSM. To form a training set, we randomly selected 80% of the data and a logistic regression model was built. The remaining data points formed the testing set and prediction of PSM was made based on the model. Randomised cross-validation was repeated 10 times and the average sensitivity, specificity, accuracy, positive predictive value (PPV), negative predictive value (NPV), and

Fig. 1 (**A**) LRS system: (a) Optical probe, (b) Single-channel charge-coupled device array spectrometer (USB 2000+, Ocean Optics, Dunedin, FL USA), and (c) Tungsten-halogen light source (HL2000HP, Ocean Optics, Inc., Dunedin, FL, USA). (**B**) Placing the optical probe on the surface of the prostate for LRS measurement.

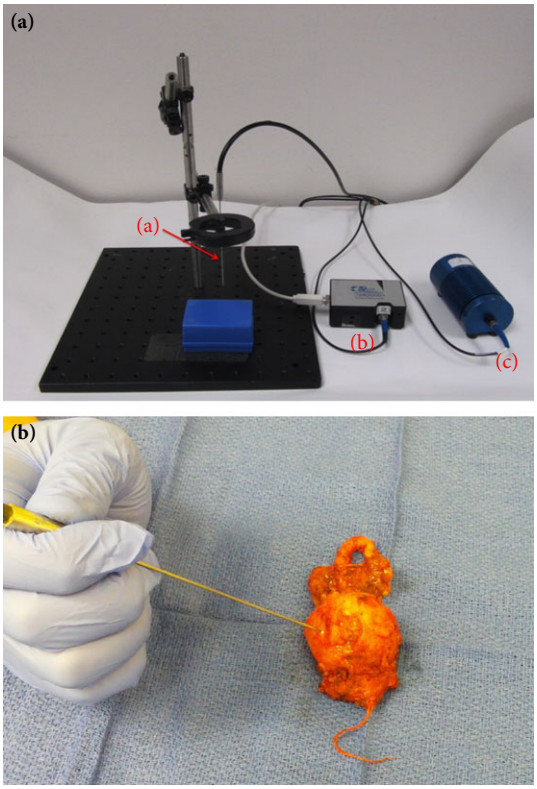

Fig. 2 Graph of representative LRS curve used for feature selection. a′ (slope) and b′ (intercept) of the line from wavelength range of 700–830 nm were significant features distinguishing benign and malignant tissue. Additional features include the slope between 580 nm and 600 nm (c′), the Δ between peak and trough at wavelengths 530–630 nm (d′), and the intensity at 750 nm (e′).

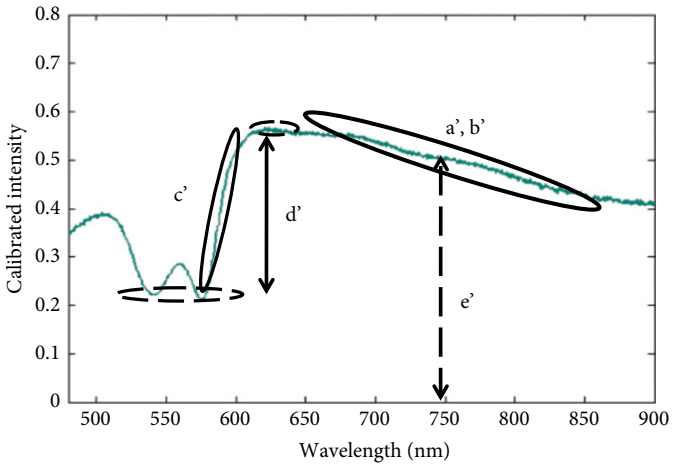

area under the receiver operating characteristic curve (AUC) were calculated.

Results

In all, 50 RP specimens were evaluated using LRS. The patient demographic and tumour characteristics are presented in Table 1. In all, there were 197 sites selected for LRS readings. Pathologically, 32 sites had PSMs with a Gleason score of ≥7, 12 sites had PSMs with a Gleason score of 6, and 153 sites had normal tissue (negative margin).

The LRS curves for Gleason score ≥7, Gleason score 6, and normal tissue pathologically confirmed at the selected margin were averaged over the given sample size and plotted in Fig. 3. Using the significant features (a′ and b′) developed from our earlier experience, we found a significant difference in a′ and b′ values between the Gleason score ≥7 group compared with the Gleason score 6 and normal tissue groups ($P < 0.001$). However, there was no significant difference in the a′ and b′ values between the Gleason score 6 and the normal tissue groups (Table 2).

Table 1 The patients' and tumour characteristics.

Variable	Value
Number of patients	50
Mean (range)	
Age, years	61.3 (38–77)
PSA level, ng/mL	7.21 (2.1–25)
%	
Gleason score ≥7	88.2
Pathological stage T3	45.1
PSM rate	58.8

Fig. 3 The mean LRS curves of benign, Gleason score 6 (GL 6), and Gleason score ≥7 (GL 7,8,9) tissue.

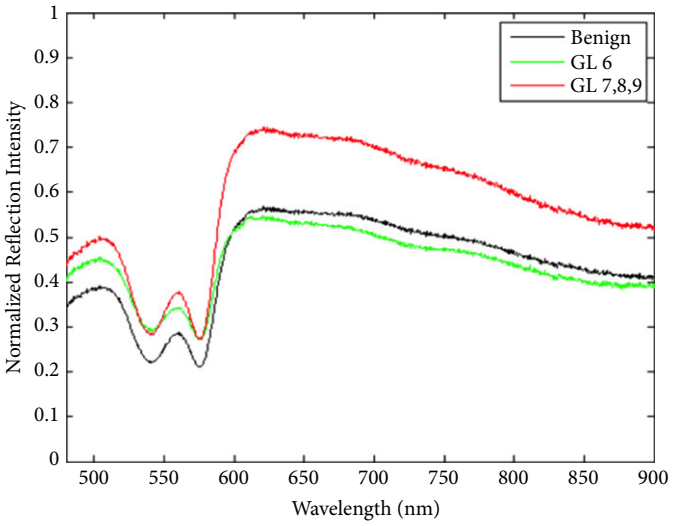

Additional features (c′, d′, e′) were added and randomised cross-validation was performed to assess how well LRS predicted a PSM. First, the ability to identify all PSMs (Gleason score 6 with Gleason score ≥7) was assessed. Based on the logistic regression model built on the randomised training set using the five significant features, LRS sensitivity for Gleason score ≥6 PSM was 65.5%, specificity 88.1%, accuracy 83.3%, PPV 66.2%, NPV 90.7%, and the AUC was 0.858. A separate randomised training set was built by grouping Gleason score 6 LRS data with normal tissue. Based on this model, LRS sensitivity for Gleason score ≥7 PSM was 91.3%, specificity 92.8%, accuracy 92.5%, PPV 73.2%, NPV 99.4%, and the AUC was 0.960 (Table 3).

Discussion

The 'pentafecta' in RP outcomes include continence, potency, biochemical recurrence-free survival, postoperative complications, and negative surgical margins [14]. Despite using new technological advances such as robot-assisted surgery and refinement in surgical technique, the rate of PSM in RP is 13.6–19.5% [15–17]. Unfortunately, PSM is associated with an increased risk of biochemical recurrence, local disease recurrence, and the need for secondary cancer treatment [8,18,19].

LRS is an emerging technology with promising applications in the biomedical field. Its utility is based on the principle that different tissue types have varying optical properties that can be differentiated by spectroscopic analysis. LRS can provide information on tissue structure and function by measuring chromophore concentrations, such as deoxygenated and oxygenated haemoglobin, along with light scattering, which varies by cell size and density [20]. Previous reports have shown that LRS can detect the increase in nuclear size of malignant tissues [21–25]. Additionally, LRS has been studied to diagnose various pathological states such as Barrett's oesophagitis and various malignancies, including breast, skin, kidney, and prostate [26–30].

In the present study, we have shown the utility of using LRS technology in identifying PSM in *ex vivo* RP specimens. We found a 91.3% sensitivity of identifying Gleason score ≥7 prostate cancer at the margin. We previously reported our initial results of 17 high-grade prostates and found a sensitivity of 86% [13]. With refinement of our technique and using additional LRS features, we were able to increase our sensitivity in detecting Gleason score ≥7 to 91.3%. However, if detection of Gleason score 6 disease is included in the statistical analysis for PSM identification, then there is a decrease in sensitivity to 80.4%.

Given that increasing Gleason score is associated with increase in cellular density and nuclear sizes [31], it is not surprising that LRS was not accurate in distinguishing low-

Table 2 Significant features of LRS curves for Gleason score ≥7, Gleason score 6, and benign tissue.

Mean (SD)	Benign	Gleason score 6	Gleason score ≥7	*P* Gleason score 6 vs benign	*P* Gleason score ≥7 vs benign
a′	0.009 (0.003)	0.009 (0.002)	0.013 (0.004)	0.732	<0.001
b′	15.6 (3.1)	15.1 (2.1)	21.0 (4.2)	0.500	<0.001

Table 3 Prediction of PSM by LRS.

Mean (SD)	Gleason score ≥7	Gleason score ≥6
Sensitivity	0.91 (0.04)	0.66 (0.05)
Specificity	0.94 (0.01)	0.88 (0.03)
Accuracy	0.925 (0.004)	0.83 (0.01)
AUC	0.96 (0.02)	0.858 (0.004)
PPV	0.73 (0.04)	0.66 (0.04)
NPV	0.98 (0.01)	0.91 (0.01)

grade Gleason score 6 tissue from benign tissue. Multi-parametric MRI also has a lower sensitivity in identifying low-grade disease compared with high-grade disease due to different tumour characteristics [32–34]. However, we think our present results demonstrate the clinical value of LRS, in that it can confidently identify a negative surgical margin from clinically significant Gleason score ≥7 cancer. The inability to distinguish Gleason score 6 at a margin is not as clinically important given the indolent nature of Gleason score 6 prostate cancer [35,36]. Of note, it must be acknowledged that currently our LRS system may overestimate the number of PSMs accounting for the lower PPV. This is explained by the following: the novel optical probe has a detection depth of 2 mm. As such, cases where there is Gleason score ≥7 cancer within 2 mm of the resection margin may be read by the optical probe to have malignant features on the LRS curves. However, when examined under the microscope, as the malignant cells are not at the true resection margin, this will be reported as a negative pathological margin and therefore a false-positive LRS margin. Further refinement in the optical probe to measure an even shallower depth of light reflectance will improve sensitivity.

Although the present results are encouraging, there are several limitations to the technology at this time. Firstly, the readings are taken after the prostate has been removed instead of in real-time. As such, it will be necessary to mark the location of the PSM and then correlate it to the surgical bed to direct further resection if necessary. This could be an imprecise venture, although much quicker than frozen section analysis. *In vivo* examination of the specimen, on the other hand, could be complicated by the presence of blood, particularly in the wavelength region of 500–600 nm due to strong light absorption by haemoglobin concentration. Other potential confounders include immune infiltration and prostatic inflammation, which could alter light absorption and scattering. Further studies need to be conducted in the near future using *in vivo* models to validate this technology.

Other limitations to this technology include the 1-mm diameter size of the detection probe, such that it will be time consuming to measure the entire surface of the prostate to identify areas of PSM. In addition, the lower PPV at this time can lead to unnecessary resection of additional tissue, which may compromise the quality of life of the patient after RP. The future of PSM detection may use LRS, although the practicality of this technology will rely on incorporating the optical probe into the camera used in minimally invasive RP, so that readings can be performed in real-time.

In conclusion, LRS can reliably detect PSMs for Gleason score ≥7 prostate cancer in *ex vivo* RP specimens. Further advances in LRS technology to identify PSM may involve cameras with real-time spectroscopy capabilities.

Conflicts of Interest

None disclosed.

References

1 **Litwin MS, Hays RD, Fink A et al.** Quality-of-life outcomes in men treated for localized prostate cancer. *JAMA* 1995; 273: 129–35

2 **Bianco FJ, Scardino PT, Eastham JA.** Radical prostatectomy: long-term cancer control and recovery of sexual and urinary function ("trifecta"). *Urology* 2005; 66: 83–94

3 **Walsh PC, Donker PJ.** Impotence following radical prostatectomy: insight into etiology and prevention. *J Urol* 2002; 167: 1005–10

4 **Walsh PC, Partin A, Epstein J.** Cancer control and quality of life following anatomical radical retropubic prostatectomy: results at 10 years. *J Urol* 1994; 152: 1831–6

5 **Catalona WJ, Carvalhal GF, Mager DE, Smith DS.** Potency, continence and complication rates in 1,870 consecutive radical retropubic prostatectomies. *J Urol* 1999; 162: 433–8

6 **Walsh PC, Lepor H, Eggleston JC.** Radical prostatectomy with preservation of sexual function: anatomical and pathological considerations. *Prostate* 1983; 4: 473–85

7 **Blute ML, Bostwick DG, Bergstralh EJ et al.** Anatomic site-specific positive margins in organ-confined prostate cancer and its impact on outcome after radical prostatectomy. *Urology* 1997; 50: 733–9

8 **Swindle P, Eastham JA, Ohori M et al.** Do margins matter? The prognostic significance of positive surgical margins in radical prostatectomy specimens. *J Urol* 2005; 174: 903–7

9 **Cangiano TG, Litwin MS, Naitoh J, Dorey F.** Intraoperative frozen section monitoring or nerve sparing radical retropubic prostatectomy. *J Urol* 1999; 162: 655–8

10 **Eichelberg C, Erbersdobler A, Haese A et al.** Frozen section for the management of intraoperatively detected palpable tumor lesions during

nerve-sparing scheduled radical prostatectomy. *Eur Urol* 2006; 49: 1011–8

11 **Schlomm T, Tennstedt P, Huxhold C et al.** Neurovascular structure-adjacent frozen-section examination (NeuroSAFE) increases nerve-sparing frequency and reduces positive surgical margins in open and robot-assisted laparoscopic radical prostatectomy: experience after 11,069 consecutive patients. *Eur Urol* 2012; 62: 333–40

12 **Adam C, Salomon G, Walther S et al.** Photodynamic diagnosis using 5-aminolevulinic acid for the detection of positive surgical margins during radical prostatectomy in patients with carcinoma of the prostate: a multicentre, prospective, phase 2 trial of a diagnostic procedure. *Eur Urol* 2009; 55: 1281–8

13 **Morgan MS, Lay AH, Wang X et al.** Light reflectance spectroscopy to detect positive surgical margins on prostate cancer specimens. *J Urol* 2016; 195: 479–84

14 **Patel VR, Sivaraman A, Coelho RF et al.** Pentafecta: a new concept for reporting outcomes of robot-assisted laparoscopic radical prostatectomy. *Eur Urol* 2011; 59: 702–7

15 **Terakawa T, Miyake H, Tanaka K, Takenaka A, Inoue TA, Fujisawa M.** Surgical margin status of open versus laparoscopic radical prostatectomy specimens. *Int J Urol* 2008; 15: 704–7

16 **Magheli A, Gonzalgo ML, Su LM et al.** Impact of surgical technique (open vs laparoscopic vs robotic-assisted) on pathological and biochemical outcomes following radical prostatectomy: an analysis using propensity score matching. *BJU Int* 2011; 107: 1956–62

17 **Ficarra V, Novara G, Artibani W et al.** Retropubic, laparoscopic, and robot-assisted radical prostatectomy: a systematic review and cumulative analysis of comparative studies. *Eur Urol* 2009; 55: 1037–63

18 **Grossfeld GD, Chang JJ, Broering JM et al.** Impact of positive surgical margins on prostate cancer recurrence and the use of secondary cancer treatment: data from the CaPSURE database. *J Urol* 2000; 163: 1171–7

19 **Vis AN, Schröder FH, van der Kwast TH.** The actual value of the surgical margin status as a predictor of disease progression in men with early prostate cancer. *Eur Urol* 2006; 50: 258–65

20 **Jacques SL.** Optical properties of biological tissues: a review. *Phys Med Biol* 2013; 58: R37–61

21 **Canpolat M, Gökhan AG, Çiftçioğlu MA, Erin N.** Differentiation of melanoma from non-cancerous tissue in an animal model using elastic light single-scattering spectroscopy. *Technol Cancer Res Treat* 2008; 7: 235–40

22 **Canpolat M, Akyüz M, Gökhan GA, Gürer EI, Tuncer R.** Intra-operative brain tumor detection using elastic light single-scattering spectroscopy: a feasibility study. *J Biomed Opt* 2009; 14: 054021–7

23 **Canpolat M, Akman-Karakaş A, Gökhan-Ocak GA, Başsorgun İC, Akif Çiftçioğlu M, Alpsoy E.** Diagnosis and demarcation of skin malignancy using elastic light single-scattering spectroscopy: a pilot study. *Dermatol Surg* 2012; 38: 215–23

24 **Denkceken T, Canpolat M, Bassorgun I et al.** Differentiation of cancerous prostate tissue from non-cancerous prostate tissue by using elastic light single-scattering spectroscopy: a feasibility study. *World Acad Sci Eng Technol* 2011; 59: 2384–6

25 **Denkçeken T, Simsek T, Erdoğan G et al.** Elastic light single-scattering spectroscopy for the detection of cervical precancerous ex vivo. *IEEE Trans Biomed Eng* 2013; 60: 123–7

26 **Parekh DJ, Lin WC, Herrell SD.** Optical spectroscopy characteristics can differentiate benign and malignant renal tissues: a potentially useful modality. *J Urol* 2005; 174: 1754–8

27 **Bensalah K, Tuncel A, Peshwani D, Zeltser I, Liu H, Cadeddu J.** Optical reflectance spectroscopy to differentiate renal tumor from normal parenchyma. *J Urol* 2008; 179: 2010–3

28 **Qiu L, Pleskow DK, Chuttani R et al.** Multispectral scanning during endoscopy guides biopsy of dysplasia in Barrett's esophagus. *Nat Med* 2010; 16: 603–6

29 **Sharma V, Shivalingaiah S, Peng Y, Euhus D, Gryczynski Z, Liu H.** Auto-fluorescence lifetime and light reflectance spectroscopy for breast cancer diagnosis: potential tools for intraoperative margin detection. *Biomed Opt Express* 2012; 3: 1825–40

30 **Sharma V, Olweny EO, Kapur P, Cadeddu JA, Roehrborn CG, Liu H.** Prostate cancer detection using combined auto-fluorescence and light reflectance spectroscopy: ex vivo study of human prostates. *Biomed Opt Express* 2014; 5: 1512–29

31 **Gibbs P, Liney GP, Pickles MD, Zelhof B, Rodrigues G, Turnbull LW.** Correlation of ADC and T2 measurements with cell density in prostate cancer at 3.0 Tesla. *Invest Radiol* 2009; 44: 572–6

32 **Villeirs GM, De Meerleer GO, De Visschere PJ, Fonteyne VH, Verbaeys AC, Oosterlinck W.** Combined magnetic resonance imaging and spectroscopy in the assessment of high grade prostate carcinoma in patients with elevated PSA: a single-institution experience of 356 patients. *Eur J Radiol* 2011; 77: 340–5

33 **Vargas HA, Akin O, Shukla-Dave A et al.** Performance characteristics of MR imaging in the evaluation of clinically low-risk prostate cancer: a prospective study. *Radiology* 2012; 265: 478–87

34 **Ikonen S, Kärkkäinen P, Kivisaari L et al.** Magnetic resonance imaging of prostatic cancer: does detection vary between high and low gleason score tumors? *Prostate* 2000; 43: 43–8

35 **Albertsen PC, Hanley JA, Fine J.** 20-year outcomes following conservative management of clinically localized prostate cancer. *JAMA* 2005; 293: 2095–101

36 **Popiolek M, Rider JR, Andrén O et al.** Natural history of early, localized prostate cancer: a final report from three decades of follow-up. *Eur Urol* 2013; 63: 428–35

Correspondence: Jeffrey A. Cadeddu, University of Texas Southwestern Medical Center at Dallas, 5323 Harry Hines Boulevard, J8.106, Dallas, TX 75390-9110, USA.

e-mail: jeffrey.cadeddu@utsouthwestern.edu

Abbreviations: AUC, area under the receiver operating characteristic curve; LRS, light-reflectance spectroscopy; PSM, positive surgical margin; (P)(N)PV, (positive) (negative) predictive value; RP, radical prostatectomy.

C.1

Measurement of optical properties of ex vivo prostate tissues and design of trans-rectal ultrasound coupled optical probe

This section is a manuscript to be submitted to the journal of Biomedical Optics Express.

***Authorship**: Venkaiah C. Kavuri, Xinlong Wang, Payal Kapur, Jeffrey A. Cadeddu, Claus Roehrborn and Hanli Liu*.*

C.1.1 Introduction

Prostate cancer (PCa) is one of the leading causes among cancer deaths for men in the United States. Despite many advances in the diagnostic techniques, fundamental questions about how to differentiate the aggressive PCa from localized PCa still exists. Statistics indicate that the lifetime risk of PCa for men in the United States is as high as 15.33%, but only 2.71% of men will die for it[137]. An autopsy study with 249 cases found that 64% of men in their seventh decade of life had undiagnosed invasive PCa and died of other causes[138]. Current treatment options for localized PCa such as radical prostatectomy and external radiation therapy (XRD) are effective in curing patients, but they carry significant risks. A 5-year outcome study indicates that, 79.3% patients suffered from erectile dysfunction due to radical prostatectomy and 63.5% due to XRD[139]. Incontinency rates about 15% in radical prostatectomy and 4% in external beam radiotherapy patients. Bowel urgency and painful hemorrhoids were more common in the external beam radiotherapy group than in the radical prostatectomy group. On the other hand, radiation therapy is associated with acute proctitis and cystitis at the rates of 20% and 30% respectively. There are dilemmas associated with the diagnosis and prognosis of PCa which has lead to the over diagnosis and over treatment of the disease.

Prediction tools for PCa have been developed to assist in the accurate diagnosis and treatment of the disease, and address a wide variety outcomes; e.g. the Partin tables[140, 141], Partin nomogram[142], Kattan and Stephenson nomograms[143] and, CAPRA score[144]. The Partin table uses clinical stage based on digital rectal exam (DRE), Gleason score (GS) of the prostate needle biopsy and serum prostate specific antigen (PSA) to predict stage[145, 146].

These specimens subject to sampling error since they are based on blind random biopsies of the prostate. Imaging modalities are also used to determine PCa stage and aggressiveness. However, these also have several limitations regarding sensitivity and cost of the procedure. Positron Emission Tomography (PET) has low sensitivity and is unable to detect differences between benign and malignant tissue. Novel methods, such as multi-parametric MRI, have demonstrated the potential for improved detection of high grade cancer and risk stratification in newly detected PCa, but confirmatory biopsies are still required. Other imaging modalities such as ultrasound and computed tomography also lack sensitivity and specificity. Further, these modalities often require the use of intravenous contrast to improve detection rates.

Because of the currently employed imperfect tools for PCa detection, many men undergo unnecessary treatment for a disease that would not have caused their deaths. Studies estimate that, in order to prevent one PCa-specific death, 100 men with low-risk PCa need to be treated[147, 148]. Another study indicates that, 42% of men diagnosed with PCa by prostate specific antigen (PSA) testing will be over-diagnosed[149]. Over-diagnosis results in increased health care costs and unnecessary morbidity from treatment-related complications. Patients with life expectancy of less than 10 years may die of other causes before experiencing any benefit from screening but are still exposed to potential harms from the screening test itself, a resulting diagnostic work up, or unnecessary treatments. An improved method to detect PCa and risk-stratify those with PCa prior to definitive therapy may reduce the over-treatment rate, while maintaining or improving mortality.

Near-infrared spectroscopy (NIRS) refers to the use of near-infrared light to non-invasively detect functional information of tissue[150, 151].Because NIR light is harmless electromagnetic radiation that can penetrate deep in soft tissue. Diffuse Optical Tomography (DOT) is the tomographic application of NIRS in imaging tissue vasculature. Since cancer has more vasculature than the surrounding tissue, hemoglobin-based absorption in tumors provides optical contrast in DOT. When imaged at multiple wavelengths, DOT is capable of measuring chromophores concentrations, such as oxy-hemoglobin, deoxy-hemoglobin, water and ICG etc. Usage of DOT for breast cancer detection and diagnosis has been extensively studied for nearly 20 years[152, 153]. DOT instrumentation can be divided into three categories based on the principle of operation. (1) Time resolved systems,[154-156] (2) Frequency domain systems[157] and (3) Continuous wave (CW) systems[158]. Measurements are made in transmission, reflection, or both. Time resolved system relies on photon counting or gated imaging which provides time of flight of photons through the tissue. However, these systems are very expensive in comparison with CW and frequency domain systems. The frequency domain

system modulates the laser diode typically in radio frequency range (~100MHz) and measures the amplitude and phase shift of the detected signal. This is similar to the mean time of flight measurements in the time resolved systems except the cost is comparatively less. Nevertheless it is still higher than CW systems. CW systems are the simplest, least expensive, and fastest in collecting the data. They are also used in video rate imaging. However, CW systems are limited by the measurement of the constant intensity of reflected/transmitted light. Therefore the absorption and the scattering of the tissue cannot be separated from CW measurements [159].

To best of my knowledge, research studies of PCa by DOT is very limited. Thus far, in vivo optical properties of prostate have been reported by references #24 to #28[160-164], and ex vivo specimen were investigated by literatures[91, 165]. Specifically L. K. Leeet al. [166] investigated PCa with interstitial trans-pernial method to collect μ_{eff} using CW diffuse optical technique. Reference literatures [161-164] performed the same method (interstitial trans-pernial method using CW light) on recurrent PCa (RPCa) and utilized differential evolution algorithm developed to recover both absorption and scattering of RPCa. Svensoon et al. utilized time domain technique to record absorption and scattering of PCa using interstitial trans-pernial method[160]. In ex vivo prostate measurements, Pantelides, M. L et al. [165] examined normal prostates using CW light. Prostates were collected from cadaver donors who died from non-urological cause. Sharma et al.[91]examined PCa and benign tissues using auto-fluorescence lifetime spectroscopy (AFLS) and light reflectance spectroscopy (LRS). AFLS used excitation at 447 nm with four emission wavelengths (532, 562, 632, and 684 nm), where their lifetimes and weights were analyzed using a double exponent model. LRS was measured between 500 and 840 nm and analyzed by a quantitative model to determine hemoglobin concentrations and light scattering. On top of Sharma's findings, targeting on the cost-effective LRS system, M. S. Morgan et al.[94]and Aaron H. Lay et al.[78]investigated with larger sample size of ex vivo prostate specimens by spectroscopic feature analysis. They demonstrated that, scattering is one of the major signatures in determining cancer tissue for point measurements (measured by 170 μm source-detector separation needle like probe). However, among all related studies, the optical signatures for PCa are scattered. For better sensitivity and accuracy, it is nowadays preferred to be measured through invasive approaches.

The goal of this study is to show that DOT has the ability to image PCa and to differentiate aggressive cancer from slow growing cancer in order to help clinicians make necessary treatment decisions. DOT has a weakness of not being able to provide anatomical images or locations for the measured organs or specimens. Since prostate cancer measurements are endoscopic, the weakness of DOT makes the measurements blind

folded. This implies that I cannot identify the exact anatomical locations of the measurement sites and reconstructed images. In order to overcome this problem, an optical attachment that can be clipped on an existing transrectal ultrasound (TRUS) probe needs to be developed. In this study, I (1) measured optical signatures of both benign versus prostate cancer tissues from ex vivo human prostate specimens right after prostatectomy in order to determine the feasibility of DOT as a possible imaging tool, (2) designed and tested a clip-on TRUS-coupled DOT assembly that can be easily attached on and used with the existing clinical TRUS utility.

C.1.2 Materials and Methods

C.1.2.1 Instruments

To investigate the feasibility of using DOT to diagnose and locate prostate cancer, a frequency domain optical system was employed to measure the differences between benign and cancerous tissues. Specifically, ISS oximeter (OxiplexTS, ISS Medical, Champaign, IL) with four channels (four sources and one detector) has been utilized. The frequency domain system contains 2 Photo Multiplier Tubes (PMT) with 16 emission laser diodes at 4 different near-infrared (NIR) wavelengths (i.e. 690 nm, 750 nm, 785 nm and 811 nm). There are 4 emission laser diodes for each wavelength. All laser outputs were modulated as 110M Hz with consistently calibrated intensity and coherently calibrated phases. When light propagates in tissue, intensity and phase information will be altered (usually decreased and delayed) due to absorption and scattering features[44]. Therefore, by detecting the intensity and phase changes at 4 different source-detector separations through PMTs, absolute values of bulk absorption and scattering coefficients can be calculated[44]. The detection depth of the optical measurement bulk is determined by the penetration depth of light in tissue, which is related to photon wavelength and source-detector separations[167]. Because the common diameter of a prostate is 3 to 4 cm. In this study, the maximum detection depth was controlled as 0.8 to 1.2 cm, which was proper for two non-overlap bulk measurements at suspicious-malignant and visually normal regions on two opposite lateral sides of prostates. Although ISS oximeter was designed to measure and determine the absolute values of scattering and hemoglobin oxygenation in tissues with multi-wavelength detection, a single wavelength (i.e. 811nm) has been utilized in this study. Reduced scattering coefficient and absorption coefficient at 811 nm were recorded on prostate specimens.

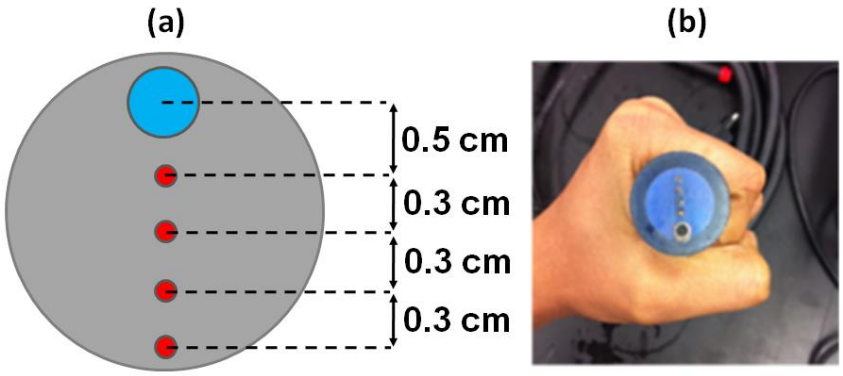

Figure C - 1(a). Source detector geometry used for the custom probe of frequency domain system; (b) the actual probe used for prostate measurements;

A custom probe holder was designed in Solidworks®. And the 3D printing was performed by a 3D printer (Makerbot®). Figure C -1(a) shows the source-detector geometry of the customized FD-NIRS probe holder made for the measurements. The nearest distance between the source and detector pair detector is 0.5 cm and the farthest is 1.4 cm. In Figure C -1(a), the large blue dot represents the detection fiber bundle, while the other 4 red dots correspond to the laser emission fibers. The custom FD-NIRS probe holder was designed as a user-friendly hand-held shape. And the diameter of the measuring surface was designed as 2 cm to ensure proper contact on prostates (Figure C -1 (b)).

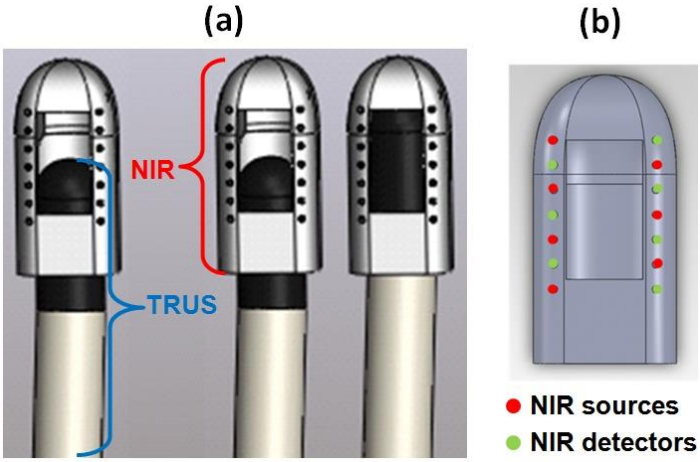

Figure C - 2 (a). The design of clip-on NIR probe to fit for BK® 8818 ultrasound transducer can fit into the probe assembly; (b) Source detector geometry of the clip-on NIR probe.

While DOT probe holders have been well developed for functional brain imaging and for breast cancer detection, studies and probe development on prostate cancer detection/imaging

by DOT are very limited due to technical challenges involved. One of the challenges in prostate cancer imaging is the rectal probe design. Since the prostate is an internal organ, only limited space is available to place optical source and detector fibers. The probe holder has to be designed with large enough source-detector separations for light to pass through the human rectum and reach a ~2 cm depth within the human prostate, but without significantly increasing the diameter of a trans-rectal probe. In my design, the axial dimension of the probe assembly was restricted within 2.5-3 cm in diameter, which should be tolerable for most of human subjects. The inner dimensions of the probe were adjusted such that BK® 8818 ultrasound transducer can fit into the probe assembly (See Fig. C -2 (a)). I deployed 18 optodes (2X9) in a very limited space by utilizing custom-made optical fibers (1.2 mm in diameter) with a thin jacket. The NIR sources and detectors were arranged as it is shown in Fig. C - 2 (b). Commercially available DYNOT system has been used to validate the newly developed probe. In DYNOT, two wavelengths between 700 nm and 850 nm are provided by two laser diodes and the light is sequentially coupled into different fiber bundles. These optical fibers deliver the light to various positions on the surface of the tissue and are used to collect transmitted light intensities.

C.1.2.2 Experiments

A total of 16 patients with age of 60.7 ± 6.0 (years) were recruited for this study (12 patients were measured with both scattering and absorption, 4 patients were measured with only scattering). Each patient underwent robotic-assisted radical prostatectomy and the prostate glands were extracted after being disconnected from their blood supply for at least 30 minutes. Patients were selected with (a) an intermediate-to-high grade of disease (GS ≥ 7) and (b) a moderate-to-high volume of prostate cancer (at least two contiguous biopsy cores, each of which had 20% or more cancer involvement and/or bulky disease by endorectal MRI), so as to optimize spectral yield in this initial study. Measurements were performed on both prostate capsule and intra-prostate tissue (i.e. parenchyma). As it is shown in Figure C - 3, the upper diagram shows the capsule measurement and the bottom one shows the intra prostate measurements after the prostate was bivalve. The dashed line denotes the location where bivalve was administered. Four regions of interest (ROI) were selected and measured on capsule and intra-prostate tissue. The first ROI on capsule was the cancer-suspicious region, and the second ROI was far away from the suspicious region on the capsule (usually on the opposite side of prostate). The frequency domain NIRS (FD-NIRS) data were collected on the

capsule (see Fig. C - 3) before the prostate was bivalve. Then another set of measurements were performed directly on intra prostate tissue after the prostate was bivalve. The ROIs on intra-prostate parenchyma were selected at the regions that were cancer-suspicious (ROI3, solid circle in Fig. C - 3) and visually normal (ROI4, dashed circle in Fig. C - 3) respectively. At each ROI, five measurements were taken. Specifically, the five optical readings were recorded by rotating the probe with ~30 degrees steps and averaged to a single data point. After the measurements, the measured tissue samples were removed from the gland (inked with appropriate colors) and sent to the histology lab for histology confirmation. Then, pathological analysis was performed to confirm the cancer and benign regions.

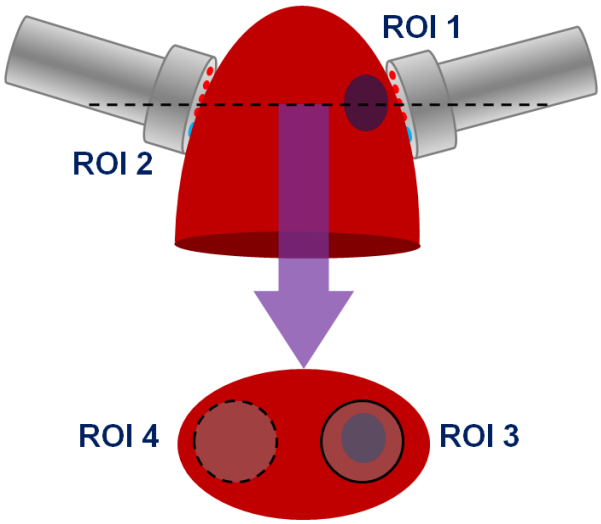

Figure C - 3Selection of ROIs on capsule (up) and intra-prostate tissue (bottom). Dashed line marks the plane, alone which prostates were bivalve. ROI1 denotes the capsule cancer suspicious region. ROI2 denotes the capsule visually normal region. ROI3 denotes the intra-prostate cancer suspicious region. ROI4 denotes the intra-prostate visually normal region.

Initially, only the scattering coefficients of prostate tissues were measured and recorded. After a few cases, encouraged by the differences in scattering between benign and cancerous tissues, absorption coefficient at 811 nm was also included in the experiment. Finally, out of 16 patients, 12 patients were measured with both scattering and absorption coefficients, 4 patients were measured with only scattering coefficients.

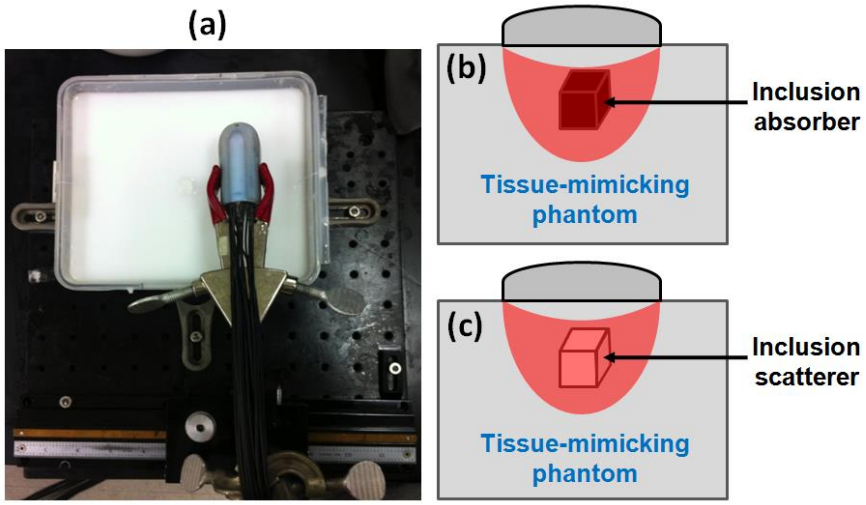

Figure C - 4Experimental setup of testing TRUS-NIR probe with cubical inclusion in tissue-mimicking phantoms. (a) top view of experimental set up, (b) diagram of side-view absorption contrast imaging and (c) diagram of side-view scattering contrast imaging.

The probe and a newly developed algorithm, hierarchical clustering method(HCM)[168], have been tested with liquid laboratory phantoms. As it is shown in Figure C - 4 (a), a homogeneous liquid tissue-mimicking phantom was prepared by filling a container with Intra-lipid solution. A cubical inclusion with dimensions of $1\times1\times1$ cm^3 was placed at 1.5-cm depth from the surface of intra-lipid. The clip-on probe assembly was placed on the surface of the intra-lipid and was connected to a linear translational stage (See Fig C - 4(b) and (c)). The initial location of the probe was adjusted such that the tip of the probe assembly was able to sense the inclusion (i.e., the probe tip was placed on top of the inclusion). Next, the assembly was translated to make the center of probe right above the inclusion and then to make the probe base sit above the inclusion. Finally, the probe was placed on the calibrating phantom to collect the reference data. In absorption contrast experiment, the background absorption was set to 0.005 mm^{-1} and scattering was set to 0.69 mm^{-1}. The absorption of inclusion was 0.01 mm^{-1} and scattering was 0.69 mm^{-1}. In scattering contrast experiment, the background absorption was set to 0.0047 mm^{-1} and scattering was set to 0.51 mm^{-1}. The absorption of inclusion was 0.0046 mm^{-1} and scattering was 1.05 mm^{-1}. Absorption-contrast (i.e. C - 4(b)) and scattering-contrast (i.e. Fig C - 4(c)) cubical inclusions were involved in two separate experiments.

C.1.2.3 Modeling

The light transport in the biological tissue can be modeled by diffusion approximation (DE) to the radiative transport equation (RTE) assuming that the scattering is much greater than the absorption. In the frequency domain the diffusion equation is given by[169]

$$-\nabla D(r)\nabla\Phi(r,\omega)+(\mu_a(r)+i\omega/c)\Phi(r,\omega)=Q_o(r,\omega) \quad \text{C-1}$$

Where Φ(r, ω) is the photon density at the position r, and ω is the modulation frequency of light. Q0(r, ω) represents the isotropic source, c is the speed of light in the medium and μ_a is the absorption coefficient and D(r) is the optical diffusion coefficient, which is defined as

$$D(r)=1/3[\mu_a+\mu_s^{'}(r)] \quad \text{C-2}$$

Where $\mu_s'(r)$ denotes the reduced scattering coefficient which is defined as $\mu_s'=\mu_s*(1-g)$. Here μ_s is the scattering coefficient and g is the anisotropic factor. Equation (C -1) is solved by applying robin-type (known as type III or mixed) boundary condition to model the refractive index mismatch at the boundary. In my study I used both continuous wave (CW) domain (ω =0) andfrequency domain (ω =110). Specifically frequency domain instrument was used to measure bulk optical properties of prostate and CW instrument was used to validate my clip-on optical probe. For frequency domain, the following equations were used to calculate the bulk optical properties,

$$G(\mathrm{r},\omega)=\frac{1}{4\pi\upsilon D}\frac{e^{-kr}}{r} \quad \text{C-3}$$

with

$$k=\left(\frac{\upsilon\mu_a-i\omega}{\upsilon D}\right)^{1/2} \quad \text{C-4}$$

In the above equations υ is the speed of light in the tissue. The three measurements recorded by the oximeter are the amplitude of the light intensity (IAC), the average light intensity (IDC) and the phase (ϕ). Knowing these values at different source-detector separations allows for the slopes of IAC, IDC and ϕ to be calculated (SAC, SDC, and S_ϕ). SAC corresponds to the slope of ln(r*IAC) plotted against r, and S_ϕ denotes the slope of phase (ϕ) against r, where r is the source/detector separation. Absorption (μ_a) and reduced scattering (μ_s'), coefficients can be calculated from the slope of S_ϕ and either SAC or SDC. Since SDC is affected by room lighting, SAC and S_ϕ are used.

DOT reconstruction is to recover the optical properties from NIR measurements taken on the boundaries. The objective function for this procedure can be written as

$$\Omega = \min_{D,\mu_a} \{\| y - F(D,\mu_a)\|^2 + \lambda \| (D,\mu_a) - (D,\mu_{a0})\|^2\} \quad \text{C-5}$$

where y is the measured data, F is the forward operator that generates model response, $||.||^2$ is the L2 norm, λ is the regularization parameter and μ_{a0} is the initial estimate of light absorption coefficient. By minimizing equation (C -1), which is achieved by setting the first derivative of eq. (C -1) with respective to μ_a to be zero following a Taylor series and ignoring the higher order terms, I arrive at the update equation

$$(J^T J + \lambda I)(\delta\mu_a) = J^T (y - F(\mu_a) + \lambda[(D,\mu_a) - (D,\mu_{a0})] \quad \text{C-6}$$

where J is the Jacobin matrix and I is the identity matrix. Using the Levenberg-Marquardt method and assuming ($\delta\mu_a = \mu_a - \mu_{a0}$) leads to

$$(J^T J + 2\lambda I)(\delta\mu_a) = J^T (y - F(\mu_a)) \quad \text{C-7}$$

Note that changes only in μa are considered here, because my DOT measurement utilizes (CW) NIR light with an assumption that variation in light scattering across the medium is minimal. The Jacobian matrix in Eq. (C -3) was then modified to J* and is given by[2]

$$J^* = JC \quad \text{C-8}$$

where C matrix had the size NN × NC (number of nodes × number of clusters). The elements of S matrix are given as follows:

$$C_{(i,j)} = \begin{cases} 1 & if\ i \in GS_j \\ 0 & else \end{cases} \quad \text{C-9}$$

At the end of each iteration, the solution vector was mapped back to each node using Eq. (C -6),

$$\delta\mu_a = C(\delta\mu_a^*) \quad \text{C-10}$$

C.1.2.4 Statistical analysis

In the ex vivo prostate optical property experiments, one out of 16 samples was excluded because the sample has necrotic tissue. After data collection, I sorted the data into four different categories according to the pathological analysis. The four categories included, capsule normal, capsule cancer, parenchyma normal and parenchyma cancer. For example, if the measurement from capsule cancer-suspicious locations turns out to be normal then I treated that sample as normal. Table.C-1 shows the final number of samples after sorting into four tissue types. Both scattering and absorption data were analyzed with one-way ANOVA and post-analysis with Tukey's multiple comparison test. Tukey's test is essentially a t-test with

corrected error rates. Since multiple groups of tissue were compared, the probability of having type-I error compounded. Therefore, applying Tukey's t-test was to maintain and ensure a statistically meaningful significance level. To further check the validity of the estimators, residual analysis was performed in order to check ANOVA assumptions.

TableC-1 Table showing number of measurements made per tissue type

Tissue Type	Scattering	Absorption
Cancer on capsule	11	9
Normal on Capsule	18	14
Cancer in Parenchyma	14	12
Normal in Parenchyma	16	12

C.1.3 Results

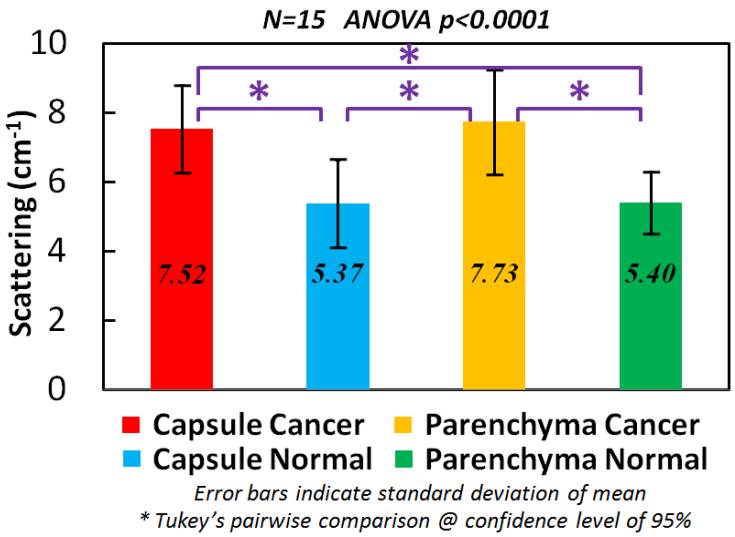

Figure C - 5 Bar plot showing the optical scattering of four prostate tissues. Error bars represents standard deviation of the mean. * represents significant differences with Tukey's pair-wire comparisons. n=15.

Figure C - 5 shows the calculated scattering coefficients from the ex vivo human prostate measurements performed on intra- and extra-capsule tissues in two regions of interests (1) on a cancer-suspiciousregion and (2) a visually normal region. It is evident that the pathology-confirmed cancer has higher scattering values on both tissue types than those of benign tissue. Moreover, the measured optical properties of PCa taken from intra- and extra-capsule tissues are very consistent. The mean reduced scattering for cancer on capsule is

7.52±1.26 cm^{-1} and on parenchyma is 7.73±1.51 cm^{-1}. The benign tissue scattering on capsule has reduced about 5.37±1.27cm^{-1} and parenchymal benign tissues has about 5.40 ± 0.9 cm^{-1}. The p-values from ANOVA (<0.001) indicate that there is a significant difference in optical scattering between cancer and normal tissues. From the Tukey's pair-wise comparisons (bars in figureC-5) I can statistically conclude the following: (1) I am 95% confident that the optical scattering coefficients of cancer on the capsule are different from those of benign tissues of capsule and parenchyma of the human prostate. (2) I also are 95% confident that the optical coefficients of PCa of the parenchyma are different from those of benign parenchyma.

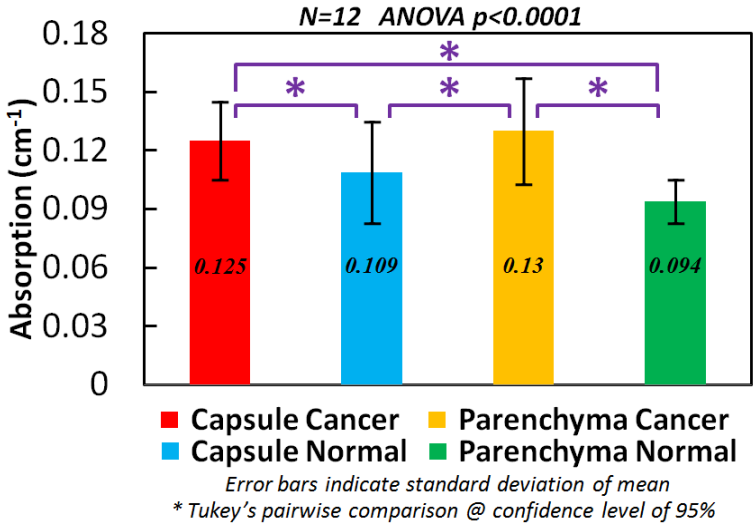

Figure C - 6Bar plot showing the optical absorption of four prostate tissues. Error bars represents standard deviation of the mean. * represents significant differences with Tukey's pair-wire comparisons. n=12.

Figure C - 6 shows the recorded absorption coefficients on the ex vivo human prostate measurements performed on intra- and extra-capsule tissues in two regions of interests (1) a cancer-suspiciousregion and (2) a visually normal region. It is evident that the pathology-confirmed cancer has slightly higher absorption values on both tissue types than those of benign tissue.Moreover, the measurements from intra- and extra-capsule tissues are similar. The mean absorption coefficient for cancer on capsule is 0.125±0.02 cm^{-1} and on parenchyma is 0.13±0.027 cm^{-1}. The benign tissue on the capsule has reduced absorption about 0.109±0.026 $cm^{-1}$and parenchymal benign tissues has about 0.094 ± 0.011cm^{-1}. The p-values from ANOVA (<0.001) indicate that there is a significant difference in optical absorption between cancer and normal tissues. From the Tukey's pair-wise comparisons (bars in figureC - 6) I can statistically conclude the following: (1) I am 95% confident that the optical absorption

coefficients of cancer on the capsule are different from those of benign tissues of capsule and parenchyma of the human prostate. (2) I also are 95% confident that the optical absorption coefficients of PCa of the parenchyma are different from those of benign parenchyma. Further assumption validation procedures are illustrated in Appendix.

Three panels in Fig. C - 7 provide reconstructed images of the embedded inclusion, where the probe assembly was placed at three different locations with respect to the absorption contrast inclusion. Figures C - 7a-c clearly show reconstructed image of the included absorber. The depth location of the absorber was also recovered accurately.

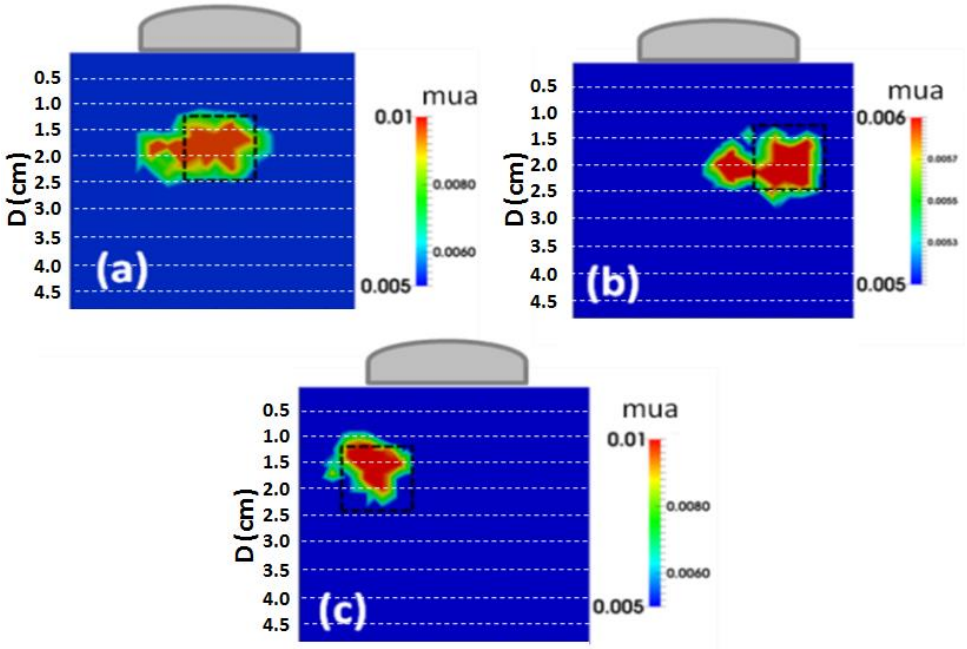

Figure C - 7 Panels (a) (b) and(c) shows the reconstructed images which depicts the translation of the inclusion (absorption contrast). Black dotted rectangles shows the target locations. White dotted lines marks depth D (cm).

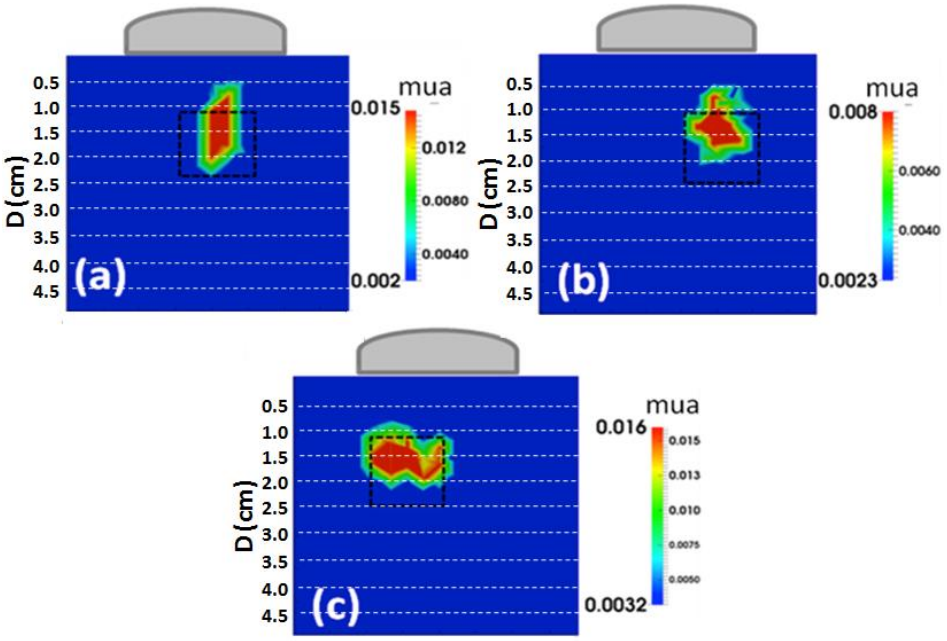

Figure C - 8 Panels (a) (b) and(c) shows the reconstructed images which depicts the translation of the inclusion (scattering contrast). Black dotted rectangles shows the target locations. White dotted lines marks depth D (cm).

Clear reconstructed images were also observed in scattering contrast experiments. Three panels in Fig. C - 8 provide reconstructed images of the embedded inclusion, where the probe assembly was placed at three different locations with respect to the scattering contrast inclusion. Figures C - 8a-c clearly show reconstructed image of the included scatterer. The depth location of the scatterer was also recovered accurately. The experiment results prove that the designed clip-on probe assembly is promising and useful to image prostate cancer in future.

C.1.4 Discussion

My long-term goal is to develop a combined NIR and TRUS probe, which can be used to detect and risk-stratify PCa prior to definitive therapy. With combined NIR and TRUS, the information from TRUS can be utilized as prior in DOT reconstruction. While the combined TRUS-NIR method improves accuracy of reconstructed DOT images, it highly relies on the ability of TRUS to locate the prostate cancer lesion. I solved the problem by creating hierarchical clustering method, which improves the image reconstruction in the absence of prior information about cancer in prostate cancer imaging using DOT. In this study, I further explored prostate cancer imaging using DOT by (1) measuring optical signatures of both benign versus

prostate cancer tissues from ex vivo human prostate specimens. (2) Designed and tested a clip-on TRUS-coupled DOT assembly that can be easily attached on and used with the existing clinical TRUS utility. Specifically, four types of prostate tissue were compared by their optical scattering and absorption coefficients measured by frequency domain optical system. Significant differences for scattering coefficient and absorption coefficient at 811 nm were observed between cancer and normal tissue on both prostate capsule and intra-prostate parenchyma regions. In addition, using the self-designed clip-on optical probe I successfully reconstructed an optical absorption inclusion and an optical scattering inclusion embedded in an optical tissue-mimicking phantom. In the next paragraph, morphological reasons behind increase of scattering and absorption in cancer tissues will be discussed.

Origin of scattering and absorption signals has been well understood and described in the literature of biomedical optics. Micrometer-sized organelles such as vesicles, mitochondria, and nucle. I am responsible for the origin of scattering signal. The increased scattering coefficient in cancerous tissues indicates larger cell sizes and higher densities (cancer cells are poorly differentiated). In my study, frequency domain data collected from ex vivo prostate specimen showed a consistent scattering and absorption differences between benign and cancerous human prostate tissue. Before explaining the specific reason for increase in scattering, the basic morphology of prostate tissues will be explained.

The normal prostate is composed of glands and fibromuscular stroma(see Fig C - 9(a) and (b)). The epithelial cells of the glands are organized as acini, which denotes a cluster of cells resembled berry that is secreted into the luminal space. Within the prostatic epithelium, there are at least three distinct cell types that can be distinguished by their morphological characteristics, functional significance and relevance for carcinogenesis[170]. The predominant cell type is the secretory luminal cell, which produces prostatic secretions. The second major epithelial cell type corresponds to the basal cells, which are found between the luminal cells and the underlying basement membrane, which form a continuous layer in the human prostate. Finally, the third prostatic epithelial cell type is the neuroendocrine cell, a minor population of uncertain embryological origin, which is believed to provide paracrine signals that support the growth of luminal cells. Fibromuscular stroma is situated on the opposite side of the basal cells. Stroma is composed of fibroblasts, smooth muscle cells, and an extracellular matrix rich in collagen fibers that intervenes between the secretory acini. The fibromuscular stroma between the glands accounts for about half of the volume of the prostate.

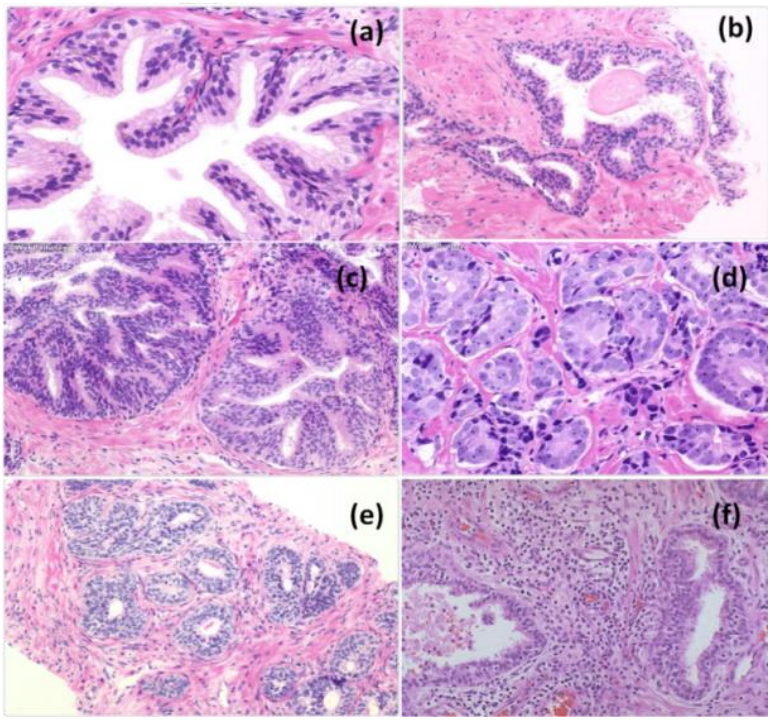

Figure C - 9Figure showing pathological slides obtained from biopsy samples. (a) Benign prostate glands (b) Benign prostate glands with stroma (c) PIN (d)Adenocarcinoma (e) Benign prostatic hyperplasia (f) Prostattitis.

Scattering changes in PCa tissues majorly comes from four conditions in the prostate: (1) Prostatic intraepithelial neoplasia (PIN), (2)Adenocarcinoma, (3) Benign prostatic hyperplasia and (d) Prostatitis. From histopathological studies of PCa tissues it is believed that PIN represent the primary precursor of human PCa[171]. A microscopic image of PIN depicts a collection of irregular luminal cells and they are confined to prostate acinus or duct (see Figure C - 9(c)). The architecture of the glands and ducts remains normal. In PCa, the abnormal cells spread beyond the boundaries of the acinus and form clusters without basal cells. Nuclei of PCa cells are enlarged round and have a single prominent nucleolus. In both PIN and PCa (adenocarcinoma) luminial cells will abnormally multiply and leads to increased scattering.

However, from the Fig. C - 9(e) and (f) BPH and Prostattit is also has increased number of cells than normal tissues. Benign enlargement of the prostate (BPH) is a hyperplastic growth of the epithelium and fibromuscular tissue of the transition zone and periurethral area (around urethra where ejaculatory ducts enter prostate)[172, 173]. Stromal changes are increased smooth muscle, lymphocytes and ducts (not associated with infectious process of Prostattitis in

most cases), reduced elastic tissue. Prostatitis is swelling and inflammation of the prostate gland. In Prostattitis the glands and stroma are filled with neutrophils explaining the presence of neutrophils on urine microscopic examination. Scattering also changes with BPH and Prostattitis and in principle it is difficult to separate scattering change is due to cancer, BPH, or Prostattitis. However, in both FD-NIRS and TRUS-NIR scenario the probing depth are approximately 1 to 2 centimeters. BPH occurs in transition zone that is in deeper location for NIR measurements to reach.

Table C -2Comparison of optical properties of prostate and various wavelengths in literature

Study	Year	wavelength	technology	Measurement	Cancer type	N	μ_a	μ_s'	μ_{eff}
Pantelides et al.	1990	633	steady state	Ex vivo	normal whole prostates	3	0.7±0.2	8.6±0.5	4.3±0.5
Whitehurst et al.	1994	633	steady state	In vivo	untreated BPH and PCa	11			3.6±0.2
Lee et al.	1995	665	steady state	In vivo	untreated BPH and PCa	11			3.9±0.5
Lee et al.	1995	630	steady state	In vivo	untreated BPH and PCa	11			3.2±0.5
Lee et al.	1999	660	steady state	In vivo	untreated PCa	7			3.5±0.7
Svensson et al.	2007	660	time-resolved	In vivo	untreated PCa	9	0.5±0.1	8.7±1.9	3.6±0.8
Weersink et al.	2005	762	steady state	In vivo	recurrent PCa	22	0.4±0.2	3.4±1.6	2.0±0.6
Zhu et al.	2005	732	steady state	In vivo	recurrent PCa	13	0.4±0.2	11.8±8.2	3.3±0.5
Svensson et al.	2007	786	time-resolved	In vivo	untreated PCa	9	0.4±0.1	7.1±1.6	2.9±0.7
This study	2014	811	Frequency domain	Ex vivo	untreated PCa	15		7.73±1.5	
Svensson et al.	2007	916	time-resolved	In vivo	untreated PCa	9	0.6±0.1	7.7±1.8	3.8±0.8
Essenpreis et al.	1992	1064	Integrating sphere	Ex vivo	normal whole prostates		1.5±0.2	6.4	

Absorption in NIR region is related to chromophore concentrations, such as HbO and HHb. Studies such as reference #43[174] indicates that there is immunohistolocal evidence that micro vessel density were associated increased long-term risk for death from PCa. However, the absorption of cancer tissue measured from ex vivo specimens is not expected to be representative. Because the blood concentration can be varied by external blood on prostate surface after prostatectomy.Also because no blood circulation exists in ex vivo prostate specimens and they are lack of natural vascular environment.

In addition, the scattering results from this work have been compared with precious literature (see Table C - 2). When comparing my results to previously published data, two important facts must be noted. First, differences such as patient groups (e.g., untreated or recurrent PCa) measurement type (ex vivo and in vivo) must be taken into account. Because the prostate physiology changes drastically upon radiation therapy. Ex vivo studies measures the prostate after isolation from blood circulation. So the measured absorption coefficient from ex vivo studies is not reliable as in vivo studies. Secondly, in some studies, CW instrumentation and global minimization techniques are utilized to calculate absorption and scattering. In addition, evolution-strategy (ES) algorithm and genetic algorithms (GAs) were applied to find global minima of objective functions. However, the noise in the measurements has significant impact on the calculated absorption and scattering values. Nevertheless, the comparison of scattering coefficients between my results with most of previous studies showed great consistency, indicating a noticeable optical signature of prostate cancerous tissue due to higher cell densities in glandular space and stroma of prostates. On the other hand, future in vivo measurements are needed for more convincing validation of absorption as a consistent signature for prostate cancer.

C.1.5 Conclusion

In this study, I measured the bulk optical properties of normal and PCa tissues from human ex vivo specimens. It is clear that the cancer tissues carry different optical signatures from the benign tissues. It is important to learn that a change in light scattering from benign to cancer tissues is more noticeable or prevailing than that in absorption. This change is attributed to higher cell densities in glandular space and stroma of prostate. Light absorption, on the other hand, remains to be further tested, as a valid optical signature of PCa for DOT, by performing in vivo human prostate measurements. In addition, I have designed and tested a clip-on optical probe compatible with existing clinical TRUS facility. Therefore, light scattering seems to be a

robust and promising biomarker for DOT to image if I wish to use DOT for high-grade PCa detection. In near future, I plan to image and characterize the prostate cancer of ex vivo prostate specimen with this newly developed probe.

Reference

[1] E. Mester, B. Szende, and P. Gartner, "[The effect of laser beams on the growth of hair in mice]," *Radiobiol Radiother (Berl),* vol. 9, pp. 621-6, 1968.

[2] J. T. Eells, M. T. Wong-Riley, J. VerHoeve, M. Henry, E. V. Buchman, M. P. Kane*, et al.*, "Mitochondrial signal transduction in accelerated wound and retinal healing by near-infrared light therapy," *Mitochondrion,* vol. 4, pp. 559-67, Sep 2004.

[3] M. T. Wong-Riley, H. L. Liang, J. T. Eells, B. Chance, M. M. Henry, E. Buchmann*, et al.*, "Photobiomodulation directly benefits primary neurons functionally inactivated by toxins: role of cytochrome c oxidase," *J Biol Chem,* vol. 280, pp. 4761-71, Feb 11 2005.

[4] R. T. Chow, M. I. Johnson, R. A. Lopes-Martins, and J. M. Bjordal, "Efficacy of low-level laser therapy in the management of neck pain: a systematic review and meta-analysis of randomised placebo or active-treatment controlled trials," *Lancet,* vol. 374, pp. 1897-908, Dec 5 2009.

[5] J. D. Kingsley, T. Demchak, and R. Mathis, "Low-level laser therapy as a treatment for chronic pain," *Front Physiol,* vol. 5, p. 306, 2014.

[6] Y. Lampl, J. A. Zivin, M. Fisher, R. Lew, L. Welin, B. Dahlof*, et al.*, "Infrared laser therapy for ischemic stroke: a new treatment strategy: results of the NeuroThera Effectiveness and Safety Trial-1 (NEST-1)," *Stroke,* vol. 38, pp. 1843-9, Jun 2007.

[7] J. A. Zivin, G. W. Albers, N. Bornstein, T. Chippendale, B. Dahlof, T. Devlin*, et al.*, "Effectiveness and safety of transcranial laser therapy for acute ischemic stroke," *Stroke,* vol. 40, pp. 1359-64, Apr 2009.

[8] M. A. Naeser, A. Saltmarche, M. H. Krengel, M. R. Hamblin, and J. A. Knight, "Improved cognitive function after transcranial, light-emitting diode treatments in chronic, traumatic brain injury: two case reports," *Photomed Laser Surg,* vol. 29, pp. 351-8, May 2011.

[9] M. A. Naeser, R. Zafonte, M. H. Krengel, P. I. Martin, J. Frazier, M. R. Hamblin*, et al.*, "Significant improvements in cognitive performance post-transcranial, red/near-infrared light-emitting diode treatments in chronic, mild traumatic brain injury: open-protocol study," *J Neurotrauma,* vol. 31, pp. 1008-17, Jun 1 2014.

[10] F. Schiffer, A. L. Johnston, C. Ravichandran, A. Polcari, M. H. Teicher, R. H. Webb*, et al.*, "Psychological benefits 2 and 4 weeks after a single treatment with near infrared light to the forehead: a pilot study of 10 patients with major depression and anxiety," *Behav Brain Funct,* vol. 5, p. 46, 2009.

[11] S. G. Disner, C. G. Beevers, and F. Gonzalez-Lima, "Transcranial Laser Stimulation as Neuroenhancement for Attention Bias Modification in Adults with Elevated Depression Symptoms," *Brain Stimul,* May 24 2016.

[12] D. Pastore, M. Greco, and S. Passarella, "Specific helium-neon laser sensitivity of the purified cytochrome c oxidase," *Int J Radiat Biol,* vol. 76, pp. 863-70, Jun 2000.

[13] X. Wang, F. Tian, S. S. Soni, F. Gonzalez-Lima, and H. Liu, "Interplay between up-regulation of cytochrome-c-oxidase and hemoglobin oxygenation induced by near-infrared laser," *Sci Rep,* vol. 6, p. 30540, 2016.

[14] X. Wang, F. Tian, D. D. Reddy, S. S. Nalawade, D. W. Barrett, F. Gonzalez-Lima*, et al.*, "Up-regulation of cerebral cytochrome-c-oxidase and hemodynamics by transcranial infrared laser stimulation: A broadband near-infrared spectroscopy study," *J Cereb Blood Flow Metab,* p. 271678X17691783, Jan 01 2017.

[15] J. C. Rojas and F. Gonzalez-Lima, "Neurological and psychological applications of transcranial lasers and LEDs," *Biochem Pharmacol,* vol. 86, pp. 447-57, Aug 15 2013.

[16] I. Tachtsidis, M. Tisdall, T. S. Leung, C. E. Cooper, D. T. Delpy, M. Smith*, et al.*, "Investigation of in vivo measurement of cerebral cytochrome-c-oxidase redox changes using near-infrared spectroscopy in patients with orthostatic hypotension," *Physiol Meas,* vol. 28, pp. 199-211, Feb 2007.

[17] D. W. Barrett and F. Gonzalez-Lima, "Transcranial infrared laser stimulation produces beneficial cognitive and emotional effects in humans," *Neuroscience,* vol. 230, pp. 13-23, Jan 29 2013.

[18] N. J. Blanco, W. T. Maddox, and F. Gonzalez-Lima, "Improving executive function using transcranial infrared laser stimulation," *J Neuropsychol,* May 28 2015.

[19] J. Hwang, D. M. Castelli, and F. Gonzalez-Lima, "Cognitive enhancement by transcranial laser stimulation and acute aerobic exercise," *Lasers Med Sci,* May 25 2016.

[20] F. Gonzalez-Lima and A. Auchter, "Protection against neurodegeneration with low-dose methylene blue and near-infrared light," *Front Cell Neurosci,* vol. 9, p. 179, 2015.

[21] F. Gonzalez-Lima, B. R. Barksdale, and J. C. Rojas, "Mitochondrial respiration as a target for neuroprotection and cognitive enhancement," *Biochem Pharmacol,* vol. 88, pp. 584-93, Apr 15 2014.

[22] F. Gonzalez-Lima and D. W. Barrett, "Augmentation of cognitive brain functions with transcranial lasers," *Front Syst Neurosci,* vol. 8, p. 36, 2014.

[23] J. C. Rojas, A. K. Bruchey, and F. Gonzalez-Lima, "Low-level light therapy improves cortical metabolic capacity and memory retention," *J Alzheimers Dis,* vol. 32, pp. 741-52, 2012.

[24] V. Quaresima, S. Bisconti, and M. Ferrari, "A brief review on the use of functional near-infrared spectroscopy (fNIRS) for language imaging studies in human newborns and adults," *Brain Lang,* vol. 121, pp. 79-89, May 2012.

[25] F. Scholkmann, S. Kleiser, A. J. Metz, R. Zimmermann, J. Mata Pavia, U. Wolf*, et al.*, "A review on continuous wave functional near-infrared spectroscopy and imaging instrumentation and methodology," *Neuroimage,* vol. 85 Pt 1, pp. 6-27, Jan 15 2014.

[26] A. E. Cerussi, V. W. Tanamai, D. Hsiang, J. Butler, R. S. Mehta, and B. J. Tromberg, "Diffuse optical spectroscopic imaging correlates with final pathological response in

breast cancer neoadjuvant chemotherapy," *Philos Trans A Math Phys Eng Sci,* vol. 369, pp. 4512-30, Nov 28 2011.

[27] S. Jiang, B. W. Pogue, K. E. Michaelsen, M. Jermyn, M. A. Mastanduno, T. E. Frazee*, et al.*, "Pilot study assessment of dynamic vascular changes in breast cancer with near-infrared tomography from prospectively targeted manipulations of inspired end-tidal partial pressure of oxygen and carbon dioxide," *J Biomed Opt,* vol. 18, p. 76011, Jul 2013.

[28] T. Durduran, R. Choe, W. B. Baker, and A. G. Yodh, "Diffuse Optics for Tissue Monitoring and Tomography," *Rep Prog Phys,* vol. 73, Jul 2010.

[29] Z. Jiang, D. Piao, G. Xu, J. W. Ritchey, G. R. Holyoak, K. E. Bartels*, et al.*, "Trans-rectal ultrasound-coupled near-infrared optical tomography of the prostate, part II: experimental demonstration," *Opt Express,* vol. 16, pp. 17505-20, Oct 27 2008.

[30] Z. Jiang, D. Piao, G. R. Holyoak, J. W. Ritchey, K. E. Bartels, G. Slobodov*, et al.*, "Trans-rectal ultrasound-coupled spectral optical tomography of total hemoglobin concentration enhances assessment of the laterality and progression of a transmissible venereal tumor in canine prostate," *Urology,* vol. 77, pp. 237-42, Jan 2011.

[31] D. A. Boas, C. E. Elwell, M. Ferrari, and G. Taga, "Twenty years of functional near-infrared spectroscopy: introduction for the special issue," *Neuroimage,* vol. 85 Pt 1, pp. 1-5, Jan 15 2014.

[32] F. Tian, S. N. Hase, F. Gonzalez-Lima, and H. Liu, "Transcranial laser stimulation improves human cerebral oxygenation," *Lasers Surg Med,* Jan 12 2016.

[33] M. a. Q. Ferrari, V., "Near infrared brain and muscle oximetry: from the discovery to current applications," *Journal of Near Infrared Spectroscopy,* vol. 20, pp. 1-14, 2012.

[34] S. J. Matcher, C. E. Elwell, C. E. Cooper, M. Cope, and D. T. Delpy, "Performance comparison of several published tissue near-infrared spectroscopy algorithms," *Anal Biochem,* vol. 227, pp. 54-68, May 1 1995.

[35] R. E. Gagnon, F. A. Gagnon, and A. J. Macnab, "Comparison of 13 published cytochrome c oxidase near-infrared spectroscopy algorithms," *Eur J Appl Physiol Occup Physiol,* vol. 74, pp. 487-95, 1996.

[36] K. Uludag, M. Kohl, J. Steinbrink, H. Obrig, and A. Villringer, "Cross talk in the Lambert-Beer calculation for near-infrared wavelengths estimated by Monte Carlo simulations," *J Biomed Opt,* vol. 7, pp. 51-9, Jan 2002.

[37] K. Uludag, J. Steinbrink, M. Kohl-Bareis, R. Wenzel, A. Villringer, and H. Obrig, "Cytochrome-c-oxidase redox changes during visual stimulation measured by near-infrared spectroscopy cannot be explained by a mere cross talk artefact," *Neuroimage,* vol. 22, pp. 109-19, May 2004.

[38] I. Tachtsidis, P. H. Koh, C. Stubbs, and C. E. Elwell, "Functional optical topography analysis using statistical parametric mapping (SPM) methodology with and without physiological confounds," *Adv Exp Med Biol,* vol. 662, pp. 237-43, 2010.

[39] C. Kolyva, I. Tachtsidis, A. Ghosh, T. Moroz, C. E. Cooper, M. Smith*, et al.*, "Systematic investigation of changes in oxidized cerebral cytochrome c oxidase concentration during frontal lobe activation in healthy adults," *Biomed Opt Express,* vol. 3, pp. 2550-66, Oct 1 2012.

[40] C. Kolyva, A. Ghosh, I. Tachtsidis, D. Highton, C. E. Cooper, M. Smith*, et al.*, "Cytochrome c oxidase response to changes in cerebral oxygen delivery in the adult brain shows higher brain-specificity than haemoglobin," *Neuroimage,* vol. 85 Pt 1, pp. 234-44, Jan 15 2014.

[41] G. Bale, S. Mitra, J. Meek, N. Robertson, and I. Tachtsidis, "A new broadband near-infrared spectroscopy system for in-vivo measurements of cerebral cytochrome-c-oxidase changes in neonatal brain injury," *Biomed Opt Express,* vol. 5, pp. 3450-66, Oct 1 2014.

[42] A. Bainbridge, I. Tachtsidis, S. D. Faulkner, D. Price, T. Zhu, E. Baer*, et al.*, "Brain mitochondrial oxidative metabolism during and after cerebral hypoxia-ischemia studied by simultaneous phosphorus magnetic-resonance and broadband near-infrared spectroscopy," *Neuroimage,* vol. 102 Pt 1, pp. 173-83, Nov 15 2014.

[43] L. Kocsis, P. Herman, and A. Eke, "The modified Beer-Lambert law revisited," *Phys Med Biol,* vol. 51, pp. N91-8, Mar 7 2006.

[44] S. Fantini, D. Hueber, M. A. Franceschini, E. Gratton, W. Rosenfeld, P. G. Stubblefield*, et al.*, "Non-invasive optical monitoring of the newborn piglet brain using continuous-wave and frequency-domain spectroscopy," *Phys Med Biol,* vol. 44, pp. 1543-63, Jun 1999.

[45] T. I. Karu, L. V. Pyatibrat, S. F. Kolyakov, and N. I. Afanasyeva, "Absorption measurements of a cell monolayer relevant to phototherapy: reduction of cytochrome c oxidase under near IR radiation," *J Photochem Photobiol B,* vol. 81, pp. 98-106, Nov 1 2005.

[46] S. L. Jacques, "Optical properties of biological tissues: a review," *Phys Med Biol,* vol. 58, pp. R37-61, Jun 7 2013.

[47] I. Tachtsidis, L. Gao, T. S. Leung, M. Kohl-Bareis, C. E. Cooper, and C. E. Elwell, "A hybrid multi-distance phase and broadband spatially resolved spectrometer and algorithm for resolving absolute concentrations of chromophores in the near-infrared light spectrum," *Adv Exp Med Biol,* vol. 662, pp. 169-75, 2010.

[48] *CRC Handbook of Chemistry and Physics (92nd ed.).* CRC Press. p. 10.233., 2011.

[49] M. R. Hamblin and T. N. Demidova, "Mechanisms for Low Light Therapy," *Proceedings of SPIE,* vol. 6140, pp. 14001-14001, 2006.

[50] M. T. T. Wong-Riley, F. Nie, R. F. Hevner, and S. Liu, "Brain cytochrome oxidase: functional significance and bigenomic regulation in the CNS," in *Cytochrome Oxidase in*

Neuronal Metabolism and Alzheimer's Disease, F. Gonzalez-Lima, Ed., ed New York: Plenum Press, 1998, pp. 1-53.

[51] P. Cassano, S. R. Petrie, M. R. Hamblin, T. A. Henderson, and D. V. Iosifescu, "Review of transcranial photobiomodulation for major depressive disorder: targeting brain metabolism, inflammation, oxidative stress, and neurogenesis," *Neurophotonics,* vol. 3, p. 031404, Jul 2016.

[52] L. D. Morries, P. Cassano, and T. A. Henderson, "Treatments for traumatic brain injury with emphasis on transcranial near-infrared laser phototherapy," *Neuropsychiatr Dis Treat,* vol. 11, pp. 2159-75, 2015.

[53] S. G. Disner, C. G. Beevers, and F. Gonzalez-Lima, "Transcranial Laser Stimulation as Neuroenhancement for Attention Bias Modification in Adults with Elevated Depression Symptoms," *Brain Stimul,* vol. 9, pp. 780-7, Sep-Oct 2016.

[54] J. Hwang, D. M. Castelli, and F. Gonzalez-Lima, "Cognitive enhancement by transcranial laser stimulation and acute aerobic exercise," *Lasers Med Sci,* vol. 31, pp. 1151-60, Aug 2016.

[55] F. Tian, S. N. Hase, F. Gonzalez-Lima, and H. Liu, "Transcranial laser stimulation improves human cerebral oxygenation," *Lasers Surg Med,* vol. 48, pp. 343-9, Apr 2016.

[56] M. Tsuji, A. duPlessis, G. Taylor, R. Crocker, and J. J. Volpe, "Near infrared spectroscopy detects cerebral ischemia during hypotension in piglets," *Pediatr Res,* vol. 44, pp. 591-5, Oct 1998.

[57] M. Tsuji, J. P. Saul, A. du Plessis, E. Eichenwald, J. Sobh, R. Crocker*, et al.*, "Cerebral intravascular oxygenation correlates with mean arterial pressure in critically ill premature infants," *Pediatrics,* vol. 106, pp. 625-32, Oct 2000.

[58] J. S. Soul, P. E. Hammer, M. Tsuji, J. P. Saul, H. Bassan, C. Limperopoulos*, et al.*, "Fluctuating pressure-passivity is common in the cerebral circulation of sick premature infants," *Pediatr Res,* vol. 61, pp. 467-73, Apr 2007.

[59] T. J. Huppert, R. D. Hoge, S. G. Diamond, M. A. Franceschini, and D. A. Boas, "A temporal comparison of BOLD, ASL, and NIRS hemodynamic responses to motor stimuli in adult humans," *Neuroimage,* vol. 29, pp. 368-82, Jan 15 2006.

[60] F. R. Ihsan, "Low-level laser therapy accelerates collateral circulation and enhances microcirculation," *Photomed Laser Surg,* vol. 23, pp. 289-94, Jun 2005.

[61] T. I. Karu, "Multiple roles of cytochrome c oxidase in mammalian cells under action of red and IR-A radiation," *IUBMB Life,* vol. 62, pp. 607-10, Aug 2010.

[62] M. Wikstrom, K. Krab, and M. Saraste, "Proton-translocating cytochrome complexes," *Annu Rev Biochem,* vol. 50, pp. 623-55, 1981.

[63] Y. Hatefi, "The mitochondrial electron transport and oxidative phosphorylation system," *Annu Rev Biochem,* vol. 54, pp. 1015-69, 1985.

[64] M. T. Gladwin and S. Shiva, "The ligand binding battle at cytochrome c oxidase: how NO regulates oxygen gradients in tissue," *Circ Res,* vol. 104, pp. 1136-8, May 22 2009.

[65] F. Gonzalez-Lima, J. Valla, and A. Cada, "Brain cytochrome oxidase activity and how it relates to the pathophysiology of memory and Alzheimer's disease," in *Free Radicals, Oxidative Stress and Antioxidants: Pathological and Physiological Significance*. vol. 296, T. Ozben, Ed., ed New York: Plenum Press, 1998, pp. 205-227.

[66] R. O. Poyton and K. A. Ball, "Therapeutic photobiomodulation: nitric oxide and a novel function of mitochondrial cytochrome c oxidase," *Discov Med,* vol. 11, pp. 154-9, Feb 2011.

[67] L. F. H. De Freitas, M.R.,, "Proposed Mechanisms of Photobiomodulation or Low-Level Light Therapy," *IEEE Journal of Selected Topics in Quantum Electronics,* vol. 22 p. 7000417, 2016.

[68] S. A. Huettel, A. W. Song, and G. McCarthy, *Functional Magnetic Resonance Imaging*, 2nd ed. Sunderland, Massachusetts, USA: Sinauer Associates, Inc. Publishers, 2009.

[69] D. Malonek and A. Grinvald, "Interactions between electrical activity and cortical microcirculation revealed by imaging spectroscopy: implications for functional brain mapping," *Science,* vol. 272, pp. 551-4, Apr 26 1996.

[70] M. Ferrari and V. Quaresima, "A brief review on the history of human functional near-infrared spectroscopy (fNIRS) development and fields of application," *Neuroimage,* vol. 63, pp. 921-35, Nov 1 2012.

[71] Y. Wang, Y. Y. Huang, Y. Wang, P. Lyu, and M. R. Hamblin, "Photobiomodulation of human adipose-derived stem cells using 810nm and 980nm lasers operates via different mechanisms of action," *Biochim Biophys Acta,* Oct 15 2016.

[72] N. J. Blanco, C. L. Saucedo, and F. Gonzalez-Lima, "Transcranial infrared laser stimulation improves rule-based, but not information-integration, category learning in humans," *Neurobiol Learn Mem,* vol. 139, pp. 69-75, Mar 2017.

[73] M. R. Hamblin, "Shining light on the head: Photobiomodulation for brain disorders," *BBA Clin,* vol. 6, pp. 113-124, Dec 2016.

[74] R. Reed and D. C. Ripple, "The effect of Interrogating Temperature profile in the Seebeck Inhomogeneity Method of test (SIMOT)," in *AIP Conference Proceedings*, 2003, pp. 491-496.

[75] C. Chen, V. C. Kavuri, X. Wang, R. Li, H. Liu, and J. Huang, "Multi-frequency diffuse optical tomography for cancer detection," in *Biomedical Imaging (ISBI), 2015 IEEE 12th International Symposium on*, 2015, pp. 67-70.

[76] B. Montcel, R. Chabrier, and P. Poulet, "Time-resolved absorption and hemoglobin concentration difference maps: a method to retrieve depth-related information on cerebral hemodynamics," *Opt Express,* vol. 14, pp. 12271-87, Dec 11 2006.

[77] K. M. Brady, J. K. Lee, K. K. Kibler, P. Smielewski, M. Czosnyka, R. B. Easley*, et al.*, "Continuous time-domain analysis of cerebrovascular autoregulation using near-infrared spectroscopy," *Stroke,* vol. 38, pp. 2818-25, Oct 2007.

[78] A. H. Lay, X. Wang, M. S. Morgan, P. Kapur, H. Liu, C. G. Roehrborn*, et al.*, "Detecting positive surgical margins: utilisation of light-reflectance spectroscopy on ex vivo prostate specimens," *BJU Int,* vol. 118, pp. 885-889, Dec 2016.

[79] C. E. Cooper and R. Springett, "Measurement of cytochrome oxidase and mitochondrial energetics by near-infrared spectroscopy," *Philos Trans R Soc Lond B Biol Sci,* vol. 352, pp. 669-76, Jun 29 1997.

[80] B. Hallacoglu, A. Sassaroli, M. Wysocki, E. Guerrero-Berroa, M. Schnaider Beeri, V. Haroutunian*, et al.*, "Absolute measurement of cerebral optical coefficients, hemoglobin concentration and oxygen saturation in old and young adults with near-infrared spectroscopy," *J Biomed Opt,* vol. 17, pp. 081406-1, Aug 2012.

[81] H. Liu, "Unified analysis of the sensitivities of reflectance and path length to scattering variations in a diffusive medium," *Appl Opt,* vol. 40, pp. 1742-6, Apr 01 2001.

[82] H. Z. Yeganeh, V. Toronov, J. T. Elliott, M. Diop, T. Y. Lee, and K. St Lawrence, "Broadband continuous-wave technique to measure baseline values and changes in the tissue chromophore concentrations," *Biomed Opt Express,* vol. 3, pp. 2761-70, Nov 01 2012.

[83] S. W. Perry, J. P. Norman, J. Barbieri, E. B. Brown, and H. A. Gelbard, "Mitochondrial membrane potential probes and the proton gradient: a practical usage guide," *Biotechniques,* vol. 50, pp. 98-115, Feb 2011.

[84] A. Ghosh, I. Tachtsidis, C. Kolyva, C. E. Cooper, M. Smith, and C. E. Elwell, "Use of a hybrid optical spectrometer for the measurement of changes in oxidized cytochrome c oxidase concentration and tissue scattering during functional activation," *Adv Exp Med Biol,* vol. 737, pp. 119-24, 2012.

[85] I. Tachtsidis, M. M. Tisdall, C. Pritchard, T. S. Leung, A. Ghosh, C. E. Elwell*, et al.*, "Analysis of the changes in the oxidation of brain tissue cytochrome-c-oxidase in

traumatic brain injury patients during hypercapnoea: a broadband NIRS study," *Adv Exp Med Biol,* vol. 701, pp. 9-14, 2011.

[86] S. J. Matcher, M. Cope, and D. T. Delpy, "Use of the water absorption spectrum to quantify tissue chromophore concentration changes in near-infrared spectroscopy," *Phys Med Biol,* vol. 39, pp. 177-96, Jan 1994.

[87] T. I. Karu and N. I. Afanas'eva, "[Cytochrome c oxidase as the primary photoacceptor upon laser exposure of cultured cells to visible and near IR-range light]," *Dokl Akad Nauk,* vol. 342, pp. 693-5, Jun 1995.

[88] T. J. Farrell, M. S. Patterson, and B. Wilson, "A diffusion theory model of spatially resolved, steady-state diffuse reflectance for the noninvasive determination of tissue optical properties in vivo," *Med Phys,* vol. 19, pp. 879-88, Jul-Aug 1992.

[89] H. Harrison, J. Herbert, and A. P. Waggoner, "Mie-theory computations of lidar and nephelometric scattering parameters for power law aerosols," *Appl Opt,* vol. 11, pp. 2880-5, Dec 01 1972.

[90] H. J. van Staveren, C. J. Moes, J. van Marie, S. A. Prahl, and M. J. van Gemert, "Light scattering in Intralipid-10% in the wavelength range of 400-1100 nm," *Appl Opt,* vol. 30, pp. 4507-14, Nov 1 1991.

[91] V. Sharma, E. O. Olweny, P. Kapur, J. A. Cadeddu, C. G. Roehrborn, and H. Liu, "Prostate cancer detection using combined auto-fluorescence and light reflectance spectroscopy: ex vivo study of human prostates," *Biomed Opt Express,* vol. 5, pp. 1512-29, May 01 2014.

[92] M. Dorigo, M. Birattari, and T. Stutzle, "Ant colony optimization," *IEEE computational intelligence magazine,* vol. 1, pp. 28-39, 2006.

[93] M. Dorigo and T. Stützle, "Ant colony optimization: overview and recent advances," in *Handbook of metaheuristics*, ed: Springer, 2010, pp. 227-263.

[94] M. S. Morgan, A. H. Lay, X. Wang, P. Kapur, A. Ozayar, M. Sayah*, et al.*, "Light Reflectance Spectroscopy to Detect Positive Surgical Margins on Prostate Cancer Specimens," *J Urol,* vol. 195, pp. 479-83, Feb 2016.

[95] G. Trytten and W. Flowers, "Optical characteristics of a proposed reflectance standard," *Appl Opt,* vol. 5, pp. 1895-7, Dec 01 1966.

[96] S. Soni, X. Wang, H. Liu, and F. Tian, "Diffuse correlation spectroscopy (DCS) study of blood flow changes during low level laser therapy (LLLT): a preliminary report," 2017, pp. 1004806-1004806-5.

[97] J. O. Holloszy, "Biochemical adaptations in muscle. Effects of exercise on mitochondrial oxygen uptake and respiratory enzyme activity in skeletal muscle," *J Biol Chem,* vol. 242, pp. 2278-82, May 10 1967.

[98] D. A. Hood, G. Uguccioni, A. Vainshtein, and D. D'Souza, "Mechanisms of exercise-induced mitochondrial biogenesis in skeletal muscle: implications for health and disease," *Compr Physiol,* vol. 1, pp. 1119-34, Jul 2011.

[99] L. R. Silveira, J. Fiamoncini, S. M. Hirabara, J. Procopio, T. D. Cambiaghi, C. H. Pinheiro*, et al.*, "Updating the effects of fatty acids on skeletal muscle," *J Cell Physiol,* vol. 217, pp. 1-12, Oct 2008.

[100] J. R. Knowles, "Enzyme-catalyzed phosphoryl transfer reactions," *Annu Rev Biochem,* vol. 49, pp. 877-919, 1980.

[101] J. P. Castillo, H. Rui, D. Basilio, A. Das, B. Roux, R. Latorre*, et al.*, "Mechanism of potassium ion uptake by the Na(+)/K(+)-ATPase," *Nat Commun,* vol. 6, p. 7622, Jul 24 2015.

[102] B. S. Khakh and R. A. North, "Neuromodulation by extracellular ATP and P2X receptors in the CNS," *Neuron,* vol. 76, pp. 51-69, Oct 04 2012.

[103] EEG and Clinical Neuroscience Society., "Clinical EEG and neuroscience : official journal of the EEG and Clinical Neuroscience Society (ENCS)," ed. Wheaton, IL: EEG and Clinical Neuroscience Society, 2004, p. volumes.

[104] M. Bortoletto, D. Veniero, G. Thut, and C. Miniussi, "The contribution of TMS-EEG coregistration in the exploration of the human cortical connectome," *Neurosci Biobehav Rev,* vol. 49, pp. 114-24, Feb 2015.

[105] P. Schestatsky, L. Morales-Quezada, and F. Fregni, "Simultaneous EEG monitoring during transcranial direct current stimulation," *J Vis Exp,* Jun 17 2013.

[106] M. Hallett, "Transcranial magnetic stimulation: a primer," *Neuron,* vol. 55, pp. 187-99, Jul 19 2007.

[107] S. Palva and J. M. Palva, "New vistas for alpha-frequency band oscillations," *Trends Neurosci,* vol. 30, pp. 150-8, Apr 2007.

[108] V. Jurcak, D. Tsuzuki, and I. Dan, "10/20, 10/10, and 10/5 systems revisited: their validity as relative head-surface-based positioning systems," *Neuroimage,* vol. 34, pp. 1600-11, Feb 15 2007.

[109] R. D. Pascual-Marqui, D. Lehmann, M. Koukkou, K. Kochi, P. Anderer, B. Saletu*, et al.*, "Assessing interactions in the brain with exact low-resolution electromagnetic tomography," *Philos Trans A Math Phys Eng Sci,* vol. 369, pp. 3768-84, Oct 13 2011.

[110] M. Lobier, F. Siebenhuhner, S. Palva, and J. M. Palva, "Phase transfer entropy: a novel phase-based measure for directed connectivity in networks coupled by oscillatory interactions," *Neuroimage,* vol. 85 Pt 2, pp. 853-72, Jan 15 2014.

[111] M. Wibral, B. Rahm, M. Rieder, M. Lindner, R. Vicente, and J. Kaiser, "Transfer entropy in magnetoencephalographic data: quantifying information flow in cortical and cerebellar networks," *Prog Biophys Mol Biol,* vol. 105, pp. 80-97, Mar 2011.

[112] A. Hillebrand, P. Tewarie, E. van Dellen, M. Yu, E. W. Carbo, L. Douw*, et al.*, "Direction of information flow in large-scale resting-state networks is frequency-dependent," *Proc Natl Acad Sci U S A,* vol. 113, pp. 3867-72, Apr 05 2016.

[113] M. Staniek and K. Lehnertz, "Symbolic transfer entropy: inferring directionality in biosignals," *Biomed Tech (Berl),* vol. 54, pp. 323-8, Dec 2009.

[114] M. Kaminski and K. J. Blinowska, "Directed Transfer Function is not influenced by volume conduction-inexpedient pre-processing should be avoided," *Front Comput Neurosci,* vol. 8, p. 61, 2014.

[115] A. Hyvarinen and E. Oja, "Simple neuron models for independent component analysis," *Int J Neural Syst,* vol. 7, pp. 671-87, Dec 1996.

[116] T. P. Jung, S. Makeig, C. Humphries, T. W. Lee, M. J. McKeown, V. Iragui*, et al.*, "Removing electroencephalographic artifacts by blind source separation," *Psychophysiology,* vol. 37, pp. 163-78, Mar 2000.

[117] D. Lehmann and W. Skrandies, "Reference-free identification of components of checkerboard-evoked multichannel potential fields," *Electroencephalogr Clin Neurophysiol,* vol. 48, pp. 609-21, Jun 1980.

[118] A. Wieraszko, "Extracellular ATP as a neurotransmitter: its role in synaptic plasticity in the hippocampus," *Acta Neurobiol Exp (Wars),* vol. 56, pp. 637-48, 1996.

[119] T. V. Bliss and G. L. Collingridge, "A synaptic model of memory: long-term potentiation in the hippocampus," *Nature,* vol. 361, pp. 31-9, Jan 07 1993.

[120] S. F. Cooke and T. V. Bliss, "Plasticity in the human central nervous system," *Brain,* vol. 129, pp. 1659-73, Jul 2006.

[121] H. Manev, M. Favaron, A. Guidotti, and E. Costa, "Delayed increase of Ca2+ influx elicited by glutamate: role in neuronal death," *Mol Pharmacol,* vol. 36, pp. 106-12, Jul 1989.

[122] M. K. Jaiswal, W. D. Zech, M. Goos, C. Leutbecher, A. Ferri, A. Zippelius*, et al.*, "Impairment of mitochondrial calcium handling in a mtSOD1 cell culture model of motoneuron disease," *BMC Neurosci,* vol. 10, p. 64, Jun 22 2009.

[123] R. L. Buckner, J. R. Andrews-Hanna, and D. L. Schacter, "The brain's default network: anatomy, function, and relevance to disease," *Ann N Y Acad Sci,* vol. 1124, pp. 1-38, Mar 2008.

[124] M. D. Greicius, G. Srivastava, A. L. Reiss, and V. Menon, "Default-mode network activity distinguishes Alzheimer's disease from healthy aging: evidence from functional MRI," *Proc Natl Acad Sci U S A,* vol. 101, pp. 4637-42, Mar 30 2004.

[125] K. Mevel, G. Chetelat, F. Eustache, and B. Desgranges, "The default mode network in healthy aging and Alzheimer's disease," *Int J Alzheimers Dis,* vol. 2011, p. 535816, 2011.

[126] M. T. Huber, J. Bartling, D. Pachur, S. Woikowsky-Biedau, and S. Lautenbacher, "EEG responses to tonic heat pain," *Exp Brain Res,* vol. 173, pp. 14-24, Aug 2006.

[127] Y. Wang, Y. Y. Huang, Y. Wang, P. Lyu, and M. R. Hamblin, "Photobiomodulation of human adipose-derived stem cells using 810nm and 980nm lasers operates via different mechanisms of action," *Biochim Biophys Acta,* vol. 1861, pp. 441-449, Feb 2017.

[128] J. Vriens, B. Nilius, and T. Voets, "Peripheral thermosensation in mammals," *Nat Rev Neurosci,* vol. 15, pp. 573-89, Sep 2014.

[129] J. Zheng, "Molecular mechanism of TRP channels," *Compr Physiol,* vol. 3, pp. 221-42, Jan 2013.

[130] S. S. Manna and S. N. Umathe, "Transient receptor potential vanilloid 1 channels modulate the anxiolytic effect of diazepam," *Brain Res,* vol. 1425, pp. 75-82, Nov 24 2011.

[131] P. Anninos, A. Chatzimichael, A. Adamopoulos, A. Kotini, and N. Tsagas, "A combined study of MEG and pico-Tesla TMS on children with autism disorder," *J Integr Neurosci,* pp. 1-17, Nov 23 2016.

[132] G. Hartwigsen, A. Weigel, P. Schuschan, H. R. Siebner, D. Weise, J. Classen*, et al.*, "Dissociating Parieto-Frontal Networks for Phonological and Semantic Word Decisions: A Condition-and-Perturb TMS Study," *Cereb Cortex,* vol. 26, pp. 2590-601, Jun 2016.

[133] E. R. Kandel, *Principles of neural science*, 5th ed. New York: McGraw-Hill, 2013.

[134] Y. Benjamini, D. Drai, G. Elmer, N. Kafkafi, and I. Golani, "Controlling the false discovery rate in behavior genetics research," *Behav Brain Res,* vol. 125, pp. 279-84, Nov 01 2001.

[135] R. A. Armstrong, "When to use the Bonferroni correction," *Ophthalmic Physiol Opt,* vol. 34, pp. 502-8, Sep 2014.

[136] J. Ranstam, "Multiple P-values and Bonferroni correction," *Osteoarthritis Cartilage,* vol. 24, pp. 763-4, May 2016.

[137] A. Jemal, M. J. Thun, L. A. Ries, H. L. Howe, H. K. Weir, M. M. Center*, et al.*, "Annual report to the nation on the status of cancer, 1975–2005, featuring trends in lung cancer, tobacco use, and tobacco control," *Journal of the National Cancer Institute,* vol. 100, pp. 1672-1694, 2008.

[138] W. A. Sakr, D. J. Grignon, J. D. Crissman, L. K. Heilbrun, B. J. Cassin, J. J. Pontes*, et al.*, "High grade prostatic intraepithelial neoplasia (HGPIN) and prostatic adenocarcinoma between the ages of 20-69: an autopsy study of 249 cases," *In Vivo,* vol. 8, pp. 439-43, May-Jun 1994.

[139] A. L. Potosky, W. W. Davis, R. M. Hoffman, J. L. Stanford, R. A. Stephenson, D. F. Penson*, et al.*, "Five-year outcomes after prostatectomy or radiotherapy for prostate cancer: the prostate cancer outcomes study," *J Natl Cancer Inst,* vol. 96, pp. 1358-67, Sep 15 2004.

[140] D. V. Makarov, B. J. Trock, E. B. Humphreys, L. A. Mangold, P. C. Walsh, J. I. Epstein*, et al.*, "Updated nomogram to predict pathologic stage of prostate cancer given prostate-specific antigen level, clinical stage, and biopsy Gleason score (Partin tables) based on cases from 2000 to 2005," *Urology,* vol. 69, pp. 1095-101, Jun 2007.

[141] A. W. Partin, L. A. Mangold, D. M. Lamm, P. C. Walsh, J. I. Epstein, and J. D. Pearson, "Contemporary update of prostate cancer staging nomograms (Partin Tables) for the new millennium," *Urology,* vol. 58, pp. 843-8, Dec 2001.

[142] Y. Huang, S. Isharwal, A. Haese, F. K. Chun, D. V. Makarov, Z. Feng*, et al.*, "Prediction of patient-specific risk and percentile cohort risk of pathological stage outcome using continuous prostate-specific antigen measurement, clinical stage and biopsy Gleason score," *BJU Int,* vol. 107, pp. 1562-9, May 2011.

[143] O. Smaletz, H. I. Scher, E. J. Small, D. A. Verbel, A. McMillan, K. Regan*, et al.*, "Nomogram for overall survival of patients with progressive metastatic prostate cancer after castration," *J Clin Oncol,* vol. 20, pp. 3972-82, Oct 01 2002.

[144] M. R. Cooperberg, D. J. Pasta, E. P. Elkin, M. S. Litwin, D. M. Latini, J. Du Chane*, et al.*, "The University of California, San Francisco Cancer of the Prostate Risk Assessment score: a straightforward and reliable preoperative predictor of disease recurrence after radical prostatectomy," *J Urol,* vol. 173, pp. 1938-42, Jun 2005.

[145] J. B. Eifler, Z. Feng, B. M. Lin, M. T. Partin, E. B. Humphreys, M. Han*, et al.*, "An updated prostate cancer staging nomogram (Partin tables) based on cases from 2006 to 2011," *BJU Int,* vol. 111, pp. 22-9, Jan 2013.

[146] M. L. Blute, E. J. Bergstralh, A. W. Partin, P. C. Walsh, M. W. Kattan, P. T. Scardino*, et al.*, "Validation of Partin tables for predicting pathological stage of clinically localized prostate cancer," *J Urol,* vol. 164, pp. 1591-5, Nov 2000.

[147] F. H. Schroder, J. Hugosson, M. J. Roobol, T. L. Tammela, S. Ciatto, V. Nelen*, et al.*, "Screening and prostate-cancer mortality in a randomized European study," *N Engl J Med,* vol. 360, pp. 1320-8, Mar 26 2009.

[148] F. H. Schroder, J. Hugosson, M. J. Roobol, T. L. Tammela, S. Ciatto, V. Nelen*, et al.*, "Prostate-cancer mortality at 11 years of follow-up," *N Engl J Med,* vol. 366, pp. 981-90, Mar 15 2012.

[149] G. Draisma, R. Etzioni, A. Tsodikov, A. Mariotto, E. Wever, R. Gulati*, et al.*, "Lead time and overdiagnosis in prostate-specific antigen screening: importance of methods and context," *J Natl Cancer Inst,* vol. 101, pp. 374-83, Mar 18 2009.

[150] Y. Gu, R. Mason, and H. Liu, "Estimated fraction of tumor vascular blood contents sampled by near infrared spectroscopy and 19F magnetic resonance spectroscopy," *Opt Express,* vol. 13, pp. 1724-33, Mar 07 2005.

[151] Y. He, H. Y. Song, A. G. Pereira, and A. H. Gomez, "Measurement and analysis of soil nitrogen and organic matter content using near-infrared spectroscopy techniques," *J Zhejiang Univ Sci B,* vol. 6, pp. 1081-6, Nov 2005.

[152] S. van de Ven, S. Elias, A. Wiethoff, M. van der Voort, A. Leproux, T. Nielsen*, et al.*, "Diffuse optical tomography of the breast: initial validation in benign cysts," *Mol Imaging Biol,* vol. 11, pp. 64-70, Mar-Apr 2009.

[153] B. J. Tromberg, B. W. Pogue, K. D. Paulsen, A. G. Yodh, D. A. Boas, and A. E. Cerussi, "Assessing the future of diffuse optical imaging technologies for breast cancer management," *Med Phys,* vol. 35, pp. 2443-51, Jun 2008.

[154] P. Taroni, G. Valentini, D. Comelli, C. D'Andrea, R. Cubeddu, D. N. Hu*, et al.*, "Time-resolved microspectrofluorimetry and fluorescence lifetime imaging of hypericin in human retinal pigment epithelial cells," *Photochem Photobiol,* vol. 81, pp. 524-8, May-Jun 2005.

[155] A. Pifferi, P. Taroni, A. Torricelli, F. Messina, R. Cubeddu, and G. Danesini, "Four-wavelength time-resolved optical mammography in the 680-980-nm range," *Opt Lett,* vol. 28, pp. 1138-40, Jul 01 2003.

[156] J. Selb, D. K. Joseph, and D. A. Boas, "Time-gated optical system for depth-resolved functional brain imaging," *J Biomed Opt,* vol. 11, p. 044008, Jul-Aug 2006.

[157] B. Pogue, M. Testorf, T. McBride, U. Osterberg, and K. Paulsen, "Instrumentation and design of a frequency-domain diffuse optical tomography imager for breast cancer detection," *Opt Express,* vol. 1, pp. 391-403, Dec 22 1997.

[158] A. Siegel, J. J. Marota, and D. Boas, "Design and evaluation of a continuous-wave diffuse optical tomography system," *Opt Express,* vol. 4, pp. 287-98, Apr 12 1999.

[159] M. Schweiger and S. R. Arridge, "Comparison of two- and three-dimensional reconstruction methods in optical tomography," *Appl Opt,* vol. 37, pp. 7419-28, Nov 01 1998.

[160] T. Svensson, S. Andersson-Engels, M. Einarsdottir, and K. Svanberg, "In vivo optical characterization of human prostate tissue using near-infrared time-resolved spectroscopy," *J Biomed Opt,* vol. 12, p. 014022, Jan-Feb 2007.

[161] R. A. Weersink, A. Bogaards, M. Gertner, S. R. Davidson, K. Zhang, G. Netchev*, et al.*, "Techniques for delivery and monitoring of TOOKAD (WST09)-mediated photodynamic therapy of the prostate: clinical experience and practicalities," *J Photochem Photobiol B,* vol. 79, pp. 211-22, Jun 01 2005.

[162] T. C. Zhu, J. C. Finlay, and S. M. Hahn, "Determination of the distribution of light, optical properties, drug concentration, and tissue oxygenation in-vivo in human prostate during motexafin lutetium-mediated photodynamic therapy," *J Photochem Photobiol B,* vol. 79, pp. 231-41, Jun 01 2005.

[163] J. Li and T. C. Zhu, "Determination of in vivo light fluence distribution in a heterogeneous prostate during photodynamic therapy," *Phys Med Biol,* vol. 53, pp. 2103-14, Apr 21 2008.

[164] K. K. Wang and T. C. Zhu, "Reconstruction of in-vivo optical properties for human prostate using interstitial diffuse optical tomography," *Opt Express,* vol. 17, pp. 11665-72, Jul 06 2009.

[165] M. L. Pantelides, C. Whitehurst, J. V. Moore, T. A. King, and N. J. Blacklock, "Photodynamic therapy for localised prostatic cancer: light penetration in the human prostate gland," *J Urol,* vol. 143, pp. 398-401, Feb 1990.

[166] L. K. Lee, C. Whitehurst, M. L. Pantelides, and J. V. Moore, "An interstitial light assembly for photodynamic therapy in prostatic carcinoma," *BJU Int,* vol. 84, pp. 821-6, Nov 1999.

[167] G. E. Strangman, Z. Li, and Q. Zhang, "Depth sensitivity and source-detector separations for near infrared spectroscopy based on the Colin27 brain template," *PLoS One,* vol. 8, p. e66319, 2013.

[168] P. Filzmoser, R. Baumgartner, and E. Moser, "A hierarchical clustering method for analyzing functional MR images," *Magn Reson Imaging,* vol. 17, pp. 817-26, Jul 1999.

[169] S. Fantini, M. A. Franceschini, and E. Gratton, "Effective source term in the diffusion equation for photon transport in turbid media," *Appl Opt,* vol. 36, pp. 156-63, Jan 01 1997.

[170] M. M. Shen and C. Abate-Shen, "Molecular genetics of prostate cancer: new prospects for old challenges," *Genes Dev,* vol. 24, pp. 1967-2000, Sep 15 2010.

[171] D. G. Bostwick and L. Cheng, "Precursors of prostate cancer," *Histopathology,* vol. 60, pp. 4-27, Jan 2012.

[172] A. Ziada, M. Rosenblum, and E. D. Crawford, "Benign prostatic hyperplasia: an overview," *Urology,* vol. 53, pp. 1-6, Mar 1999.

[173] C. G. Roehrborn, "Benign prostatic hyperplasia: an overview," *Rev Urol,* vol. 7 Suppl 9, pp. S3-S14, 2005.

[174] T. Kosaka, Y. Miyazaki, A. Miyajima, S. Mikami, Y. Hayashi, N. Tanaka*, et al.*, "The prognostic significance of vasohibin-1 expression in patients with prostate cancer," *Br J Cancer,* vol. 108, pp. 2123-9, May 28 2013.

Biographical Information

Xinlong Wang was born and brought up in Beijing, P. R. China. He earned his undergraduate degree in Applied Physics (in Optical and Electrical Engineering) from Beijing University of Technology, P. R. China. in the year of 2012. He joined the Department of Bioengineering, the University of Texas at Arlington in 2013. He was engaged in a prostate cancer research project in 2013-2014, the Diffuse Correlation Spectroscopy research project in 2015, and the Transcanial Photobiomodulation research project in 2015-2017. His research work has resulted in three peer-reviewed, 1st-author journal papers, two peer-reviewed, co-author journal papers, and several manuscripts under review or under smooth preparation that can be submitted very soon. He has given 7 research presentations and published 3 conference proceeding papers at either SPIE conferences or OSA Biomedical Optics topical meetings. His areas of research interests include experimental design, computational modeling, statistical analysis and optical instrumentation.